Light propagation in free-form dielectric waveguides: a modal perspective

Zur Erlangung des akademischen Grades eines

DOKTORS DER NATURWISSENSCHAFTEN (Dr. rer. nat.)

von der KIT-Fakultät für Physik des
Karlsruher Instituts für Technologie (KIT)
vorgelegte

DISSERTATION

von

Maria Bogusława Paszkiewicz-Idzik
aus Łódź, Polen

am Institut für Theoretische Festkörperphysik

Tag der mündlichen Prüfung:	25. April 2025
Referent:	Prof. Dr. Carsten Rockstuhl
Korreferent:	Prof. Dr. Willy Dörfler

Abstract

Light propagation in curved waveguides has recently attracted increasing attention due to their numerous applications and advancements in fabrication technologies. For instance, emerging three-dimensional nano-printing techniques enable the production of photonic wire bonds that connect different photonic integrated circuits to form complete chips. Curved waveguides and ring resonators can also be employed to generate nonclassical states of light on a chip, provided that nonlinear effects occur in these structures. The nonclassical states of light are crucial for on-chip quantum photonic technologies such as quantum communication and computation.

While numerical solvers for Maxwell's equations facilitate the study of light propagation in free-form waveguides, the large spatial extent of the waveguides often excludes these approaches. This limitation necessitates the development of approximate methods to describe light propagation in curved waveguides, exploiting the fact that light is guided through propagating modes. An understanding of the modal properties of curved photonic structures such as waveguides and disk-shaped resonators is essential for their effective design.

This thesis investigates light propagation and mode interactions in curved waveguides from various perspectives. We present a modal approach to analyse light propagation and losses in free-form waveguides. Changing the curvature of a waveguide may lead to excitement of multiple-modes in this waveguide. The number of supported modes depends on the size and refractive index contrast between the waveguide's core and the cladding. We introduce a multi-mode approximation method for calculating transmission through free-form waveguides. The obtained transmission is used as an objective function to identify the optimal waveguide trajectory in just a few minutes. These trajectories are optimised to minimise propagation losses caused by bends, while adhering to various constraints.

Additionally, we explore the enhancement of nonlinearity in bent waveguides, while considering propagation losses. We demonstrate that bending a waveguide may reduce the effective mode area, which in turn locally increases the intensity of the guided light. This enhances nonlinear interactions and boosts photon pair generation rates, significantly improving the efficiency of signal-processing devices in integrated photonic circuits.

Finally, we analyse mode interactions in disk-shaped whispering gallery resonators. Similarly to the bent waveguides, where the electromagnetic field localises near the outer side of the bend, in disk-shaped resonators, the field localises at the rim, creating resonances through the formation of standing waves. These resonators can be viewed as extreme cases of bent waveguides with a constant radius of curvature. The radiation modes emitted from these structures pose challenges in capturing their properties. We utilise a cross-energy scalar product to analyse these radiation modes, determining the resonator's dimensions at which the orthogonality between resonant modes is disrupted, leading to interactions between them.

Publications

In the course of this thesis, the author contributed to research published in peer-reviewed articles, articles submitted for review, and conference presentations listed below.

Peer-reviewed articles

- [P1] Nesic, A., Blaicher, M., Orlandini, E., Olariu, T., **Paszkiewicz, M.**, Negredo, F., Kraft, P., Sukhova, M., Hofmann, A., Dörfler, W., Rockstuhl, C., Freude, W., Koos, C., "Transformation-optics modeling of 3D-printed freeform waveguides," Optics Express **30**, 38856–38879 (2022).
- [P2] **Paszkiewicz, M.**, Sukhova, M., Dörfler, W., Rockstuhl, C., "Approximation method for fast calculation of transmission in multi-mode waveguides," Journal of the Optical Society of America A **41**, 174–184 (2024).
- [P3] **Paszkiewicz, M.**, Rockstuhl, C., "Enhancement of the photon pair generation rate by spontaneous four-wave mixing in bent waveguides," Physical Review A **111**, 013507 (2025).

Articles submitted for review

- [S1] **Paszkiewicz-Idzik, M.**, Rebholz, L., Rockstuhl, C., Fernandez-Corbaton, I., "A scalar product for radiating resonant modes," arXiv preprint arXiv:2411.02892 (2024).

Conference contributions

- [C1] **Paszkiewicz-Idzik, M.**, Sukhova, M., Dörfler, W., Rockstuhl, C., "Optimizing the trajectories of freeform waveguides using a modal theory," in Computational optics 2024, Vol. PC13023, edited by D. G. Smith and A. Erdmann (International Society for Optics and Photonics, 2024), PC1302305, Apr. 07–11, 2024, SPIE Optical Systems Design, Strasbourg, France.
- [C2] **Paszkiewicz-Idzik, M.**, Sukhova, M., Dörfler, W., Rockstuhl, C., "Optimizing the trajectories of freeform waveguides using a modal theory," in Optical modeling and performance predictions XIV, Vol. 13129, edited by M. A. Kahan and C. Merrill (International Society for Optics and Photonics, 2024), p. 1312903, Aug. 18–22, 2024, SPIE Optics + Photonics, San Diego, California, USA.
- [C3] **Paszkiewicz, M.**, Nesic, A., Koos, C., Dörfler, W., Rockstuhl, C., "Fast calculation of transmission along waveguides supporting propagation of higher order modes," Minisymposium 06: Advances in Inverse Design for Wave Propagation Problems,

Feb. 21–22, 2022, Conference on Mathematics of Wave Phenomena 2022, Karlsruhe, Germany.

[C4] **Paszkiewicz, M.**, Sukhova, M., Bao, Y., Koos, C., Dörfler, W., Rockstuhl, C., "Approximation methods for the fast calculation of transmission of photonic wire bonds," May 4–5, 2023, The XXIX International Workshop on Optical Wave and Waveguide Theory and Numerical Modelling, Marseille, France.

[C5] **Paszkiewicz, M.**, Sukhova, M., Dörfler, W., Rockstuhl, C., "Approximation methods for fast calculation of transmission in multimode waveguides," Inverse Problems, Sept. 27–29, 2023, MathSEE Symposium: Mathematics in Sciences, Engineering and Economics, Karlsruhe, Germany.

[C6] **Paszkiewicz-Idzik, M.**, Sipe, J. E., Rockstuhl, C., "Enhancement of the photon pair generation rate by spontaneous four-wave mixing in bent waveguides," May 23–24, 2024, The XXX International Workshop on Optical Wave and Waveguide Theory and Numerical Modelling, Kiel, Germany.

[C7] **Paszkiewicz, M.**, Sipe, J. E., Rockstuhl, C., "Enhancement of the photon pair generation rate in bent waveguides," in Optical modeling and performance predictions XIV, Vol. 13129, edited by M. A. Kahan and C. Merrill (International Society for Optics and Photonics, 2024), 131290R, Aug. 18–22, 2024, SPIE Optics + Photonics, San Diego, California, USA.

Conference contributions presented by others

[CO1] Bao, Y., **Paszkiewicz, M.**, Krimmer, J., Freude, W., Randel, S., Rockstuhl, C., Koos, C., "Loss prediction and 3D trajectory design of photonic wire bonds using artificial neural networks (ANN)," SM1I. Advances in Integrated Photonics, May 5–10, 2024, CLEO, Charlotte, North Carolina, USA.

[CO2] Sukhova, M., **Paszkiewicz, M.**, Dörfler, W., Rockstuhl, C., "Map of transmission coefficients for open bent waveguides with constant curvature," May 4–5, 2023, The XXIX International Workshop on Optical Wave and Waveguide Theory and Numerical Modelling, Marseille, France.

[CO3] Sukhova, M., **Paszkiewicz, M.**, Dörfler, W., Rockstuhl, C., "Map of transmission coefficients for open bent waveguides with constant curvature," Mathematical Modeling, Differential Equations, Numerics, Simulation, Sept. 27–29, 2023, MathSEE Symposium: Mathematics in Sciences, Engineering and Economics, Karlsruhe, Germany.

Contents

1 | Introduction

Waveguides are fundamental components of photonic integrated circuits (PICs) [1]. The PICs were introduced in 1969 [2] to miniaturise complicated and spacious optical setups into complex circuit patterns integrated onto a single microchip. Photonic integration not only reduces the size and weight of systems but also promises lower energy consumption and production costs, while increasing the efficiency of the optical systems [3]. The idea of a PIC is analogous to electronic integrated circuits. However, instead of using electrons, photonics relies on the generation, processing, and detection of photons. Harnessing the unique properties of photons opens new possibilities such as the use of various other materials that enhance data transfer speeds and bandwidths [4], as well as applications in metrology, sensing, and medical diagnostics [5, 6]. Some of the most intriguing applications include logical operations and computation [7–12], as well as quantum computations on a system of photonic chips [13].

The success of PICs is determined by our ability to suppress the usual diffraction that causes the spread of laser light upon propagation. By locally increasing the refractive index with respect to the background material, light can indeed be confined by total internal reflection and routed along carefully selected paths [2]. Such a supporting structure is what we call a *waveguide*. These waveguide patterns can be fabricated on a flat substrate (a *wafer*) using photolithographic techniques, as follows [2]. Firstly, a light-sensitive photoresist is deposited on a wafer. Next, a mask is placed over the photoresist to expose only the desired patterns. Subsequently, the refractive index in the exposed areas is altered using chemical processes such as diffusion, bombardment, or ion replacement. Depending on the design of the waveguide, a top layer of lower refractive index may be added on the surface. Of course, such approach should only serve as a loose description and many variants exists.

Initially, glass was suggested as a substrate, motivated by the fabrication of glass fibres known at the time [2]. However, many other material platforms have been developed since then. One example is silicon on insulator (SOI) [14], which consists of a thin insulating layer of silicon dioxide (SiO_2) sandwiched between two layers of silicon (Si). Waveguides in SOI platform are created by patterning the silicon layer to define the waveguide structure, followed by etching the silicon layer to form rib-shaped waveguides. Other material platforms include lithium niobate ($LiNbO_3$) [15, 16], silicon nitride (Si_3N_4) [17, 18], silica on silicon [19], III-V semiconductors such as indium phosphide (InP) [1] and gallium arsenide (GaAs) [20, 21], as well as various polymers [22, 23].

The PICs can host a range of devices, including lasers (sources), photodetectors, power splitters, filters, optical modulators, and amplifiers [1, 3, 24]. Waveguides are crucial for transmitting optical signals between these devices. Moreover, waveguides fabricated from nonlinear materials such as silicon, silicon nitride or aluminium gallium arsenide can also be used directly for generating non-classical states of light. It is possible due to the waveguide's ability to confine light. This enhances nonlinear processes through locally increased light intensity in a nonlinear material [18, 25, 26]. Integrating non-classical light sources on photonic chips facilitates quantum communication and optical quantum computation on a chip [27, 28]. The SOI platform is compatible with CMOS technology, allowing for the integration of optical components, which enable high-speed signalling and sensing, together with electronics for logical operations and computations [3, 29]. Ultimately, photonic chips require packaging and connections to other devices to form a functional system [24].

Different chips can be connected with three-dimensional (3D) free-form optical waveguides [30]. These waveguides are fabricated by means of the 3D nano-printing technology, also referred to as 3D laser lithography [31] or 3D direct laser writing [32, 33]. In this printing process, schematically presented in Figure 1.1, the substrate is immersed in a photopolymerising material that solidifies in those volumes into which a near-infrared laser is focused [34]. Other areas remain unaffected because the photoresist is transparent to the near-infrared light [34]. At the focal point of the laser beam, the density of photons is sufficiently high such that the *initiators* within the photoresist absorb pairs of photons and reach an excited state [35, 36], thus becoming *radicals*.[1] The chemical activity of these radicals initiates a chain reaction resulting in polymerisation and, consequently, local solidification of the photoresist. The absorption rate of photons is proportional to the square of the photon density [34, 38] because two near-infrared photons need to be absorbed by an electron simultaneously. The short lifetime of electrons in virtual (intermediate) excited states requires the use of femtosecond pulsed lasers [39]. In the case of single-photon absorption, the absorption rate is directly proportional to the photon density [34] because single photons of higher energy (at UV frequency) are absorbed [40]. This means that the solidification initiated by *two-photon absorption* occurs in smaller areas than the single-photon absorption because the required intensity of the light is higher [40]. Therefore, the *two-photon lithography* allows for the fabrication of 3D objects with a spatial resolution down to 120 nm [41]. This is sufficient for creating free-form waveguides of lateral dimensions between 1 µm and 2 µm [42].

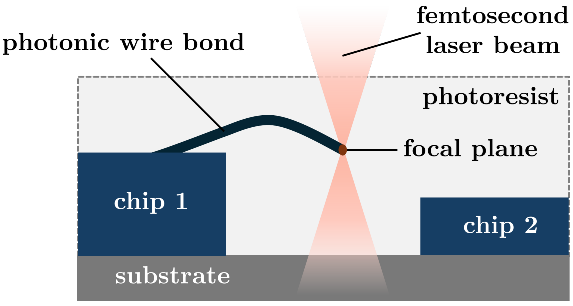

Figure 1.1.: Schematic view of a 3D printing of free-form waveguide (photonic wire bond) by means of two-photon polymerisation. The two chips, mounted on a common substrate, are immersed in a photopolymerising material that solidifies in those volumes into which a femtosecond laser beam is focused. The positions of the focal plane of the laser beam follow the trajectory of the free-form waveguide.

A free-form waveguide is fabricated by focusing the femtosecond laser pulses in a photoresist along a 3D path that connects two optical interfaces [43]. The 3D laser lithography

---

[1] Radicals are atoms or molecules with at least one unpaired valence electron [37]. They exist in excited, unstable state and are therefore very reactive.

provides precise control over the waveguide trajectory, as the laser can be moved freely in space. Similarly to how metal wire bonds connect integrated circuits to external components in electronics, polymer free-form waveguides connect photonic circuits located on different chips. Free-form waveguides represent a significant advancement in complex photonic circuits, enabling connections between chips made from different materials that cannot be integrated on a single chip [30]. For instance, III-V semiconductors are ideal for active components used to generate or detect light [44]. In contrast, SOI-based optical chips allow for dense integration of passive optical components, germanium photodetectors, and electro-optical modulators [42]. By utilising free-form optical waveguides, also known as *photonic wire bonds* (PWBs) [30, 42, 45–47, P1], these different constituents can be assembled into a single multifunctional architecture.

Photonic wire bonds offer great flexibility in connecting photonic chips, allowing for both out-of-plane and in-plane connections [42, 48]. This flexibility relaxes tight alignment requirements in the horizontal and vertical positioning of chip interfaces, introducing additional degrees of freedom compared to straight, flat waveguides. However, bending or twisting a waveguide can increase propagation losses [49]. Additionally, a change in curvature along the trajectory of the waveguide may excite higher-order modes or cause scattering of the guided modes into radiation modes [50, 51]. This excitation may impair the transmission through a waveguide because power carried by the fundamental mode may be lost to the higher-order or radiation modes [P2].

To minimise the propagation loss, it is essential to optimise the trajectories of the waveguides while adhering to several constraints [43]. The basic requirement is a smooth change of the curvature that should be free of sharp bends. Furthermore, the end facets of the PWBs must align with the ports of the waveguides that connect the PWBs to the chip interfaces, referred to as *waveguide couplers*. Moreover, the orientations of the end segments of the PWBs must coincide with the directions of the waveguide couplers. The designed trajectory should also avoid obstacles, such as chip edges or other PWBs. To account for placement inaccuracies of the chips, all the constraining positions are measured and the optimal trajectory is determined shortly before its fabrication. Therefore, a fast and reliable optimisation procedure is required for this task. To date, many methods have been developed to perform this trajectory optimisation [30, 42, 43, 46, P1, P2, 52, C1, C2, CO1, 53], including the procedures described in Chapter 3 and Chapter 4 of this thesis.

As the curvature of a waveguide changes, the modal properties of the waveguide change as well. Depending on the size and the refractive index of the waveguide, it can support multiple propagating modes. This thesis demonstrates that a careful study of the mode field profiles, including their symmetries and effective mode area, allows one to explain various phenomena occurring within these curved waveguides. In Chapter 3, for example, we study the coupling between modes at interfaces of waveguide sections with slightly different properties. Based on broken orthogonality between the modes, we determine the fraction of power interchanged between the modes in the process of transmission. Additionally, in Chapter 5, we explore the enhancement of nonlinearity in waveguides due to an increased confinement of the mode field profile when the waveguide is bent, while also accounting for the simultaneous increase in propagation loss.

When a waveguide is bent, the electromagnetic field of the modes tends to be localised near the outer side of the bend. A similar effect occurs in microrings or disk-shaped resonators, where the electromagnetic field is localised at the rim of these circular structures. A microring can be considered an extreme case of a bent waveguide in which the waveguide is fabricated so that its trajectory forms a circle [54]. Integrating microring resonators into a photonic chip is a common approach to enhance the nonlinearity through high confinement of light in the microrings [55]. Microrings and disk resonators are used as amplifiers, ring couplers [56, 57], spectral filters or modulators [58, 59], as well as sources of quantum states of light [60, 61]. These structures create resonances by forming standing waves localised at their rims [57]. The resonant modes are not purely guided, but also radiate outside the resonator. In Chapter 6, we analyse the radiating modes of a disk resonator to explore its modal properties. Understanding these properties is important for the design and tuning of these resonators.

Structure of the thesis

This thesis is organised into five main chapters. It begins with Chapter 2, which introduces the fundamentals of the waveguide theory. The purpose of that chapter is to provide the necessary background to understand modal phenomena explored in this thesis. We start by discussing Maxwell's equations and the constitutive relations, then formulate Helmholtz wave equations for electric and magnetic fields, ultimately finding plane wave solutions for these fields in the homogenous space. Further, we explain the propagation of light in a slab waveguide from both an intuitive ray-optical perspective and a more accurate wave-optical picture. We introduce the concept of a propagating mode and eigenmode expansion for electric and magnetic fields. Then, we provide a brief overview of the numerical methods employed to calculate modes in channel waveguides. We then discuss loss mechanisms in curved waveguides and describe a *fundamental mode approximation* method for calculating waveguide transmission, assuming the propagation of a single mode.

Up to this point, the thesis summarises the state of the art and the work done prior to this thesis. From the following chapter on, novel contributions to the advancement of science are described. The results presented in Chapters 3, 4, and 5 represent the primary scientific contributions made by the author of this thesis, while Chapter 6 originates from a project developed in significant extent by the co-authors of [S1].

Chapter 3 extends fundamental mode approximation from the introductory chapter to accommodate higher-order propagating modes that may be excited due to changes in the curvature of a waveguide. This *multi-mode approximation* method is described and used to calculate the transmission through exemplary waveguides. The results are compared with the transmission obtained using the fundamental mode approximation as well as with results from a commercial Maxwell solver. It is demonstrated that multi-mode approximation can predict the transmission sufficiently accurate in less than a second for a typical waveguide trajectory, in contrast to several hours required for numerical calculations with the Maxwell solver. Additionally, we discuss the potential for training artificial neural networks to approximate waveguide transmission based on their trajectories. That would be an alternative method to predict the transmission losses through curved waveguides in a short time.

In Chapter 4, the transmission obtained with the multi-mode approximation is utilised to determine values of an objective function for optimising trajectories of PWBs, satisfying the given set of constraints. The results and optimisation times are shown for several possible on-chip scenarios.

Chapter 5 touches on nonlinear effects in waveguides. Waveguides made of nonlinear materials can be employed to create quantum states of light. Third-order nonlinear effects can be exploited to create pairs of entangled photons in waveguides. We demonstrate that the generation rate of photon pairs can be increased by bending a waveguide. The influence of bending on the photon pair generation rate is studied on the example of waveguides made of third-order nonlinear materials. We consider here typical materials that are discussed in the context of PICs where the waveguides are integrated directly onto a chip, but we also consider a free-form waveguide made of polymer. This study includes a comprehensive analysis of changes in the effective nonlinear coefficient, effective mode area, effective refractive index, and group velocity of the fundamental mode as a function of the curvature of several waveguide examples. The study concludes with a comparison of the efficiency of nonlinear processes affected by propagation losses.

In Chapter 6, we investigate the interaction of resonant modes in a disk-shaped whispering gallery resonator. The modes are commonly arranged by ascending order of their resonance frequencies. However, when the thickness of the disk changes, some modes experience spectral crossings, while others undergo anti-crossings at the thicknesses for which the resonant frequencies near each other. We show that computing the scalar product of the radiation modes corresponding to the resonant modes can indicate the disk geometry at which the anti-crossings occur, revealing the broken orthogonality of the modes and their interaction.

Finally, Chapter 7 summarises the research described in the previous chapters and provides an outlook for further developments in the field of free-form waveguides.

This thesis is equipped with a separate list of symbols and abbreviations, located directly after the concluding chapter. Although all symbols and acronyms are explained upon first use, it may be more convenient for the Reader to refer to the list for their meanings rather than searching through the main text.

2 | Waveguide theory

This chapter provides a concise overview of the fundamentals of optical waveguide theory. The theory described here is limited to the aspects necessary to understand the research done as a part of this thesis. This chapter starts with the introduction of classical electromagnetism in Section 2.1. Afterwards, the phenomenon of guiding light in waveguides is described from both ray-optical and wave-optical perspectives in Section 2.2 in the first two dedicated subsections. Subsequently, in Subsection 2.2.3, the concept of the propagating modes is introduced, along with the orthogonality relations between the modes covered in Subsection 2.2.4. Additionally, Section 2.3 explains briefly the numerical methods used to identify the eigenmodes of the electromagnetic field confined within a waveguide. This section also describes how to compute the transmission through complicated waveguide trajectories using numerical tools that directly solve Maxwell's equations. Such an analysis serves as a benchmark for the approximation methods developed as part of this PhD research. Later, Section 2.4 discusses various loss mechanisms in waveguides. Section 2.5 introduces the fundamental mode approximation that is used to predict the transmission through a waveguide trajectory while considering only the propagation of the fundamental mode. This approximation method is described here in the background chapter, as it has been already known prior the current PhD research. In the subsequent chapter this method is extended to accommodate also higher-order modes.

2.1. Classical electromagnetism

The theoretical description begins with the governing equations that describe all observable phenomena of electromagnetic fields. The presence of matter is not treated at the level of individual charges, but we consider a macroscopic, i.e., a continuum description of materials. The associated macroscopic[1] electromagnetic phenomena in the presence of media are governed by the Maxwell equations[2]

$$\nabla \cdot \widetilde{\mathbf{D}}(\mathbf{r},t) = \varrho(\mathbf{r},t)\,, \tag{2.1}$$

$$\nabla \cdot \widetilde{\mathbf{B}}(\mathbf{r},t) = 0\,, \tag{2.2}$$

$$\nabla \times \widetilde{\mathbf{E}}(\mathbf{r},t) = -\frac{\partial \widetilde{\mathbf{B}}(\mathbf{r},t)}{\partial t}\,, \tag{2.3}$$

$$\nabla \times \widetilde{\mathbf{H}}(\mathbf{r},t) = \widetilde{\mathbf{J}}(\mathbf{r},t) + \frac{\partial \widetilde{\mathbf{D}}(\mathbf{r},t)}{\partial t}\,. \tag{2.4}$$

The physical quantities in the expressions (2.1)–(2.6) are expressed in SI units, according to the convention in Table 2.1. The presence of sources is captured by the electric charge density $\varrho(\mathbf{r},t)$ and electric current density $\widetilde{\mathbf{J}}(\mathbf{r},t)$, where vector $\mathbf{r} = (x,y,z)^{\mathrm{T}}$ defines a

---

[1] Macroscopic fields or sources mean the average of the fields or sources over a volume large compared to the volume occupied by the single particle [62].

[2] The Maxwell equations together with in-depth explanation can be found in many electrodynamics and optics textbooks. In this thesis the description is based on [62–64].

Table 2.1.: Electromagnetic quantities in frequency domain.[3] The corresponding quantities with *tilde* placed above the letter are considered in time domain.

symbol	meaning	units
$\mathbf{D}$	electric displacement	$\mathrm{C{\cdot}m^{-2}}$
$\mathbf{B}$	magnetic induction	T
$\mathbf{E}$	electric field	$\mathrm{V{\cdot}m^{-1}}$
$\mathbf{H}$	magnetic field	$\mathrm{A{\cdot}m^{-1}}$
$\mathbf{J}$	current density	$\mathrm{A{\cdot}m^{-2}}$
ϱ	charge density	$\mathrm{C{\cdot}m^{-3}}$
$\mathbf{P}$	polarisation	$\mathrm{C{\cdot}m^{-2}}$
$\mathbf{M}$	magnetisation	$\mathrm{A{\cdot}m^{-1}}$

position in three-dimensional space, and t denotes time. To solve the above set of equations, one needs to express the derived (auxiliary) fields, $\widetilde{\mathbf{D}}$ and $\widetilde{\mathbf{H}}$, in terms of $\widetilde{\mathbf{E}}$ and $\widetilde{\mathbf{B}}$. These connections are known as *constitutive relations*

$$\widetilde{\mathbf{D}}(\mathbf{r},t) = \varepsilon\widetilde{\mathbf{E}}(\mathbf{r},t) + \widetilde{\mathbf{P}}(\mathbf{r},t)\,, \tag{2.5}$$

$$\widetilde{\mathbf{B}}(\mathbf{r},t) = \mu\widetilde{\mathbf{H}}(\mathbf{r},t) + \widetilde{\mathbf{M}}(\mathbf{r},t)\,. \tag{2.6}$$

Here, ε and μ are the electric permittivity and magnetic permeability of a considered medium, respectively.

In linear optics, it is common to express the Maxwell equations in frequency domain. The initial equations in time domain (2.1)–(2.4) can be transformed to the frequency domain using the Fourier transform defined as

$$\mathbf{F}(\mathbf{r},\omega) = \int\limits_{-\infty}^{+\infty} \widetilde{\mathbf{F}}(\mathbf{r},t)\mathrm{e}^{\mathrm{i}\omega t}\mathrm{d}t\,, \qquad \widetilde{\mathbf{F}}(\mathbf{r},t) = \frac{1}{2\pi}\int\limits_{-\infty}^{+\infty} \mathbf{F}(\mathbf{r},\omega)\mathrm{e}^{-\mathrm{i}\omega t}\mathrm{d}\omega\,, \tag{2.7}$$

with $\mathbf{F}(\mathbf{r},\omega)$ being the Fourier transform of the field $\widetilde{\mathbf{F}}(\mathbf{r},t)$,[4] ω denoting the angular frequency of a monochromatic wave, and i representing the imaginary unit. Throughout this thesis, the theoretical analysis is performed in frequency domain.

The constitutive relations (2.5)–(2.6) express the response of the material to the field. For isotropic, homogeneous, linear media, and for time-harmonic fields [64], the polarisation and magnetisation depend linearly on the electric and magnetic field, respectively. Therefore,

---

[3] Following the convention from [62]. It is interesting to note that the electromagnetic quantities are called by different names in the literature, e.g. $\mathbf{D}$ – electric flux density [65]; $\mathbf{B}$ – magnetic field [63], magnetic flux density [65]; $\mathbf{E}$ – electric field strength [65], electric field intensity [66], electric vector [64]; $\mathbf{H}$ – magnetic vector [64], auxiliary magnetic field [63], magnetic field strength [65], magnetic field intensity [66, 67]. The vectors are defined in Cartesian coordinates $\mathbf{F} = (F_x, F_y, F_z)^{\mathrm{T}}$, with $\mathbf{F}$ denoting either of the vectorial quantities.

[4] Although it is more common to use *tilde* for quantities in frequency domain, it is skipped here to simplify the notation later in the thesis.

the constitutive relations can be written as simple as:

$$\mathbf{D}(\mathbf{r},\omega)=\varepsilon(\omega)\mathbf{E}(\mathbf{r},\omega)\quad\text{and}\quad\mathbf{B}(\mathbf{r},\omega)=\mu(\omega)\mathbf{H}(\mathbf{r},\omega)\,, \tag{2.8}$$

where a dielectric material is characterised by its permittivity $\varepsilon(\omega)=\varepsilon_0\varepsilon_r(\omega)$ and magnetic permeability $\mu(\omega)=\mu_0\mu_r(\omega)$. The subscript 0 expresses a relation to the values for vacuum and subscript r indicates the relative values. In this thesis, only non-magnetic media are assumed, for which $\mu_r=1$ [68].

The Maxwell equations in (2.1)–(2.4) can be simplified by performing the Fourier transform (2.7). The resulting expressions can be rewritten in terms of $\mathbf{E}(\mathbf{r},\omega)$ and $\mathbf{H}(\mathbf{r},\omega)$ after considering constitutive relations (2.8). In the absence of free charges and currents, and in non-magnetic media, the Maxwell equations in frequency domain are expressed as follows

$$\nabla\cdot\mathbf{E}(\mathbf{r},\omega)=0\,, \tag{2.9}$$

$$\nabla\cdot\mathbf{H}(\mathbf{r},\omega)=0\,, \tag{2.10}$$

$$\nabla\times\mathbf{E}(\mathbf{r},\omega)=\mathrm{i}\omega\mu_0\mathbf{H}(\mathbf{r},\omega)\,, \tag{2.11}$$

$$\nabla\times\mathbf{H}(\mathbf{r},\omega)=-\mathrm{i}\omega\varepsilon(\omega)\mathbf{E}(\mathbf{r},\omega)\,. \tag{2.12}$$

Taking the curl of equations (2.11) and (2.12), rewriting them utilising the identity $\nabla\times\nabla\times\mathbf{F}=\nabla(\nabla\cdot\mathbf{F})-\nabla^2\mathbf{F}$, with $\mathbf{F}$ being either $\mathbf{E}$ or $\mathbf{H}$, while considering relations (2.9) – (2.12), the Helmholtz wave equations [62, Section 7.1] can be derived separately for the electric or magnetic field:

$$\nabla^2\mathbf{E}(\mathbf{r},\omega)+k_0^2(\omega)\varepsilon_r(\omega)\mathbf{E}(\mathbf{r},\omega)=0\,, \tag{2.13}$$

$$\nabla^2\mathbf{H}(\mathbf{r},\omega)+k_0^2(\omega)\varepsilon_r(\omega)\mathbf{H}(\mathbf{r},\omega)=0\,. \tag{2.14}$$

In the above equations, $k_0(\omega)=\omega\cdot c_0^{-1}=\omega\sqrt{\varepsilon_0\mu_0}$ is the free-space vacuum wavenumber, where c_0 denotes the speed of light in vacuum.

The Helmholtz wave equations (2.13) and (2.14) are solved by plane waves of the form

$$\mathbf{E}(\mathbf{r},\omega)=\mathbf{E}_0\mathrm{e}^{\mathrm{i}(\mathbf{k}(\omega)\cdot\mathbf{r}-\omega t)}, \tag{2.15}$$

$$\mathbf{H}(\mathbf{r},\omega)=\mathbf{H}_0\mathrm{e}^{\mathrm{i}(\mathbf{k}(\omega)\cdot\mathbf{r}-\omega t)}, \tag{2.16}$$

where $\mathbf{k}(\omega)=k_0(\omega)\sqrt{\varepsilon_r(\omega)}\,\hat{\mathbf{k}}$ is a wave vector defining the direction of propagation of the electromagnetic wave, with unit vector $\hat{\mathbf{k}}$. The divergence equations (2.9) and (2.10) require that both vectors, $\mathbf{E}_0$ and $\mathbf{H}_0$, are perpendicular to the direction of propagation of the electromagnetic wave $\mathbf{k}(\omega)$. This kind of wave is called a *transverse wave* [62, Chapter 7].

The relative dielectric function can be expressed as $\varepsilon_r(\omega)=n(\omega)^2$, where $n(\omega)=n^{(r)}(\omega)+\mathrm{i}n^{(i)}(\omega)$ is the complex refractive index with real part $n^{(r)}(\omega)$ expressing the phase variation of the propagating plane wave. The imaginary part $n^{(i)}(\omega)$ represents the attenuation (if positive) or amplification (if negative) of the propagating plane wave (cf. equations (2.15) and (2.16)). The wavenumber of a medium is related to the complex refractive index by $k(\omega)=k_0n(\omega)$.

A propagating electromagnetic wave carries energy. For a time-harmonic field, the time-averaged energy flux is given by the average of the Poynting vector $\overline{\mathbf{S}}(\mathbf{r},\omega)$ over time [62, Chapter 7]

$$\overline{\mathbf{S}}(\mathbf{r},\omega)=\frac{1}{2}\mathrm{Re}\{\mathbf{E}(\mathbf{r},\omega)\times\mathbf{H}^*(\mathbf{r},\omega)\}, \tag{2.17}$$

with * denoting complex conjugate.

In this section, it is assumed that the wave propagates in vacuum or a homogeneous dielectric medium. The next section introduces the concept of a waveguide, in which the wave is guided along a waveguide core. In a ray-optical picture, this guidance can be attributed to the total internal reflection of the rays at plane interfaces between different dielectrics. In a wave-optical picture, we would rather seek for elementary solutions to the Maxwell equations that propagate along the waveguides without diffraction. The next section discusses in more detail the light propagation of such waveguide modes in slab and rectangular waveguides. We start with a ray-optical picture and complement the consideration with an analysis using a wave-optical picture.

2.2. Light propagation in a waveguide

In this section, the theory presented in Section 2.1 is applied to study a wave confined inside a waveguide. The propagation of light in the waveguide is analysed both geometrically, based on the total internal reflection of optical rays, and by starting from Maxwell's equations. For the specific aspects that matter to this thesis, both approaches offer comparable insights. Concerning the argumentation to explain specific effects, it is sometimes useful to rely on a wave-optical and sometimes on a ray-optical description. Therefore, both approaches are presented.

2.2.1. Slab waveguide

A slab waveguide is a structure made of an inner layer (core) of guiding material with refractive index n_1 and thickness h, surrounded by a cladding with smaller refractive index n_2, as depicted in Figure 2.1(a). So the material is inhomogeneous along a single coordinate (here, the x-direction). The structure of the slab waveguide is invariant along the two remaining directions, y and z. Here, the z direction is considered as the principal propagation direction. In the following derivations, the two materials are considered to be non-dispersive, hence $\varepsilon_{1,2}(\omega) = \varepsilon_{1,2}$ and so $n_{1,2}(\omega) = n_{1,2}$. In this thesis, only symmetric waveguides are considered, made of identical cladding material on adjacent sides of the core. Accommodating an asymmetric environment is also possible but not necessary for the purposes of this work.

Ray-optical picture

In a ray-optical picture light is considered to consist of rays that propagate along straight paths. The rays are reflected and transmitted at interfaces between different media, and so they change their direction of propagation. Moreover, the light that propagates along these paths accumulates the same phase that a plane wave propagating in that medium would accumulate. To describe important effects for a waveguide theory a transverse electromagnetic plane wave is associated with each ray, following [69, Chapter 7].

Waveguides exploit the phenomenon of total internal reflection to guide light, as illustrated in Figure 2.1(a). To achieve this effect, the refractive index of the core n_1 must be higher than the refractive index of the cladding n_2. This observation follows directly from the Snell's law [70]

$$n_1 \sin\theta_1 = n_2 \sin\theta_2, \tag{2.18}$$

which describes the relation between the angle of incidence θ_1 and the angle of refraction θ_2 that depends on the refractive indices of the different isotropic media, when the wave passes through a boundary between these two media, see Figure 2.1(b). When light rays strike the core-cladding interface incident from the core, at an angle of incidence $\theta_1 = \theta$ higher than the critical value θ_c, for which $\theta_2 = \frac{\pi}{2}$, the light undergoes total internal reflection. As a result, the electromagnetic field is confined within the waveguide core. For a mode to occur, the field needs to reproduce periodically. For the following analysis, both media are assumed to be lossless, meaning that the refractive indices are real.

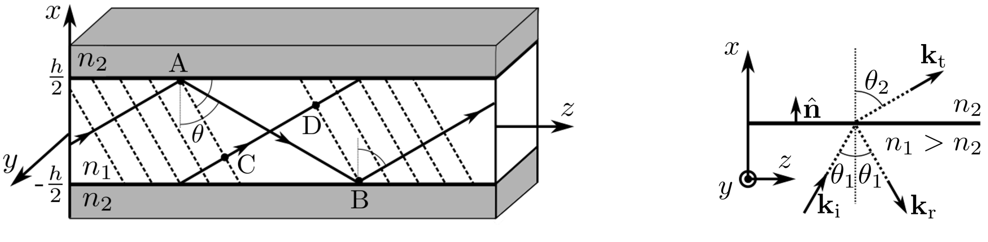

(a) (b)

Figure 2.1.: (a) Two exemplary rays traversing a slab waveguide core (refractive index n_1 and height h). The waves at points B and D must agree in phase in order to result in a propagating wave in z-direction. In the figure n_2 denotes the refractive index of the cladding and θ is the angle of incidence of the guided rays (all marked angles have the same value) on the interface between the core and the cladding. Dashed lines represent wavefronts equal in phase (distance between them is the wavelength λ). The wavefronts are perpendicular to the direction of rays. (b) Reflection and transmission of incident ray at the plane interface. The vectors $\mathbf{k}_\mathrm{i}$, $\mathbf{k}_\mathrm{r}$ and $\mathbf{k}_\mathrm{t}$ denote the direction of incident, reflected and transmitted wave, respectively. Surface normal is represented by a unit vector $\hat{\mathbf{n}}$.

The following explanation is based on the configuration shown in Figure 2.1(a), which illustrates a cross-section of a slab waveguide. The propagating rays, with the direction indicated by arrows, are used to describe the field that propagates inside the waveguide. The surfaces of equal phase, perpendicular to the rays, are marked with dashed lines. In analogy to propagating wave, these surfaces are called here *wavefronts*. To reproduce the wavefronts, the phase difference accumulated between rays along the paths |AB| and |CD| must be a multiple of 2π. From geometric considerations, the following dispersion relation must be satisfied:

$$\begin{aligned} &\frac{h}{\cos\theta}k_1 - 2\phi - \left(\frac{h}{\cos\theta}k_1 - 2hk_1\cos\theta\right) = 2\pi m \\ \iff\quad &2hk_1\cos\theta = 2\phi + 2\pi m\,. \end{aligned} \tag{2.19}$$

Here, $k_1 = n_1 k_0$ is the wave number of the wave propagating inside the waveguide core, ϕ is a phase shift accumulated by the wave upon each reflection[5] at the core-cladding interface and m is a non-negative integer indicating the mode number. The wave number is defined as $2\pi\lambda^{-1}$, where λ is a distance between wavefronts. The relation (2.19) is solved for the effective refractive index $n_\mathrm{eff} = n_1\cos\theta$ by changing the considered angle θ. In order to evaluate this equation, the phase shift ϕ is determined in the following.

---

[5] The ray at point B has been reflected two times more than the ray at point D in Figure 2.1(a).

Reflection from a plane dielectric boundary

To compute the phase shift, we need to determine essentially the complex-valued reflection coefficient of a plane wave at a planar interface between the core and the cladding. Figure 2.1(b) illustrates the incident (subscript i), reflected (r), and transmitted (t) plane waves on the interface between the core and the cladding. The field components of the associated plane waves are perpendicular to the propagation direction indicated by the ray, denoted by $\mathbf{k}_\mathrm{i}$, $\mathbf{k}_\mathrm{r}$ and $\mathbf{k}_\mathrm{t}$ for incident, reflected, and transmitted (refracted) wave, respectively. Inserting the solutions (2.15) and (2.16) into equations (2.11) and (2.12), the incident fields of linearly polarised wave in the waveguide core ($-\frac{h}{2} \leq x \leq \frac{h}{2}$) can be expressed as:

$$\mathbf{E}_\mathrm{i}(\mathbf{r}) = \mathbf{E}_{0,\mathrm{i}} \mathrm{e}^{\mathrm{i}\mathbf{k}_\mathrm{i} \cdot \mathbf{r}} = -\frac{1}{\omega n_1^2} \mathbf{k}_\mathrm{i} \times \mathbf{H}_{0,\mathrm{i}} \mathrm{e}^{\mathrm{i}\mathbf{k}_\mathrm{i} \cdot \mathbf{r}}, \tag{2.20}$$

$$\mathbf{H}_\mathrm{i}(\mathbf{r}) = \frac{1}{\omega \mu_0} \mathbf{k}_\mathrm{i} \times \mathbf{E}_{0,\mathrm{i}} \mathrm{e}^{\mathrm{i}\mathbf{k}_\mathrm{i} \cdot \mathbf{r}}, \tag{2.21}$$

$$\mathbf{D}_\mathrm{i}(\mathbf{r}) = \epsilon_0 n_1^2 \mathbf{E}_\mathrm{i}(\mathbf{r}) \,, \tag{2.22}$$

$$\mathbf{B}_\mathrm{i}(\mathbf{r}) = \mu_0 \mathbf{H}_\mathrm{i}(\mathbf{r}) \,, \tag{2.23}$$

where $\mathbf{k}_\mathrm{i} = (k_{\mathrm{i},x}, 0, k_{\mathrm{i},z})^\mathrm{T} = n_1 k_0 (\cos\theta, 0, \sin\theta)^\mathrm{T}$ is the wave vector of the incident wave in the waveguide core. The frequency and time dependence is omitted because it is not relevant for the following derivation. We always assume time harmonic fields. The corresponding expressions to describe the reflected and transmitted field components and wave vectors are analogous.

The individual components of the incident, reflected, and transmitted fields are related through the interface conditions. First, we require the continuity of the normal components of $\mathbf{D}$ and $\mathbf{B}$

$$(n_1^2 \mathbf{E}_\mathrm{i} + n_1^2 \mathbf{E}_\mathrm{r} - n_2^2 \mathbf{E}_\mathrm{t}) \cdot \hat{\mathbf{n}} = 0 \,, \tag{2.24}$$

$$(\mathbf{k}_\mathrm{i} \times \mathbf{E}_\mathrm{i} + \mathbf{k}_\mathrm{r} \times \mathbf{E}_\mathrm{r} - \mathbf{k}_\mathrm{t} \times \mathbf{E}_\mathrm{t}) \cdot \hat{\mathbf{n}} = 0 \,. \tag{2.25}$$

Second, we require the continuity of the tangential components of $\mathbf{E}$ and $\mathbf{H}$

$$(\mathbf{E}_\mathrm{i} + \mathbf{E}_\mathrm{r} - \mathbf{E}_\mathrm{t}) \times \hat{\mathbf{n}} = 0 \,, \tag{2.26}$$

$$(\mathbf{k}_\mathrm{i} \times \mathbf{E}_\mathrm{i} + \mathbf{k}_\mathrm{r} \times \mathbf{E}_\mathrm{r} - \mathbf{k}_\mathrm{t} \times \mathbf{E}_\mathrm{t}) \times \hat{\mathbf{n}} = 0 \,. \tag{2.27}$$

In both expressions, $\hat{\mathbf{n}}$ denotes the unit vector normal to the interface [62, Chapter 7]. The above conditions allow for two linear polarisations that do not mix at the interface – one with non-zero E_y, H_x and H_z field components – the so called transverse electric (TE) polarisation, and another one with non-zero H_y, E_x and E_z field components – the so called transverse magnetic (TM) polarisation [69].

To determine the phase shift upon reflection, a reflection coefficient needs to be derived. It is defined as the ratio of $E_{\mathrm{r},y}$ to $E_{\mathrm{i},y}$ in the case of TE-polarisation or $H_{\mathrm{r},y}$ to $H_{\mathrm{i},y}$ for TM-polarisation. Considering the expressions (2.20)–(2.23), the relations between the y-components of the electric field are obtained from the interface conditions (2.26) and (2.27):

$$\begin{cases} E_{\mathrm{i},y} + E_{\mathrm{r},y} = E_{\mathrm{t},y} \,, \\ n_1 \cos\theta_1 E_{\mathrm{i},y} - n_1 \cos\theta_1 E_{\mathrm{r},y} - n_2 \cos\theta_2 E_{\mathrm{t},y} = 0 \,. \end{cases} \tag{2.28}$$

Utilising the above relations, the reflection coefficient for TE-polarised waves is obtained as

$$r_{\mathrm{TE}} = \frac{E_{\mathrm{r},y}}{E_{\mathrm{i},y}} = \frac{n_1 \cos\theta_1 - n_2 \cos\theta_2}{n_1 \cos\theta_1 + n_2 \cos\theta_2} = \frac{k_{\mathrm{i},x} - k_{\mathrm{t},x}}{k_{\mathrm{i},x} + k_{\mathrm{t},x}}\,. \tag{2.29}$$

Similarly, the reflection coefficient for TM-polarisation can be derived from the interface conditions (2.24) and (2.25) as

$$r_{\mathrm{TM}} = \frac{H_{\mathrm{r},y}}{H_{\mathrm{i},y}} = \frac{n_2 \cos\theta_1 - n_1 \cos\theta_2}{n_2 \cos\theta_1 + n_1 \cos\theta_2} = \frac{n_2^2 k_{\mathrm{i},x} - n_1^2 k_{\mathrm{t},x}}{n_2^2 k_{\mathrm{i},x} + n_1^2 k_{\mathrm{t},x}}\,. \tag{2.30}$$

Moreover, the interface conditions (2.24)–(2.27) must be fulfilled at all points of the (y, z)-plane simultaneously, which implies

$$k_{\mathrm{i},y} = k_{\mathrm{r},y} = k_{\mathrm{t},y} = 0 \quad \text{and} \quad k_{\mathrm{i},z} = k_{\mathrm{r},z} = k_{\mathrm{t},z}. \tag{2.31}$$

The above relations make the angle of incidence equal to the reflection angle and lead to Snell's law for the transmitted wave (2.18).

Recall that in the case of a slab waveguide, the condition $n_1 > n_2$ implies that $\theta_2 > \theta_1$. The total internal reflection occurs when the angle $\theta_1 = \theta$ exceeds a critical value θ_c, for which $\theta_2 = \frac{\pi}{2}$. In case $\theta > \theta_c$, equations (2.31) and (2.18) result in

$$k_{\mathrm{t},z} = k_{\mathrm{i},z} = n_1 k_0 \sin\theta > n_1 k_0 \sin\theta_c = n_2 k_0. \tag{2.32}$$

At the same time, $k_{\mathrm{t},x}^2 + k_{\mathrm{t},z}^2 = k_0^2 n_2^2$, which implies that $k_{\mathrm{t},x}$ must be purely imaginary: $k_{\mathrm{t},x} = \pm \mathrm{i} k_0 \sqrt{n_1^2 \sin^2\theta - n_2^2} = \pm \mathrm{i} k_{\mathrm{t},x}^{(i)}$. If it is positive, it results in an evanescent transmitted field in the cladding (cf. equation (2.20)). Including this observation leads to the reflection coefficients for TE and TM polarisation in the form

$$r_{\mathrm{TE}} = \frac{k_{\mathrm{i},x} - \mathrm{i} k_{\mathrm{t},x}^{(i)}}{k_{\mathrm{i},x} + \mathrm{i} k_{\mathrm{t},x}^{(i)}} = \mathrm{e}^{\mathrm{i}\phi_{\mathrm{TE}}}, \tag{2.33}$$

$$r_{\mathrm{TM}} = \frac{n_2^2 k_{\mathrm{i},x} - \mathrm{i} n_1^2 k_{\mathrm{t},x}^{(i)}}{n_2^2 k_{\mathrm{i},x} + \mathrm{i} n_1^2 k_{\mathrm{t},x}^{(i)}} = \mathrm{e}^{\mathrm{i}\phi_{\mathrm{TM}}}. \tag{2.34}$$

In the above relations, it can be seen that the amplitude remains unchanged but the reflected wave is shifted in phase with respect to the incident wave. The phase shift ϕ for TE and TM polarisation equals

$$\phi = 2 \arctan\left(p \frac{\sqrt{n_1^2 \sin^2\theta - n_2^2}}{n_1 \cos\theta} \right) \quad \text{with} \quad p = \begin{cases} 1, & \text{for TE case} \\ \frac{n_1^2}{n_2^2}, & \text{for TM case} \end{cases}. \tag{2.35}$$

Having calculated the phase shift ϕ, equation (2.19) can be solved. The approach presented here can be also found in textbooks, e.g. [62, 71].

Effective refractive index of guided modes

As mentioned in the beginning of this section, equation (2.19) determines the effective refractive index n_{eff}^m of the guided modes of different order m. To proceed, we make the following substitutions:

$$\begin{aligned} k_1 \cos\theta &= \sqrt{n_1^2 k_0^2 - \beta^2} = \frac{2}{h} u \quad \text{with parameter } u, \\ \beta &= k_1 \sin\theta, \\ V &= \frac{h}{2} k_0 \sqrt{n_1^2 - n_2^2}\,, \end{aligned} \tag{2.36}$$

with β denoting propagation constant, expressing the phase accumulation of the permissible plane wave along the principal propagation direction that is z, i.e., along the waveguide. The V expresses normalised frequency [71, Chapter 2], or simply waveguide parameter [72, Section 6e]. By using the above relations and the phase shift (2.35), the dispersion relation (2.19) can be transformed into

$$u \tan\left(u - m\frac{\pi}{2}\right) = p\sqrt{V^2 - u^2}\,. \tag{2.37}$$

The solutions to equation (2.37) can be found graphically. In Figure 2.2(a), both the right-hand side (RHS) and left-hand side (LHS) of this equation are plotted against the parameter u, for integer numbers $m = 0, 1, 2, \ldots$. The intersection points of the two plots indicate the possible solutions for the parameter u. From these solutions, one can find the propagation constants $\beta_m = n_{\text{eff}}^m k_0$, and consequently determine the effective refractive index n_{eff}^m. The integer m represents the mode number, with $m = 0$ corresponding to the fundamental mode and $m > 0$ indicating higher-order modes. Figure 2.2(a) indicates the possibility of two propagating modes each of polarisation: TE and TM.

With a little bit of patience, equation (2.37) can be transformed into the form

$$V = \frac{\arctan\left(p\sqrt{\frac{B}{1-B}}\right) + m\frac{\pi}{2}}{\sqrt{1-B}}\,, \tag{2.38}$$

with $B = \frac{n_{\text{eff}}^2 - n_2^2}{n_1^2 - n_2^2}$ being a function of n_{eff} [71, Chapter 2]. The dependency of n_{eff} on V is plotted in Figure 2.2(b). Note, that the superscript m is omitted in case of continuous variables, meaning that the discrete variable with superscript m is the particular solution for mode m. The number of modes guided within the waveguide depends on its design parameters: h, n_1 and n_2. It can be observed that the bigger the core height h and the larger the refractive index contrast $n_1^2 - n_2^2$ between the core and the cladding, the more solutions can be found, which implies more propagating modes in a waveguide. The above considerations show also that equation (2.37) has solutions for discrete values of incident angles θ_m, for which the interference forms standing waves.

Wave-optical picture

For the slab waveguide presented in Figure 2.1(a), the waveguide structure and the electric and magnetic fields are invariant along y-direction. This implies the condition $\frac{\partial \mathbf{E}}{\partial y} = \frac{\partial \mathbf{H}}{\partial y} = 0$

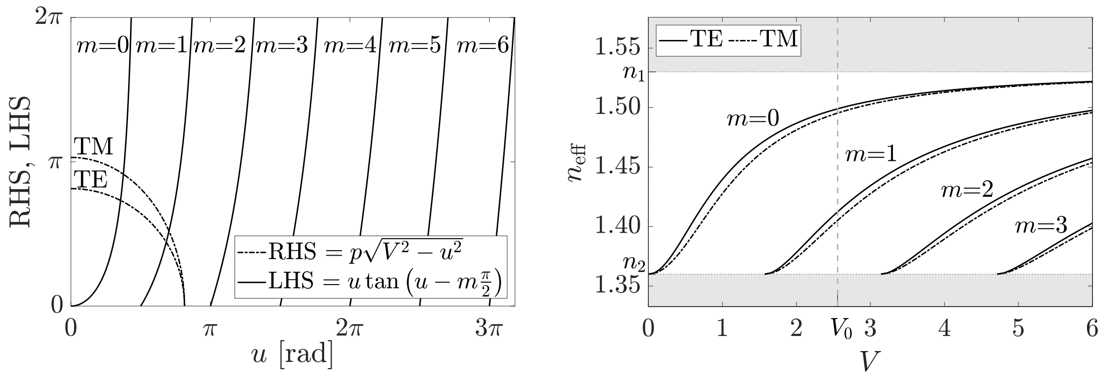

(a) (b)

Figure 2.2.: (a) The intersections of solid and dashed lines indicate the solutions to equation (2.37) for a slab waveguide of height $h = 1.8\,\mu\text{m}$, refractive indices: $n_1 = 1.53$ and $n_2 = 1.36$, and vacuum wavelength $\lambda_0 = 1.55\,\mu\text{m}$. For the given parameters, only two guided modes are present in each polarisation. (b) Possible values of the effective refractive index n_{eff} as a function of normalised frequency V. Intersections with dashed vertical line indicate the solutions for given waveguide design parameters resulting in V_0. The possible values of effective refractive index n_{eff}^m of the propagating modes m lie between n_2 and n_1.

and the respective terms drop from the curl equations (2.11) and (2.12). Using this fact, the aforementioned curl equations can be transformed into the following set of equations:

$$\left\{\begin{aligned} -\frac{\partial}{\partial z}E_y &= \mathrm{i}\omega\mu_0 H_x \\ \frac{\partial}{\partial z}E_x - \frac{\partial}{\partial x}E_z &= \mathrm{i}\omega\mu_0 H_y \\ \frac{\partial}{\partial x}E_y &= \mathrm{i}\omega\mu_0 H_z \end{aligned}\right. \quad \text{and} \quad \left\{\begin{aligned} -\frac{\partial}{\partial z}H_y &= -\mathrm{i}\omega\varepsilon E_x \\ \frac{\partial}{\partial z}H_x - \frac{\partial}{\partial x}H_z &= -\mathrm{i}\omega\varepsilon E_y \\ \frac{\partial}{\partial x}H_y &= -\mathrm{i}\omega\varepsilon E_z \end{aligned}\right. . \tag{2.39}$$

The above equations can be separated into two sets – one for TE and another for TM polarisation. The different solutions to these sets of equations are called the modes of the waveguide. These can be interpreted as field patterns that can propagate in the waveguide without changing the pattern shapes [68].

The m-th eigenmode for the electric $\mathbf{E}$ and magnetic $\mathbf{H}$ fields propagating in the z-direction can be written in the form [68]

$$\mathbf{E}_m(x, z) = \boldsymbol{\mathcal{E}}_m(x)\mathrm{e}^{\mathrm{i}\beta_m z}, \tag{2.40}$$

$$\mathbf{H}_m(x, z) = \boldsymbol{\mathcal{H}}_m(x)\mathrm{e}^{\mathrm{i}\beta_m z}, \tag{2.41}$$

where $\boldsymbol{\mathcal{E}}_m(x)$ and $\boldsymbol{\mathcal{H}}_m(x)$ are the transverse field amplitudes. The propagation constant β_m determines how the fields propagate in z-direction. When β_m is real-valued, then the exponential function accounts for modes propagating in an oscillating manner through the waveguide core. In case of non-zero positive imaginary part of a propagation constant, the field attenuates. The wavefronts propagate with the phase velocity v_{ph}, related to the propagation constant by $v_{\text{ph}} = \omega \cdot \beta_m^{-1}$. The electromagnetic waves are sent into waveguide as time-dependent optical signals consisting of different frequency components. These pulses propagate with group velocity v_{g}, defined as the reciprocal of the derivative of propagation constant with respect to frequency.

Inserting the ansatz (2.40) or (2.41) into (2.39) results in the wave equation

$$\left(\frac{\partial^2}{\partial x^2} + \omega^2 \varepsilon_0 \mu_0 n^2(x)\right) \psi_m(x) = \beta_m^2 \psi_m(x)\,, \tag{2.42}$$

where the m-th mode field $\psi_m(x)$ denotes either $\mathcal{E}_y^m(x)$ (TE mode) or $\mathcal{H}_y^m(x)$ (TM mode). Equation (2.42) describes an eigenvalue problem with propagation constant β_m and eigenfunction $\psi_m(x)$ of mode m [68]. Given the frequency ω, the wave equation can be solved only for certain values β_m, which indicate the set of discrete eigenmodes of the waveguide.

Transverse field profiles ψ_m can be determined using the constraint of evanescently decaying amplitude in the cladding for $x \to \pm\infty$. In case of TE mode, the ansatz for the amplitude of modes $m = 0, 1, 2, 3, \ldots$ reads [68]

$$\mathcal{E}_y^m(x) = \begin{cases} A_m \mathrm{e}^{k_{2,x}^{(i)}\left(\frac{h}{2}+x\right)}, & \text{for } x \le -\frac{h}{2} \\ B_m \cos(k_{1,x}x + \frac{\pi}{2}m), & \text{for } -\frac{x}{2} \le x \le \frac{h}{2} \\ C_m \mathrm{e}^{k_{2,x}^{(i)}\left(\frac{h}{2}-x\right)}, & \text{for } \frac{h}{2} \le x \end{cases}, \tag{2.43}$$

with x-components of the wave vectors of the core $k_{1,x} = \sqrt{n_1^2 k_0^2 - \beta_m^2}$ and the cladding $k_{2,x}^{(i)} = \sqrt{\beta_m^2 - n_2^2 k_0^2}$. The solution can be separated into even and odd modes, which is indicated with the component $\frac{\pi}{2}m$ in the argument of the trigonometric functions. The amplitudes A_m, B_m, C_m can be derived by enforcing continuity of $\mathcal{E}_y^m$ on the interface between the core and the cladding. The resulting electric field amplitude distribution of the four lowest modes is presented in Figure 2.3. The magnetic field components, $\mathcal{H}_x^m(x)$ and $\mathcal{H}_z^m(x)$, are then calculated, employing relations (2.39), as $\mathcal{H}_x^m(x) = -\frac{\beta_m}{\omega\mu_0}\mathcal{E}_y^m(x)$ and

$$\mathcal{H}_z^m(x) = \frac{\mathrm{i}}{\omega\mu_0} \begin{cases} A_m k_{2,x}^{(i)} \mathrm{e}^{k_{2,x}^{(i)}\left(\frac{h}{2}+x\right)}, & \text{for } x \le -\frac{h}{2} \\ -B_m k_{1,x} \sin(k_{1,x}x + \frac{\pi}{2}m), & \text{for } -\frac{x}{2} \le x \le \frac{h}{2} \\ C_m k_{2,x}^{(i)} \mathrm{e}^{k_{2,x}^{(i)}\left(\frac{h}{2}-x\right)}, & \text{for } \frac{h}{2} \le x \end{cases}. \tag{2.44}$$

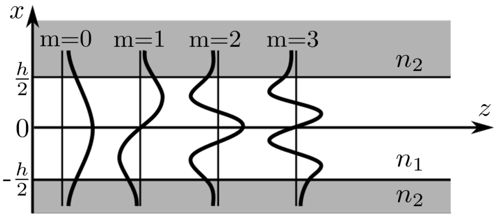

Figure 2.3: Slab waveguide with core refractive index n_1 and height h, cladded with material of refractive index $n_2 < n_1$. Bold lines show the lowest four TE modes. The field decays exponentially in the cladding. Figure adapted from [68].

Imposing the continuity conditions on $\mathcal{H}_z^m(x)$ at $x = \pm\frac{h}{2}$ results in equations for the mode propagation constant β_m. Rearranging the obtained relations, regarding parameters V, B and u, introduced before, results in the eigenvalue problem (2.38). In case of TM modes, the field components $\mathcal{H}_y^m(x)$, $\mathcal{E}_x^m(x)$ and $\mathcal{E}_z^m(x)$ are derived similarly, leading to the eigenvalue problem differing in constant p from the TE case, cf. equation (2.35). The eigenvalue problem can be solved in the same way as presented earlier in this section.

2.2.2. Channel waveguide

Although the slab waveguide is convenient for the theoretical analysis, in practical applications the waveguide core must have finite thickness in y-direction. There are various designs of such channel waveguides, including rib, embedded, strip/ridge, and buried waveguide [73, Section 10.5]. The examples are schematically presented in Figure 2.4. The last type corresponds to the design of free-form waveguide. Usually,[6] the waveguides are considered to have rectangular cross-section characterised by height h and width w. Such waveguides confine light in two transverse directions, x and y. The approximate solutions for the propagating modes can be found with semi-analytical methods, for example Marcatili [78], Kumar [79], and effective index method [80]. In this thesis, the modes in rectangular waveguides are only calculated numerically (see Section 2.3). Therefore, the semi-analytical methods are not described in detail. Only some assumptions and results are mentioned briefly, as they are helpful in understanding the modal analysis described in the core of this thesis. The detailed description, derivation, and comparison of all three methods can be found in [71, Section 2.2].

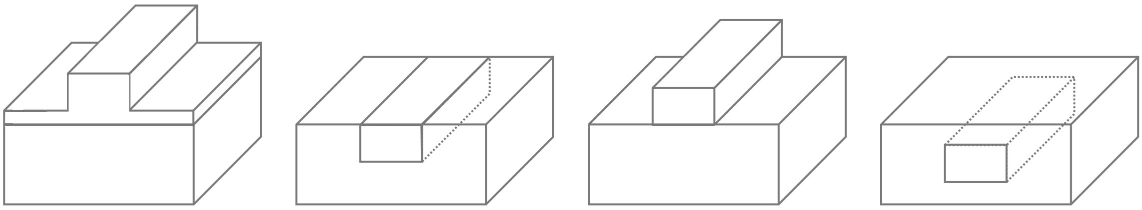

rib embedded ridge buried

Figure 2.4.: Different types of positioning channel waveguides with respect to the cladding.

The approximation methods treat the rectangular cross-section as a composition of two slab waveguides: one invariant in the x- and the other in y-direction, as shown in Figure 2.5. This composition allows for distinguishing different areas in the x-y plane, each with specific properties. The main assumption is a low index contrast between the core and the cladding: $n_1 \approx n_2$. At the same time the waveguide is assumed to be operated far from the cut-off of the considered mode (cf. Figure 2.2(b)). This condition ensures that the mode is confined mostly in the waveguide core and the field in the shaded areas in Figure 2.5 can be neglected [71, 78].

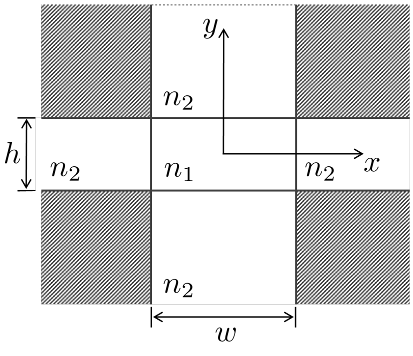

Figure 2.5: Cross-section of a rectangular waveguide, perpendicular to the propagation of the modes. The core and cladding structure is divided into four different regions. The electromagnetic field is neglected in the shaded regions. This approximation is valid if the field is mostly confined to the waveguide core. Figure adapted from [71].

The guided transverse fields are separated into two modes: quasi-transverse-electric (TE) $\mathcal{E}_x$-modes, with dominating field components $\mathcal{E}_x$ and $\mathcal{H}_y$, and $\mathcal{H}_x = 0$; and quasi-transverse-magnetic (TM) $\mathcal{E}_y$-modes with dominating field components $\mathcal{E}_y$ and $\mathcal{H}_x$, and $\mathcal{H}_y = 0$. With

---

[6] There are works, where waveguides of trapezoidal cross-section are studied, cf. [74–77]. However, these studies result mostly from the need for modelling of processing (etching) imperfections.

these assumptions, the relations (2.9)–(2.12), and ansatz for the total electric and magnetic field

$$\mathbf{E}(x,y,z) = \boldsymbol{\mathcal{E}}(x,y)\mathrm{e}^{\mathrm{i}\beta z}, \tag{2.45}$$

$$\mathbf{H}(x,y,z) = \boldsymbol{\mathcal{H}}(x,y)\mathrm{e}^{\mathrm{i}\beta z}, \tag{2.46}$$

the wave equation takes the form

$$\left(\frac{\partial^2}{\partial x^2} + \frac{\partial^2}{\partial y^2} + \omega^2\varepsilon_0\mu_0 n^2\right)\psi = \beta^2\psi\,, \tag{2.47}$$

with ψ being either $\mathcal{H}_x$ or $\mathcal{H}_y$ field, β representing the corresponding propagation constant, and n denoting effective refractive index of the core or cladding of the waveguide. This eigenvalue problem can be solved for the fields and propagation constants analogously as in case of the slab waveguide. The detailed explanation can be found in [71, Section 2.2].

The modes found analytically can be classified as $\mathcal{E}_x^{p,q}$ or $\mathcal{E}_y^{p,q}$, depending on the dominant transverse component of the electric field. The integers $p = 1, 2, \dots$ and $q = 1, 2, \dots$ correspond to the number of extrema along x and y direction, respectively. The example of the three modes of the lowest order are presented in Figure 2.6.

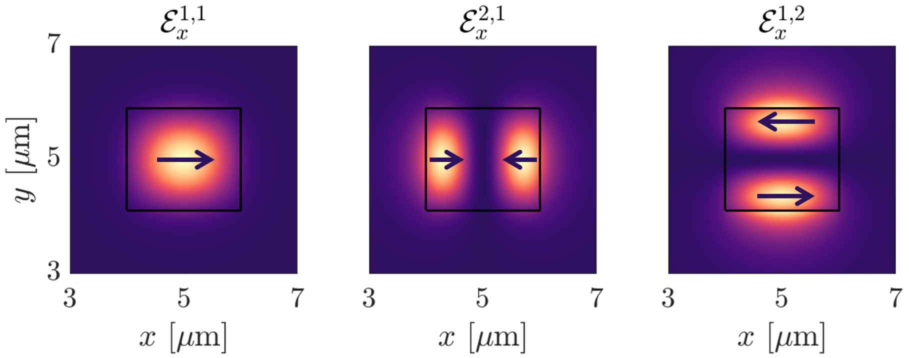

Figure 2.6.: Intensity of the $\mathcal{E}_x^{p,q}$-mode fields in a rectangular channel waveguide. Arrows indicate the orientation of the dominant transverse electric component $\mathcal{E}_x$. The integers p and q denote the number of extrema of the field in x- and y-direction, respectively.

However, it is important to stress that this approximation is well suited for low refractive index contrast, which is not the case of the waveguides considered in this thesis. For example, the waveguide studied in Subsection 2.4.1 has refractive indices: $n_1 = 1.57$, $n_2 = 1.34$ and the waveguide discussed in Chapter 3 is characterised by refractive indices: $n_1 = 1.53$, and $n_2 = 1.36$. Therefore, in this thesis the modes are determined numerically with the methods described in Section 2.3.

2.2.3. Eigenmode expansion

The electromagnetic wave propagating in a waveguide can be expressed as a superposition of its eigenmodes. The complete set of eigenmodes comprises guided (bound) modes, (2.45) and (2.46), and radiation modes [70, Chapter 25]. The bound modes are related to energy guided along a non-absorbing waveguide, while radiation modes correspond to refracted rays (in ray-optical picture), or transversely oscillatory waves, external to the waveguide core.

The total electromagnetic fields propagating along z-direction in an optical waveguide can be represented as the sum of all guided and radiation modes [70, Chapter 25]

$$\mathbf{E}(\mathbf{r}) = \sum_{i=0}^{\infty} a_i \boldsymbol{\mathcal{E}}_i(x,y)\mathrm{e}^{\mathrm{i}\beta_i z} + \sum_{j=0}^{\infty} \int_0^{\infty} a_j(q)\boldsymbol{\mathcal{E}}_j(x,y,q)\mathrm{e}^{\mathrm{i}\beta_j(q)z}\mathrm{d}q\,, \tag{2.48}$$

$$\mathbf{H}(\mathbf{r}) = \sum_{i=0}^{\infty} a_i \boldsymbol{\mathcal{H}}_i(x,y)\mathrm{e}^{\mathrm{i}\beta_i z} + \sum_{j=0}^{\infty} \int_0^{\infty} a_j(q)\boldsymbol{\mathcal{H}}_j(x,y,q)\mathrm{e}^{\mathrm{i}\beta_j(q)z}\mathrm{d}q\,, \tag{2.49}$$

with modal amplitudes $a_j(q)$, and a continuous propagation constant $\beta_j(q)$, which is a function of parameter q. The continuous parameter q can be chosen as transverse wavenumber of a plane wave $q = \sqrt{k^2 - \beta_j^2}$, where k is the free-space wavenumber [81]. Subscript j labels additionally the dependence on a given mode [81]. The first summations in equations (2.48) and (2.49) include forward- and backward-propagating modes. Due to the continuity of the propagation constant, an integration over all values of β_j is necessary. The propagation constant can take any value satisfying $0 < |\beta_j| < k_0 n_2$ for propagating radiation mode, while in case of evanescent mode $\mathrm{Re}\{\beta_j\} = 0$ and $0 < \mathrm{Im}\{\beta_j\} < \infty$ [70, Chapter 25] (see also the discussion of the reflection from a plane dielectric boundary in Subsection 2.2.1 in this thesis). Therefore, the parameter q can vary between 0 and ∞. Throughout this thesis, all fields contain the implicit time dependence $\mathrm{e}^{-\mathrm{i}\omega t}$, which is omitted because it does not influence the orthogonality of the modes.

In order to represent the electromagnetic field as a sum over guided and radiating modes, they need to form an orthogonal basis. The orthogonality conditions are necessary to calculate the coefficients a_i and $a_j(q)$. Here, in Section 2.2.4, the derivation of orthogonality of the guided modes is presented, similarly to [49, 71, 82]. The similar derivation can be performed for orthogonality of radiation modes and between the radiation and the bound modes. This derivation is shown in [70, Section 11.4 and Section 31.3], and is omitted in this thesis.

2.2.4. Orthogonality relations

The derivation begins with the Maxwell equations (2.11) and (2.12). They are satisfied by the electric and magnetic fields of two distinct modes, i and j. The electric field of one mode $\mathbf{E}_i$ and magnetic field of another mode $\mathbf{H}_j$, are represented by equations (2.45) and (2.46), respectively.

Firstly, equation (2.11) is applied to mode i. Next, a dot product is calculated between both sides of equation (2.11) with $\mathbf{H}_j^*(\mathbf{r})$, where * denotes complex conjugate. This procedure is repeated with equation (2.12) for mode j but in this case, the dot product is calculated for $\mathbf{E}_i(\mathbf{r})$ with the complex conjugate of both sides of (2.12). Subtracting the two resulting expressions yields:

$$\mathbf{H}_j^* \cdot (\nabla \times \mathbf{E}_i) - \mathbf{E}_i \cdot (\nabla \times \mathbf{H}_j^*) = \mathrm{i}\omega(\mu_0 \mathbf{H}_i \mathbf{H}_j^* - \varepsilon \mathbf{E}_i \mathbf{E}_j^*)\,. \tag{2.50}$$

With use of the identity $\nabla \cdot (\mathbf{F} \times \mathbf{G}) = \mathbf{G} \cdot (\nabla \times \mathbf{F}) - \mathbf{F} \cdot (\nabla \times \mathbf{G})$, for vector fields $\mathbf{F}$ and $\mathbf{G}$, equation (2.50) can be rewritten as

$$\nabla \cdot (\mathbf{E}_i \times \mathbf{H}_j^*) = \mathrm{i}\omega(\mu_0 \mathbf{H}_i \mathbf{H}_j^* - \varepsilon \mathbf{E}_i \mathbf{E}_j^*)\,. \tag{2.51}$$

Next, the expressions (2.45) and (2.46) are inserted into the above relation (2.50). Applying now the identities $\nabla \times (\Phi \mathbf{F}) = \Phi(\nabla \times \mathbf{F}) + (\nabla \Phi) \times \mathbf{F}$, with a scalar function Φ, and regarding the previous relations, leads to

$$\nabla_t \cdot (\boldsymbol{\mathcal{E}}_i \times \boldsymbol{\mathcal{H}}_j^*) + \mathrm{i}(\beta_j - \beta_i)(\boldsymbol{\mathcal{E}}_i \times \boldsymbol{\mathcal{H}}_j^*) = \mathrm{i}\omega(\varepsilon \boldsymbol{\mathcal{H}}_i \boldsymbol{\mathcal{H}}_j^* - \mu_0 \boldsymbol{\mathcal{E}}_i \boldsymbol{\mathcal{E}}_j^*)\,, \tag{2.52}$$

with two-dimensional differential operator $\nabla_t = \hat{\mathbf{x}}\frac{\partial}{\partial x} + \hat{\mathbf{y}}\frac{\partial}{\partial y}$ in the (x, y)-plane [71], where $\hat{\mathbf{x}}$, $\hat{\mathbf{y}}$ and $\hat{\mathbf{z}}$ are the unit vectors in x-, y- and z-direction, respectively. Integrating the above equation over the entire plane A comprising waveguide's cross-section, perpendicular to the propagation direction $\hat{\mathbf{z}}$, results in

$$\int_A \nabla_t \cdot (\boldsymbol{\mathcal{E}}_i \times \boldsymbol{\mathcal{H}}_j^*)\,\mathrm{d}x\mathrm{d}y + \mathrm{i}(\beta_j - \beta_i) \int_A (\boldsymbol{\mathcal{E}}_i \times \boldsymbol{\mathcal{H}}_j^*) \cdot \hat{\mathbf{z}}\,\mathrm{d}x\mathrm{d}y = \mathrm{i}\omega \int_A (\varepsilon \boldsymbol{\mathcal{H}}_i \boldsymbol{\mathcal{H}}_j^* - \mu_0 \boldsymbol{\mathcal{E}}_i \boldsymbol{\mathcal{E}}_j^*)\,\mathrm{d}x\mathrm{d}y\,. \tag{2.53}$$

The first integral on the left-hand side of the above expression can be rewritten with use of the Gauss divergence theorem [63, Subsection 1.3.4] to

$$\int_A \nabla_t \cdot (\boldsymbol{\mathcal{E}}_i \times \boldsymbol{\mathcal{H}}_j^*)\,\mathrm{d}x\mathrm{d}y = \int_{\partial A} (\boldsymbol{\mathcal{E}}_i \times \boldsymbol{\mathcal{H}}_j^*) \cdot \hat{\mathbf{n}}\,\mathrm{d}x\mathrm{d}y\,, \tag{2.54}$$

where $\hat{\mathbf{n}}$ is a unit normal vector outward of the boundary ∂A. In case of guided modes, the field strength decays exponentially to zero as $x^2 + y^2 \to \infty$ so the integral on the right-hand side of (2.54) vanishes as the area becomes infinite. Consequently, equation (2.53) takes the form

$$(\beta_j - \beta_i) \int_A (\boldsymbol{\mathcal{E}}_i \times \boldsymbol{\mathcal{H}}_j^*) \cdot \hat{\mathbf{z}}\,\mathrm{d}x\mathrm{d}y = \omega \int_A (\varepsilon \boldsymbol{\mathcal{H}}_i \boldsymbol{\mathcal{H}}_j^* - \mu_0 \boldsymbol{\mathcal{E}}_i \boldsymbol{\mathcal{E}}_j^*)\,\mathrm{d}x\mathrm{d}y\,. \tag{2.55}$$

Subtracting equation (2.55) from its complex-conjugated form (with interchanged indices) results in

$$(\beta_i - \beta_j) \int_A [(\boldsymbol{\mathcal{E}}_i \times \boldsymbol{\mathcal{H}}_j^*) + (\boldsymbol{\mathcal{E}}_j^* \times \boldsymbol{\mathcal{H}}_i)] \cdot \hat{\mathbf{z}}\,\mathrm{d}x\mathrm{d}y = 0\,. \tag{2.56}$$

In case of non-degenerate modes, for which $\beta_i \neq \beta_j$, the above condition is satisfied only if the integral vanishes.

The propagating modes carry power. The total, time average of power flow, associated with mode j, can be written as

$$\mathcal{P}_j = \int_A \overline{\mathbf{S}} \cdot \hat{\mathbf{z}}\,\mathrm{d}x\mathrm{d}y = \frac{1}{2} \int_A \mathrm{Re}\{\boldsymbol{\mathcal{E}}_j \times \boldsymbol{\mathcal{H}}_j^*\} \cdot \hat{\mathbf{z}}\,\mathrm{d}x\mathrm{d}y\,, \tag{2.57}$$

which includes the time-averaged energy flux $\overline{\mathbf{S}}$, described by equation (2.17). Taking into account the relations (2.56) and (2.57), the orthogonality relation for modes i and j can be expressed as

$$\frac{1}{4} \int_A (\boldsymbol{\mathcal{E}}_i \times \boldsymbol{\mathcal{H}}_j^* + \boldsymbol{\mathcal{E}}_j^* \times \boldsymbol{\mathcal{H}}_i) \cdot \hat{\mathbf{z}}\,\mathrm{d}x\mathrm{d}y = \mathcal{P}_j \delta_{ij}, \tag{2.58}$$

where δ_{ij} denotes the Kronecker delta.

The derivation of equation (2.58) includes conjugated electric and magnetic fields. Equation (2.58) is referred to as *conjugated* form of orthogonality [70, Chapter 31]. This form is convenient, because it provides a physical interpretation in terms of power flow, equation (2.57). However, it is only valid for non-absorbing waveguides, for which $n_{\text{eff}}^* = n_{\text{eff}}$ holds.[7] This condition is true for real valued refractive indices. This may be the case of a straight waveguide with invariant geometry when the waveguide is made of a non-absorbing material, and the roughness of its walls is neglected. However, in the case of bending, the imaginary part of effective refractive index is non-zero and increases along with bending (decreasing radius of curvature), as visible in Figure 2.14. For both absorbing and non-absorbing waveguides holds the unconjugated form of orthogonality [70, Chapter 31-3]:

$$\int_A \boldsymbol{\mathcal{E}}_i \times \boldsymbol{\mathcal{H}}_j \cdot \hat{\mathbf{z}}\, \mathrm{d}x\mathrm{d}y = \int_A \boldsymbol{\mathcal{E}}_j \times \boldsymbol{\mathcal{H}}_i \cdot \hat{\mathbf{z}}\, \mathrm{d}x\mathrm{d}y = 0, \quad \text{for} \quad i \neq j, \tag{2.59}$$

between mode i and j, where the integration is performed over the infinite cross-section A perpendicular to the propagation direction $\hat{\mathbf{z}}$. Particularly, every bound mode is orthogonal to all radiation and leaky modes [70]. Based on (2.58) and (2.59), the following orthogonality operation between two modes is defined [52]

$$\langle \mathcal{M}_i | \mathcal{M}_j \rangle = \frac{1}{4} \int_A (\boldsymbol{\mathcal{E}}_i \times \boldsymbol{\mathcal{H}}_j + \boldsymbol{\mathcal{E}}_j \times \boldsymbol{\mathcal{H}}_i) \cdot \hat{\mathbf{z}}\, \mathrm{d}x\mathrm{d}y = \begin{cases} 1, & i = j \\ 0, & i \neq j \end{cases} \tag{2.60}$$

which can be interpreted as projection of mode $|\mathcal{M}_i\rangle$ onto mode $|\mathcal{M}_j\rangle$. Following the *ket* notation from [50, 83], the mode is represented as

$$|\mathcal{M}_j^{\pm}\rangle = (\mathcal{E}_{j,x}, \mathcal{E}_{j,y}, \pm\mathcal{H}_{j,x}, \pm\mathcal{H}_{j,y})^{\mathrm{T}}, \tag{2.61}$$

where $\mathcal{E}_{j,x}$, $\mathcal{E}_{j,y}$, $\mathcal{H}_{j,x}$ and $\mathcal{H}_{j,y}$ denote, respectively, x- and y-components of electric and magnetic field profiles of j-th mode, and ± superscript indicates the forward or backward propagation direction, along the z-axis. In this thesis, the quasi-TE modes are considered. In the case of TE modes, only the sign of the magnetic field changes, while the orientation of the electric field remains the same when considering different propagation directions. The electric and magnetic fields are normalised to obtain unit power flow (2.60) in the propagation direction for the lossless propagating modes [52].

2.3. Numerical simulation

The calculations of the electromagnetic field in this work rely on commercially available software: JCMsuite [65], CST Microwave Studio [84], and Ansys Lumerical [85]. The choice of the software depends on the characteristics of the problem being addressed, such as the structure or materials involved. Some software packages offer great flexibility, making them suitable for complex 3D geometries, while others are dedicated to particular structures like spheres or waveguides. The latter options are typically optimised for faster computation [86]. This section provides a brief overview of the numerical methods implemented in the selected software.

---

[7] The explanation comes from the derivation of unconjugated and conjugated reciprocity theorem between the two field solutions of Maxwell's equations. The details can be found in [70, Chapter 31].

2.3.1. Finite element method

The electromagnetic fields that define the mode in (2.61), along with the propagation constants of the guided eigenmodes are calculated with the aid of the finite element method (FEM) solver, JCMsuite [65, 87]. In this software, the eigenmode equation for the electric field

$$\nabla \times \nabla \times \mathbf{E}(\mathbf{r}) - \omega^2 \varepsilon(\mathbf{r})\mathbf{E}(\mathbf{r}) = 0, \tag{2.62}$$

$$\text{where} \quad \mathbf{E}(\mathbf{r}) = \boldsymbol{\mathcal{E}}(x, y)\mathrm{e}^{\mathrm{i}\beta z}, \tag{2.63}$$

is solved numerically in the frequency domain for the electric field profile, $\boldsymbol{\mathcal{E}}(x, y)$, across the waveguide cross-section, and the propagation constant β. Analogous equations are considered for the magnetic field $\mathbf{H}(\mathbf{r})$. The propagation constant of mode m is given in the form of effective refractive index $n_{\mathrm{eff}}^m = \beta_m k_0^{-1}$ [87].

Finite element method for Maxwell's equations

Let us consider a bounded domain $\Omega \subset \mathbb{R}^3$ where we want to find solutions to equation (2.62). We call such a domain a *computational domain.* The electromagnetic field is computed and represented only within this region. Equation (2.62) represents a *strong form* of the wave equation. This equation holds only in regions with smooth parameter function $\varepsilon(\mathbf{r})$ [88, 89]. However, this requirement is not satisfied in case of domains containing waveguides, consisting of two different homogeneous materials characterised by the refractive indices of the core and cladding. The material parameters are no longer continuous as they *jump* at the surface separating the cladding and the core. In the case of Maxwell's equations, it is necessary to require the continuity of the tangential field components, which is ensured by the *transmission boundary conditions* at the surface separating the two media (for example, see equations (1.16), (1.17) in [89]). To apply the finite element method, we need to derive a variational formulation of equation (2.62), called *weak* formulation [88]. For the weak formulation, an appropriate function space is used that considers the continuity of the tangential components of the modes at the interface of the materials. Below, we briefly explain, how to derive the weak formulation for equation (2.62).

Together with the boundary conditions on $\partial\Omega$, the eigenvalue problem for the electric field $\mathbf{u} := \mathbf{E}(\mathbf{r})$ reads [90, Section 1.4]

$$\nabla \times (\nabla \times \mathbf{u}) = \omega^2 \varepsilon \mathbf{u} \text{ in } \Omega, \tag{2.64}$$

$$\nabla \cdot (\varepsilon \mathbf{u}) = 0 \text{ in } \Omega, \tag{2.65}$$

$$\hat{\mathbf{n}} \times \mathbf{u} = 0 \text{ on } \partial\Omega\,, \tag{2.66}$$

where $\hat{\mathbf{n}}$ is a unit vector normal to the boundary $\partial\Omega$ and the boundary condition (2.66) refer to the divergence condition (2.1) in the absence of charges and conducting boundary condition (2.26), respectively [90, Subsection 1.2].

To analyse Maxwell's equations, we consider a vector field $\mathbf{v} : \Omega \to \mathbb{C}^3$ in a *Sobolev* space $H(\mathrm{curl}, \Omega)$ defined as the linear space [90, Subsection 3.5.3]

$$H(\mathrm{curl}, \Omega) := \{\mathbf{v} \in L^2(\Omega)^3 : \nabla \times \mathbf{v} \in L^2(\Omega)^3\}$$

with the norm

$$\|\mathbf{v}\|^2_{H(\mathrm{curl},\Omega)} := \|\mathbf{v}\|^2_{L^2(\Omega)^3} + \|\nabla \times \mathbf{v}\|^2_{L^2(\Omega)^3}\,,$$

where L^2 denotes the normed linear space of functions for which the square of the absolute value is Lebesgue integrable. The vector field $\mathbf{v}$ is piecewise smooth and tangentially continuous at interfaces. The fields $\mathbf{E}$ and $\mathbf{H}$ are elements of $H(\mathrm{curl}, \mathbb{C}^3)$ [88]. Therefore, the continuity of the tangential components of $\mathbf{E}$ and $\mathbf{H}$ is satisfied automatically.

The weak formulation of the eigenvalue problem (2.64) is obtained after multiplying (2.64) with a test function $\overline{\mathbf{v}} \in H(\mathrm{curl}, \Omega)$ and integrating by parts, taking into account equations (2.65) and (2.66), and reads [91]

$$\int_\Omega \nabla \times \mathbf{u} \cdot \nabla \times \overline{\mathbf{v}} \, \mathrm{d}\mathbf{r} = \int_\Omega \omega^2 \varepsilon \mathbf{u} \cdot \overline{\mathbf{v}} \, \mathrm{d}\mathbf{r} \, . \tag{2.67}$$

The derivation of the weak formulation utilises the *weak curl* of $\mathbf{u}$, explained in Appendix A. The numerical approximation of an electric or magnetic field $\mathbf{u}$ can be found using the Ritz–Galerkin method [92, 93][94, Section 5.3], which is briefly described below.

The computational domain Ω is discretised (*meshed*) into small elements, most commonly in the shape of tetrahedrons for 3D structures or triangles for 2D geometries. The mesh consists of *nodes* and *edges*, as illustrated in Figure 2.7.

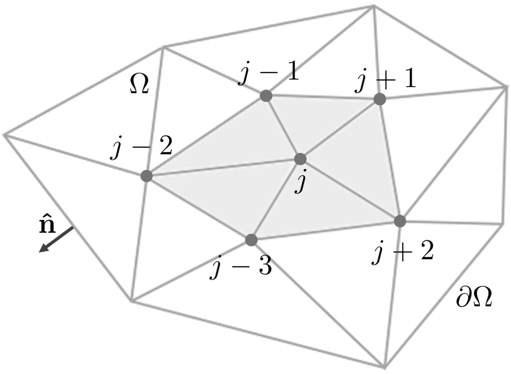

Figure 2.7: Depiction of the edges and internal nodes within the exemplary computational domain, denoted as Ω. The vicinity of node j is shaded in grey.

To solve the problem (2.67), we need *curl conforming* polynomial function space. Curl conforming means that polynomial functions from such a space must fulfil continuity of $\hat{\mathbf{n}} \times \overline{\mathbf{v}}$ over the boundaries between these elements, see Figure 2.8(a). The choice of Nédélec elements provides the required continuity conditions [95]. For example, the linear Nédélec elements have a basis of vectorial basis functions [90, Subsection 5.5.1]

$$\mathbf{w}(\mathbf{r}) = \mathbf{a} + \mathbf{b} \times \mathbf{r} \quad \text{where} \quad \mathbf{a}, \mathbf{b} \in \mathbb{C}^3 \tag{2.68}$$

that are curl conforming [96][90, Section 5.5]. The mesh elements have the form of tetrahedrons (in case of $\mathbb{R}^3$). The determination of the six constants is based on the six edges of the element, therefore the elements are called *edge elements*, see Figure 2.8(b). The basis functions are assigned to edges.

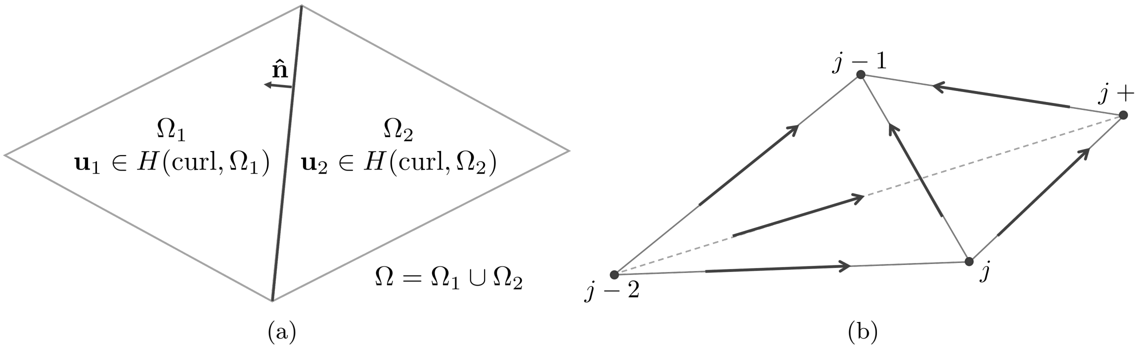

(a) (b)

Figure 2.8.: (a) Interface between two subspaces Ω_1 and Ω_2, with a normal unit vector $\hat{\mathbf{n}}$. In our considerations of Maxwell's equations (2.9)–(2.12), the electric permittivity is assumed to be a smooth function that may be discontinuous along smooth material interfaces, which is the case of the interface between core and cladding of a waveguide. Therefore, we consider an interface problem, where the material parameters can *jump*. (b) Lowest-order Nédélec element. Degrees of freedom are the average value of the tangential components of the vector fields on each edge [90, Section 5.5].

For each internal edge j the solution for the magnetic or electric field can be approximated with the function [93]

$$\mathbf{u}^{\mathrm{approx}} = \sum_{j=1}^{N} c_j \mathbf{w}_j, \tag{2.69}$$

with the number of edges N, amplitude c_j, valid in the respective subdomain, which fulfil (2.67) in the spatial region around the edge j and the boundary conditions at the edges of the subdomain [93, 95]. The mesh size (number of subdomains) determines the accuracy of the approximation [87].

The next step is to determine the set of amplitudes c_j that minimise the residual between the exact solution $\mathbf{u}$ and its approximation $\mathbf{u}^{\mathrm{approx}}$. This can be achieved by inserting equation (2.69) into (2.67). Because the resulting formulation is the linear combination of the basis functions, the problem can be formulated as a system of linear equations, with a matrix that can be inverted.

JCMsuite implementation and settings

In JCMsuite the computational domain $\Omega \subset \mathbb{R}^2$ contains waveguide cross-section, which is enclosed by surrounding cladding, shown in Figure 2.9. Although the analysis focuses on two-dimensional cross-sections, JCMsuite also accommodates bending and twisting of the waveguide based on specified parameters: *AxisPositionX* for bending and *Twist* for twisting [65, 97]. This functionality allows for straightforward computation of modes in bent waveguides.

The radii of curvature R considered in this solver, vary from 6 µm up to 100 µm. The lower limit is determined by the size of the computational domain, $d = 10\,\mu\mathrm{m}$. The centre of curvature must be positioned outside the computational domain, meaning the bending radius must be greater than 5 µm. At the same time, the domain must be big enough to ensure sufficient field decay on the domain boundaries. This trade-off between the computational domain size and the lowest radius of curvature, result from the bending implementation in

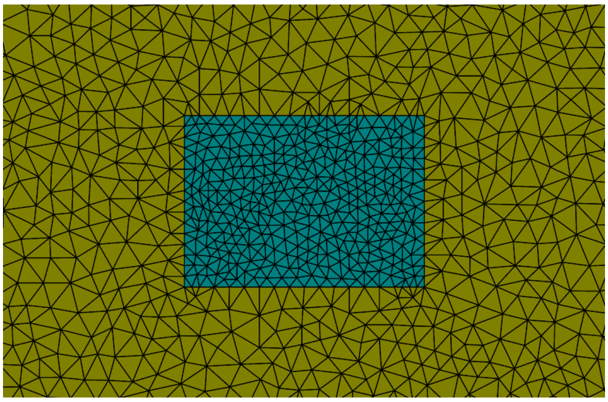

Figure 2.9: Zoomed-in view of the computational domain containing the waveguide core (in blue) with a finer mesh, surrounded by the cladding (in green) that has a coarser mesh.

JCMsuite [65], as illustrated in Figure 2.10. This figure presents a central cross-section of a solid of a revolution created by rotating the computational domain around an axis located at a distance R from the centre of the computational domain. The number of grid points N_x in the bending direction x spans twice the radius of curvature plus the domain size. The choice of N_x results from trade-off between computation time and the radius size. A larger maximum radius of curvature necessitates a greater number of equally spaced grid points, which in turn increases computation time.

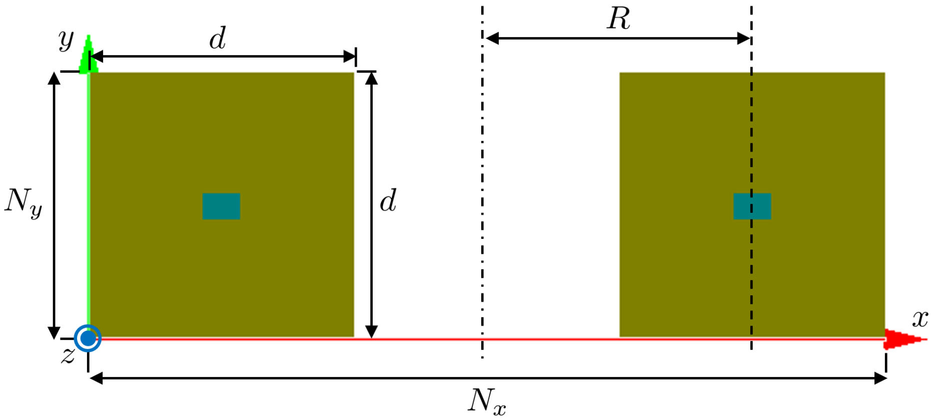

Figure 2.10.: Illustration of bending implementation in JCMsuite. A bent waveguide is modelled as a body of revolution. The figure shows a cross-section of the considered body of revolution obtained by rotating the computational domain in (x, y)-plane arround the axis of rotation displaced from domain centre by a distance labelled R (referred to as *AxisPositionX* in JCMsuite documentation [65]). The number of equally spaced grid points N_x depends on the radius of curvature as $2R + N_y$ with $N_y = 1000$ being fixed. The number of grid points coinciding with the computational domain is fixed, therefore the greater the bending radius, the higher the number of grid points N_x.

The choice of N_x and N_y determines the resolution of the computed field profiles, $\boldsymbol{\mathcal{E}}(x, y)$ and $\boldsymbol{\mathcal{H}}(x, y)$, for each mode. The fields are stored as matrices that contain the field values in x-y plane. The size of matrices is determined by N_x and N_y.

To implement FEM in JCMsuite, the basis functions are defined as polynomials. In the simplest case, where the functions are smooth and differentiable, the accuracy of the solution is influenced by both the polynomial degree and the size of the mesh element [65]. To achieve the most precise solution, it is important to use a small mesh size and a high polynomial degree. However, in certain situations – such as when singularities are present in the solution – simply increasing polynomial degree does not significantly improve the accuracy, while still increasing the computation time. A finer mesh provides higher accuracy of the results, but this also leads to increased computational time and memory usage. Therefore, the software automatically adapts the mesh size and polynomials to meet the requested accuracy of the solution, based on the initial polynomial degree, required precision and refinement steps provided by the user.

The electromagnetic field of the mode is expected to decay exponentially in the cladding as shown in Figure 2.3 and eventually be zero at infinity, outside the computational domain. In order to avoid back-reflection and interference of radiation into the computational domain, a layer of absorbing material surrounds the domain boundaries. The wave impedance of this layer must match the one of the computational domain. Therefore, this approach is called perfectly matched layers (PML) method [98, 99]. The number and thickness of the layers is adjusted automatically in JCMsuite [65, 99].

The FEM implemented in JCMsuite allows for computation of the modes propagating through straight or bent waveguide. The mode field profiles are used to calculate transmission through the waveguide, while the propagation constant is utilised for calculation of bending losses. The exact procedure of this calculation is described in Section 2.4.1 and Section 2.5.

2.3.2. Finite integration technique

While JCMsuite is convenient for calculating mode profiles, other solvers are better suited for computing the transmission characteristics of three-dimensional waveguide structures. This type of computation is referred to as *full-wave simulation.* Here, the software used for this purpose is CST Microwave Studio® [84]. It is a full-wave 3D electromagnetic field simulation software that allows for calculation of field amplitude distribution across the entire 3D space. The simulations are performed using both the time domain solver based on finite integration technique (FIT) [84], and the frequency domain solver, which utilises FEM. The time domain solver is the default choice for high-frequency applications. However, CST only offers a hexahedral mesh for this solver [84]. In contrast, the frequency domain solver can use a tetrahedral mesh, making it suitable for more complex geometries, such as structures with multiple ports or ports that are not parallel to each other. Since FEM was described in the previous section, this section briefly presents FIT.

In the FIT, the Maxwell equations in the integral form

$$\oint_{A(V)} \widetilde{\mathbf{D}} \cdot \mathrm{d}\mathbf{A} = \int_V \varrho \cdot \mathrm{d}V \,, \tag{2.70}$$

$$\oint_{A(V)} \widetilde{\mathbf{B}} \cdot \mathrm{d}\mathbf{A} = 0 \,, \tag{2.71}$$

$$\oint_{C(A)} \widetilde{\mathbf{E}} \cdot \mathrm{d}\mathbf{s} = -\int_A \frac{\partial \widetilde{\mathbf{B}}}{\partial t} \cdot \mathrm{d}\mathbf{A} \,, \tag{2.72}$$

$$\oint_{C(A)} \widetilde{\mathbf{H}} \cdot \mathrm{d}\mathbf{s} = \int_A \left(\widetilde{\mathbf{J}} + \frac{\partial \widetilde{\mathbf{D}}}{\partial t} \right) \cdot \mathrm{d}\mathbf{A} \,, \tag{2.73}$$

are discretised and converted to matrix equations which can be solved numerically [100, 101]. The bounded spatial region is divided into cells, similarly as in Figure 2.7. The edges are characterised by their *orientation*, which facilitates the description of the connected edges as a *directed graph* [101, 102]. For each cell with volume $V_{i,j,k-1}$, depicted in Figure 2.11(a), electric grid voltages $\widetilde{\mathbf{e}}$ on its edges and magnetic fluxes $\widetilde{\mathbf{b}}$ through the surfaces of the cell are assigned. In addition to the primary grid, an orthogonal auxiliary *dual* grid is introduced, consisting of magnetic grid voltages $\widetilde{\mathbf{h}}$ and electric flux $\widetilde{\mathbf{d}}$ through the surfaces [101, 103]. A pair of primary and a dual grid cells is presented in Figure 2.11(b). Within this paired cell complex $\{G, \widetilde{G}\}$ the discrete matrix equations, referred to as *Maxwell-Grid-Equations* can be represented as follows

$$\mathbf{K}_{\text{Dual}} \cdot \widetilde{\mathbf{d}} = \widetilde{\mathbf{q}}\,, \tag{2.74}$$

$$\mathbf{K} \cdot \widetilde{\mathbf{b}} = 0\,, \tag{2.75}$$

$$\mathbf{C} \cdot \widetilde{\mathbf{e}} = -\frac{\partial \widetilde{\mathbf{b}}}{\partial t}\,, \tag{2.76}$$

$$\mathbf{C}_{\text{Dual}} \cdot \widetilde{\mathbf{h}} = \widetilde{\mathbf{j}} + \frac{\partial \widetilde{\mathbf{d}}}{\partial t}\,, \tag{2.77}$$

where the matrix $\mathbf{C}$ corresponds to curl and matrix $\mathbf{K}$ corresponds to divergence. The subscript “Dual” indicates that these operations are performed on the dual grid. A detailed derivation of these matrices can be found in [101]. Including the discretised version of the constitutive relations (2.5)–(2.6), the Maxwell-Grid-Equations can be solved iteratively for the entire mesh until the desired level of accuracy is achieved.

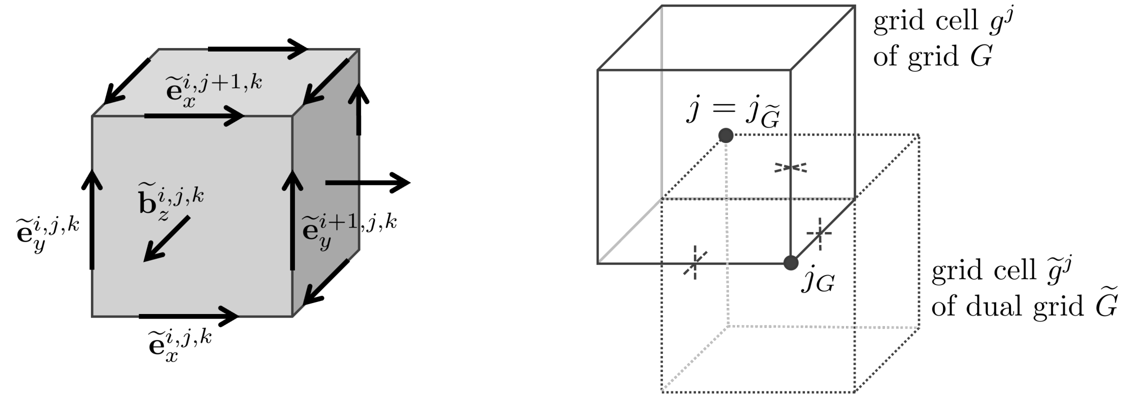

(a) (b)

Figure 2.11.: (a) A cell of volume V of a cell complex grid G with electric grid voltages $\widetilde{\mathbf{e}}$ on the edges of one surface and the magnetic flux $\widetilde{\mathbf{b}}$ through that surface. (b) Primary grid G and its dual grid $\widetilde{G}$. These figures have been adapted from [101].

The mesh density is defined by the number of cells per wavelength, which in this study is set to 10. Local mesh refinements are applied automatically at the core boundaries and curved surfaces to enhance accuracy. The computational domain is a cuboid that encloses the entire waveguide. To compute and visualise the field amplitude distribution properly, a space is left between the waveguide core and the walls of the computational domain. The boundaries of the computational domain are set to open, which is equivalent to the PML method [84]. At one end of the waveguide an input port 1 is defined, and at the opposite end an output port 2 is defined, both of which are important for S-matrix computation. The S-matrix contains the fractions of complex amplitudes that are scattered through port 1 or port 2 when the system is excited through either port. The S-matrix relates each mode of the waveguide ports with all the modes. The off-diagonal matrix components represent transmission (or reflection) from one mode of a waveguide port into another mode of another waveguide port, while diagonal components represent the reflection of each mode back into itself. The S-parameters obtained with CST Microwave Studio are used for validation of the results obtained with *fundamental mode approximation* and *multi-mode approximation* described later in this thesis. The visualisation of field profiles is helpful in identification of possible loss mechanisms.

2.3.3. Finite-difference time-domain method

The previous section describes discretisation of space, while the time dependence of Maxwell-Grid-Equations remains continuous. However, for numerical calculations in time domain it is necessary to discretise time as well [101]. From the Maxwell curl equations (2.3) – (2.4) and constitutive relations (2.5) – (2.6) it is evident that the spatial change of the H-field (curl) is related to the change of E-field in time (time derivative), and *vice versa.* This observation led to the formulation of finite difference equations by Kane Yee in 1966 [104] and the algorithm that simultaneously handles both electric and magnetic fields in time and space. In this formulation, later called Finite-Difference Time-Domain (FDTD) method, the computational domain is meshed into a *Yee lattice.* In this lattice, the electric and magnetic field components are located at the centres of the grid lines and surfaces such that each E-field component is surrounded by four H-field components and *vice versa* [105]. An example of a Yee cell from the lattice is presented in Figure 2.12.

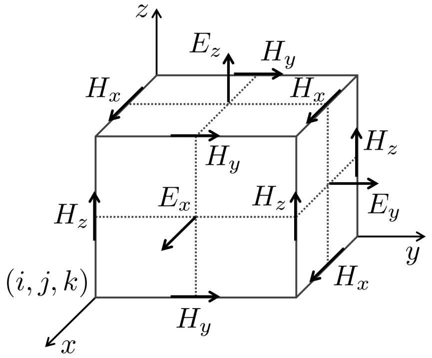

Figure 2.12: Yee cell. The Cartesian components of E and H are interleaved on a cell with the origin $(i,\ j,\ k)$. The fields are offset half a cell with respect to each other. This figure has been adapted from [105].

Utilising the Yee lattice, the first-order partial derivatives of Maxwell's curl equations both in time and space can be approximated using central differences and solved with a *leapfrog* scheme [105–108]. While the FDTD method seems to be a natural choice for electromagnetic problems, it can only be implemented on a cubic Cartesian mesh. This limitation may lead to inaccuracies on curved interfaces between two media, which arise from the *staircase* permittivity mesh. An FDTD software used in this thesis, Ansys Lumerical [85], includes several methods to enhance accuracy on curved surfaces, for example Yu–Mittra method [109], where the parameters of the media are determined at the centres of the cells, rather than at the locations of the fields. In this method, the values of the fields are calculated as the average of the fields surrounding that particular location [109].

In this thesis, Lumerical is used to calculate modes propagating in nonlinear, dispersive materials in Chapter 5, as this software provides materials database with the tool to model dispersive materials. The scripting language allows for automation of the calculation for a wide frequency ranges and varying geometries.

All numerical simulations and calculation of parameters for this thesis, where the computation times are compared, are performed on a desktop computer characterised by the parameters: Intel(R) Xenon(R) CPU E5-2650 v4 @ 2.20 GHz, 16 GB RAM. In case of the computer software CST Microwave Studio and Ansys Lumerical an automated accelerated computation is set up to two devices (processor cores).

2.4. Optical loss mechanisms in waveguides

In a waveguide with a non-invariant cross-section, in contrast to the ideal setting, some of the electromagnetic field may be lost as it propagates, resulting in lower output energy compared to the input energy. Ideally, a straight waveguide made of a non-absorbing material, where the cross-section remains unchanged, would have no loss [52]. Otherwise, a waveguide is considered *lossy* [P1]. Losses can occur if the waveguide is curved, leading to *bending losses*. Additionally, any change in waveguide's geometry, such as variations in the radius of curvature or cross-section, results in *transition losses* [110, 111]. These are the primary loss mechanisms considered in this thesis.

Further losses can result from impurities in the core material or from scattering that occurs on the sidewalls due to surface roughness [74]. This surface roughness may arise, for example, from an imperfect etching process during waveguide fabrication [112, 113]. Due to their randomness, these scattering losses cannot be calculated exactly, however, they can be estimated using theoretical models [114–117]. Although scattering losses are significant in practice, they are not considered in this study, as they affect both straight and bent waveguides. This thesis examines how waveguide geometry variations affect losses, assuming this change is independent of surface roughness.

2.4.1. Bending loss in a curved waveguide

The information regarding the losses affecting each mode m due to bending is captured by the propagation constant β_m. Its real part is related to the phase of the mode, while for attenuated fields it acquires a positive imaginary component [118]. This relationship can be observed based on the formulas for mode fields (2.40) and (2.41).

Figure 2.13 shows the real part of the electric field component in x-direction, computed using JCMsuite for different radii of curvature. The cross-sectional view is shown in the x-y-plane, and the waveguides are curved in the y-direction (in the y-z plane). The geometrical and material parameters of the waveguides are the same as in [52], i.e. 1.0 µm in x-direction and 1.4 µm in y-direction. The core is made from a material with $n_{\mathrm{co}} = 1.57$. The cladding is made from a material with $n_{\mathrm{cl}} = 1.34$. There is no noticeable difference between the fields supported by a straight and bent waveguide with radius of curvature $R = 100\,\mu\mathrm{m}$. In both cases, the propagation constant is purely real at the chosen accuracy. When the radius decreases to $R = 20\,\mu\mathrm{m}$, a shift of the field maximum in outward direction of the bend can be recognised. In case of smaller radii, a part of the eigenmode field is found oscillating outside the core. This is a clear indication for the onset of notable radiation losses. This

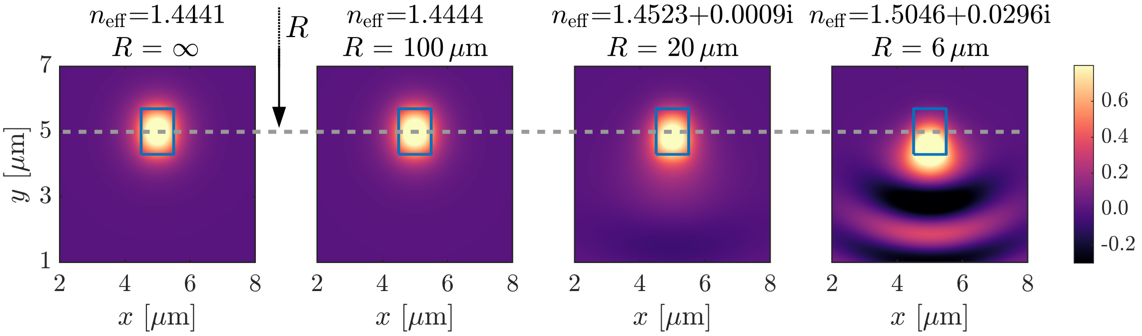

Figure 2.13.: Real part of $\mathcal{E}_x$ field, normalised to the maximum field value in the straight waveguide. Each plot corresponds to a different radius of curvature. The waveguide is bent along y-direction, which is marked with an arrow, directed from the centre of curvature. Dashed line crosses the centres of the core cross-section. The core of the waveguide is highlighted with a blue rectangle. The surrounding cladding is cropped to highlight the mode profile leaking into the cladding.

behaviour, where the field propagates out of the waveguide core, is complemented by an increased imaginary part of the effective refractive index, and consequently the propagation constant. The effective refractive indices of the modes themselves are indicated in the top of the plots in Figure 2.13.

The power transmission in mode m of a waveguide characterised by length l and radius of curvature R can be calculated as

$$T_b = \mathrm{e}^{-2\,\mathrm{Im}\{\beta_m(R)\}l}. \tag{2.78}$$

Figure 2.14 shows the imaginary part of the propagation constant of the fundamental mode as a function of radius of curvature. The fundamental mode is characterised by the smallest imaginary part among all the modes considered. The discrete values of β_0 are calculated with JCMsuite, while the connecting line is obtained with an exponential fit. The results are in agreement with those presented in [52]. As the imaginary part of the propagation constant increases for a decreasing radius of curvature, the bending loss also increases, which is calculated as $(1 - T_b)\cdot 100\,\%$. The percentage values for selected radii of curvature are listed in Table 2.2. In this table, a 90° bend is considered. It can be seen that for radii greater or equal than 50 µm, the bending loss is smaller than 1 %. As the radius decreases, the bending loss increases significantly, exceeding 70 % for radii as small as 10 µm.

To account for the reduced bending losses, a waveguide with a radius of curvature greater than 100 µm is considered a straight waveguide. This simplifies and accelerates the calculations because calculating modes in JCMsuite for higher radii of curvature is computationally difficult, cf. Subsection 2.3.1.

2.4.2. Transition loss due to geometry changes

Any change in the shape of a waveguide, such as its trajectory or cross-section, results in a redistribution of energy. At the interface between two waveguide sections with different geometries, the incoming electromagnetic field of the fundamental mode can be transmitted,

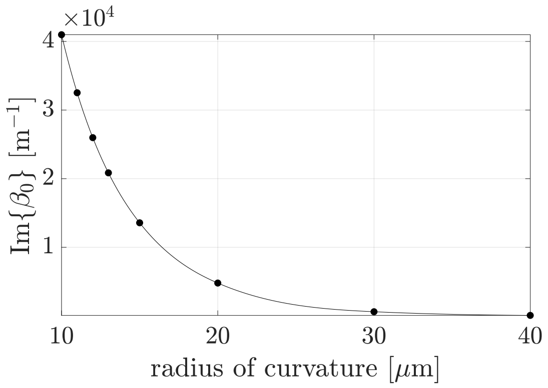

Figure 2.14.: Imaginary part of propagation constant of the fundamental mode as a function of radius of curvature. The radii are limited to a range in which the differences are notable. The results are calculated for $n_{\mathrm{cl}} = 1.34$, $n_{\mathrm{co}} = 1.57$ and a waveguide cross-section 1.4 µm × 1.0 µm (width × height). Bending occurs in the direction of the width.

Table 2.2.: Bending loss after a 90-degree bend for different radii of curvature.

Radius [µm]	Bending loss [%]
10	74.26
20	26.69
30	6.18
40	2.33
50	0.43
60	0.12
70	0.10
80	0.08
90	0.05
100	0.04

back-reflected, scattered into radiation modes, or coupled to higher-order guided modes [52, 110, 111]. Consequently, only a portion of the power remains guided, while the rest leaves the system.

The fraction of reflected and transmitted energy is quantified by the absolute values of reflection coefficient $|r_0|$ and transmission coefficient $|t_0|$, respectively. These coefficients can be determined using the *fundamental mode approximation*, which is presented in the following section. The fraction of power transmitted after the interface is calculated using the formula

$$T_t = |t_0|^2 \,. \tag{2.79}$$

Similarly to the case of bending loss, the value of T_t is used to calculate the transition loss as $(1 - T_t) \cdot 100\,\%$.

2.5. Fundamental mode approximation

While FEM, FIT, and FDTD computations can yield results that closely match experimental data, these simulations often demand significant time and memory resources. In scenarios where quick computations are essential – such as when optimising the shape of a waveguide by iteratively enhancing transmission – numerical methods employed in commercial software may not be adequate. Therefore, this section introduces the *fundamental mode approximation*, which originates from [52].

The fundamental mode approximation (FMA) is based on the assumption that waveguides predominantly transmit the energy in a single mode [52]. As illustrated in the Figure 2.2(a), in Section 2.2.1, the number of guided modes depends on the design of the waveguide. By selecting the height of the waveguide core appropriately, it can support one TE and one TM mode. Although both the TE and TM modes are supported, the two modes are orthogonal to each other, which means that energy transfer between them is not possible, cf. Subsection 2.2.4. Therefore, the problem can be simplified to focus on a single propagating mode, as the choice of polarisation does not influence the results [52].

The approximation method involves pre-calculation of the propagation constants and mode field profiles for waveguides of different radii of curvature. The FMA is realised by treating the waveguide as a series of arcs with specific curvatures. This method also takes into account the losses within the arcs and at the interfaces between them, which is discussed in the following subsections.

2.5.1. Interface problem

In Subsection 2.4.1 it is described how to calculate the propagation loss caused by bending. Subsection 2.4.2 mentions the transition loss between two segments due to the change in the shape of a waveguide. Here, we focus on the transmission through the interface that separates two waveguide segments with different curvatures, a situation referred to as *interface problem*, presented in Figure 2.15. The incident mode $|\mathcal{L}_0^+\rangle$ can be transmitted through the interface as mode $|\mathcal{R}_0^+\rangle$, reflected back as $|\mathcal{L}_0^-\rangle$, scattered into a continuum of radiation modes, $|\mathcal{L}_q^-\rangle$ or $|\mathcal{R}_q^+\rangle$, or coupled to discrete higher order modes, $|\mathcal{L}_m^-\rangle$ or $|\mathcal{R}_m^+\rangle$, with $m > 0$. The continuity of the tangential components of the electromagnetic field implies [52]

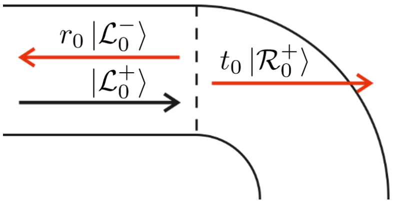

Figure 2.15: An interface between straight and bent waveguide section. A fundamental mode $|\mathcal{L}_0^+\rangle$ is incident from the left side of the interface. A part of the fundamental mode is transmitted into the right side and the rest is reflected back.

$$\begin{aligned}|\mathcal{L}_0^+\rangle + r_0\,|\mathcal{L}_0^-\rangle + \sum_{m>0} r_m\,|\mathcal{L}_m^-\rangle + \int r_q\,|\mathcal{L}_q^-\rangle\,\mathrm{d}q \\ = t_0\,|\mathcal{R}_0^+\rangle + \sum_{m>0} t_m\,|\mathcal{R}_m^+\rangle + \int r_q\,|\mathcal{R}_q^+\rangle\,\mathrm{d}q\,.\end{aligned} \tag{2.80}$$

In the above equation, t denotes amplitude transmission coefficient and r corresponds to amplitude reflection coefficient. The subscripts denote the particular mode number.

The difference between profiles of the fundamental modes $|\mathcal{L}_0^+\rangle$ and $|\mathcal{R}_0^+\rangle$ results in the excitation of higher order and radiation modes at the interface. However, if the deviation is small, most of the power will be transmitted in the fundamental mode. Under this assumption the higher-order modes in equation (2.80) are neglected, leading to the following relationship:

$$|\mathcal{L}_0^+\rangle + r_0\,|\mathcal{L}_0^-\rangle + \int r_q\,|\mathcal{L}_q^-\rangle\,\mathrm{d}q \;=\; t_0\,|\mathcal{R}_0^+\rangle + \int r_q\,|\mathcal{R}_q^+\rangle\,\mathrm{d}q\,. \tag{2.81}$$

The scattering coefficients r_0 and t_0 measure the fraction of reflected and transmitted amplitude, respectively. The amplitude reflection coefficient can be extracted from equation

(2.81) by projecting $|\mathcal{L}_0^+\rangle$ and $|\mathcal{L}_0^-\rangle$ on both sides of this equation and results in

$$r_0 = -\frac{\langle\mathcal{L}_0^-|\mathcal{R}_0^+\rangle}{\langle\mathcal{L}_0^+|\mathcal{R}_0^+\rangle}\,. \tag{2.82}$$

The amplitude transmission coefficient can be obtained further by projecting $|\mathcal{R}_0^+\rangle$ and $|\mathcal{R}_0^-\rangle$ onto (2.81) and utilising expression (2.82) as

$$t_0 = \langle\mathcal{L}_0^+|\mathcal{R}_0^+\rangle \cdot (1 - r_0^2)\,. \tag{2.83}$$

In the above derivation of the coefficients, the orthogonality relation (2.60) is applied, recognising that discrete modes are orthogonal to the continuum of radiation modes. Further in this thesis, the amplitude transmission and reflection coefficients are referred to simply as transmission and reflection coefficients, respectively. To avoid confusion, it is explicitly stated when the transmission of power is being considered.

2.5.2. Transmission coefficient for the infinite computational domain

To compute the transmission coefficient (2.83), the integral in (2.60) must be evaluated over the entire $\mathbb{R}^2$. However, this is not possible in practice. Therefore, the computational domain used in JCMsuite for calculating modes must be limited to a size that ensures the desired accuracy. Figure 2.16 shows how the absolute value of the transmission coefficient $|t_0|$ between two different waveguide segments varies depending on the computational domain size. The values oscillate in an exponentially damped manner, eventually converging to the proper value of the transmission coefficient $\bar{t}_0$ as the computational domain size approaches infinity. Note that although the transmission coefficient (2.83) is complex in general, only its absolute value is required to compute power transmission (2.79). Therefore, the value of $|t_0|$ is discussed in the following subsections.

The values of the integral (2.60), represented as a function $\ell \mapsto f(\ell)$, are calculated for different computational domain sizes ℓ. The asymptotic $\bar{t}_0$ can then be determined by fitting the computed data to the expression

$$f(\ell) = \bar{t}_0 + \mathrm{Re}\left\{2\tau \mathrm{e}^{\nu\ell}\right\}, \tag{2.84}$$

with τ and ν being complex parameters, similarly as in [52]. The values of all the parameters are determined iteratively using MATLAB's *fminsearch* function [119].

As shown in Figure 2.16, it is sufficient to consider a computational domain size of 10 µm to determine the asymptotic value $\bar{t}_0$. In subsequent calculations, this value $\bar{t}_0$ is used to calculate transition loss. The consideration of a result obtained for computational domain size 10 µm only, may be affected by a relative error up to 0.2 %. However, the oscillations are more pronounced for smaller radii of curvature, likely due to a significant portion of the eigenmode fields extending beyond the waveguide core in cases of small bending radii, as illustrated in Figure 2.13.

In practice, it is sufficient to restrict the computational domain to 10 µm × 10 µm for straight waveguides and bends of low curvature, cf. Figure 2.13. However, to improve accuracy for bends, the domain is extended to 20 µm in the outer bow direction. This is the direction where the mode *stretches* and leaks into the cladding.

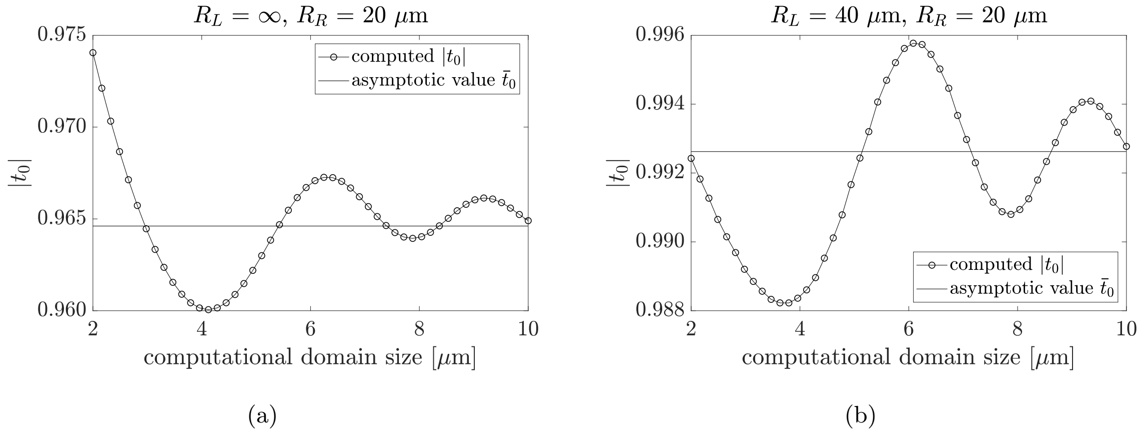

Figure 2.16.: Absolute values of transmission coefficients as a function of computational domain size for an interface between (a) straight and bent waveguide section of radius $R_R = 20\,\mu\text{m}$ and (b) two bent waveguide sections of radii $R_L = 40\,\mu\text{m}$ and $R_R = 20\,\mu\text{m}$.

2.5.3. Map of transmission coefficients

The range of possible radii of curvature spans a wide spectrum, covering essentially all real numbers. However, in reality, modes can only be computed for a limited set of radii of curvature. First of all, in the mode calculations, we limit the radii of curvature to positive values. The mode profile of radius $-R$ can be obtained from R by flipping the corresponding mode profile along the bending direction. The propagation constant remains the same. Moreover, the considered radii of curvature are bound to a reasonable interval. The lower bound for the considered radius of curvature is determined to be 6 µm, based on the implementation of bending in JCMsuite [65] as previously explained in Subsection 2.3.1. When the radii of curvature are very small, the modes are no longer guided, resulting in significant losses. Consequently, waveguides with extremely sharp bends are typically not considered in practice. Nevertheless, some studies [120–123] explore bends of 10 µm and below, which are already categorised as very sharp. The investigation of mode coupling is relevant for higher radii of curvature, where the broken orthogonality is not only a perturbation due to loss. Generally, the upper bound of the radius of curvature considered in this analysis is infinity, which corresponds to a straight waveguide. Here, however, the value 100 µm is selected as the upper bound. This choice is justified by the minimal change observed in the fields when the radius is 100 µm or greater. Another factor is the increased computation time in case of higher radii of curvature. To mitigate this issue, the values of the radii of curvature are not spaced evenly. A coarser sampling is sufficient for weaker bending, while a finer sampling becomes necessary for radii smaller than 50 µm due to the higher variation of the fields within this range. Once the set of radii of curvature is defined, the guided modes are computed for each radius.

Equation (2.83) allows for calculating the transmission coefficients only for two segments of particular radii of curvature. To account for all possible combinations of radii of curvature, lookup tables of transmission coefficients, later called *t-maps*, are generated. The exemplary t-map is presented in Figure 2.17. The transmission matrices are computed for each combination of radii from the set defined earlier. Then, the values of the transmission coefficient are refined with using MATLAB function *griddata*. This built-in function interpolates the known values of transmission to correspond to a finer set of radii of curvature.

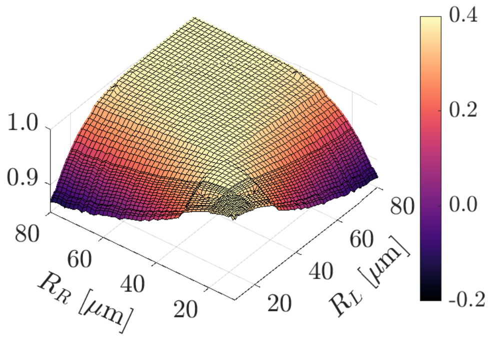

Figure 2.17: Map of transmission coefficients for a waveguide of 1.4 µm×1.0 µm core of $n_{\mathrm{co}} = 1.57$ and cladding $n_{\mathrm{cl}} = 1.34$.

2.5.4. Generalisation to arbitrary 2D trajectory

In the previous section, the connection of only two segments is considered. To calculate transmission in a waveguide of arbitrary[8] trajectory, it can be divided into segments approximated with arcs of constant radii of curvature, as shown in Figure 2.18. For each segment, the transmission in the presence of bending is calculated according to formula (2.78) and the transmission coefficients are evaluated for the interfaces between consecutive segments.

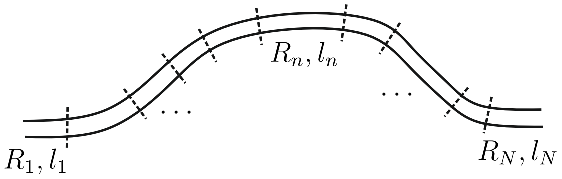

Figure 2.18.: Waveguide trajectory divided into N segments of length l_n and constant radius of curvature R_n, with $n = 1, \cdots, N$.

The fraction of power transmitted to the output of the waveguide is then determined as

$$T = T_b \cdot T_t \tag{2.85}$$

where T_b denotes transmission weakened by bending and T_t indicates transmission through all the interfaces between waveguide sections, calculated as

$$T_b = \prod_{n=1}^{N} \exp(-2\,\mathrm{Im}\{\beta(R_n)\} l_n)\,, \tag{2.86}$$

$$T_t = \prod_{n=1}^{N-1} |t_n|^2. \tag{2.87}$$

The presented FMA method is applicable to single-mode waveguides in optimal scenarios in which the waveguides are optimised for maximum transmission. The extension of this method to higher-order modes is presented in Section 3.2.

---

[8] In this work only bending in one plane is considered. Twisting of the waveguide is not taken into account.

2.6. Summary

This chapter provides a concise introduction to waveguide theory, beginning with Maxwell's equations. It explains light confinement and propagation in slab and channel waveguides. Furthermore, this chapter introduces the concept of an eigenmode expansion of the electromagnetic field. This concept is later used in the approximation methods to calculate the transmission of free-form waveguides. The modes are determined using a FEM solver, while the transmission of the waveguides is computed using FIT and FDTD solvers and is used later as a reference for approximation methods. All used numerical methods are explained in this chapter. The final section introduces the fundamental mode approximation, which assumes that the waveguide supports only the fundamental mode. In this method the waveguide trajectory is approximated using arcs with a constant radius of curvature. The calculated transmission results from propagation loss in the segments and transition loss at the intersections between segments. This approximation method is further expanded in Chapter 3 to include higher-order modes propagating through the waveguides.

3 | Fast calculation of transmission in multi-mode waveguides

This chapter presents approximation methods for computing the transmission through bent waveguides significantly more efficiently than full-wave simulations. This means that the approximate simulations are faster and require less computing resources while solving the problem with sufficient accuracy. The focus is on waveguides that support the propagation of multiple modes. The first approximation, referred to as multi-mode approximation (MMA), is introduced in Section 3.2. The content of this section has been published in [P2] and presented at conferences [C3–C5]. The new approximation method extends the FMA, as discussed in Section 2.5, to include higher-order propagating modes. The Section 3.2 provides a detailed description of the MMA, covering the analysis of higher-order modes and their orthogonality, propagation and transition loss, t-maps, and trajectory segmentation, analogous to Section 2.5. The method is applied to several examples in Section 3.3 and compared against numerical simulations performed with CST Microwave Studio [84]. The second approach discussed in this chapter, detailed in Section 3.4, utilises artificial neural networks (ANNs). The networks have been trained to learn the relation between trajectory and transmission using a large amount of precomputed data. Various architectures are explored to evaluate their ability to predict transmission in a waveguide based on its trajectory. Each example is assessed based on the time required to obtain the result and the accuracy of the result compared to the reference.

3.1. Introduction

The propagation of higher-order modes in waveguides is sometimes not only unavoidable but may be desired in silicon photonics. It increases the number of channels to transmit data in mode-division-multiplexed systems [124], where multiple guided modes carry signals. Multi-mode silicon-on-insulator (SOI) waveguides may be used to directly couple few-mode optical fibers and photonic chips [125, 126]. Silicon waveguides sustaining higher-order modes find applications also in on-chip add-drop optical filters based on a multi-mode Fabry-Perot cavities [127] and on-chip polarisation-handling devices [128]. Furthermore, allowing multi-mode transmission and waveguide shapes deviating from a straight path expands the possibilities of waveguide design. Flexibility and compactness of photonic devices [129, 130] can be achieved through bending, as demonstrated in multiple studies [120–122, 130].

Here, we consider propagation of higher order modes in free-form waveguides, fabricated by high-resolution 3D laser lithography. The exemplary waveguides are presented in Figure 3.1(a). Their purpose is to connect different components on a silicon photonic chip [53]. When placing the chip components onto a common substrate during mass production, the exact positions of the components may vary from sample to sample. These relaxed alignment tolerances facilitate the production process. To accommodate the placement inaccuracies, the waveguide connections, also referred to as *photonic wire bonds* PWBs, are fabricated *in situ* [42, 45, 46]. This means that the trajectories cannot be designed in advance. An optimal trajectory with minimal transmission loss needs to be calculated only after examining the spatial locations of input and output ports. Given the target fabrication cycle of at most tens of seconds, a fast and reliable strategy is essential to compute the optimal trajectory with minimal loss. This optimisation process requires a tool to accurately and reliably predict the loss [52]. Employing a full-wave numerical solution to Maxwell's equations is not feasible due to the large spatial extent of the waveguides, which can be on the order of hundreds of micrometers [P1], making it impractical within the time constraints of the optimisation.

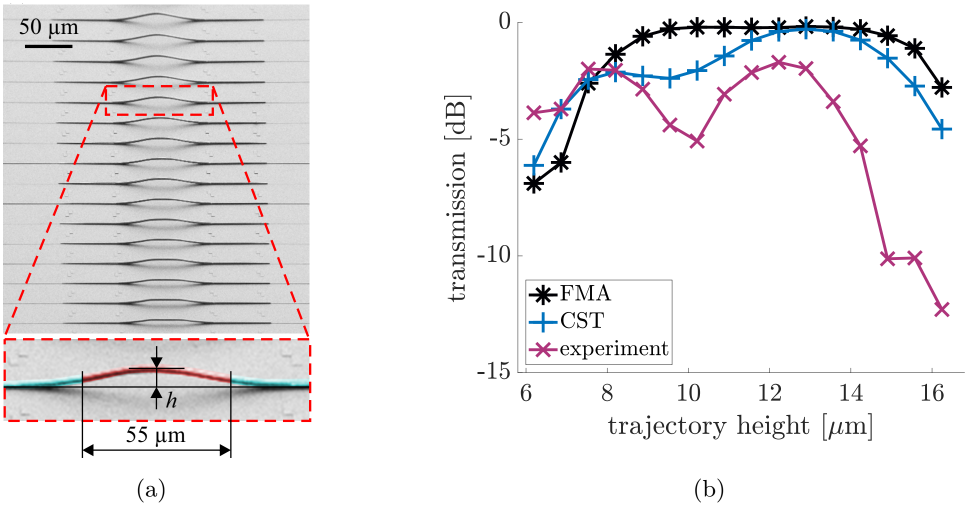

(a) (b)

Figure 3.1.: (a) An SEM (scanning electron microscope) picture of a series of photonic wire bonds spanning over 100 µm, differing by heights h; figure adapted from [P1]. (b) Comparison of transmission determined with different methods: FMA, CST and experimental measurement. The fabricated trajectories are characterised by their height. The result of approximation method is not accurate for some waveguides. The experimental results were provided by colleagues from the research group of Prof. Christian Koos from the Institute of Photonics and Quantum Electronics (IPQ) at the Karlsruhe Institute of Technology.

To predict the transmission from these PWBs, simplified methods for quick modelling of large optical waveguide structures are needed. Using a numerical solution to Maxwell's equations (such as the finite element method or finite-difference time-domain approach) is no longer feasible. It was shown in Section 2.5 that the transmission through free-form waveguides can be predicted based on the FMA [52]. This approach assumes that the energy is carried along the waveguide only by a fundamental mode with a given polarisation. An arbitrary trajectory of a photonic wire bond is divided into segments with a constant radius of curvature. The total loss can be calculated by accumulation of the bending and transition losses. Bending loss occurs in segments of small radius of curvature and is linked to the complex-valued propagation constant [49]. Transition loss occurs at the interfaces between waveguide segments with different radii of curvature. In the FMA, the loss is computed from the transmission coefficient of the fundamental mode propagating in consecutive waveguide segments. While the results of this approach agree with numerical simulations for simple-shaped waveguides, the obtained transmission does not entirely align with experiments, which is presented in Figure 3.1(b). For some advanced trajectories the FMA overestimates the transmission [P1]. These issues motivated us to develop a framework to obtain information about the transmission of higher-order modes in such approximate setting, which could be useful for designing multi-mode waveguides efficiently.

3.2. Multi-mode approximation

The multi-mode approximation (MMA) aims to address the limitations of the FMA when dealing with waveguides where higher order modes are excited with a notable amplitude [P1]. This occurs, for instance, in spatial areas with a sudden change in the radius of curvature. Examples of such trajectories are presented in Figure 3.2. The figure shows the real part of electric field amplitude that propagates in photonic wire bonds of different shapes. The amplitude is shown on a y-z plane which intersects with the centre of the waveguide core. In the middle example the curvature of the trajectory changes smoothly, while in the remaining two waveguides kinks are present, where a fraction of the amplitude is visually present in the surroundings. In such cases, light is also significantly coupled to higher-order modes, impacting the transmission of the fundamental mode. In analogy to the FMA, the MMA requires precomputation of modal properties of guided modes for a chosen set of radii of curvature. While not necessary for the method itself, precomputing modal properties greatly accelerates the prediction of loss, which is a prerequisite for prospective optimisation.

The MMA procedure involves tracking the amplitudes of a few selected modes guided along the waveguide. The trajectories should be made of smooth C^2 curves, with at least a C^1 connection between straight and curved segments [110]. We assume that the curvature changes in one plane and the cross-section is constant along the trajectory, so the potential tapers are not considered. The waveguide with the arbitrary trajectory is divided into a finite number of segments, each with a constant radius of curvature. Within each waveguide segment, the propagation of modes can be described as a multiplication of their modal amplitudes with an exponential function. This exponential function includes the length of the waveguide segment multiplied by the complex propagation constant of the respective mode. The real part of the propagation constant corresponds to a certain phase accumulated by the mode, and the non-zero imaginary part of the propagation constant implies a decrease in modal amplitude due to non-vanishing radiation loss. At the interface between the waveguide segments with different radii of curvature, the orthogonality of the modes is broken, and the modes can mutually couple. This effect is quantified by a transmission matrix that contains the inter- and intra-mode transmission coefficients. To calculate these transmission matrices, we need to know the tangential field profiles of the modes in the two neighbouring segments. To make future simulations faster, we calculate the modal properties for finely sampled radii of curvature in advance. We use t-maps that contain information on how transmission coefficients change between waveguide segments with different radii of curvature. In this work, we consider two modes supported in a waveguide, and the trajectories confined to a single plane.

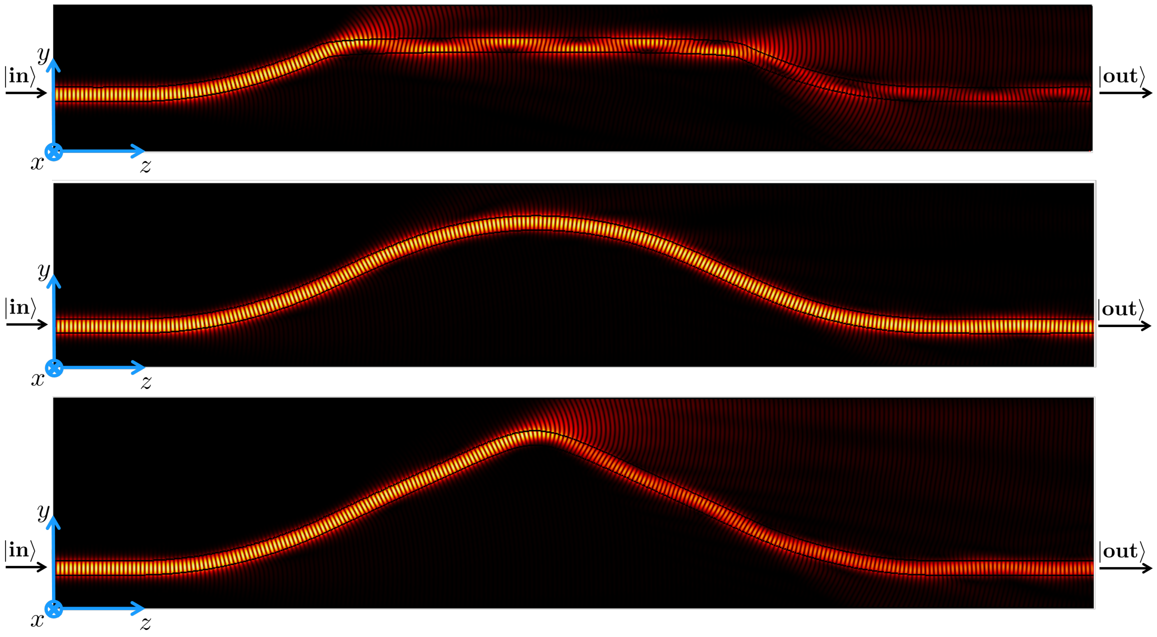

Figure 3.2.: The amplitude of the real part of the propagating electric field in photonic wire bonds, which span over 100 µm, and differ by shape and trajectory height. The input and the output modes are denoted with |**in**⟩ and |**out**⟩, respectively. The uppermost trajectory features two *kinks*, which correspond to spots of significant radiation loss. An oscillating interference pattern is also observable within this trajectory. The trajectory in the bottom consists of one kink, where the field is lost due to radiation. The optimal trajectory, shown in the middle image, is smooth and exhibits minimal loss. The fields were computed with CST Microwave Studio for the entire 3D structures with the simulation settings according to the Subsection 2.3.2. The trajectories are chosen from the set presented in Figure 3.1(a), based on geometry parameters provided by Dr. Aleksandar Nesic from the Institute of Photonics and Quantum Electronics (IPQ) at the Karlsruhe Institute of Technology. The simulation was performed for waveguide cross-section 1.8 µm×2.0 µm (height×width), $n_{\text{co}} = 1.53$, $n_{\text{cl}} = 1.36$, and wavelength 1.55 µm.

3.2.1. Higher-order modes

The photonic wire bonds that are studied here, are characterised by rectangular cross-sections and confine light in two transverse directions [71], labelled as x and y. The modes are guided along the waveguide core if their effective refractive index n_{eff} satisfies the condition $n_{\text{cl}} \leq n_{\text{eff}} \leq n_{\text{co}}$ [68, 69, 131]. The waveguides being studied have the following parameters [P1]: height 1.8 µm, width 2.0 µm, wavelength 1.55 µm, refractive index of the core $n_{\text{co}} = 1.53$ and the cladding $n_{\text{cl}} = 1.36$. A mode analysis shows the propagation of six modes, including three quasi-transverse-electric (TE) modes and three quasi-transverse-magnetic (TM) modes. This motivates consideration of a multi-modal approach to accurately predict the transmission.

To calculate the propagating modes, we analyse a waveguide cross-section perpendicular to the direction of propagation of the modes. The electric and magnetic fields carried by the modes are computed with the commercially available finite element method (FEM) solver JCMsuite [65]. The field distribution and propagation constants are obtained by solving Maxwell's equations as an eigenvalue problem [132] for source-free media in the frequency domain [62, 133, 134]. Despite being limited to two-dimensional cross-sections, the software can accommodate bending and twisting of the waveguide.

JCMsuite can identify several propagating modes. The field profiles differ in terms of amplitude, and shape, as well as the positions and number of positive and negative extrema. Figure 3.3 displays the real part of the x-component of the normalised electric field of three lowest-order modes of the same polarisation, found in a straight (top row) and bent waveguide (bottom row). The modes are arranged based on their decreasing effective refractive index. The effective refractive index of the respective mode m is related to the propagation constant β_m by $n_{\mathrm{eff}}^m = k_0^{-1}\beta_m$, with vacuum wave number $k_0 = 2\pi\lambda^{-1}$, and wavelength λ. To make the notation match the description in this chapter, the modes are numbered with positive integers $m = 1, 2, 3, \ldots$, with $m = 1$ denoting the fundamental mode, and $m > 1$ denoting higher-order modes. Note, that in Chapter 2, the numbering starts with 0, which is required for the derivation in Subsection 2.2.1. To simplify the notation, we also skip the superscript m in the representation of effective refractive index further in this thesis.

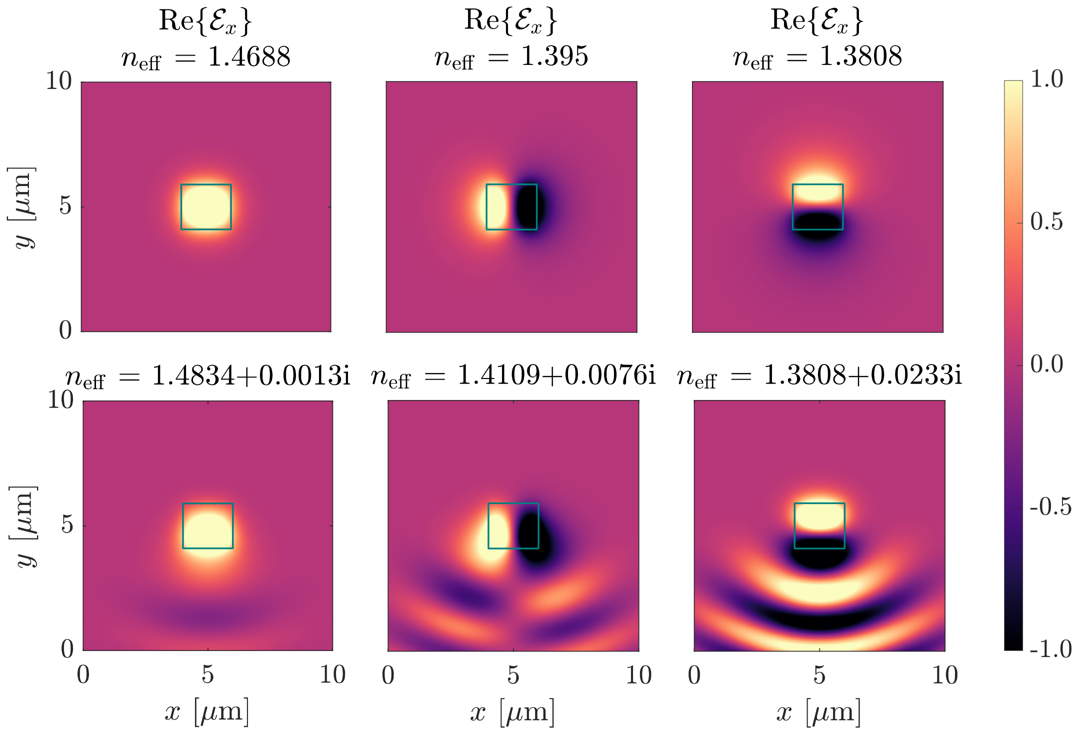

Figure 3.3.: Mode profiles of the real part of the x-component of the normalised electric field calculated with JCMsuite. The field is normalised to the maximum of the field in the fundamental mode of a straight waveguide, which is characterised by $n_{\mathrm{eff}} = 1.4688$. The columns represent different modes. The top row displays the fields in a straight waveguide, while the bottom row shows the fields in a waveguide bent along the y-axis, with a radius of curvature 20 µm, measured from the centre of curvature to the centre of the waveguide's cross-section. The centre of curvature is located above the depicted mode profiles. The figure also provides information on the effective refractive indices of the corresponding modes. The core of the waveguide, indicated by a green rectangle, is surrounded by the cladding. The computational domain is limited to a 10 µm × 10 µm square. This figure is reprinted from [P2]. Copyright © 2024 Optica Publishing Group.

In this study, we focus on two propagating modes: the fundamental mode and a second higher-order mode with the same polarisation and symmetry. It means that if the waveguide is bent along the y-direction, the modes shall exhibit the same symmetry in x-direction and possibly one additional amplitude node in the y-direction, as shown in the third column in Figure 3.3. These characteristics enable mode coupling if the waveguide's curvature changes.

In a bent waveguide, the modes become concentrated in the outer region of the waveguide and are no longer centred in the core. As it is visible in Figure 3.3, with a smaller radius of curvature, the mode profile deforms and shifts away from the centre of the waveguide. Additionally, the introduction of finite radiation loss causes these fields to oscillate outside the waveguide. Consequently, the mirror symmetry of the modes along the bending direction is broken. This disrupted mirror symmetry allows for coupling between modes at interfaces of waveguide segments with different radii of curvature, as the mode profiles start to overlap (cf. the maximum of the third mode in the bent waveguide with the maximum of the first mode in the straight waveguide in Figure 3.3). This coupling affects the transmission between adjacent waveguide segments, the effect we aim to capture in the MMA.

Another modal parameter affected by curvature is the effective refractive index n_{eff}, which is shown in Figure 3.4. Figure 3.4(a) illustrates the real part of n_{eff}, representing phase accumulation of the modes upon propagation. Depending on the mode number, the phase may either increase or decrease with bending. When a waveguide is bent, the change of the real part of the effective refractive index depends on the core-cladding index contrast and the parameter V [135], cf. Subsection 2.2.1. The change in the effective refractive index can be intuitively explained with the localisation of the mode field profile. If the mode is strongly confined to the waveguide core, its field profile tends to be *squeezed* when the waveguide is bent. This can be seen in case of the fundamental mode in the first column in Figure 3.3. Therefore, the effective refractive index increases and approaches n_{co}. On the other hand, when the significant part of the mode field is localised in the waveguide core, the effective refractive index of this mode is lower, and decreases when the waveguide is bent, because more field leaks to the cladding. In this case, the effective refractive index approaches n_{cl}.

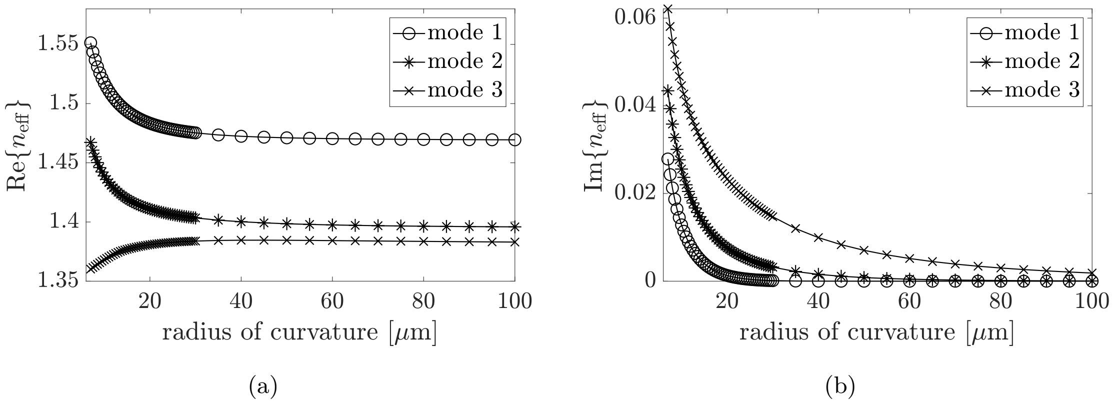

(a)

(b)

Figure 3.4.: The real part (a) and imaginary part (b) of the effective refractive index as a function of radius of curvature of the waveguide for the three lowest-order modes. Figure is reprinted from [P2]. Copyright © 2024 Optica Publishing Group.

Figure 3.4(b) presents the imaginary part of n_{eff}, which indicates the attenuation of the modal amplitude. It is apparent from Figure 3.4(b) that the imaginary part of the effective refractive index increases with a decreasing radius of curvature, indicating an increase in bending loss. When the radius of curvature becomes very small, the modes are no longer guided but are weakly coupled to the continuum of free space modes.

The guided modes are calculated individually for each radius of curvature, and they are ordered based on the decreasing real part of the effective refractive index [65]. It is important to consider the same mode by keeping the symmetry and sign of the corresponding modes consistent across all radii of curvature. The problem of symmetry and ordering of modes is explained in more detail in Chapter 6.

3.2.2. Bending: propagation loss

In the MMA, similarly to the FMA, we analyse the *bending loss* if the waveguide is no longer straight, and the *transition loss* if the radius of curvature of the waveguide changes. We neglect the possible loss caused by the quality of fabrication or material impurities [52].

As already explained in Subsection 2.4.1, the bending loss is quantified by the imaginary part of the propagation constant of the mode. It increases with decreasing radius of curvature, which is shown in Figure 2.14 for the fundamental mode in a waveguide. The transmission of the mode m along the bent segment n scales with

$$\mathrm{e}^{(\mathrm{i}\mathrm{Re}\{\beta_m(R_n)\}-\mathrm{Im}\{\beta_m(R_n)\})l_n},$$

where l_n is the length of the segment and R_n denotes its radius of curvature. Note the sign convention in the exponent, suggesting a positive value of the imaginary part of the propagation constant.

3.2.3. Interface problem: transition loss

Along with calculating the bending loss experienced by each mode while travelling through a curved segment of the waveguide, we calculate the change in the mode amplitudes at the intersection of two waveguide segments characterised by different radii of curvature. From the different modal field amplitudes, we calculate the transmission of the modes through the interface.

Therefore, we consider an *interface problem*, sketched in Figure 3.5, which shows the plane separating two waveguide segments of different curvatures. In the figure, we assume that the modes propagate from the left segment (input) to the right segment (output). The arbitrary superposition of modes $|\mathcal{L}_m^+\rangle$ approaching the interface excites the transmitted modes $|\mathcal{R}_m^+\rangle$ and reflected modes $|\mathcal{L}_m^-\rangle$. Any irregularity in the trajectory (such as the change in curvature in this case) causes also scattering of the guided modes into a continuum of radiation modes $|\mathcal{L}_q^-\rangle$ or $|\mathcal{R}_q^+\rangle$ [50], not shown in Figure 3.5. On the output side, we may detect also the backward propagating modes $|\mathcal{R}_m^-\rangle$, reflected from the following interfaces. However, their influence on the transmission is minor because the multiple reflections do not yield significant field amplitudes [52]. Therefore, they are not considered in the computations.

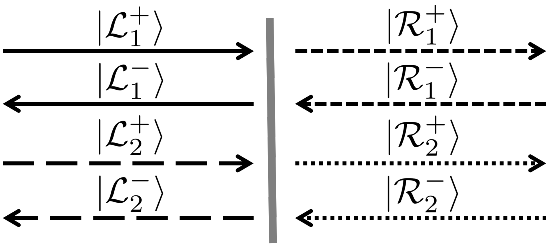

Figure 3.5.: Two forward propagating incident modes, denoted as $|\mathcal{L}_1^+\rangle$ and $|\mathcal{L}_2^+\rangle$, are present on the left-hand side of the interface. These modes are transmitted into two forward-propagating modes, $|\mathcal{R}_1^+\rangle$ and $|\mathcal{R}_2^+\rangle$, on the right-hand side of the interface. The incident modes are also reflected at the interface and propagate back as modes $|\mathcal{L}_1^-\rangle$ and $|\mathcal{L}_2^-\rangle$. On the right side, there are also backward-propagating modes, $|\mathcal{R}_1^-\rangle$ and $|\mathcal{R}_2^-\rangle$. These backward modes may be created by reflections from subsequent interfaces or could also be present if the principal direction of propagation were reversed. Figure is reprinted from [P2]. Copyright © 2024 Optica Publishing Group.

The tangential field components of the propagating modes need to be the same on both sides of the interface between the two segments. This means that the combined modal fields at the inlet (left) must be equal to the combined fields at the outlet (right) [50, 51]:

$$\sum_m i_m |\mathcal{L}_m^+\rangle + \sum_m r_m |\mathcal{L}_m^-\rangle + \int r_q^- |\mathcal{L}_q^-\rangle \, \mathrm{d}q = \sum_m t_m |\mathcal{R}_m^+\rangle + \int r_q^+ |\mathcal{R}_q^+\rangle \, \mathrm{d}q \,, \tag{3.1}$$

where r_m and t_m represent the reflection and transmission coefficients, respectively, while i_m indicates the amplitude distribution among the incident modes. The profiles of the fundamental modes $|\mathcal{L}_1^+\rangle$ and $|\mathcal{R}_1^+\rangle$ are different, which causes the excitation of higher-order and radiation modes at the interface. This can be observed in the values of the inner product (2.60) between the modes propagating in adjacent waveguide segments. We do not consider all the propagating modes in the sums of (3.1) but only those modes that propagate to the following waveguide segments with minimal loss and that are excited at the interface by a notable amplitude. Our calculations assume that the waveguide is excited with the fundamental mode, which is typical in practical applications [30, 136, 137]. As the fundamental mode propagates, higher-order modes are excited at locations where the radius of curvature changes. These higher-order modes are essential to satisfy the interface condition (3.1) with improved accuracy compared to the fundamental mode approximation [52]. In the following, we consider two lowest-order modes.

In order to proceed, we require the scattering coefficients r_m and t_m. These can be obtained by projecting the transposed modes $\langle\mathcal{R}_m^+|$ and $\langle\mathcal{R}_m^-|$ onto both sides of the equation (3.1), for each mode. Considering a total of M modes results in a set of $2M$ equations, which in the case of two modes leads to the following set of equations:

$$i_1 \langle\mathcal{R}_1^+|\mathcal{L}_1^+\rangle + i_2 \langle\mathcal{R}_1^+|\mathcal{L}_2^+\rangle + r_1 \langle\mathcal{R}_1^+|\mathcal{L}_1^-\rangle + r_2 \langle\mathcal{R}_1^+|\mathcal{L}_2^-\rangle = t_1 \langle\mathcal{R}_1^+|\mathcal{R}_1^+\rangle + t_2 \langle\mathcal{R}_1^+|\mathcal{R}_2^+\rangle \tag{3.2}$$

$$i_1 \langle\mathcal{R}_2^+|\mathcal{L}_1^+\rangle + i_2 \langle\mathcal{R}_2^+|\mathcal{L}_2^+\rangle + r_1 \langle\mathcal{R}_2^+|\mathcal{L}_1^-\rangle + r_2 \langle\mathcal{R}_2^+|\mathcal{L}_2^-\rangle = t_1 \langle\mathcal{R}_2^+|\mathcal{R}_1^+\rangle + t_2 \langle\mathcal{R}_2^+|\mathcal{R}_2^+\rangle \tag{3.3}$$

$$i_1 \langle\mathcal{R}_1^-|\mathcal{L}_1^+\rangle + i_2 \langle\mathcal{R}_1^-|\mathcal{L}_2^+\rangle + r_1 \langle\mathcal{R}_1^-|\mathcal{L}_1^-\rangle + r_2 \langle\mathcal{R}_1^-|\mathcal{L}_2^-\rangle = t_1 \langle\mathcal{R}_1^-|\mathcal{R}_1^+\rangle + t_2 \langle\mathcal{R}_1^-|\mathcal{R}_2^+\rangle \tag{3.4}$$

$$i_1 \langle\mathcal{R}_2^-|\mathcal{L}_1^+\rangle + i_2 \langle\mathcal{R}_2^-|\mathcal{L}_2^+\rangle + r_1 \langle\mathcal{R}_2^-|\mathcal{L}_1^-\rangle + r_2 \langle\mathcal{R}_2^-|\mathcal{L}_2^-\rangle = t_1 \langle\mathcal{R}_2^-|\mathcal{R}_1^+\rangle + t_2 \langle\mathcal{R}_2^-|\mathcal{R}_2^+\rangle \tag{3.5}$$

Some terms in (3.2)–(3.5) vanish due to the orthogonality relations (2.60). Rearranging the equations (3.2)–(3.5) enables us to express the formulas for transmission and reflection coefficients concisely in matrix form,

$$\begin{aligned}|\mathbf{t}\rangle &= \begin{pmatrix} \langle\mathcal{R}_1^+|\mathcal{R}_1^+\rangle & \langle\mathcal{R}_1^+|\mathcal{R}_2^+\rangle \\ \langle\mathcal{R}_2^+|\mathcal{R}_1^+\rangle & \langle\mathcal{R}_2^+|\mathcal{R}_2^+\rangle \end{pmatrix}^{-1} \begin{pmatrix} \langle\mathcal{R}_1^+|\mathcal{L}_1^+\rangle & \langle\mathcal{R}_1^+|\mathcal{L}_2^+\rangle \\ \langle\mathcal{R}_2^+|\mathcal{L}_1^+\rangle & \langle\mathcal{R}_2^+|\mathcal{L}_2^+\rangle \end{pmatrix} \begin{pmatrix} i_1 \\ i_2 \end{pmatrix} \\ &= \begin{pmatrix} t_{11} & t_{12} \\ t_{21} & t_{22} \end{pmatrix} \begin{pmatrix} i_1 \\ i_2 \end{pmatrix} = \hat{\boldsymbol{t}}\,|\mathbf{i}\rangle\,, \end{aligned} \tag{3.6}$$

$$|\mathbf{r}\rangle = -\begin{pmatrix} \langle\mathcal{R}_1^-|\mathcal{L}_1^-\rangle & \langle\mathcal{R}_1^-|\mathcal{L}_2^-\rangle \\ \langle\mathcal{R}_2^-|\mathcal{L}_1^-\rangle & \langle\mathcal{R}_2^-|\mathcal{L}_2^-\rangle \end{pmatrix}^{-1} \begin{pmatrix} \langle\mathcal{R}_1^-|\mathcal{L}_1^+\rangle & \langle\mathcal{R}_1^-|\mathcal{L}_2^+\rangle \\ \langle\mathcal{R}_2^-|\mathcal{L}_1^+\rangle & \langle\mathcal{R}_2^-|\mathcal{L}_2^+\rangle \end{pmatrix} \begin{pmatrix} i_1 \\ i_2 \end{pmatrix} = \hat{\boldsymbol{r}}\,|\mathbf{i}\rangle\,, \tag{3.7}$$

with $|\mathbf{r}\rangle = (r_1, r_2)^{\mathrm{T}}$ and $|\mathbf{t}\rangle = (t_1, t_2)^{\mathrm{T}}$ being the vectors of reflection and transmission coefficients, respectively. The vector $|\mathbf{i}\rangle = (i_1, i_2)^{\mathrm{T}}$ represents the incident field distribution. When an incident single-mode field encounters the interface, its amplitude is expressed as the fundamental mode, denoted as $|\mathbf{i}\rangle = (1, 0)^{\mathrm{T}}$. In equation (3.6), the vector $|\mathbf{i}\rangle$ is multiplied with the transmission matrix $\hat{\boldsymbol{t}}$, where each entry represents the transmission from an input waveguide segment to an output waveguide segment. The coefficients t_{11} and t_{22} indicate the transmission of mode 1 and 2 through the interface as mode 1 and 2, respectively. The off-diagonal coefficients t_{12} (t_{21}) indicate the fraction of mode 2 (1) coupled to mode 1 (2). The highest off-diagonal coefficients are used here to determine the higher-order mode to be considered in the multi-mode approximation presented here. In general, the dimensions of the matrices appearing in (3.6) and (3.7) depend on the number of considered modes. In this work, the transmission coefficients are collected in 2×2 matrices, while in the case of fundamental mode approximation, only the values of t_{11} are present. Additionally, the matrix of reflection coefficients can be obtained from equation (3.7). However, it is not necessary for calculating the transmission and is not used in the following approximation method.

3.2.4. Transmission maps

In contrary to the fundamental mode approximation (Section 2.5), in the presence of higher-order modes, the transmission coefficients take a matrix form. Therefore, the t-maps are created separately for real (Figure 3.6) and imaginary parts (Figure 3.7) of all the entries of the transmission matrix $\hat{\boldsymbol{t}}$. The calculation of t-maps was presented also in conferences by Dr. Mariia Sukhova [CO2, CO3] and described in her PhD thesis [138].

The t-map does not account for a change in sign of curvature after passing a possible inflection point. However, this should not be a problem in optimisation procedures, which aim to find waveguide trajectories with low loss. For such trajectories, a smooth transition between segments is expected, with a gradual change of the waveguide curvature meaning no sudden variation of the bending radius, especially not a change in sign. This expectation is confirmed by selected full-wave simulations of light propagation through a sequence of segments where the radius of curvature is constant, using CST Microwave Studio. In particular, we consider a waveguide decomposed into four segments: a straight segment, two bends of radius 10 µm and another straight segment. We look at two cases: when the

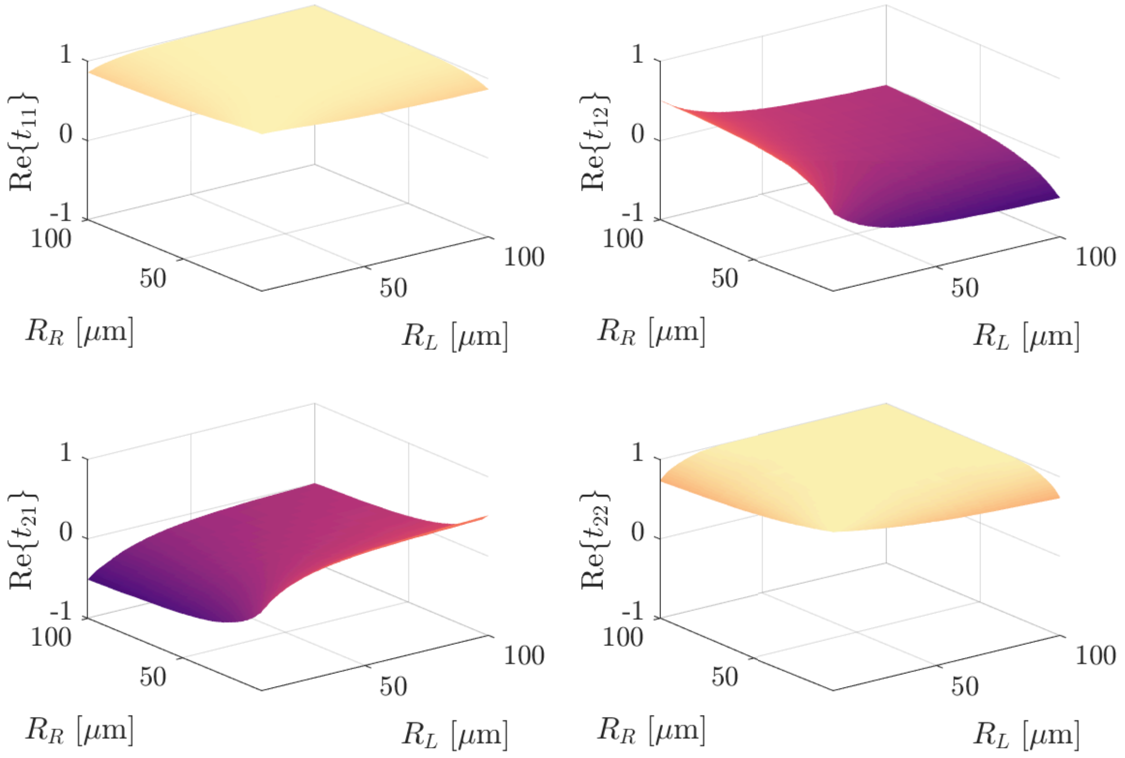

Figure 3.6.: Transmission maps for the real part of each component of the transmission matrix $\hat{\boldsymbol{t}}$. The coefficients are calculated for all combinations of bending radii of adjacent segments from the selected set. The values of the transmission coefficient are interpolated with MATLAB function *griddata* to create smooth surfaces. For readability, the displayed range is limited to a maximum of 100 µm. Figure is reprinted from [P2]. Copyright © 2024 Optica Publishing Group.

bending direction remains the same (Figure 3.8(a)) and when it changes (Figure 3.8(b)). Figure 3.8 shows the absolute value of electric field amplitudes in a central cross-section of the waveguide (in the y-z-plane at $x = 0$). In the subfigures, the total transmission into the fundamental mode in both configurations is indicated. Both configurations suffer from the same bending loss and the same loss at the interface between the straight and the bend segments, according to the approximation theory. However, the total transmission is smaller in the S-bend, where the curvature sign changes. This change of sign causes additional losses. Therefore, an abrupt sign change should be avoided.

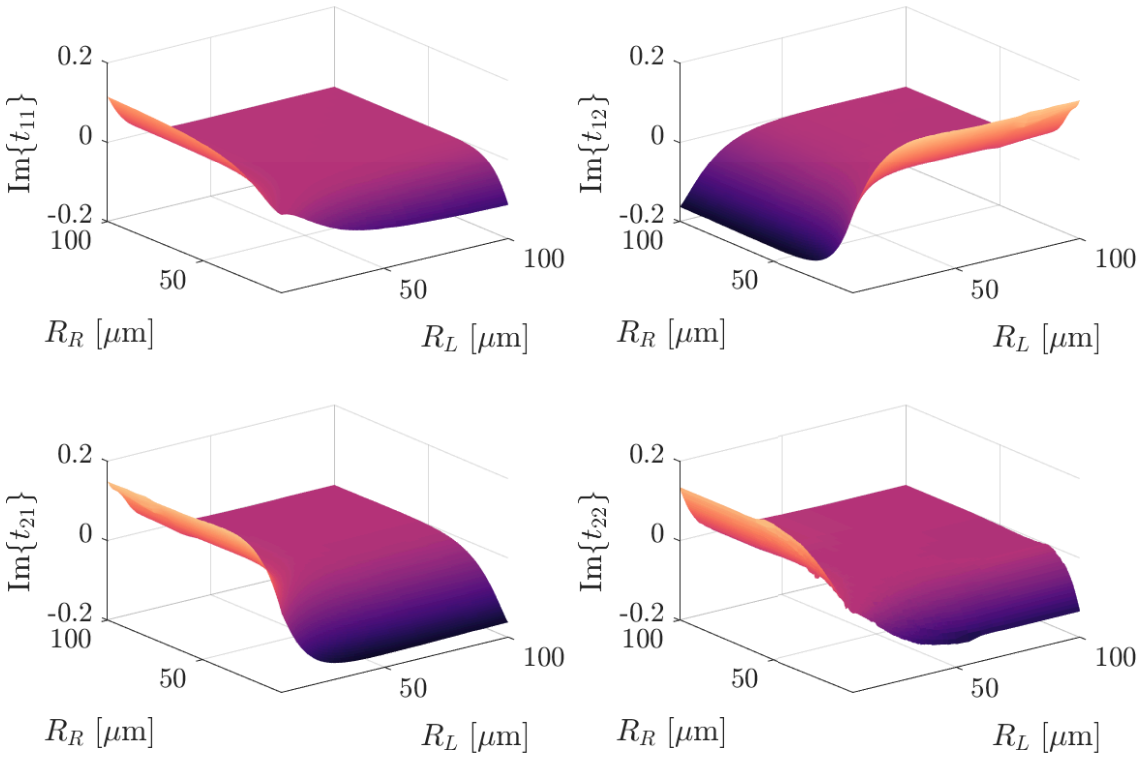

Figure 3.7.: Transmission maps for the imaginary part of each component of the transmission matrix $\hat{\boldsymbol{t}}$. The coefficients are calculated for all combinations of bending radii of adjacent segments from the selected set. The values of the transmission coefficient are interpolated with MATLAB function *griddata* to create smooth surfaces. For readability, the displayed range is limited to a maximum of 100 µm. Figure is reprinted from [P2]. Copyright © 2024 Optica Publishing Group.

Figure 3.8(c) shows an S-bend of the same cross-section and comparable size, but with the curvature modelled as a sine function multiplied with the reciprocal of the radius of curvature, with a minimum radius of curvature of 6 µm. This shape approximates a continuous variation of the radius of curvature and avoids abrupt changes. Even though the minimum bending radius is smaller than in the case of the simple S-bend, the transmission approaches the model with the constant sign of radius of curvature because of the gradual change of the radius of curvature. This comparison shows that in the case of the small changes in radii of curvature, which is the case for optimal trajectories, we do not lose much accuracy by neglecting the change of the curvature sign.

To evaluate the expected accuracy of the approximated transmission between two waveguide segments, we examine the conservation relations between incoming and outgoing optical powers. In a system without scattering loss, the transmission matrix entries should satisfy the condition $t_{11}t_{12}^{*} + t_{21}t_{22}^{*} = 0$ [69]. Figure 3.9 shows the absolute value of the left-hand side of this condition. The non-zero values for the high *curvature contrast* suggest higher energy loss.

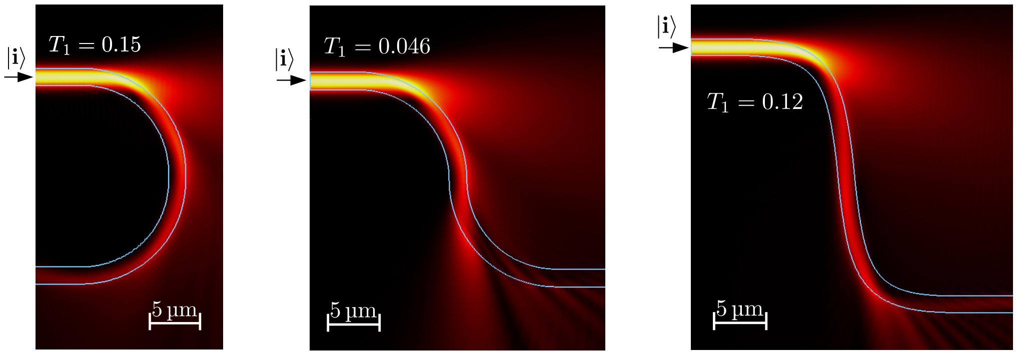

(a) C-bend

(b) S-bend

(c) S-bend, gradual

Figure 3.8.: The absolute value of the amplitude of the electric field, when considering the fundamental mode of a straight waveguide at the input in case of a waveguide composed of (a) two arcs of the same sign and radius 10 µm, (b) both arcs having the same radius of curvature 10 µm but with opposite curvature sign, meaning the bending in opposite directions; and (c) S-bend of comparable size featuring a gradual change of curvature with the smallest bending radius 6 µm. Figure is reprinted from [P2]. Copyright © 2024 Optica Publishing Group.

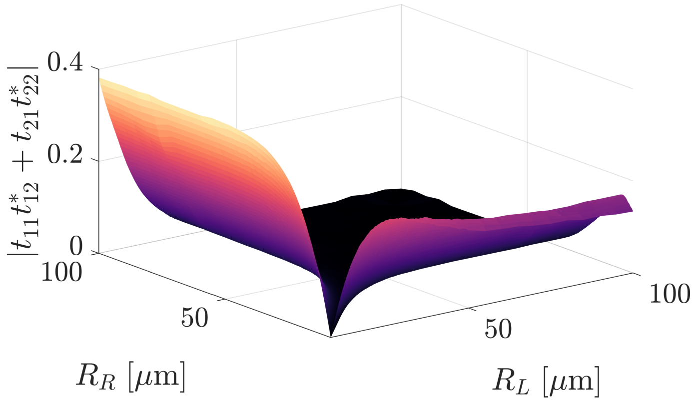

Figure 3.9.: Evaluation of the energy loss occurring at the interface between two waveguide segments. Values that deviate from zero indicate the amount of energy lost to modes not included in the respective subset of modes being tracked in the MMA. This energy loss can become significant and may restrict the applicability of the MMA, which is limited to two propagating modes, particularly for certain combinations of bending radii. This is especially relevant when segments with low curvature connect to more sharply curved sections. Figure is reprinted from [P2]. Copyright © 2024 Optica Publishing Group.

3.2.5. Segmentation of the trajectory

In order to proceed with transmission computation, the trajectory is sliced into segments, the same way it is presented in Subsection 2.5.4. For the described method, the trajectory must be entirely contained in a 2D-plane, which means no twisting is taken into account. The waveguide can be arbitrarily rotated in a 3D space, as this does not influence the transmission. Therefore, the waveguide's trajectory can be described as a series of arcs characterised by a radius of curvature and an arc length. Ideally, the bends should not be too sharp, but in case this happens and the radius of curvature is smaller than the lower bound of 7 µm, it is set as equal to 7 µm for the further computations. Radii of curvature larger than the upper limit of 1000 µm are treated as straight segments.

Figure 3.10 presents the schematics of a trajectory divided into $N+1$ segments. The first and the last segment are assumed to be straight. The first segment guides the input mode $|\mathbf{in}\rangle$ and the output modes $|\mathbf{out}\rangle$ are defined in the last segment. The N interfaces between the segments are marked with double vertical lines in Figure 3.10.

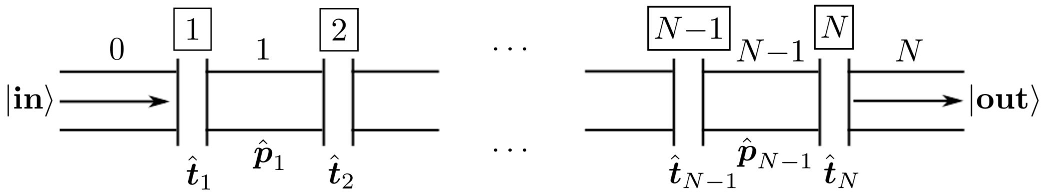

Figure 3.10.: Waveguide trajectory sliced into segments of constant radius of curvature labelled with integer numbers from 0 to N. The first and last segments are straight with no propagation loss assumed. The interfaces are numbered from 1 to N. Figure is reprinted from [P2]. Copyright © 2024 Optica Publishing Group.

The waveguide is excited with an input signal in the fundamental mode, expressed as an amplitude vector denoted by $|\mathbf{in}\rangle = (1, 0)^{\mathrm{T}}$. As the incoming field reaches the interface, denoted as $\boxed{1}$, its amplitude distribution is changed by multiplying it with the complex transmission matrix, $\hat{\boldsymbol{t}}_1$, that corresponds to the transmission through the first interface. The fields then continue to propagate through the segment, where they can experience attenuation due to bending and an accumulation of phase. The propagation of each mode is influenced by a different complex propagation constant. This effect is taken into account by multiplication with a propagation matrix

$$\hat{\boldsymbol{p}}_n = \begin{pmatrix} \mathrm{e}^{(\mathrm{i}\mathrm{Re}\{\beta_1(R_n)\} - \mathrm{Im}\{\beta_1(R_n)\})l_n} & 0 \\ 0 & \mathrm{e}^{(\mathrm{i}\mathrm{Re}\{\beta_2(R_n)\} - \mathrm{Im}\{\beta_2(R_n)\})l_n} \end{pmatrix}, \tag{3.8}$$

with n denoting the number of the segment. The matrix in equation (3.8) contains the values of the propagation constant both for fundamental, subscript 1, and second higher-order mode, subscript 2, multiplied with the waveguide segment length l_n and radius of curvature R_n.

The matrix multiplication is performed repeatedly for the subsequent interfaces and segments between them. Ultimately, the amplitude transmission through the entire free-form waveguide can be calculated as

$$|\mathbf{out}\rangle = \hat{\boldsymbol{t}}_N \hat{\boldsymbol{p}}_{N-1} \hat{\boldsymbol{t}}_{N-1} \cdots \hat{\boldsymbol{t}}_2 \hat{\boldsymbol{p}}_1 \hat{\boldsymbol{t}}_1 \, |\mathbf{in}\rangle \,. \tag{3.9}$$

When performing matrix multiplication, it is important to specify the input and output of the waveguide, as the results may vary depending on the direction of propagation. The transmission of particular mode amplitudes at the output of the waveguide can be represented by the vector $|\mathbf{out}\rangle = (t_1, t_2)^{\mathrm{T}}$. The values $T_1 = |t_1|^2$ and $T_2 = |t_2|^2$ correspond to the power transmission of the fundamental mode and the fraction of power carried by the second higher-order mode, respectively. These are the key quantities we discuss for a waveguide with a particular trajectory.

3.3. Calculation of transmission in exemplary waveguides

In the following, three examples are considered: a 90° bow, a waveguide composed of alternating arcs, and an S-bend with a continuous change of curvature. These exemplary waveguides are characterised by varying radius of curvature, which means the presence of interfaces where the coupling of modes can occur. The transmission obtained with the MMA and FMA is compared to the results from full-wave simulation software CST Microwave Studio®. The simulations within CST Microwave Studio are conducted using the time-domain solver based on the Finite Integration Technique (FIT) [84]. This computational method is described in more detail in Subsection 2.3.2. The mesh density is set to 10. It defines the number of discretisation cells per wavelength. The mesh is automatically refined at the boundaries of the waveguide core and curved surfaces to enhance accuracy. The waveguide is positioned within a cuboidal computational domain, ensuring that the minimum distance between the walls of the waveguide core and the boundaries of the computational domain is set to twice the core width. This distance is crucial for accurate computation and visualisation of the field amplitude distribution. The boundaries of the computational domain are set to open, equivalent to the PML method [84, 139]. To compute the scattering matrix (S-matrix) [82, 140], an input port is defined at one end of the waveguide, and an output port corresponds to the opposite end. The S-matrix contains the fractions of complex amplitudes scattered through the input or output port when the system is excited via either port. It describes a relationship between each mode of the waveguide ports and the other modes present. The off-diagonal components of the matrix represent the transmission (or reflection) of one mode from a waveguide port into another mode of a different waveguide port, while the diagonal components indicate the reflection of each mode back into itself.

Subsequently, the computation times of numerical simulations in CST Microwave Studio are compared to the transmission calculations using the MMA and FMA. These computations were performed on a desktop computer featuring an Intel(R) Core(TM) i7-7700 CPU running at 3.60 GHz,with 16 GB RAM. All waveguide simulations utilised the same CST acceleration settings: CPU acceleration of up to two devices and the use of four CPU threads. The time-consuming pre-computation of modes and t-maps, necessary for the approximation methods, was carried out on an external computer cluster.

3.3.1. A 90° bow

A bow made of straight channel waveguides connected with 90° arc is the simplest shape of practical interest [121, 122, 130]. The structure comprises two interfaces where a mode coupling can occur: straight-bent and bent-to-straight. This scenario serves as a classical example of intramode mismatch and intermode coupling, which result in loss and cross-talk between modes [124]. Figure 3.11(a) illustrates a curved waveguide with a radius of curvature of 10 µm. The shown amplitude of the real part of the propagating electric field suggests that most of the loss occurs at the first interface. At the interface between waveguide segments characterised by different radii of curvature, a significant portion of the field couples to free-space radiation, which contributes to the loss. Figure 3.11(b) compares the transmission through the waveguide bend calculated with FMA, MMA, and full-wave simulation. These transmission values are derived from the amplitudes recorded in the terminating straight waveguide segment. The transmission of the fundamental, as well as the higher order mode, computed with the approximation methods in general agrees with the results from full-wave simulations. In case of the fundamental mode, the approximation methods tend to disagree slightly from the full-wave simulation for very sharp bends, below 15 µm. It is caused by high radiation loss, not explicitly included in the approximated calculations. Similarly, the transmission of second mode differs between the two methods in case of sharp bends and also when the high damping of the second mode occurs for waveguide bend approaching straight segments. The slight drop in the transmission of the second order mode near the radius of curvature 20 µm is caused by an increase in transmission of the next mode (not shown in Figure 3.11 due to low transmission). The limitation of the MMA to two modes accounts for its insensitivity to this effect. Note that in the FMA no prediction on the transmission of the higher-order mode can be made, simply because it is not considered in this method.

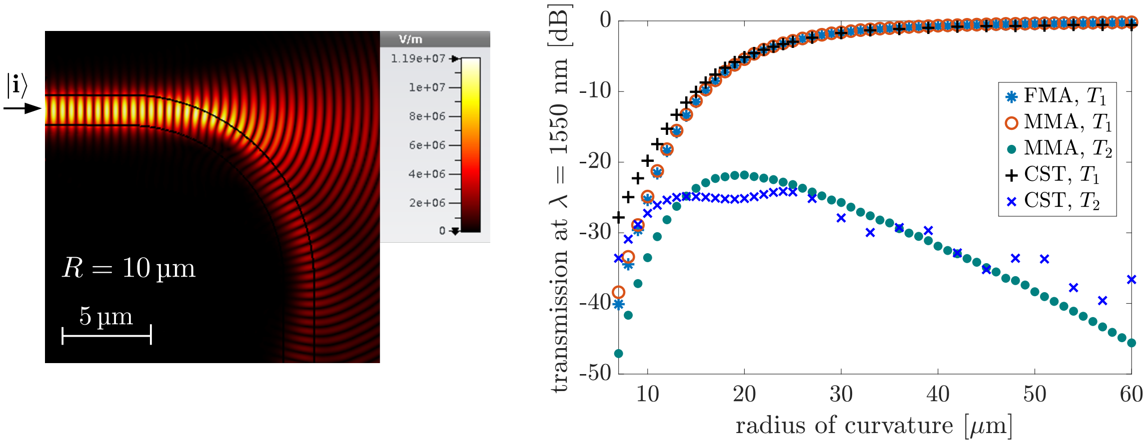

(a) (b)

Figure 3.11.: (a) The amplitude of the real part of the electric field in a dielectric waveguide of a straight-bent-straight form, considering the fundamental mode of a straight waveguide as the illumination source. (b) Comparison of corresponding power transmitted in the fundamental mode T_1 and the second higher-order mode T_2 as a function of radius of curvature. Figure is reprinted from [P2]. Copyright © 2024 Optica Publishing Group.

The relationship between the transmission coefficients and the radius of curvature is quite intuitive. When the radius of curvature is very large, the smooth variation of the modal properties, with respect to a straight waveguide, results in a negligible mismatch between the modes supported in different segments, leading to nearly perfect transmission into the fundamental mode. In this scenario, the excitation of the next higher-order mode is negligible. As the radius of curvature decreases, while curving the straight waveguide, the excitation of the next higher-order mode increases, while the transmission of the fundamental mode declines. When the radius of curvature becomes extremely small, transmission in both modes drops significantly due to the onset of notable coupling to radiating modes. In Figure 3.11(b), the CST results for the transmission of the second mode exhibit fluctuations, as the discretisation accuracy in the simulation has been reached. Nevertheless, a general decreasing trend is apparent.

The most important conclusion to be drawn from this analysis concerns the accelerated prediction of transmission in these scenarios. The time required to compute the results using the MMA with 94 trajectories, each sliced into segments of 1 µm long, and with bending radii ranging from 7 µm to 100 µm, was approximately 24 seconds. In comparison, the full-wave CST simulations of 32 bends, with radii ranging from 6 µm to 60 µm, took 7 hours and 20 minutes. It is important to note that the time needed to pre-compute the modal properties and the t-maps should not be overlooked. This process took nearly four days (without parallelisation) across 88 different radii of curvature. However, these computations of the modal properties need to be done only once. Afterwards, arbitrary trajectories can be studied as these 2D simulations, which account for the waveguide cross-sections, provide all the necessary information to proceed with the MMA.

3.3.2. *Snake*-shaped waveguides

Another example involves waveguides constructed from a series of six arcs, each with an angle of 10° and alternating signs for the radius of curvature (but the same absolute value). Due to this shape they are called *snake*-shaped waveguides in the following. This design is particularly interesting because of its periodicity. Such an example shows the significance of the phase of the propagating wave. With the change of radius of curvature, changes also the distance between repeating parts of a waveguide. This example represents an extreme case to help us understand some of the limiting aspects of the MMA.

Figure 3.12(a) compares the transmission obtained using the three methods for radii of curvature ranging from 7 µm to 50 µm. This example demonstrates that considering only a single propagating mode is insufficient for accurately predicting the transmission. In this case, the transmission is primarily determined by the radius of curvature, which for FMA means that transmission just decreases with decreasing radius of curvature. Including second higher-order mode in the calculations (as done in MMA) results in higher transmission of the fundamental mode, even for sharp bends. This suggests that the second mode may couple back to the fundamental mode at the positions in the waveguide where the curvature changes. The transmission of the fundamental mode computed with the MMA aligns with the reference CST values for radii of curvature between 26 µm and 36 µm. The transmission obtained with the MMA is also mainly influenced by the radius of curvature, leading to an increase in transmission for larger bending radii, and transmission decay in case of sharp bends. Consequently, the transmission of the second higher-order mode decreases with the increase of the transmission of the fundamental mode.

However, the full-wave simulations in CST reveal few significant aspects. As can be seen in Figure 3.12(b), the waveguide with sharp arc segments of radii of curvature 6 µm is short and the variation in trajectory is negligible relatively to the waveguide core dimensions. This results in a high transmission of the fundamental mode. Along the increment of the radius of curvature, the periodicity imposed by the periodic change of the radius of curvature of the arcs leads to oscillations of transmission of both the fundamental and second-order mode. This phenomenon is likely due to the consecutive mode coupling, scattering loss, and back-propagation of modes. It can be understood as a scattering process where the mismatch in the propagation constant between the fundamental and the next higher-order mode is compensated due to the periodicity of the waveguide trajectory that provides an additional wave vector component. When the phase matching is satisfied, the modes interfere constructively, resulting in amplification of the higher-order mode [141]. Likely, the complete description of this phenomenon requires the consideration of both forward and backward propagating modes, comparable to the appearance of a Fabry-Pérot resonance in a stack of layers with alternating optical properties [142–144]. This feature is not considered in the approximate descriptions of the problem but only in the full-wave simulations. The transmission of the fundamental mode drops significantly when the radius of curvature exceeds approximately 40 µm. At a certain critical radius of curvature, transmission into the fundamental mode is completely suppressed. This is partially illustrated in Figure 3.12(b), showing the electric field in the longitudinal cross-section of the waveguide trajectory for a radius of 50 µm. Simultaneously to the drop in transmission of the fundamental mode, the transmission of the second mode increases.

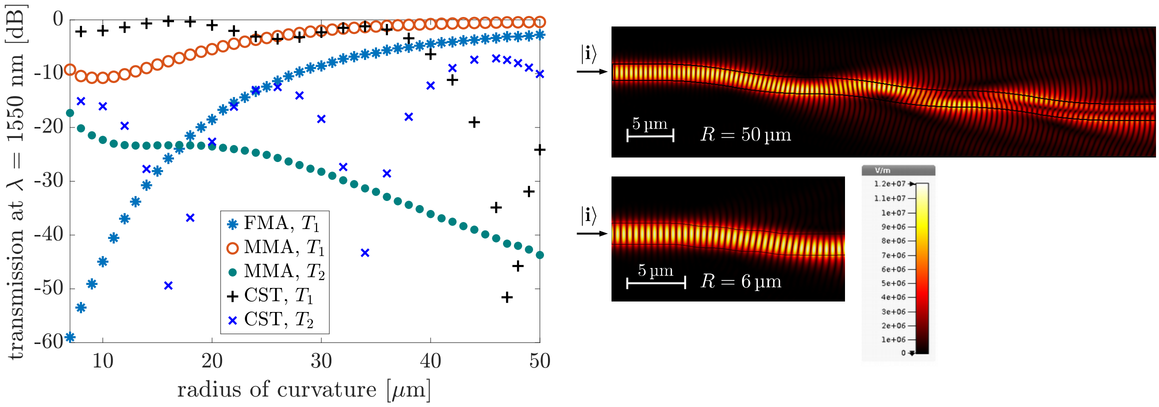

(a) (b)

Figure 3.12.: (a) Transmission of the fundamental and second-order mode calculated using various methods. (b) The amplitude of the real part of the electric field in a dielectric waveguide of a *snake*-shaped form, with different radii of curvature, taking into account the fundamental mode of a straight waveguide from where the waveguide trajectory is excited. Figure is reprinted from [P2]. Copyright © 2024 Optica Publishing Group.

In the implementation of the MMA and FMA, the change in a curvature sign is not treated accurately. During the segmentation of the trajectory, the segments containing inflection points between consecutive arcs are approximated with straight waveguides. Additionally, the backward propagating modes are not considered. Therefore, both FMA and MMA are unable to capture the effects related to periodically changing curvature sign and cannot accurately predict the transmission. While the MMA can detail phenomena outside of the resonant regime, it continues to provide inaccurate predictions for extremely small radii of curvature, reflecting limitations also noted in the previous example, and in the case when the radius of curvature is chosen in such a way that such a collective resonance is excited.

For this type of trajectory, using the approximation method also significantly reduces computation time. Transmission calculations for 45 trajectories were completed in just 6 seconds using the MMA method. In contrast, full-wave simulations performed in CST took between 5.5 min for the smallest bending radius to 21.5 min for the largest bending radius. These extreme trajectory examples are illustrated in Figure 3.12(b).

3.3.3. S-bend with continuous change of curvature

The last example discussed in this section is an S-bend, with the curvature modelled as $\kappa = (R_{\min})^{-1} \sin \varphi$, where $R_{\min}$ represents the minimum radius of curvature of a waveguide, and the angle φ varies from 0 to 2π. The transmissions of the fundamental and the second order mode, computed with FMA, MMA, and full-wave simulation, are presented in Figure 3.13(a). Despite the change in the sign of curvature, cf. Figure 3.13(b), the curvature changes smoothly (up to the discretisation of angle φ), which suggests that the approximation methods should be applicable, as illustrated in Figure 3.8. This expectation is confirmed in Figure 3.13(a). The transmission of the fundamental mode deviates from CST simulation only for minimum radii of curvature below 15 µm. The transmission of the second higher-order mode computed with MMA is higher for minimum radii of curvature smaller than 10 µm. For smaller minimum radii of curvature the transmission of the fundamental and second order mode increases with increasing radius of curvature. For higher minimum radii of curvature, for which the power is carried mostly by the fundamental mode, the fraction of the second mode decreases. The transmission of the second mode from CST oscillates around the values of MMA. It may be caused by interaction with higher order modes.

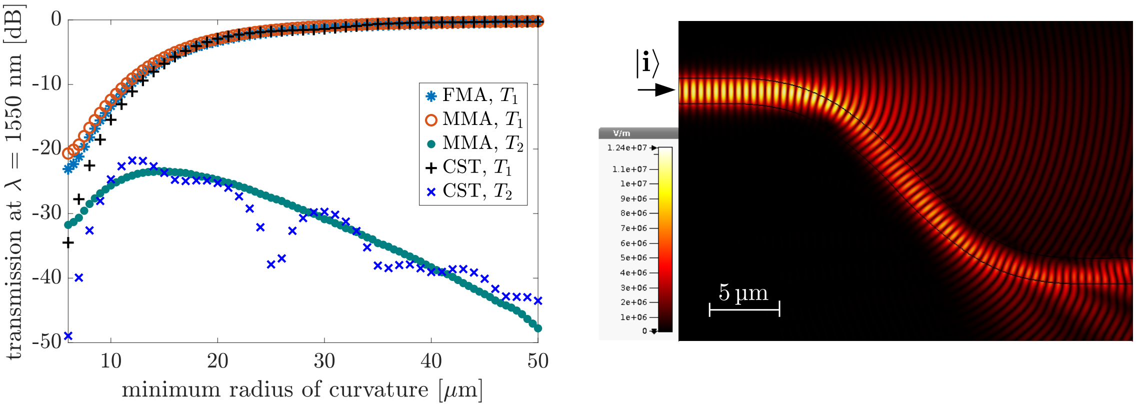

(a)

(b)

Figure 3.13.: (a) The transmission of the fundamental and second order mode analysed as a function of the minimum bending radius for an S-bend with continuous change of curvature. (b) The amplitude of the real part of the electric field in a dielectric waveguide with an S-shaped design and a minimum radius of curvature 10 µm, considering the fundamental mode of a straight waveguide as the source of illumination. Figure is reprinted from [P2]. Copyright © 2024 Optica Publishing Group.

The computation time of the transmission for 89 trajectories while using the MMA was approximately 53 seconds. In comparison, the full-wave simulations using CST took from about 11 min for the shortest trajectory up to 4 h 52 min in case of the longest trajectory considered for Figure 3.13(a).

3.3.4. Summary

This section presented the approximation method for calculating the transmission of both a fundamental mode and a higher-order mode in a curved waveguide trajectory. Its application is demonstrated while considering three exemplary 3D waveguide shapes. The trajectory in this method is represented by a sequence of arcs. The total loss is derived from accumulation of propagation loss in the segments, as well as the transmission between the adjacent arcs. In the multi-mode approximation method, we consider the possible coupling between two propagating modes as a result of a variation of the radius of curvature. This effect is quantified using a transmission matrix. Consecutive multiplication of the propagation and transmission matrices results in the total transmission. The approximated results are compared to the reference transmission, obtained with the full-wave solver CST Microwave Studio. The comparison indicates that the approximation methods are reliable for transmission of the fundamental mode in trajectories with continuously varying curvature. The multi-mode approximation can also be utilised for trajectories consisting of only a few segments. The fundamental mode approximation remains efficient and effective for calculating transmission in single-mode 3D waveguides and can serve as a merit function for optimising their geometry. In instances where changes in curvature lead to the excitation of higher-order modes, the MMA allows for rapid computation of the transmission of these modes, resulting in more accurate transmission assessments. This method significantly reduces computation time from hours to tenths of seconds. However, the MMA is more sensitive to the accuracy of the calculated transmission coefficients compared to the FMA. As a result, it may not be suitable for complex trajectories that involve sharp bends with bending radii less than 20 µm.

3.4. Artificial neural networks for finding transmission of free-form waveguides

Another approach to calculate the transmission of a waveguide with an arbitrary trajectory much faster than a full-wave solution is to use artificial neural networks (ANNs). When provided with a sufficient amount of training data, an ANN can be constructed and trained to predict the result, which in this context is the transmission of the waveguide. The ANNs can be used to model structure-property relations. In the current example the structure is the shape and the trajectory of the waveguide and the property is the transmission. This approach is particularly beneficial when the functional dependencies between the various waveguide parameters and the resulting transmission are not well understood.

Once trained, ANNs can provide instantaneous predictions, offering a significant advantage over full-wave solvers. However, the effort required to train an ANN including the actual generation of the training data is only justified if the ANN is later applied to multiple instances of the same problem. For individual design tasks, dedicated methods for solving the inverse problem are usually more effective. In the present context, the requirement for repeated application of the ANN is met. Identifying the optimal trajectory in real-time, once the input and output ports of the waveguides are determined, is expected to happen repetitively in a fabrication line. Therefore, using ANNs to solve this problem is very appealing.

While primarily used to categorise large datasets [145–147], ANNs can also be adapted to predict various phenomena, for example the electromagnetic field patterns in waveguides [148, 149], the optical response of photonic power splitters [150], or the effective refractive index of the fundamental mode in channel waveguides [151], to name just a few. Deep learning in photonics is frequently applied in the context of inverse design [145, 150, 152–156]. The objective of this section is to determine the transmission of a waveguide based on its shape and possibly to identify the trajectory that results in the highest transmission, given certain geometrical constraints. The content of this section was developed in close collaboration with M.Sc. Yiyang Bao from Prof. Christian Koos's research group at the Institute of Photonics and Quantum Electronics (IPQ), Karlsruhe Institute of Technology.

3.4.1. Theoretical background on feed-forward neural networks

An ANN takes as an input a trajectory stored as a vector of fixed length. This vector can consist of Cartesian coordinates of N trajectory points (x_i, y_i, z_i), denoted as $\mathbf{X} = [x_1, \ldots, x_N, y_1, \ldots, y_N, z_1, \ldots, z_N]$. In cases involving waveguides bent only in one plane, the $x-$coordinates are zero and are neglected further. Since only two coordinates are needed here to describe these trajectories, we refer to them as 2D trajectories in this section. An alternative representation is a vector of arc lengths and the corresponding radii of curvature $\mathbf{X} = [l_1, \ldots, l_N, R_1, \ldots, R_N]$. The latter representation is chosen here because it is independent of waveguide orientation in space, which, as such, does not influence the transmission. The length of the input vector is fixed for a specific ANN architecture, so the waveguide must be sliced accordingly. The architecture that is chosen in this work is a feed-forward network.

One layer of the ANN is constructed in such a way that each component X_i of the input vector $\mathbf{X}$ is multiplied by a weight w_{ij}. Additionally, a bias b can be added to adjust the solution. The resulting value for a node Y_j comes from the expression

$$Y_j = \sum_{i=1}^{2N} w_{ij} X_i + b\,. \tag{3.10}$$

The output of all the nodes within a single layer serves then as the input to the next layer of the ANN. The relation (3.10) is linear. To introduce nonlinearity, a nonlinear function $f(\cdot)$ is applied to each output Y_j. Common nonlinear functions include the rectified linear unit (ReLU) $f(Y_j) = \max(0, Y_j)$, sigmoid functions such as hyperbolic tangent $f(Y_j) = (\mathrm{e}^{Y_j} - \mathrm{e}^{-Y_j})/(\mathrm{e}^{Y_j} + \mathrm{e}^{-Y_j})$, and the logistic function $f(Y_j) = 1/(1 + \mathrm{e}^{-Y_j})$ [146]. In the course of the work, multiple of these nonlinear functions were explored.

The mathematical description (3.10), featuring nonlinear functions, concerns all the nodes in the first, and the subsequent layers. The total number of connections, characterised by their respective weights and biases, contributes to the trainable parameters of the network, which are also referred to as the network's *degrees of freedom*. An example of a fully connected neural network architecture is shown in Figure 3.14. This structure is the foundational architecture of a neural network known as a multilayer perceptron [157]. It can be defined by the number of layers and the number of nodes within each layer. The layers may vary in the number of nodes, eventually decreasing to produce a single output value representing transmission, which ranges between 0 and 1.

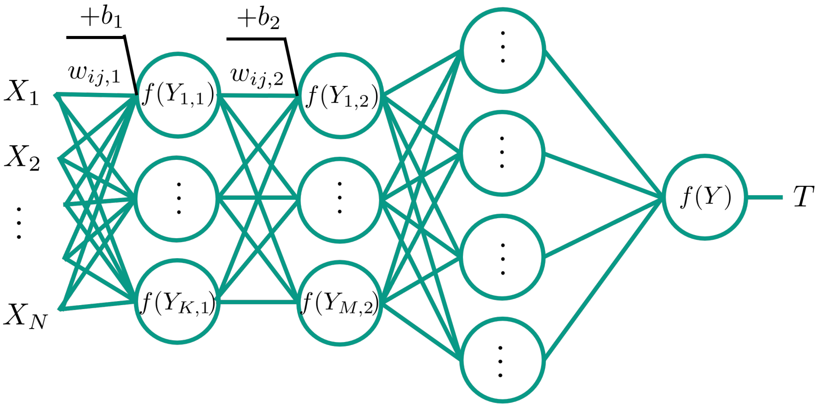

Figure 3.14.: Schematics showing the idea of fully-connected neural network architecture. The network maps an input vector $\mathbf{X}$ onto one output variable T. The circles represent the nodes. The first column of nodes on the left is called an input layer and and the following columns form hidden layers. To simplify the schematics, the activation functions are labelled with the same letter f, even though these may be different functions. In the notation for weights w and node values Y, the first subscript denotes the number of a node and the second subscript corresponds to the number of layer. This type of architecture is called *feed-forward* neural network as it contains no recurrent loops, and the input is processed only forward in the direction of the output.

After the neural network architecture is established, the network undergoes training using a dataset, which is typically divided into training, validation, and testing subsets. During the first iteration (epoch) the weights and biases are initialised, the values $f(Y_j)$ are calculated, and the output is determined. This process is known as a *forward pass* because the output is derived from the input. Following this, the training error, measured as the mean squared error (MSE), is computed using the formula:

$$\mathrm{MSE} = \frac{1}{n}\sum_{j=1}^{n}(d_j - T_j)^2, \tag{3.11}$$

where n is the number of training data (batch size), and d_j and T_j represent the desired and the actual outputs, respectively. After calculating the MSE, the gradients between nodes are determined using the chain rule in a *backward pass* [146, 156]. This backward pass works backward through the layers, from output to input. The gradients indicate how much each weight and bias should be changed to minimise the MSE in the next epoch $t+1$. This can be achieved through methods like stochastic gradient descent [146]. The weights are updated according to

$$w_{ij}(t+1) = w_{ij} + \zeta \cdot \Delta_j \cdot Y_j, \tag{3.12}$$

where ζ is the *learning rate* and Δ_j denotes the error term for each unit. This learning procedure is repeated epoch by epoch until the desired MSE is attained.

3.4.2. Neural network implementation

The ANN to calculate transmission is implemented using the Python machine learning library PyTorch [158]. This library supports automatic differentiation, crucial for neural network training. While searching for the optimal architecture, several activation functions, different learning rates, optimisers (Adam, SGD or Adamax), as well as the number and size of hidden layers were considered. These parameters, called *hyperparameters*, were determined with the use of the *Optuna* framework [159]. The final architecture of the network is presented in Figure 3.15, and the parameters are collected in Table 3.1.

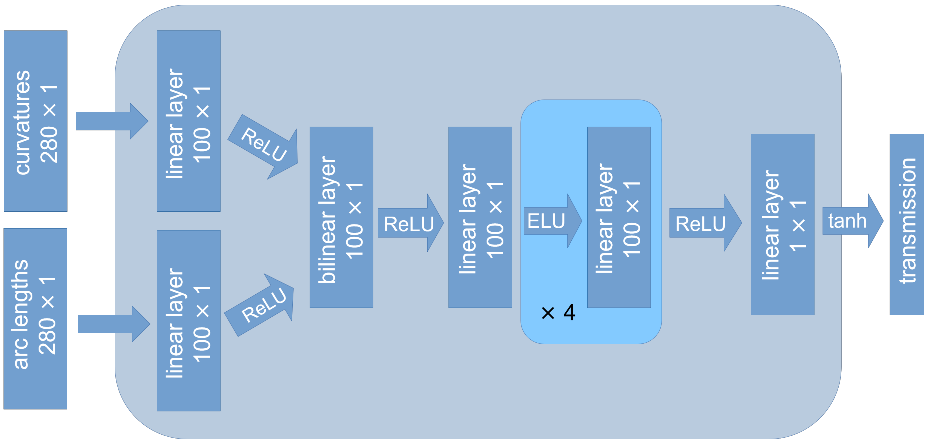

Figure 3.15.: Schematics showing the architecture of the multilayer perceptron. The linear layer with the ELU activation function is repeated four times.

Table 3.1.: Parameters used for the training of the neural network.

parameter	value
epochs	100
optimiser	Adam
initial learning rate	0.001
error type	MSE
parameter size	1.2×10^6

Initially, two different descriptions of the trajectories were considered: Cartesian coordinates of trajectory points, and a sequence of arcs described with curvatures and lengths. The input based on curvatures gave better results than the input based on the Cartesian coordinates. This observation is reasonable because the curvatures have more physical meaning in influencing transmission than the Cartesian coordinates on their own. Such an insight would go along the ideas of a physics-informed neural network [160, 161]. As explained in the previous section, the transmission through the waveguide trajectory is determined by the sequence of radii of curvature. The varying radius of curvature explicitly affects both the bending and the transition losses. Now, instead of requiring the neural network to learn the definition of the radius of curvature from the coordinates of the trajectory, this information can be offered directly. Such an additional information simplifies the problem that the ANN has to solve, leading to the observed predictive capability. The result is also improved by application of 1D batch normalisation on the input values. Batch normalisation is implemented in PyTorch [162]. The input data is given as two vectors of 280 values containing the curvatures of the waveguide segments and 280 values of segment lengths. They are merged together in an initial bilinear layer. For most of the nodes, the ReLU activation function is applied. To the others, an exponential linear unit (ELU) $f(X)$, defined as X for $X > 0$ and $a\left(\mathrm{e}^X - 1\right)$ for $X \leq 0$ and some parameter a, is applied [163]. The activation function for the output is chosen as hyperbolic tangent to translate the positive values from the last layer into the transmission between 0 and 1.

3.4.3. Training and comparison of results

The data used for training of the network were generated using the fundamental mode approximation. This method allows for the creation of a large dataset in a short period. Please note that this study has a value on its own, but it most importantly serves the purpose of exploring a possible network architecture that can be used for later purposes. In the interest of the accuracy and the predictive power of the ANN, in the end it might not be trained with data obtained from an approximation method but with data obtained from full-wave simulations or even experimental data. Nevertheless, for the purpose of exploring such a concept, the considerations of transmissions using the FMA is fully sufficient.

For the training of ANN, 27,500 trajectories were accessible. These trajectories were derived from 250 photonic wire bond trajectories spanning over 100 µm as shown in Figure 3.1(a). These trajectories, which were created with B-splines [47, 164], were provided by Prof. Christian Koos's group from Institute of Photonics and Quantum Electronics (IPQ) at Karlsruhe Institute of Technology. The pool of trajectories was expanded to 27,500 by multiplying the y-components of each trajectory by a factor from range 0.01, 0.02, …, 1.10, resulting in 110 possibilities. An example of 14 samples created from a single trajectory is presented in Figure 3.16(a). The corresponding transmission, calculated with FMA is presented in Figure 3.16(b).

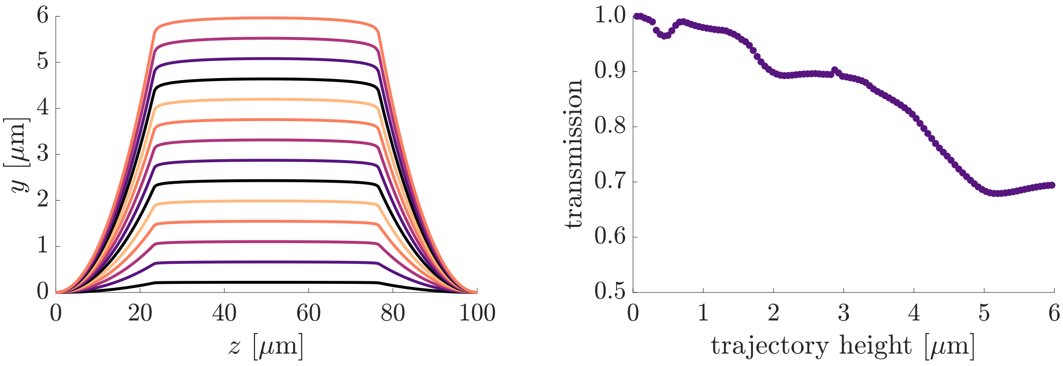

(a)

(b)

Figure 3.16.: (a) Trajectories created from the trajectory with a height of 6.2 µm by multiplying the y-Cartesian-components by a factor between 0.01 and 1.10. (b) Transmission of the generated trajectories, calculated with FMA and MMA. The transmission of the second-higher order mode is minor.

The accessible dataset is randomly divided (using the default random number generator of PyTorch) into a training set (90 % of the data) and testing set (10 % of the data). From the training set, 20 % of the data is dedicated only for validation (testing the accuracy of each epoch during training). The batch size used for training is 55. The training process takes approximately one hour. After the network is trained, the transmission for each trajectory is calculated in tenths of a second. The convergence of the training as well as the results of testing are presented in Figure 3.17(a) and Figure 3.17(b), respectively. Both the accuracy of training and the resulting transmission are characterised by fluctuations, which reduce the accuracy of ANN predictions. The achieved correlation is slightly below 0.96.

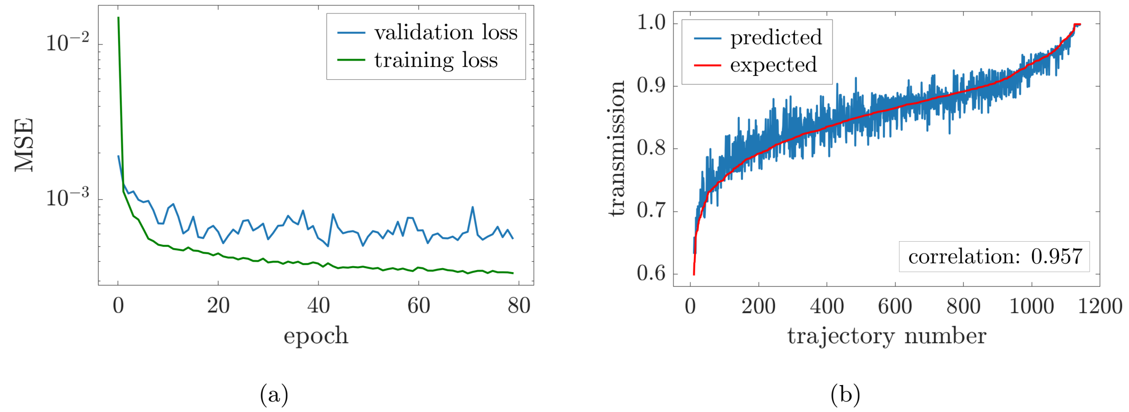

Figure 3.17.: (a) Convergence of the training loss, compared to the validation loss. (b) Comparison of transmission calculated with ANN to the expected transmission based on FMA, showing correlation of 0.95697. These results were obtained for the number of trajectory segments: 280. The plot shows also distribution of transmission among 1,200 trajectories chosen from the testing set, which was not used for training.

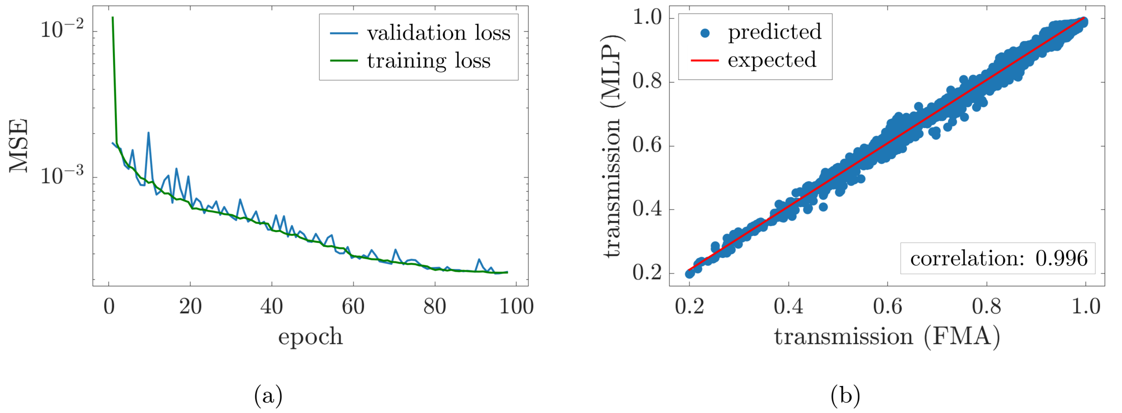

Figure 3.18.: (a) Convergence of the training loss, compared to the validation loss. (b) Comparison of transmission calculated with ANN to the expected transmission based on FMA, showing correlation of 0.99625. These results were obtained for the number of segments equal to 452. The number of samples for verification equals 2,500.

Increasing the number of trajectory segments from 280 to 452 leads to improved results, as shown in Figure 3.18. The results for higher number of trajectory points exhibit smaller fluctuation and a higher correlation, approaching a value of 1. This can be explained with a denser sampling of the trajectory that gives more information about the trajectory to the ANN. The next subsection discusses the dependency of the training results on the number of samples.

3.4.4. Dependence of accuracy on the number of training samples

For the training described in the previous subsection, the number of samples can, in principle, be arbitrarily large because they are generated using a fast approximation method. However, in the case of full-wave simulations of exact transmission, the number of trajectories may be limited due to the time required to generate the data (which can take several hours per trajectory). Therefore, this subsection analyses the dependence of training accuracy on the number of training samples.

The number of samples used for training varies between 1 % and 100 % of 25,000 trajectories from the previous subsection. The remaining 2,500 trajectories are reserved for testing. These testing trajectories are randomly chosen from the pool using the pseudo-random number generator module in Python. All the trajectories are divided into 452 segments, as this input length allows for more effective training of the network. Each training set of size starting from 250 is chosen randomly from the total of 25,000 trajectories, and is trained with 150 epochs. Figure 3.19(a) presents the mean squared error achieved after 150 epochs as a function of number of trajectories. The validation loss predominantly overlaps with the training loss toward the end of the training phase. Generally, the more trajectories utilised for training, the smaller the error.

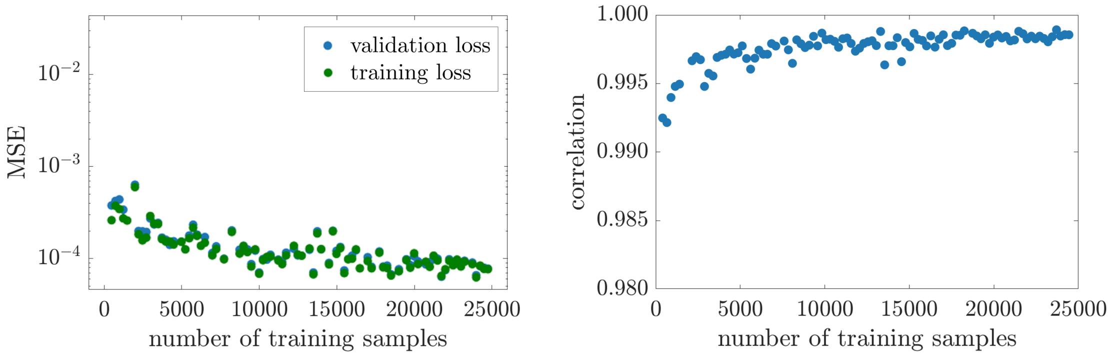

(a) training

(b) transmission prediction

Figure 3.19.: (a) Attained MSE loss after 150 epochs as a function of the number of training samples. (b) Correlation between expected transmission and transmission computed with the neural network as a function of number of trajectories used for training.

Figure 3.19(b) shows how the correlation of the transmission from the test samples changes with the number of trajectories considered in the training. The achieved correlation increases with the number of samples. However, the accuracy saturates, indicating that fewer samples may be sufficient, which would speed up the training. Specifically, starting from 5,000 samples, there is almost no noticeable improvement in accuracy. In fact, using just 1,000 trajectories may be sufficient to train a reliable neural network for the trajectories of similar form.

This study demonstrates that a pool of just a few thousands samples may be enough to train a neural network effectively. This finding is particularly relevant for 3D free-form waveguides, where access to a smaller amount of data obtained from a full-wave solver is common. The application of ANN to predict the transmission of 3D free-form waveguides based on the transmission from a full-wave solver is described in the next subsection.

3.4.5. Extension to 3D free-form trajectories

In the first approach, the feed-forward neural network with the established architecture is trained using 3D trajectories, described by a set of points in Cartesian coordinates. Unlike in the previous subsection, here the trajectories may be curved both in x- and y-directions and the position of the output may vary between the trajectories. Therefore, three parameters are required to fully describe the trajectory. The transmission of the waveguides was computed with FDTD solver Ansys Lumerical. The setup and results were provided for this thesis by the courtesy of M.Sc. Yiyang Bao from the Institute of Photonics and Quantum Electronics (IPQ) at the Karlsruhe Institute of Technology.

Training of feed-forward neural network with transmission of 3D trajectories

The available dataset comprises 2,300 samples in total. From this dataset 90 % are used for training (including validation) and the results are tested on the remaining 10 % of data samples. The trajectories are divided into 452 segments as in the previous subsection but the ANN input consists now of three vectors, each containing one of the three Cartesian coordinates of the trajectory points. Because of this, two bilinear layers are added to the network from Figure 3.15. One bilinear layer merges the vectors of x- and the y-coordinates into one vector. The second bilinear layer merges the resulting vector with the z-coordinates of the input. The convergence of the MSE during the training is presented in Figure 3.20(a). The resulting correlation between the prediction of the network and the expected value from the FDTD solver is presented in Figure 3.20(b).

The achievable accuracy after 100 epochs is lower than in the case of 2D trajectories. The MSE is does not decrease below 0.001. The poorer result is also visible in the lower correlation, slightly below 0.80. Especially, for the trajectories characterised by lower transmission, the prediction differs from the expected values. It is caused by the higher variation of data and the smaller amount of data for the lower values of transmission. Another reason may be the description of the trajectories with Cartesian coordinates, which was already deemed less accurate in Subsection 3.4.2. Therefore, a different approach was studied as a part of the cooperation with the research group of Prof. Christian Koos, and is presented shortly in the next subsection.

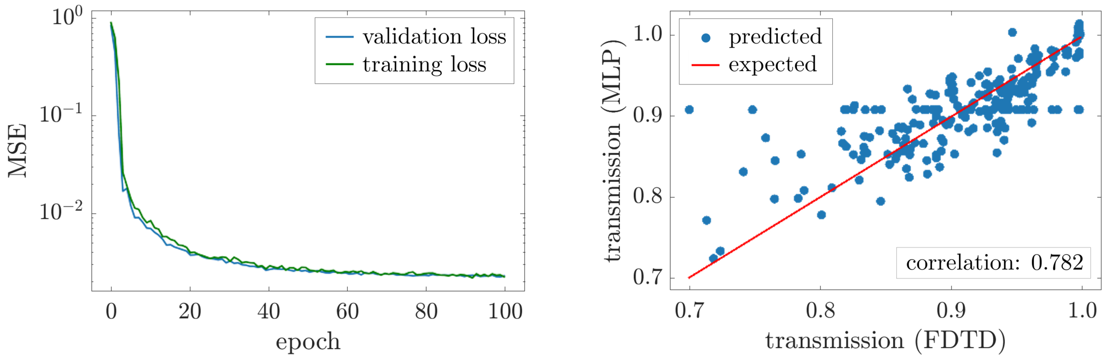

(a) (b)

Figure 3.20.: (a) Convergence of the training (trained with 90 % of data set: 2,070 samples). (b) Validation of the predicted results (with 10 % of data set: 230 samples) represented as comparison of the predicted and expected transmission.

Alternative solution

An alternative approach to solve the problem was mainly developed and presented by M.Sc. Yiyang Bao in [CO1]. This approach is also based on trajectories divided into segments. However, each segment is described by three parameters: the length of a segment, its normal vector of a curve, and the vector tangential to the curve in the middle of the segment. Moreover, instead of the feed-forward network introduced before, the ANN considered in this part of the work is composed mainly from two cascaded long short-term memory (LSTM) [165] modules connected through a single fully connected layer. LSTM is a type of recurrent neural network. The portions of information within the network modules are stored for a certain time or discarded to attain the highest training accuracy. After the second LSTM module, two additional layers reduce the size to a scalar transmission value. Because the input segments are processed sequentially, the output is independent on the number of segments. The network is trained as well with a transmission calculated with Ansys Lumerical [85], for 2,712 photonic wire bonds. The data are randomly divided into 64:16:20 ratio sets, accordingly initial training, validation, and test. The transmission computation is significantly accelerated to 10 ms per trajectory on average, on a desktop computer. The predicted values lie in agreement with the reference values, quantified by MSE of 2.025×10^{-5}, which is three orders of magnitude better than in the primary attempt using feed-forward neural network. Consequently, the resulting correlation is basically 1. This method was mainly developed and presented by M.Sc. Yiyang Bao in [CO1].

3.5. Summary and conclusions

This chapter presents alternative methods for calculating the transmission of free-form waveguides. It is divided into two main parts: one describing the MMA and another about ANN. The first section discusses the multi-mode approximation, which extends the fundamental mode approximation to include higher-order modes that propagate in a waveguide. The applicability of the method is demonstrated on three examples: a 90° bow, comprising two interfaces between a bent and a straight waveguide, where modes can couple; a *snake*-waveguide composed of arcs with alternating signs of curvature; and an S-bend where the radius of curvature gradually changes. The MMA method effectively predicts the transmission of both the fundamental and the second higher-order mode, achieving greater accuracy for waveguides with higher transmission. However, the *snake*-waveguide demonstrates fluctuations in transmission, highlighting the limitations of the approximation method. These limitations come from neglecting back-propagated and radiation modes, as well as the inaccurate description of the change in the curvature sign. This negative effect can be mitigated by gradually altering the radius of curvature, as shown in the example of the S-bend, which improves the accuracy of the MMA.

The second part of this chapter explores the application of artificial neural network to calculate the transmission of the waveguides. Two architectures are considered: a multilayer perceptron (MLP) and a long short-term memory (LSTM) network. The MLP is trained using trajectories changing both in 2D and 3D. The 2D transmission data is generated using the FMA, while the results for 3D waveguides come from full-wave simulations. The network trained with 2D data demonstrates higher accuracy due to the bigger quantity and lower variety of samples available for 2D waveguides. The accuracy is improved further with a different description of 3D trajectory and different neural network architecture, namely LSTM.

Both the multi-mode approximation and the artificial neural networks significantly reduce computation time from hours to tenths of seconds per trajectory. While the neural networks have the potential to achieve higher accuracy and are easier to apply to 3D trajectories, the computational effort (in terms of time and resources) required for full-wave simulations of the entire waveguides and training the LSTM neural network is considerably higher than that of the MMA. The primary pre-computational effort in MMA arises from calculating the modes and transmission maps, which is faster than full-wave simulations of entire waveguides. On the other hand, the trained neural network can provide transmission in few milliseconds, while the MMA takes a few tenths of seconds to yield transmission data. The following chapter demonstrates how these approximate solvers can be used to optimise the trajectory of waveguides.

4 | Optimisation of trajectories of free-form waveguides

The primary reason for developing approximation methods for calculating transmission through free-form waveguides is to enable the rapid evaluation of the merit function during the optimisation of their trajectory. In the optimisation process, the material and cross-section of a waveguide are predefined and fixed. Only the trajectory of a free-form waveguide is optimised. Since the optimisation may converge only after tens or even hundreds of iterations, it is essential that the calculation of transmission in each iteration is as fast as possible. This is particularly critical for a prospective *in-situ* fabrication, where the complete optimisation and fabrication of the waveguide along its trajectory should be completed in just a few minutes or even faster [47, P1].

This chapter is dedicated to present the work of the author of this thesis to optimise the trajectories of waveguides using the approximate methods to predict the transmission as discussed in the previous chapter. This chapter is structured into three sections. Section 4.1 provides a brief overview of the optimisation methods that may be applicable to waveguide trajectories. Following that, Section 4.2 describes the application of the MMA to optimise trajectories, and presents the results of the optimisation on a few examples. The last section concludes the chapter with a summary.

4.1. Optimisation methods – a brief overview

Optimisation is a vast topic on its own. Therefore, this section aims to provide a concise overview of some ideas found in the literature regarding optimisation methods applicable to waveguide trajectories. The goal of such an optimisation is to determine the most optimal trajectory, connecting the endpoints that constitute the input and output ports of a photonic integrated circuits. The orientation of the end segments of the trajectories is enforced by the direction of waveguide couplers. Additionally, the design of trajectory must account for the presence of possible obstacles to be avoided. These obstacles may be different components on the photonic integrated circuit, including other waveguides. In some instances, it may be also necessary to define the available space or the length of the trajectory. The merit function for optimisation is the transmission (loss), which needs to be maximised (or minimised).

The choice of the optimisation method may depend on the parametrisation of a trajectory. The trajectory can be parametrised using Cartesian coordinates of points, curvatures and arc lengths, or segment lengths along with corresponding normal vectors and tangent vectors at the midpoint of each segment. The last description relates directly to the first and second derivatives of a trajectory, allowing for direct optimisation of the individual trajectory segments. Alternatively, trajectories can be parametrised by functions [166], such as polynomials (including Chebyshev polynomials [167]), or splines, described for example with Bézier curves defined with Bernstein polynomials [168]. A convenient method for describing waveguide trajectories is through the use of basis splines (B-splines) [169, Chapter 5][164]. B-splines are linear combinations of basis functions, where the basis functions are multiplied by corresponding coefficients known as control points [170]. The basis functions can be computed recursively using De Boor's algorithm [171, 172], which is already implemented in interpolation packages of common programming environments such as MATLAB [119] or Python [173]. For instance, in [47], B-splines are employed to connect two points in 3D space with a smooth line while adhering to a minimum radius of curvature constraint. In this case, the coefficients of the functions are optimised to maximise the transmission of the full trajectory.

In this section, we distinguish between gradient-based optimisation and direct search optimisation methods. In gradient-based algorithms, the search direction toward an extremum of a function is determined by the gradient of that function at a given point in the abstract parameter space. One example is the gradient descent method, which is a first-order iterative optimisation algorithm used to find a local minimum of a differentiable function [174]. Gradient-based optimisation is often employed in shape optimisation [175]. On the other hand, direct search methods optimise a function through multiple iterations that converge to the best solution. One example is the Nelder-Mead Method, implemented in MATLAB function *fminsearch* [119]. This method employs a simplex of $n+1$ vertices in n dimensions, searching for an optimal solution by performing various operations on the simplex based on the values of the merit function at its vertices [176]. Direct search optimisation is particularly useful when the derivatives of the merit function do not exist or are too expensive to compute. For example, this type of optimisation is used to optimise the positions of control points of B-splines that describe waveguide trajectories in [52]. In this optimisation problem, the coefficients of the B-splines are determined to minimise the objective function (loss) under specific constraints. Different optimisation methods can be advantageous depending on the nature of the problem. The methods can be selected based on factors such as optimisation time, robustness, flexibility, or the ability to find global versus local extrema. This brief discussion of optimisation methods is complemented with a few examples of trajectory optimisation below.

The first example describes the optimisation of a path to reach a target point, initially intended for the flight path of an aeroplane [177]. However, the description closely resembles the scenario of free-form waveguides. The main purpose of this approach relies on generating a number of reasonable trajectories with a suitable approach and evaluating their transmission. The path in [177] is generated using quadratic Bézier curves. In the beginning, a set of points is sampled from the space available for the trajectories. This set includes the vertices that define the boundaries of the available space and the positions of point obstacles.[1] The available space is then divided into regions by a Delaunay triangulation [178], see Figure 4.1(a). This triangulation is already implemented in MATLAB, where the set of points corresponds to the vertices of the triangles. If the triangulation is too coarse, other arbitrarily chosen points may be added to refine the resulting mesh. Next, the centroids of these triangles are determined, creating a new set of points. The positions of the input and output of the waveguide are added to this new set. Then, another mesh is created by

---

[1] In the presence of obstacles of arbitrary size and shape, the points on their boundary are chosen that enclose the regions later excluded from the *available space* [177].

applying Delaunay triangulation to this new set of points. This creates a graph. An example of such a graph is presented in Figure 4.1(b).

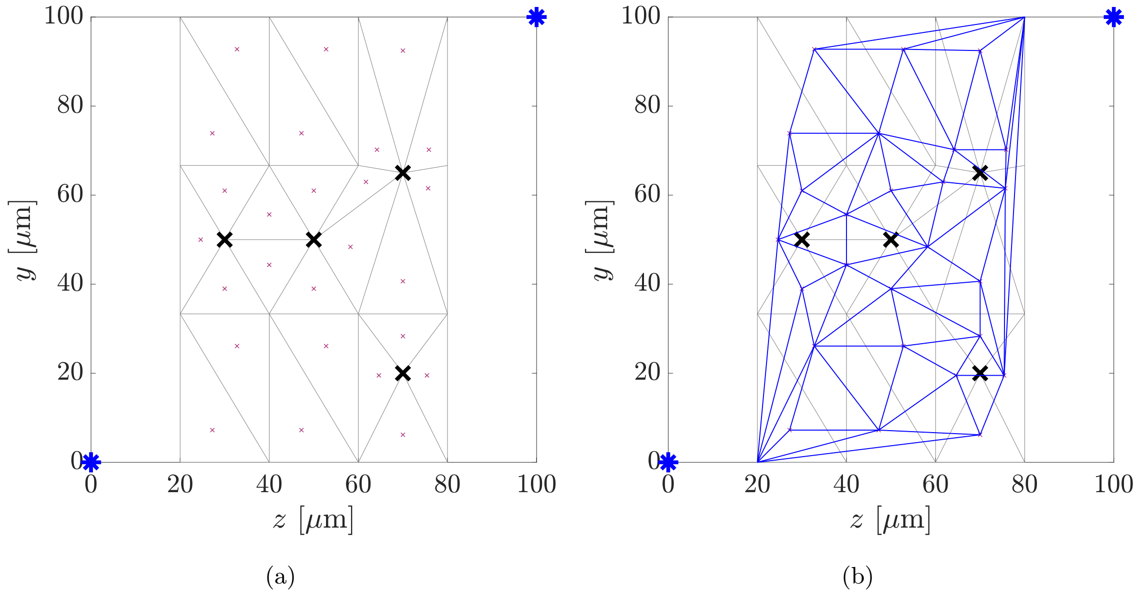

(a)

(b)

Figure 4.1.: (a) Division of available space by Delaunay triangulation shown with grey lines. Black "X" mark the positions of the obstacles. Blue "*" show the initial and final end positions. The 2D space spans over 100 µm in both directions. The distances between the end positions and the triangulated region account for a straight segments of a waveguide that align with the horizontal direction of waveguide couplers. Small pink "x" mark the centroids of the triangles. (b) The *secondary* triangulation is shown with the blue lines. It is created by connecting the centroids of the triangles created with the first triangulation.

From this graph, all the possible connections between the input and output node are identified. These connections are ranked from the shortest to the longest. We consider a chosen number of the shortest ones. Using the shortest connections, curves that represent the trajectories are generated as shown in Figure 4.2(a). These curves can be created using Bézier curves defined with Bernstein polynomials [177]. The vertices and midpoints of the graph edges serve as the control points for these curves. Alternatively, a Gaussian smoothing technique can be applied to the vertices, as demonstrated in Figure 4.2. The smooth paths correspond to waveguide trajectories. The transmission of the corresponding waveguides can then be evaluated rather quickly when using an approximation method. The trajectory with the highest transmission can be selected from these paths. These trajectories are presented in Figure 4.2(b), along with their corresponding transmissions. The resulting trajectories may be not the most optimal. To obtain better transmission, a larger number of triangles would be necessary. However, refining the triangular mesh leads to increased computation time. Additionally, constraints on maximum curvature may be applied to the curves. This approach is not explored further in this thesis because the arbitrary triangulation may cause the algorithm to omit the optimal solution. Otherwise, the optimisation is too time consuming because the computation time increases with the number of triangles.

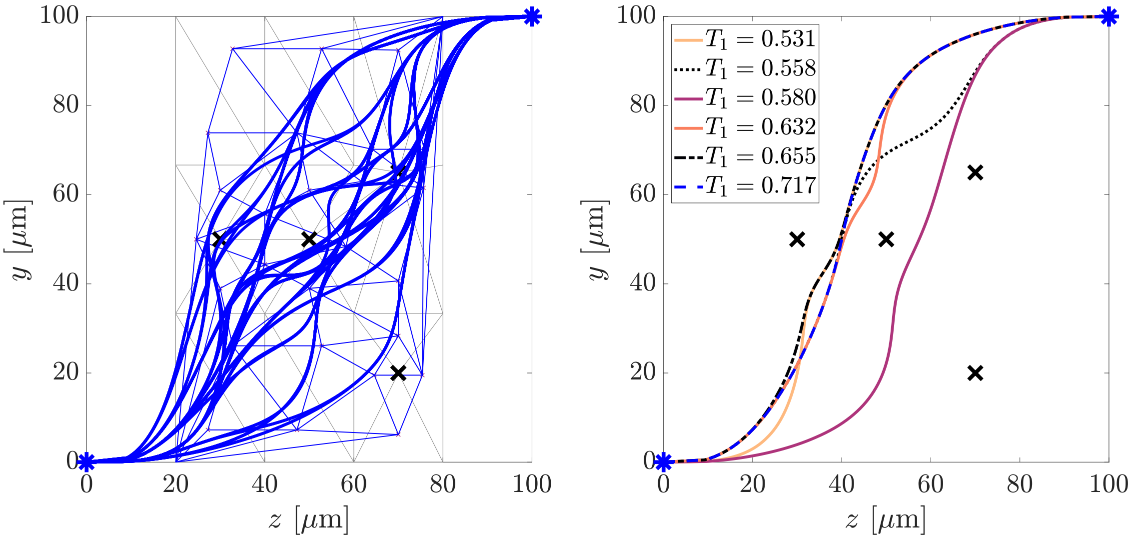

(a) (b)

Figure 4.2.: Optimisation of the trajectories with Delaunay triangulation. The obstacles are marked with black “X”, and the end points of the trajectories are marked with blue “*”. (a) The bold blue lines show the trajectories created based on the shortest paths in the graph. The trajectory results from smoothing the paths using a Gaussian-weighted moving average filter implemented in MATLAB. (b) The lines show the trajectories resulting in the highest transmission given in the legend. The transmission of the fundamental mode was calculated with MMA for a waveguide described by $n_{\mathrm{co}} = 1.53$, $n_{\mathrm{cl}} = 1.36$, $w = 2.0\,\mu\mathrm{m}$, $h = 1.8\,\mu\mathrm{m}$.

Another interesting example of a path planning algorithm is described in [179]. In this approach, the trajectory is composed of arcs cut from the circumferences of circles connected tangentially with straight lines. This description of a trajectory is potentially compatible with FMA and MMA, as the radii of curvature are known while designing the paths. All possible paths that meet the given constraints, such as minimum radius of curvature and obstacle avoidance, are stored as a graph consisting of the centres of the circles. These centres are uniformly spaced in the space free of obstacles. The search algorithm is based on Dijkstra’s algorithm, which is used to find the shortest paths [180]. To optimise the waveguide trajectories, a penalty function related to the loss associated with the paths would need to be introduced. However, this path planning algorithm does not account for continuous change of curvature, like for example Euler bends [181–183]. This may lead to high radiation losses and the excitation of higher-order modes at the interfaces between straight and bent segments. As this is unfavourable for the future operation, such an approach is not investigated in further detail.

In each iteration of the optimisation in the methods presented in this chapter, the transmission can also be computed using a pre-trained artificial neural network (ANN), as detailed in Section 3.4. Especially, the LSTM neural network, presented in [CO1], could be utilised.

The next section focuses on the optimisation of waveguide trajectories, where the trajectories are represented using Cartesian coordinates that are expressed as polynomials of a curve parameter. This method is based on the work [46], with the key difference that the calculation of the objective function is performed using the MMA. This optimisation procedure is described in details because it proved to be the most efficient among the methods investigated during this doctoral research.

4.2. Optimisation with multi-mode approximation

This section outlines the optimisation procedure, where the waveguide transmission is used as the merit function. The transmission is calculated using the multi-mode approximation as discussed in Chapter 3. The performance of this optimisation is presented on a few examples that involve different positions of waveguide endpoints and obstacles. The content of this section was presented at various conferences [C1, C2].

4.2.1. Optimisation procedure

In the current work, the trajectory is described by the position vector $\mathbf{r}(s) = (y(s), z(s))^{\mathrm{T}}$, which contains Cartesian coordinates y and z that describe every possible position within the space where the trajectory can be placed. In agreement with [46, Section 2.2], the coordinates of the possible trajectory are expressed as 5th order polynomials (4.1), (4.2) of the curve parameter $s \in [0, 1]$

$$y(s) = a_0 s^5 + a_1 s^4 + a_2 s^3 + a_3 s^2 + a_4 s + a_5 \,, \tag{4.1}$$

$$z(s) = b_0 s^5 + b_1 s^4 + b_2 s^3 + b_3 s^2 + b_4 s + b_5 \,. \tag{4.2}$$

The number of unknowns, consisting of the twelve polynomial coefficients: $a_0, \ldots, a_5$ and $b_0, \ldots, b_5$, can be reduced using the following boundary conditions. First, the start position (y_0, z_0) and the end position (y_1, z_1) of the trajectory are known. Additionally, the trajectory at these positions must be tangential to the directions imposed by couplers. In the considered case, these directions are described by the horizontal unit vector $\hat{\mathbf{v}}$. The list of these constraints is expressed as:

$$\mathbf{r}(s=0) = \mathbf{r}_0 = (y_0, z_0)^{\mathrm{T}}, \tag{4.3}$$

$$\frac{\dot{\mathbf{r}}(s=0)}{|\dot{\mathbf{r}}(s=0)|} = \hat{\mathbf{v}}_0 = (1, 0)^{\mathrm{T}}, \tag{4.4}$$

$$\mathbf{r}(s=1) = \mathbf{r}_1 = (y_1, z_1)^{\mathrm{T}}, \tag{4.5}$$

$$\frac{\dot{\mathbf{r}}(s=1)}{|\dot{\mathbf{r}}(s=1)|} = \hat{\mathbf{v}}_1 = (1, 0)^{\mathrm{T}}, \tag{4.6}$$

where $\dot{\mathbf{r}}$ means the derivative of $\mathbf{r}$ with respect to s. The constraints (4.3)-(4.6) eliminate six degrees of freedom from the system. Therefore, only six parameters need to be optimised. The possible paths are restricted to the Cartesian coordinates contained within rectangular area that defines the available space, in which the trajectory shall be placed. For a rectangular space limited by $y_{\min}$ and $y_{\max}$ in y-direction, and by $z_{\min}$ and $z_{\max}$ in z-direction, this restriction of the coordinates is formulated as:

$$y_{\min} \leq y(s) \leq y_{\max} \quad \text{for} \quad s \in [0, 1], \tag{4.7}$$

$$z_{\min} \leq z(s) \leq z_{\max} \quad \text{for} \quad s \in [0, 1]. \tag{4.8}$$

Additionally, the trajectory must avoid potential obstacles. Their positions and sizes are specified by the user and provided as additional input to the optimisation algorithm. Figure 4.3 illustrates an exemplary trajectory that satisfies the constraints, while avoiding the obstacles, which are depicted as pink circles.

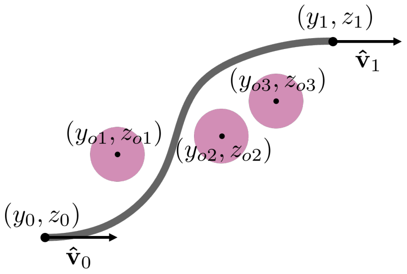

Figure 4.3: Exemplary drawing showing waveguide trajectory (grey), satisfying the constraints and avoiding obstacles (pink circles). The figure is annotated with the positions of trajectory ends, (y_0, z_0) and (y_1, z_1), together with the their tangential vectors $\hat{\mathbf{v}}$, and the centres of the obstacles (y_{oi}, z_{oi}).

A trajectory is defined as a curve $\boldsymbol{\gamma}$ created from $\mathbf{r}(s)$ after considering the entire range $s \in [0, 1]$. In practice, s is discretised depending on the required accuracy. Here, it consists of 1000 points. The curve $\boldsymbol{\gamma}$ effectively depends only on the polynomial coefficients $\mathbf{a} = (a_0, \ldots, a_5)$ and $\mathbf{b} = (b_0, \ldots, b_5)$. The optimal trajectory is the one for which the objective function

$$f(\boldsymbol{\gamma}) = 1 - T_1(\boldsymbol{\gamma}) + g(\boldsymbol{\gamma}) \tag{4.9}$$

reaches its minimum value. The optimisation process focusses only on the polynomial coefficients $\mathbf{a}$, $\mathbf{b}$ that minimise the objective function (4.9). This function is structured as 1 minus the transmission of the fundamental mode $T_1(\boldsymbol{\gamma})$, computed using the multi-mode approximation, equation (3.9). To ensure that the resulting trajectory avoids obstacles, we add a penalty function

$$g(\boldsymbol{\gamma}) = \int_0^1 \sum_{i=1}^{N_o} a_o \mathrm{e}^{-\left(\frac{(y(s)-y_{oi})^2}{2\sigma_y^2}\right)^p} \mathrm{e}^{-\left(\frac{(z(s)-z_{oi})^2}{2\sigma_z^2}\right)^p} \mathrm{d}s, \tag{4.10}$$

with $p = 2$, standard deviations $\sigma_y = \sigma_z = 5\,\mu\mathrm{m}$, $a_o = 10$ and number of obstacles N_o. These parameters were determined empirically. The penalty function is modelled as a sum of higher-order Gaussian functions with centres aligned to the obstacle locations, and the standard deviation reflecting the obstacle size. Such a penalty function facilitates the avoidance of obstacles. Gradually decreasing the value of the objective function as the trajectory moves away an obstacle allows for the convergence of the search algorithm towards the minimum. In cases where obstacles have arbitrary shapes, a procedure outlined in [46, Subsection 2.2.2] could be utilised. In [46], the obstacle shape deviating from a circle is determined based on user input of the obstacle corners.

Another important constraint is the minimum radius of curvature of the waveguide. As discussed in Section 3.2, not only does the MMA lose accuracy for smaller radii of curvature, but losses also increase. For this reason, the minimum radius of curvature must be considered, which in this section is defined as $R_{\min} = 7\,\mu\mathrm{m}$. This condition is expressed as

$$[\kappa(s)]^{-1} = \frac{\left[\dot{y}^2(s) + \dot{z}^2(s)\right]^{\frac{3}{2}}}{|\dot{y}(s)\ddot{z}(s) - \ddot{y}(s)\dot{z}(s)|} \geq R_{\min}\,, \tag{4.11}$$

where $\kappa(s)$ denotes the curvature at the waveguide position parameter s, and dots represent the derivatives with respect to s.

The whole optimisation problem for a trajectory can then be formulated as:

$$
\begin{aligned}
\underset{\mathbf{a},\mathbf{b}}{\text{minimise}} \quad & f(\boldsymbol{\gamma}(\mathbf{a},\mathbf{b})) && (4.12)\\
\text{subject to} \quad & \mathbf{r}(0) = (y_0, z_0)^{\mathrm{T}}, && (4.13)\\
& \mathbf{r}(1) = (y_1, z_1)^{\mathrm{T}}, && (4.14)\\
& \frac{\dot{\mathbf{r}}(0)}{|\dot{\mathbf{r}}(0)|} = \frac{\dot{\mathbf{r}}(1)}{|\dot{\mathbf{r}}(1)|} = (1,0)^{\mathrm{T}}, && (4.15)\\
& y_{\min} \le y(s) \le y_{\max} \quad \text{for} \quad s \in [0,1], && (4.16)\\
& z_{\min} \le z(s) \le z_{\max} \quad \text{for} \quad s \in [0,1], && (4.17)\\
& [\kappa(s)]^{-1} \ge R_{\min} \quad \text{for} \quad s \in [0,1]. && (4.18)
\end{aligned}
$$

For the optimisation, we utilise MATLAB's built-in nonlinear programming solver *fmincon* [119]. The solver effectively searches for a local minimum while satisfying specified conditions, using a *sequential quadratic programming* (SQP) algorithm [184, Chapter 18], ensuring that boundary conditions are satisfied throughout all iterations. The computations are performed on an Intel(R) Xeon(R) CPU E5-2630 v4 @ 2.20GHz, RAM 512 GB, running on Debian GNU/Linux 9 (stretch) 4.9.0-19-amd64. The *maxNumCompThreads* setting is configured to 20. The results of the optimisation for a few examples are shown in the following section.

4.2.2. Optimisation results

The optimisation scheme is applied to a few examples that differ in the positions of the input and output ports of the waveguide, as well as the distribution of obstacles. Figure 4.4 presents four cases. The grey line represents the initial trajectory and the green line shows the trajectory after optimisation. The trajectory is initialised with unconstrained polynomial coefficients of $y(s)$ and $z(s)$ set to 1's. This setting results in the shortest initial path, presented in Figure 4.4. In both Figure 4.4(a) and Figure 4.4(b), the input port is at position $(0, 0)$ [µm] and the output port is at $(100, 100)$ [µm], but the spatial distribution of obstacles is different. In the first case, some obstacles overlap with the initial waveguide trajectory, causing the trajectory to be *trapped* between the centres of two obstacles. In the second example, shown in Figure 4.4(b) the obstacles are accumulated in one part of the domain. These two examples demonstrate the ability of the algorithm to avoid all obstacles.

Figure 4.4(c) shows a setup similar to the case presented in [52]. Here, the initial trajectory is also trapped between obstacles, and the optimisation algorithm forces a shift of the trajectory to avoid the obstacles. The most challenging scenario is presented in Figure 4.4(d), where the input and output ports are at the same y-coordinate. Consequently, the initial trajectory is a straight line characterised by the highest possible transmission equal to 1. However, this trajectory passes through the obstacles. To force the algorithm to change the trajectory, the parameters of the penalty function need to be modified to $p = 1$, $\sigma_y = \sigma_z = 5\,\mu\text{m}$, and $a_o = 100$. The minimal radius of curvature should be reduced to 5 µm. The optimisation time for all the examples in Figure 4.4 varies between 3 and 10 minutes.

In all presented cases, minimising the objective function reduces the transmission compared to the initial, shortest-path trajectory. However, achieving maximal transmission is not always feasible in practice because the path would intersect with obstacles. The aim of the optimisation is to find the best possible alternative path. One potential drawback of using polynomials (4.1) and (4.2) is the varying weight of the terms, which strongly depends on the curve parameter s. For example, the higher-order terms may be negligible when the curve parameter approaches 0. A possible solution would be to choose different polynomials, such as Chebyshev polynomials or Bernstein polynomials. However, this is not explored further here, as the optimisation is not the focus of this thesis.

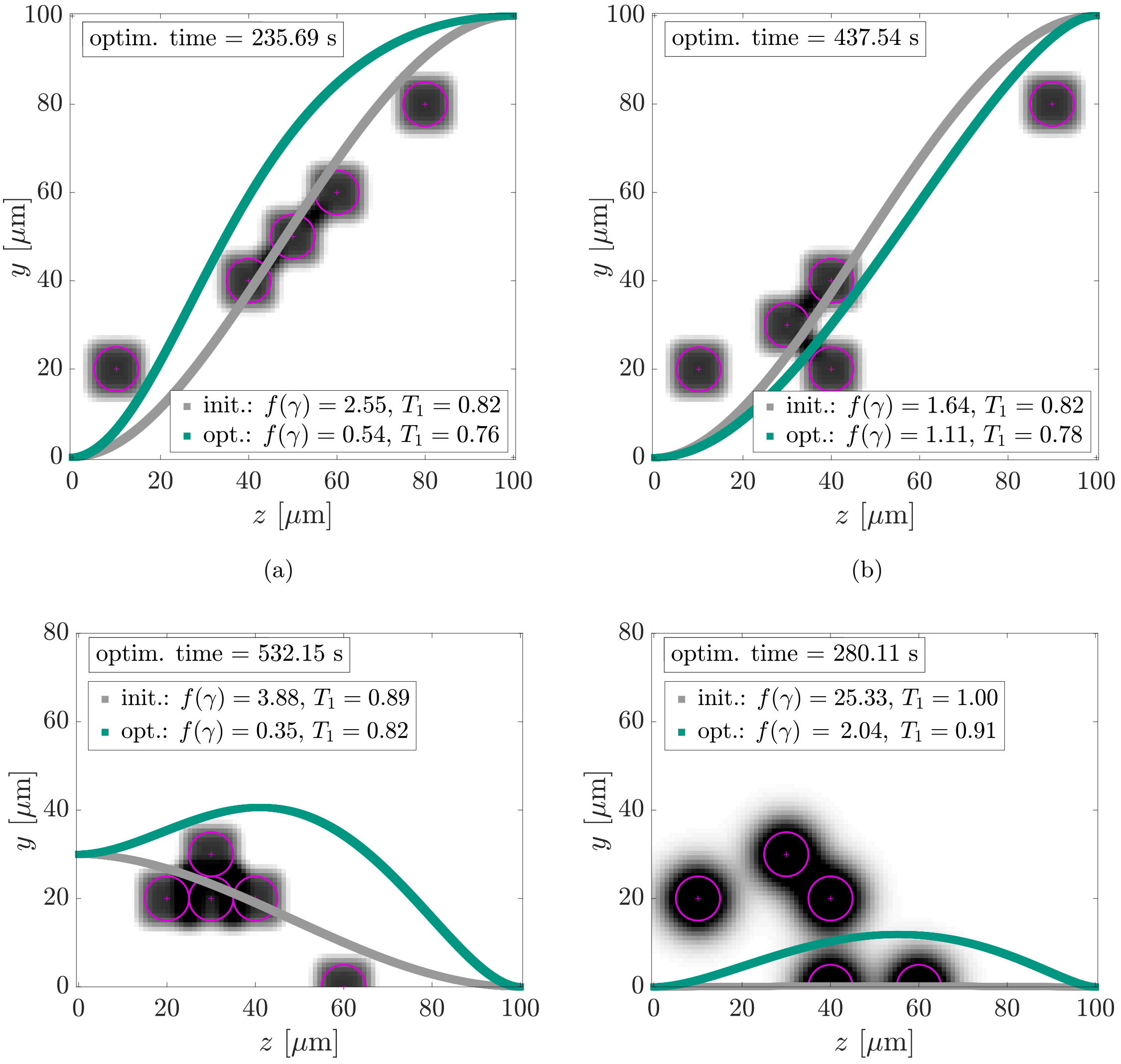

(a)

(b)

(c)

(d)

Figure 4.4.: Examples of initial trajectories (grey) and optimised trajectories (green), together with their transmissions. The transmission was calculated with MMA for a waveguide of 2.0 µm × 1.8 µm (width × height), core $n_{\mathrm{co}} = 1.53$, cladding $n_{\mathrm{cl}} = 1.36$, and wavelength 1.55 µm. The optimisation time in seconds is given in the upper-left corner of each plot. The obstacles are marked with pink circles. The dark shadows represent the penalty function, with the peaks in the centres of the obstacles. The parameters of the penalty function are: (a–c) $p = 2$, $\sigma_y = \sigma_z = 5$ µm, $a_o = 10$, and (b) $p = 1$, $\sigma_y = \sigma_z = 5$ µm, and $a_o = 100$.

4.3. Summary and conclusions

In this chapter, we have discussed various methods for optimising the trajectories of free-form waveguides. The main assumption is a bending within a 2D plane, which reduces the dimensionality of the optimisation problem by eliminating the effect of torsion. The first section presented an overview of path optimisation methods potentially applicable to waveguides, including searching for the shortest path with Delaunay triangulation or optimisation with neural networks. The trajectories can be described with polynomials, B-splines, Bézier curves or smoothened graph paths. Section 4.2 presents an optimisation procedure in which the Cartesian coordinates of the trajectory are described with a 5^{th} order polynomials, with curve parameter ranging from 0 to 1. The function of merit is composed of unity decreased by the transmission of the fundamental mode (computed with MMA) and increased by the penalty function modelling the position of the obstacles with the Gaussian function. The aim of the optimisation is to find the trajectory that minimises the objective function. Whenever the trajectory intersects with an obstacle, the objective function increases. The results of this optimisation scheme are presented in a few examples with predefined input and output ports, as well as the positions of obstacles and available space. Based on the given setting, the optimal trajectory can be determined in a few minutes. This is an acceptable time for the *in situ* production of photonic wire bonds.

The next chapter presents further study on the curvature of waveguides. The study focuses on nonlinear effects such as spontaneous four wave mixing, which may be enhanced with the bending of a waveguide made of nonlinear material.

5 | Enhancement of the photon pair generation rate by spontaneous four-wave mixing in bent waveguides

In this chapter, we examine the impact of bending on the photon pair generation rate in waveguides made from materials with a nonlinear response. We focus on the generation of photon pairs through a four-wave mixing process, governed by a third-order electric susceptibility. This chapter covers results of a research project co-supervised by Prof. John E. Sipe at the University of Toronto. The expertise of Prof. John E. Sipe includes nonlinear quantum optical effects in integrated photonic devices, particularly waveguides coupled to resonator structures. The research discussed here originated from the more general investigation of nonlinear effects in curved waveguides. The content of this chapter has been published in [P3] and was presented at conferences [C6, C7].

This chapter is organised into several sections to thoroughly explore photon pair generation in bent waveguides. Section 5.1 provides a brief introduction to the fundamental concepts of nonlinear optics that are referenced throughout this chapter. Afterwards, Section 5.2 outlines the motivation for enhancing the rate of photon pair generation in waveguides. Section 5.3 describes the formalism used to calculate the nonlinear coefficients and photon pair generation rates for channel waveguides. Section 5.4 examines the various types of losses in waveguides, then Section 5.5 outlines the different waveguide systems considered, and Section 5.6 describes the details of the numerical simulations. Section 5.7 presents the results of the calculations for commonly used nonlinear waveguides with different cross-sections, as well as for a lossy waveguide. Specifically, we study how the radius of curvature of the waveguide affects the nonlinear response. The results for two distinct material systems are presented in detail. Additionally, we provide the values of the calculated nonlinear coefficients and the photon pair generation rates for several waveguide configurations in a comprehensive table to give a broader overview on how bending affects the nonlinear properties of the waveguides. We also investigate how different modal parameters, such as effective mode area, group velocity, or effective refractive index, change as a function of radius curvature. We conclude with the physical discussion of the obtained results.

5.1. A brief introduction into nonlinear optics

In the previous chapters, only linear optical effects are considered. Therefore, this section briefly explains the basic concepts of nonlinear optics as far as it is needed to understand the discussions in this chapter. In the following, we describe the nonlinear response of the polarisation $\mathbf{P}(\mathbf{r}, \omega)$ to the electric field $\mathbf{E}(\mathbf{r}, \omega)$, outline basic nonlinear phenomena, and discuss the phase-matching condition. A detailed study of nonlinear optics can be found in many dedicated textbooks [72, 185–188].

5.1.1. Nonlinear response of a material

In nonlinear optics, the polarisation $\widetilde{\mathbf{P}}(\mathbf{r}, t)$ in the constitutive relation for the electric field (2.5) responds nonlinearly to this electric field. In frequency domain, the polarisation can be expressed as [187, Section 1.2]

$$\mathbf{P}(\mathbf{r}, \omega) = \mathbf{P}^{(1)}(\mathbf{r}, \omega) + \mathbf{P}^{(2)}(\mathbf{r}, \omega) + \mathbf{P}^{(3)}(\mathbf{r}, \omega) + \cdots \tag{5.1}$$

with the vector components

$$P_i^{(1)}(\mathbf{r}, \omega) = \varepsilon_0 \sum_j \chi_1^{ij}(\mathbf{r}, \omega; \omega) E_j(\mathbf{r}, \omega), \tag{5.2}$$

$$P_i^{(2)}(\mathbf{r}, \omega) = \varepsilon_0 \sum_{jk} \sum_{(mn)} \chi_2^{ijk}(\mathbf{r}, \omega_m + \omega_n; \omega_m, \omega_n) E_j(\mathbf{r}, \omega_m) E_k(\mathbf{r}, \omega_n), \tag{5.3}$$

$$P_i^{(3)}(\mathbf{r}, \omega) = \varepsilon_0 \sum_{jkl} \sum_{(mno)} \chi_3^{ijkl}(\mathbf{r}, \omega_m + \omega_n + \omega_o; \omega_m, \omega_n, \omega_o) E_j(\mathbf{r}, \omega_m) E_k(\mathbf{r}, \omega_n) E_l(\mathbf{r}, \omega_o). \tag{5.4}$$

The indices $ijkl$ refer to the Cartesian components of the field, and summation over (mn) implies that the summation must be performed over all possible ω_m and ω_n such that $\omega = \omega_m + \omega_n$. The same applies to the summation over (mno) [185, Chapter 1]. Further in this chapter, the summation sign is omitted. We follow the Einstein notation and assume that the expressions are summed over the repeated indices. The quantity $\chi_1^{ij}(\mathbf{r}, \omega; \omega)$ denotes the linear susceptibility and is represented as a second-rank tensor, while $\chi_2^{ijk}(\mathbf{r}, \omega_m + \omega_n; \omega_m, \omega_n)$ is the second-order nonlinear susceptibility expressed as a third-rank tensor, and $\chi_3^{ijkl}(\mathbf{r}, \omega_m + \omega_n + \omega_o; \omega_m, \omega_n, \omega_o)$ represents the third-order nonlinear susceptibility as a fourth-rank tensor.[1]

Both, the linear and nonlinear susceptibilities, characterise the optical properties of a bulk medium. The number of independent parameters in higher-order nonlinear susceptibilities is usually reduced because of the crystalline symmetries and the permutation symmetry of the involved frequencies. In centrosymmetric materials, which display inversion symmetry, the second-order nonlinear susceptibility vanishes. This applies to the materials examined in this chapter. For isotropic materials, the third-order susceptibility reduces to three independent elements [185, Section 4.2]. Depending on the involved frequencies, the additional relations between these three elements can be found, which reduce the number of independent elements. For example, a third-harmonic generation process[2] is described by only one independent element of the susceptibility tensor [185, Section 4.2]. Similarly, in the case of degenerate four-wave mixing,[2] the two remaining components can be derived from the one independent element [185, Section 4.2][189]. The characteristic value of the nonlinear susceptibility, χ_3^{1111}, is measured for a material, and the components of the tensor are calculated [189–191].

---

[1] For the sake of readability, we omit the arguments of the susceptibility later in the text.

[2] Explained in Subsection 5.1.2.

The nonlinear components in equation (5.1) and possible combinations of frequencies are related to various nonlinear processes. These nonlinear processes are briefly discussed in the next subsection. We strictly concentrate on third-order nonlinear processes.

5.1.2. Nonlinear processes

When a monochromatic wave with angular frequency ω is directed into a nonlinear optical material, it can excite new waves oscillating at multiples of this frequency. In the presence of a third-order susceptibility, the frequency can be tripled in a third-harmonic generation (THG) process, which is shown graphically in Figure 5.1(a). Additionally, the refractive index of a medium changes with the intensity of the electric field. In case the propagation of a pulse is considered and not a monochromatic wave, the modified refractive index leads to a phase shift in the pulse, resulting in pulse broadening [185]. This effect is called *self-phase modulation* (SPM) when a phase shift arises from a wave oscillating at the same frequency, or *cross-phase modulation* when the stronger wave oscillating at one frequency induces a phase shift in a second wave, oscillating at lower frequency.

Another third-order nonlinear effect is four-wave mixing (FWM). This is a typical third-order nonlinear optical process, in which two output frequencies are generated from two input frequencies, as presented in Figure 5.1(b). The FWM can be non-degenerate if all frequencies are different, or degenerate if at least two of the involved frequencies are identical. FWM can occur either classically or spontaneously, depending on whether an external input signal is provided alongside a pump [18]. In this chapter, we focus on spontaneous four-wave mixing (SFWM), in which the annihilation of two pump photons results in the creation of a pair of one signal and one idler photon. The generated photons are typically entangled, and their superposition creates pairs of photons in form of squeezed states of light.[3] The entanglement and creation of squeezed states are of significant interest in quantum information processing protocols [193].

Other third-order nonlinear effects include two-photon absorption (TPA) and stimulated Raman scattering (StRS). In TPA process, an atom is excited to a higher energy level by the simultaneous absorption of two photons, as shown in Figure 5.1(c). In stimulated Raman scattering, a photon of frequency ω is annihilated and a photon of a lower frequency $\omega_{\mathrm{S}} = \omega - \omega_{\mathrm{v}}$ is created, leaving the atom in an excited state with energy $\hbar\omega_{\mathrm{v}}$, referred to as *vibrational energy* [185]. This scenario is illustrated in Figure 5.1(d).

When plane waves are considered in the bulk medium, the field intensities of the generated waves vary with wavevector mismatch Δk, which results from the nonlinear processes [185, Section 2.3]. The next section describes the *phase-matching condition* $\Delta k = 0$, mentions its importance and shows a way to satisfy this condition.

---

[3] A squeezed state of light is characterised by a standard deviation smaller than $\frac{1}{2}$ in one of the state's quadratures, at the expense of an increase in standard deviation of the second quadrature relative to the initial state. Therefore, it is called a *squeezed* state. The quadratures in quantum optics correspond to dimensionless position and momentum operators [192].

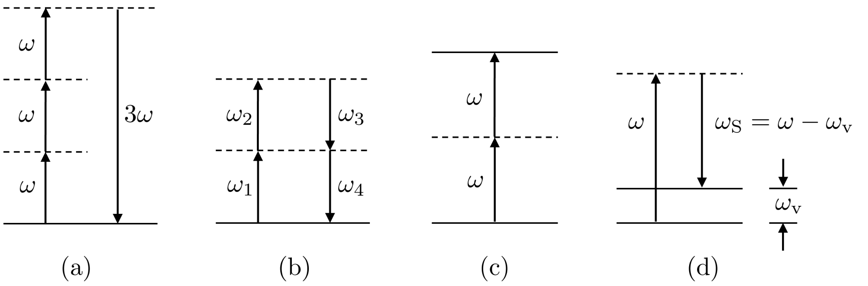

Figure 5.1.: Energy-level diagrams of nonlinear processes: (a) third-harmonic generation, (b) four-wave mixing, (c) two-photon absorption, and (d) stimulated Raman scattering.

5.1.3. Phase-matching condition

The presence of a nonlinearity can lead to a phase difference between polarisation and the applied electric field of a plane wave. As a consequence, the generated waves cannot extract energy from the incident waves efficiently [185]. For example, in non-degenerate third order nonlinear optical mixing process, the intensity of the generated field at frequency $\omega_4 = \omega_1 + \omega_2 + \omega_3$ is influenced by the wavevector mismatch $\Delta k = k_1 + k_2 + k_3 - k_4$. The efficiency of the nonlinear process decreases if the phase-matching condition $\Delta k = 0$ is not satisfied [185]. The phase-matching condition is related to conservation of momentum.

Maintaining the phase-matching condition in practice can be challenging because the refractive index of a material is a dispersive quantity. Typically, the refractive index increases with increasing frequency, which is known as *normal dispersion*. In terms of frequencies, the phase-matching condition for the considered third order nonlinear effect can be expressed as

$$\frac{n(\omega_1)\omega_1}{c_0} + \frac{n(\omega_2)\omega_2}{c_0} + \frac{n(\omega_3)\omega_3}{c_0} = \frac{n(\omega_4)\omega_4}{c_0}. \tag{5.5}$$

Phase-matching can be achieved by exploiting the birefringence of crystals. The refractive index of an anisotropic medium is characterised by the *index ellipsoid* that is derived from the principal refractive indices that shape the ellipsoid. The principal refractive index expresses the refractive index experienced by a plane wave that is linearly polarised along one principal axis, while propagating along another principal axis [69]. Phase matching can be satisfied between waves propagating in different polarisations. In birefringent crystals, these directions are referred to as *ordinary* and *extraordinary* polarisations.

Figure 5.2 shows an example of a phase matching for THG, for which the phase-matching condition (5.5) simplifies to $n(3\omega_1) = n(\omega_1)$. In the figure, the fundamental wave is polarised in ordinary direction and the third harmonic is polarised in extraordinary direction. This method exploits the different frequency dependencies of the refractive indices in the two polarisation directions. Alternatively, the dispersion of waveguide modes can be exploited for the same purpose.

This section has briefly explained the basic concepts of nonlinear optics, which are essential for understanding the nonlinear processes or phase-matching issues, mentioned later in this study. In the next section, we motivate our work on photon pair generation in waveguides made of nonlinear materials.

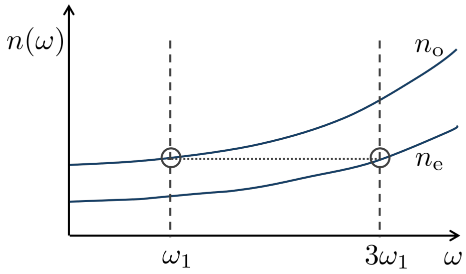

Figure 5.2: Phase matching for third harmonic generation. The fundamental wave is polarised in ordinary direction, while the third harmonic wave is polarised along extraordinary direction, both resulting in the same refractive indices.

5.2. Motivation

The generation of photon pairs in waveguides and ring resonators results in the creation of entangled states of light [194]. This capability is crucial for enabling on-chip quantum photonic technologies [25, 195], as photon pair sources can be integrated into compact and complex quantum circuits [19, 194, 196]. A notable advantage of this approach is that the photon pairs do not need to be injected from an external source, thereby eliminating coupling losses [197]. The on-chip generation of entangled photon pairs in waveguides has been successfully demonstrated using two spiral waveguides, each measuring 5.2 mm in length [198]. Another example is the on-chip photon pair generation with two microring resonators, presented in [199], which can be applied to quantum interferometry. The integration of photon pair sources on photonic chips paves the way for applications in quantum communications and optical quantum computation [27, 28], e.g., Gaussian boson sampling [200], as well as quantum metrology of light-sensitive samples [201].

Photon pairs can be created by pumping a nonlinear crystal with a laser beam [202]. The pairs emerge from the conversion of one pump photon in second-order nonlinear materials, or two pump photons if the process occurs in third-order nonlinear materials. The higher the intensity of the pump the stronger the considered nonlinear effect. The primary advantage of second-order effects is their immunity to spontaneous Raman scattering (SpRS). Otherwise, uncorrelated noise photons close to the pump frequency would be generated due to SpRS [203]. On the other hand, the SpRS can be mitigated by selecting the appropriate crystal orientation, signal and idler frequencies, and light polarisation [204]. Therefore, with the use of a proper setting, the third-order nonlinear process FWM can also generate photon pairs characterised by high brightness and strong correlation. FWM is especially advantageous because this process is natural in silicon-based optical structures due to the centrosymmetry of silicon. However, FWM is a classical process requiring an external signal alongside the pump signal. For quantum applications, spontaneous four-wave mixing (SFWM) is more advantageous, as it generates photon pairs spontaneously without external stimulation [25]. SFWM in a third-order nonlinear material has been theoretically predicted and experimentally verified as an efficient source of quantum correlated photon pairs [197, 205].

Enhancing nonlinearities can significantly increase the efficiency of signal-processing devices in integrated photonic circuits [206]. However, the nonlinearity is an intrinsic property of a material and thus difficult to change. Therefore, the most common solution to boost nonlinear effects is to confine the light within a waveguide to increase the light intensity. It is schematically presented in Figure 5.3, where a waveguide is pumped with a laser beam of pump frequency ω_P, resulting in the generation of photon pairs of frequency ω_S and ω_I.

Additionally, a proper cladding should be chosen to ensure high index contrast to increase the confinement. Further improvement involves increasing the interaction length by elongating the nonlinear waveguides. However, this approach is not always feasible due to limited chip size. With the trend towards denser integration of photonic components, it is desirable to enhance their nonlinear response while keeping the spatial footprint of nonlinear components small. One proposed solution is the systematic bending of waveguides. It was shown that the waveguide length can be extended to several centimetres by forming low-loss spirals using smooth Euler bends [18, 207]. This way of gradual bending minimises higher-order mode coupling [P2, 112].

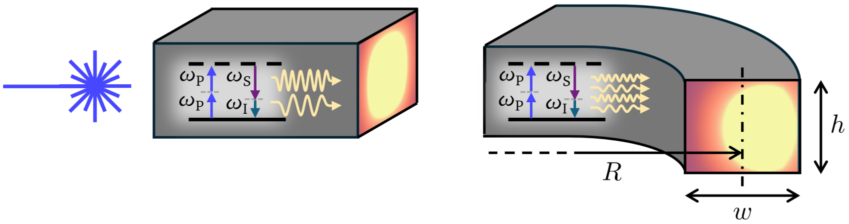

Figure 5.3.: Schematic sketch of a straight, rectangular waveguide (left) being pumped with a laser at the pump frequency ω_P. This pumping leads to a four-wave mixing process, presented graphically on a waveguide. This process results in creating idler and signal photons of angular frequencies ω_I and ω_S, respectively. The waveguide is sectioned to reveal the field profile of the fundamental mode guided in the waveguide core. In the bent waveguide (right), the number of signal and idler photons may increase. The relevant dimensions: radius of curvature R, width w and height h, are indicated in the picture. Figure is reprinted from [P3]. Copyright © 2011 by American Physical Society.

A common approach to enhance the nonlinearity is to use microring resonators [55]. Microring resonators are compact so they are characterised by a small footprint on a chip. The choice between waveguides and microring resonators depends on the selected material platform, chip architecture, or manufacturing facilities. Microring resonators offer advantages such as high quality-factor, compact structure, and resonance enhancement, which makes the microring resonators effective at lower pump powers compared to waveguides [208]. However, the strong spatial confinement of the optical field and resonance effects can be also disadvantageous as they may cause temperature changes in the device due to the increment of the optical field, even at low power [208, 209]. These temperature changes can result in phase shifts that require an active control, often involving external power and reducing the energy efficiency of the overall system. Additionally, ring resonators suffer from losses, when coupling them to channel waveguides. This coupling loss reduces the photon pair generation rate. In this situation, the use of waveguides instead of microring resonators aids to avoid both coupling losses and high energy usage. Moreover, the bendability makes the waveguide structures more flexible and, therefore, easier to place on the chip. The ongoing development of waveguides makes them an interesting subject for studying third-order nonlinear effects.

In some instances of integrated photonic platforms, waveguides can be bent with a reasonable radius without significantly increasing losses [207, 210]. This property has been previously explored in literature [18, 112, 207] in terms of extending the waveguide length without affecting the spatial footprint on a chip. However, the impact of bending on waveguide nonlinearity has been disregarded. It is reasonable to expect an enhancement of the nonlinearity, as bending the waveguide alters its modal properties, most notably improving field localisation. This directly influences the effective nonlinearity of the waveguide, potentially making any nonlinear effect more efficient. Nevertheless, the main question is whether these advantages surpass the negative impact of increased losses when the waveguides are bent. This chapter aims to address this issue, focusing on the example of the photon pair generation rate in a spontaneous four-wave mixing process. To provide a detailed answer, we consider several waveguide systems that could be used for the purpose of photon pair generation, utilising various material platforms.

5.3. Photon pair generation rate

The photon pair generation rate expresses the number of photon pairs generated in time. This rate is calculated here based on the derivation in [211] and reads

$$\mathcal{R} = \frac{\text{number of generated pairs}}{\text{time}} = \frac{2\pi}{\hbar^2} \int\limits_{-\infty}^{\infty} \int\limits_{-\infty}^{\infty} \delta(\Delta\omega(\omega_\mathrm{S}, \omega_\mathrm{I})) |M(\omega_\mathrm{S}, \omega_\mathrm{I})|^2 \frac{1}{v_\mathrm{S}} \frac{1}{v_\mathrm{I}} \mathrm{d}\omega_\mathrm{S} \mathrm{d}\omega_\mathrm{I} \,. \tag{5.6}$$

In equation (5.6), ω_S and ω_I represent the angular frequencies of signal and idler photons, respectively. The integration in (5.6) is performed over the available frequency spectrum. The group velocities of the signal and idler modes are denoted by v_S and v_I, respectively. The Dirac delta distribution $\delta(\cdot)$ depends on $\Delta\omega(\omega_\mathrm{S}, \omega_\mathrm{I})$, which expresses the angular frequency difference of the annihilated and created photons $\Delta\omega(\omega_\mathrm{S}, \omega_\mathrm{I}) = 2\omega_\mathrm{P} - \omega_\mathrm{S} - \omega_I$, where ω_P denotes a fixed frequency of the pump photons. Note that we consider only the degenerate case, where the two pump photons have the same frequency. The condition $\Delta\omega(\omega_\mathrm{S}, \omega_\mathrm{I}) = 0$ ensures conservation of energy. The quantity $M(\omega_\mathrm{S}, \omega_\mathrm{I})$ with units $\mathrm{m}^3\mathrm{s}^{-2}\mathrm{kg}$ corresponds to the FWM generation efficiency [25]. The photon pair generation rate is required to be in units of Hz, i.e., pairs per second. The formula (5.6) comes directly from equation (A16) in [211] upon replacing wavenumbers with the corresponding angular frequencies in the double integral. The formula (5.6) was originally derived in [193] and [211] based on Fermi's golden rule [212–215] with continuous-wave (CW) pump, after defining an interaction Hamiltonian for creating signal and idler photons, and annihilating pump photons. The detailed derivation can be found in [216, Appendix A.1].

The FWM generation efficiency $M(\omega_\mathrm{S}, \omega_\mathrm{I})$ is the essential quantity to evaluate. The explicit formula for $M(\omega_\mathrm{S}, \omega_\mathrm{I})$ is derived from equation (A6) and (11) in [211] as

$$M(\omega_\mathrm{S}, \omega_\mathrm{I}) = \frac{6\pi\mathcal{P}_\mathrm{P}}{\varepsilon_0 \hbar \omega_\mathrm{P} v_\mathrm{P}} \int_{\mathcal{D}} \Gamma_3^{ijkl}(\mathbf{r}) [D_i^\mathrm{S}(\mathbf{r})]^* [D_j^\mathrm{I}(\mathbf{r})]^* D_k^\mathrm{P}(\mathbf{r}) D_l^\mathrm{P}(\mathbf{r}) \mathrm{d}\mathbf{r} \,, \tag{5.7}$$

with the vacuum permittivity ε_0, the power and the group velocity of the pump source, $\mathcal{P}_\mathrm{P}$ and v_P, respectively, and

$$\Gamma_3^{ijkl}(\mathbf{r}) = \frac{\chi_3^{ijkl}(\mathbf{r})}{\varepsilon_0^2 \varepsilon_1^2(\mathbf{r}; \omega_\mathrm{P}) \varepsilon_1(\mathbf{r}; \omega_\mathrm{I}) \varepsilon_1(\mathbf{r}; \omega_\mathrm{S})} \tag{5.8}$$

expressing a normalised nonlinearity, where the third-order nonlinear susceptibility tensor $\chi_3^{ijkl}(\mathbf{r})$ is normalised to the electric permittivity of the waveguide $\varepsilon_1(\mathbf{r}; \omega_\mathrm{J})$. The index J denotes the pump P, signal S, or idler I, i.e., $\mathrm{J} \in \{\mathrm{P}, \mathrm{S}, \mathrm{I}\}$. Quantities with indices i, j, k, and l refer to the Cartesian components, which are summed over repeated indices.

Equation (5.7) contains Cartesian components of electric displacement fields for the waveguide modes of the pump, idler, and signal. Following equation (4) from [211], the electric displacement field is defined as

$$\mathbf{D}^{\mathrm{J}}(\mathbf{r}) = \sqrt{\frac{\hbar\omega_{\mathrm{J}}}{4\pi}}\boldsymbol{\mathcal{D}}^{\mathrm{J}}(\mathbf{r}_{\perp})\mathrm{e}^{\mathrm{i}\beta_{\mathrm{J}}z}\,. \tag{5.9}$$

In the equation (5.9), the displacement field amplitude $\boldsymbol{\mathcal{D}}^{\mathrm{J}}(\mathbf{r}_{\perp})$ of the mode J is evaluated in a plane $\mathcal{D}$ perpendicular to the propagation direction z of the mode J. The propagation constant of the mode J is denoted by β_{J}. The displacement field amplitudes are normalised following the equation (70) from [193]

$$\int_{\mathcal{D}} \frac{[\boldsymbol{\mathcal{D}}^{\mathrm{J}}(x,y)]^{*}\cdot\boldsymbol{\mathcal{D}}^{\mathrm{J}}(x,y)}{\varepsilon_0\varepsilon_1(x,y;\omega_{\mathrm{J}})}\frac{v_{\mathrm{ph}}(x,y;\omega_{\mathrm{J}})}{v_{\mathrm{g}}(x,y;\omega_{\mathrm{J}})}\mathrm{d}x\mathrm{d}y = 1. \tag{5.10}$$

The quantities $v_{\mathrm{ph}}(x,y;\omega_{\mathrm{J}})$ and $v_{\mathrm{g}}(x,y;\omega_{\mathrm{J}})$ denote the local phase velocity and local group velocity, respectively. The local phase and group velocities are related to the bulk material that is at a specific point (x,y) in the waveguide's cross-section, and account for material dispersion [217].

Taking into account the formula for the displacement field (5.9) and the expression (5.8), one can rewrite $M(\omega_{\mathrm{S}},\omega_{\mathrm{I}})$ as

$$\begin{aligned} M(\omega_{\mathrm{S}},\omega_{\mathrm{I}}) = {}& \frac{6\pi\mathcal{P}_{\mathrm{P}}}{\varepsilon_0\hbar\omega_{\mathrm{P}}v_{\mathrm{P}}}\frac{\hbar^2\sqrt{\omega_{\mathrm{S}}\omega_{\mathrm{I}}}\omega_{\mathrm{P}}}{16\pi^2}\int_{-\frac{L}{2}}^{\frac{L}{2}}\mathrm{e}^{\mathrm{i}z(2\beta_{\mathrm{P}}-\beta_{\mathrm{S}}-\beta_{\mathrm{I}})}\mathrm{d}z \\ & \cdot\varepsilon_0^2\int_{\mathcal{D}}\chi_3^{ijkl}(x,y)\left(\mathcal{E}_i^{\mathrm{S}}(x,y)\mathcal{E}_j^{\mathrm{I}}(x,y)\right)^{*}\mathcal{E}_k^{\mathrm{P}}(x,y)\mathcal{E}_l^{\mathrm{P}}(x,y)\mathrm{d}x\mathrm{d}y\,, \end{aligned} \tag{5.11}$$

where the wave is considered to propagate over a waveguide of length L. The above formula (5.11) is derived taking into account the relation between the electric field and the displacement field: $\mathcal{D}_i^{\mathrm{J}}(\mathbf{r}_{\perp}) = \varepsilon_0\varepsilon_1(\mathbf{r}_{\perp};\omega_{\mathrm{J}})\mathcal{E}_i^{\mathrm{J}}(\mathbf{r}_{\perp})$ and

$$\begin{aligned} &\int_{\mathcal{D}}\Gamma_3^{ijkl}(\mathbf{r}_{\perp})[\mathcal{D}_i^{\mathrm{S}}(\mathbf{r}_{\perp})]^{*}[\mathcal{D}_j^{\mathrm{I}}(\mathbf{r}_{\perp})]^{*}\mathcal{D}_k^{\mathrm{P}}(\mathbf{r}_{\perp})\mathcal{D}_l^{\mathrm{P}}(\mathbf{r}_{\perp})\mathrm{d}\mathbf{r}_{\perp} \\ &\qquad = \varepsilon_0^2\int_{\mathcal{D}}\chi_3^{ijkl}(x,y)\left(\mathcal{E}_i^{\mathrm{S}}(x,y)\mathcal{E}_j^{\mathrm{I}}(x,y)\right)^{*}\mathcal{E}_k^{\mathrm{P}}(x,y)\mathcal{E}_l^{\mathrm{P}}(x,y)\mathrm{d}x\mathrm{d}y\,. \end{aligned} \tag{5.12}$$

The derivation is based on the equations (380–382) in [193] in the context of channel waveguides. Integrating over $\mathrm{d}\mathbf{r}_{\perp} = \mathrm{d}x\mathrm{d}y$ means integrating over the entire plane $\mathcal{D}$ perpendicular to the propagation direction of the waves.

Formula (5.11) can be simplified further, by introducing the nonlinear coefficient [193] for channel waveguides

$$\gamma_{\mathrm{SFWM}} = \frac{3(\omega_{\mathrm{S}}\omega_{\mathrm{I}}\omega_{\mathrm{P}}^2)^{\frac{1}{4}}\varepsilon_0}{4\sqrt{v_{\mathrm{S}}v_{\mathrm{I}}v_{\mathrm{P}}^2}}\int_{\mathcal{D}}\chi_3^{ijkl}(x,y)\left(\mathcal{E}_i^{\mathrm{S}}(x,y)\mathcal{E}_j^{\mathrm{I}}(x,y)\right)^{*}\mathcal{E}_k^{\mathrm{P}}(x,y)\mathcal{E}_l^{\mathrm{P}}(x,y)\mathrm{d}x\mathrm{d}y\,. \tag{5.13}$$

The nonlinear coefficient γ_{SFWM} quantifies the nonlinearity in a specific structure, related to the strength of spontaneous four-wave mixing [112]. This coefficient is useful for comparing the nonlinearity of various materials and structures. The nonlinear coefficient is typically defined with the use of an effective area of the waveguide mode [193, 218, 219]

$$A_{\mathrm{eff}} = \frac{N_{\mathrm{P}} N_{\mathrm{P}} N_{\mathrm{I}} N_{\mathrm{S}}}{\int \frac{\chi_3^{ijkl}(x,y)}{\bar{\chi}_3} \left[\mathcal{E}_i^{\mathrm{S}}(x,y)\mathcal{E}_j^{\mathrm{I}}(x,y)\right]^* \mathcal{E}_k^{\mathrm{P}}(x,y)\mathcal{E}_l^{\mathrm{P}}(x,y)\mathrm{d}x\mathrm{d}y}\,, \tag{5.14}$$

with

$$N_{\mathrm{J}} = \sqrt{\int \frac{n(x,y;\omega_{\mathrm{J}})v_{\mathrm{J}}}{v_{\mathrm{g}}(x,y;\omega_{\mathrm{J}})\bar{n}_{\mathrm{J}}} [\boldsymbol{\mathcal{E}}^{\mathrm{J}}(x,y)]^* \cdot \boldsymbol{\mathcal{E}}^{\mathrm{J}}(x,y)\mathrm{d}x\mathrm{d}y}\,, \tag{5.15}$$

where $\bar{n}_{\mathrm{J}}$ is the value of the refractive index of the waveguide core at wavelength λ_{J} and $\bar{\chi}_3$ represents the characteristic value of the susceptibility tensor components of the waveguide core. The above derivation uses the normalisation condition (5.10). With the formulas (5.14) and (5.15), the nonlinear coefficient simplifies to

$$\gamma_{\mathrm{SFWM}} = \frac{3(\omega_{\mathrm{S}}\omega_{\mathrm{I}}\omega_{\mathrm{P}}^2)^{\frac{1}{4}}\bar{\chi}_3}{4\varepsilon_0\sqrt{\bar{n}_{\mathrm{S}}\bar{n}_{\mathrm{I}}\bar{n}_{\mathrm{P}}\bar{n}_{\mathrm{P}}}c_0^2}\frac{1}{A_{\mathrm{eff}}}\,. \tag{5.16}$$

Collecting all of the above equations allows one to rewrite $M(\omega_{\mathrm{S}},\omega_{\mathrm{I}})$ in the form

$$M(\omega_{\mathrm{S}},\omega_{\mathrm{I}}) = \frac{6\pi\mathcal{P}_{\mathrm{P}}}{\varepsilon_0\hbar\omega_{\mathrm{P}}v_{\mathrm{P}}}\frac{\hbar^2(\omega_{\mathrm{S}}\omega_{\mathrm{I}}\omega_{\mathrm{P}}^2)^{\frac{1}{4}}\varepsilon_0}{12\pi^2}\sqrt{v_{\mathrm{S}}v_{\mathrm{I}}v_{\mathrm{P}}^2}\,\gamma_{\mathrm{SFWM}}\int_{-\frac{L}{2}}^{\frac{L}{2}} \mathrm{e}^{\mathrm{i}z\Delta\beta}\mathrm{d}z\,, \tag{5.17}$$

where the phase matching, corresponding to conservation of momentum, is quantified with $\Delta\beta = 2\beta_{\mathrm{P}} - \beta_{\mathrm{S}} - \beta_{\mathrm{I}}$. Eventually, the equation for $M(\omega_{\mathrm{S}},\omega_{\mathrm{I}})$ takes the form

$$M(\omega_{\mathrm{S}},\omega_{\mathrm{I}}) = \frac{\mathcal{P}_{\mathrm{P}}\hbar(\omega_{\mathrm{S}}\omega_{\mathrm{I}})^{\frac{1}{4}}}{2\pi}\sqrt{\frac{v_{\mathrm{S}}v_{\mathrm{I}}}{\omega_{\mathrm{P}}}}\gamma_{\mathrm{SFWM}}L\mathrm{sinc}\left(\Delta\beta\frac{L}{2}\right)\,, \tag{5.18}$$

with $\mathrm{sinc}(x) = \frac{\sin(x)}{x}$. The equation (5.18) can be inserted into the expression (5.6) to explicitly show the influence of the particular parameters on the photon pair generation rate

$$\mathcal{R} = \frac{\mathcal{P}_{\mathrm{P}}^2 L^2}{2\pi}\int\limits_{-\infty}^{\infty}\int\limits_{-\infty}^{\infty}\delta(\Delta\omega(\omega_{\mathrm{S}},\omega_{\mathrm{I}}))\frac{\sqrt{\omega_{\mathrm{S}}\omega_{\mathrm{I}}}}{\omega_{\mathrm{P}}}\gamma_{\mathrm{SFWM}}^2\left|\mathrm{sinc}\left(\Delta\beta\frac{L}{2}\right)\right|^2\mathrm{d}\omega_{\mathrm{S}}\mathrm{d}\omega_{\mathrm{I}}\,. \tag{5.19}$$

Based on equations (5.18) and (5.19), it is evident that the photon pair generation rate increases with the applied pump power $\mathcal{P}_{\mathrm{P}}$, waveguide length L, nonlinear coefficient γ_{SFWM}, and when the phase-matching condition $\Delta\beta = 0$ is satisfied. The nonlinear coefficient in equation (5.16) decreases as the effective area of the modes increases, or when the group velocities of the mixing waves increase, because these group velocities influence the effective area via equations (5.14) and (5.15). The influence of the group velocities is known as *slow-light enhancement* of the nonlinearity [220, 221]. In Section 5.7, the influence of the aforementioned parameters on the photon pair generation rate is discussed in more detail. The following section discusses the possible losses in nonlinear waveguides.

5.4. Treatment of losses

The derivation in Section 5.3 does not explicitly discuss possible losses caused by scattering or absorption. Section 5.4 explains the different sources of losses and their influence on photon pair generation rate in different materials and waveguide structures.

Equation (5.19) indicates that the photon pair generation rate increases with pump power. However, this increase in a waveguide is limited by two-photon absorption (TPA), quantified by the corresponding absorption coefficient as

$$\alpha_{\mathrm{TPA}} = \frac{3\omega_{\mathrm{P}}}{2\varepsilon_0 c_0^2 n_{\mathrm{co}}^2}\mathrm{Im}\{\chi_3\}\,. \tag{5.20}$$

The TPA is proportional to the imaginary part of the nonlinear susceptibility [222]. This phenomenon is especially problematic, because the generated photon pairs can be lost due to TPA induced free carrier absorption (FCA) [223, 224]. Particularly in silicon-on-insulator (SOI) systems [225], the TPA occurs when the photon frequencies (pump, signal, or idler) exceed the silicon bandgap frequency [25]. This is especially the case at telecommunication wavelengths [226]. Additional consequence of FCA is a free carrier dispersion effect, in which the change in concentration of electrons and holes in a semiconductor changes the effective refractive index [227].

To minimise the TPA, the pump needs to be shifted to a longer wavelength or an alternative material must be used, such as silicon nitride, which has a larger bandgap and is characterised by lower nonlinear and linear losses at telecommunication wavelengths [18]. TPA, FCA, and dispersion [221] can be also mitigated by using lower pump powers. Experimental results [228] reveal that the correlated photons can still be distinguished from accidental coincidences for a CW pump power of 10 mW at wavelengths close to 1.55 µm. The presence of TPA and FCA saturates optical power. It was shown in [221] for the same wavelength that a pump power around 100 mW remains below the saturation limit for conversion efficiency (defined as the ratio between the output idler power and input probe power) [221]. In this thesis, we choose a pump power of 100 mW. However, considering the square relationship between the photon pair generation rate and the pump power, our findings should also be applicable to lower powers.

Additional issues are propagation losses caused by scattering on sidewalls due to surface roughness [74]. This surface roughness can arise, for example, from an imperfect etching process during the waveguide fabrication [112, 113]. In silicon nanowires, this effect can impair the generation of high absolute idler powers [112]. Although scattering losses are significant in practice, the theoretical study in this thesis does not explicitly address losses caused by fabrication imperfections because these losses affect both straight and bent waveguides. Instead, we focus on the change in losses caused by the bending of waveguides.

To account for bending loss in equation (5.17) the integrand is modified to the form

$$\int_{-\frac{L}{2}}^{\frac{L}{2}} \mathrm{e}^{\mathrm{i}\mathrm{Re}\{\Delta\beta\}z}\mathrm{e}^{-\beta_{\mathrm{im}}\left(z+\frac{L}{2}\right)}\mathrm{d}z\,, \tag{5.21}$$

where the total imaginary part of the propagation constant equals $\beta_{\mathrm{im}} = 2|\mathrm{Im}\{\beta_{\mathrm{P}}\}| + |\mathrm{Im}\{\beta_{\mathrm{S}}\}| + |\mathrm{Im}\{\beta_{\mathrm{I}}\}|$. The absolute values are used to ensure that the imaginary parts are positive, regardless of the employed convention. Note that the second exponential in (5.21) takes a distance from 0 to L as the effective argument. This formulation ensures that the losses are properly accumulated while considering propagation in a waveguide section of length L. Evaluating the integral (5.21) results in

$$\int_{-\frac{L}{2}}^{\frac{L}{2}} \mathrm{e}^{\mathrm{i}\mathrm{Re}\{\Delta\beta\}z}\mathrm{e}^{-\beta_{\mathrm{im}}\left(z+\frac{L}{2}\right)}\mathrm{d}z = \frac{2\mathrm{e}^{-\frac{L}{2}\beta_{\mathrm{im}}}\sinh\left(\frac{L}{2}(\beta_{\mathrm{im}} - \mathrm{i}\mathrm{Re}\{\Delta\beta\})\right)}{\beta_{\mathrm{im}} - \mathrm{i}\mathrm{Re}\{\Delta\beta\}} \,. \tag{5.22}$$

The second exponential on the left-hand side of the equation (5.22) expresses the losses. When the phase-matching condition is satisfied, the peak photon pair generation rate occurs for $\Delta\beta = 0$. In this case, the integral (5.22) approaches $-\frac{\mathrm{e}^{-\beta_{\mathrm{im}}L}-1}{\beta_{\mathrm{im}}}$, which is analogous to formula (30) in [211].

In an experimental realisation, the number of photon pairs is determined via detection of created idler and signal photons [229]. A detected photon is *heralded* if the corresponding twin photon is detected as well [230, 231]. Coincidence measurements determine if the two created photons belong to one pair [232, 233]. An important measure for photon pair generation efficiency is the signal-to-noise ratio SNR $= \frac{c_a+c_p}{c_a}$, where c_a is the number of accidental coincidences and c_p is the number of coincidences due to correlated photons [228]. This efficiency may be affected by free carrier absorption and bending loss. Therefore, the quantum information application of generated photon pairs may be limited, as the heralding of photons may be inaccurate due to the loss of either the signal or idler photons [196, 234]. One way to reduce the bending loss is the proper choice of polarisation of the pump wave [207]. Another option is to choose a material characterised by low linear loss (bending loss). In the case of silicon [113] and silicon nitride the bending loss is almost negligible, in comparison to other materials. The guided mode is strongly confined to the waveguide core due to high index contrast [113]. The mode confinement is discussed in more detail in Section 5.7.

The last important consideration is the photon pair heralding efficiency, which quantifies the probability that if an idler photon was detected, the signal photon would also be detected (and vice versa). The presence of losses impairs the heralding efficiency because of the loss of either idler or signal photons from the pairs. The influence of absorption loss on heralding efficiency (HE) was studied in [197]. The HE is defined as the ratio between the coincidence-count rate and the single-photon-count rate. The simplified formula for the heralding efficiency HE, assuming negligible phase mismatch parameter $\Delta kL \approx 0$, is provided there as

$$\mathrm{HE} \approx \frac{(\alpha L)^2}{2(\mathrm{e}^{\alpha L} - \alpha L - 1)} \,, \tag{5.23}$$

where α is the absorption coefficient. Here, α is directly related to the attenuation, resulting from bending, so we put $\alpha = \beta_{\mathrm{im}}$. This choice is justified also by the derivation of the formula (5.23) in [197], compared to the considerations in Section 5.3. Equation (5.23) is used in Section 5.7 to compare the heralding efficiency for different waveguide structures and radii of curvature.

5.5. Description of the exemplary waveguides

This section describes the waveguides studied in this chapter. To maintain a general perspective, the selected waveguides are examples previously studied in the literature. These examples comprise waveguides made of different materials: silicon nitride (Si_3N_4) buried in silicon dioxide (SiO_2) [18, 235], silicon (Si) photonic wires [222], silicon on insulator (SOI) [112, 113, 221], aluminium gallium arsenide (AlGaAs) [26, 236] and a free-form waveguide [P2] made of IP-Dip photoresist (Nanoscribe GmbH) [237]. Free-form waveguides can be fabricated with three-dimensional additive manufacturing techniques [P1, 238], and cladded with a non-dispersive material of refractive index $n_{\text{cl}} = 1.36$. This is the configuration discussed also in Chapter 3. The waveguides being considered vary not only in their core and cladding materials but also in the sizes of their cores. All the investigated waveguide systems are summarised in Table 5.1.

Table 5.1.: Investigated materials of waveguide core and cladding, as well as core cross-section. The examples of IP-Dip, silicon nitride, silicon, silicon on insulator and aluminium gallium arsenide, investigated in more details later in this chapter, are highlighted with dark background.

core material	cladding material	core cross-section (w [µm]$\times$ h [µm])
IP-Dip	$n_{\text{cl}} = 1.36$	2.0×1.8
Si_3N_4	SiO_2	2.0×1.8
Si_3N_4	SiO_2	1.7×0.711
Si_3N_4	SiO_2	1.0×1.0
Si_3N_4	SiO_2	1.0×0.5
Si_3N_4	SiO_2	0.46×0.3
Si	SiO_2	2.0×1.8
Si	SiO_2	0.45×0.22
Si	air/SiO_2	1.0×0.32
Si	air/SiO_2	0.45×0.22
AlGaAs	SiO_2	2.0×1.8
AlGaAs	SiO_2	0.45×0.27

In practice, the choice of materials and dimensions depends mostly on available fabrication methods [18], material availability, as well as price and compatibility with other materials on a chip. Silicon is a widely used core material due to its high nonlinearity and ability to tightly confine light, owing to its high refractive index [18]. Moreover, the compatibility of silicon with CMOS technology offers the advantage of integrating electronics and photonics on the same chip [18]. However, a significant limitation of silicon is TPA. To address this issue, silicon nitride platforms have been developed, which help to reduce nonlinear losses at telecommunications wavelengths [18, 112]. Another approach to mitigate TPA is the use of gallium arsenide, with the addition of aluminium during the epitaxial growth to shift the band gap [26]. Although aluminium gallium arsenide is not a CMOS-compatible material, it is frequently reported in experimental studies due to its high nonlinearity and potential applications in all-optical networks [26]. Here, we study AlGaAs with 30 % of aluminium, based on data from [236].

In addition to highly nonlinear materials, we also present an example of a photonic wire-bond made of a polymer IP-Dip, characterised by weak nonlinearity and a relatively low refractive index. This combination of material properties facilitates the discussion of the trade-off between bending loss and the potential enhancement of the nonlinear effects. For each considered core material, we perform exemplary calculations for a cross-section measuring 2.0 µm×1.8 µm. Although this cross-section is mentioned only in the literature concerning IP-Dip, we chose this cross-section as common basis for all the studied materials to be able to compare them directly, and remain consistent with the free-form waveguides studied in Chapter 3 and Chapter 4.

5.6. Details of numerical simulations

This section outlines the computational procedure to calculate the photon pair generation rate as a function of radius of curvature for each structure from Table 5.1. We begin by determining the supported waveguide modes with the use of Ansys Lumerical [85]. To numerically calculate the modes, the computational domain is limited to the waveguide cladding of dimensions three times bigger than the core width. The core is immersed in the middle of the cladding. The finite difference eigenmode (FDE) simulation region is limited to 1.2 times the cladding width. To consider also radiation loss in bent waveguides, the perfectly matched layers (PML) are placed at the boundaries of the computational domain $\mathcal{D}$. The PML are implemented as an absorbing material to minimise reflections [85]. As the result of mode computation, the TE-polarised electric field of the fundamental mode, effective refractive index, effective area, loss, and group velocity of that fundamental mode are stored and used for further calculations.

The modes are determined, while changing two parameters. First, we consider different radii of curvature from 4 µm to 100 µm, with the bending defined in the width direction (cf. Figure 5.3). Moreover, the modes are computed for wavelengths ranging from 1510 nm to 1600 nm, with 5 nm step. This range includes the common telecommunication wavelength 1550 nm. The limits of the wavelength range result from the difficulty in finding propagating modes for certain materials and cross-sections for wavelengths outside this range, particularly for smaller bending radii. The minimum radius of curvature 4 µm was selected to ensure that the centre of curvature remains outside the simulation region for all the considered waveguide cross-sections. The smallest radius of curvature is feasible because it was shown experimentally in several studies [113, 207, 239, 240] that silicon-based waveguide bends can be fabricated with a radius of curvature as small as 3 µm. The exception is IP-Dip, for which the software cannot find modes for radii of curvature smaller than 6 µm, for the applied settings. The maximum radius of curvature is limited to 100 µm because for this radius of curvature all the results approach a straight waveguide. The modes are calculated also for a straight waveguide for the same wavelength range, as a reference.

For silicon, silica, and silicon nitride, the refractive index values at the considered wavelengths were calculated from the Sellmeier equation [241, 242], with the parameters obtained by fitting the sample data points from the Ansys Lumerical database. In the case of IP-Dip, the refractive index values were similarly fitted using sample data from [237]. To perform analogous fitting for AlGaAs, the sample data were obtained from [243], based on [244]. The air and the cladding of the IP-Dip waveguide are considered non-dispersive. The values and formulas for the components of the third-order susceptibility tensor were taken from [185]. The local phase and group velocities were calculated using equations (68) and (69) from [193]. The obtained values are presented in Appendix B.

The nonlinear coefficients are calculated using equation (5.16) for each combination of pump, signal, and idler wavelengths from the precomputed modes, employing the formula for the effective area (5.14). The highest value of γ_{SFWM}, obtained for $\omega_{\mathrm{S}} = \omega_{\mathrm{I}} = \omega_{\mathrm{P}} \approx 193.42 \cdot 2\pi$ THz, corresponding to the wavelength $\lambda = 1.55$ µm, is selected to compare different waveguides. This nonlinear coefficient is then used to compute $M(\omega_{\mathrm{S}}, \omega_{\mathrm{I}})$ from equation (5.18) for each combination of pump, signal, and idler wavelengths from the precomputed set of modes.

The photon pair generation rate is determined using equation (5.6) for each pump wavelength from the previously specified range. In computational practice, this range contains only a limited set of discrete wavelengths, therefore the delta function is modelled with a Gaussian distribution as

$$\delta(\Delta\omega) = \frac{1}{\sqrt{\pi a^2}} \mathrm{e}^{-\frac{(\Delta\omega)^2}{a^2}}, \tag{5.24}$$

with the parameter a determined empirically to be $a = 10^{12}$ Hz. The photon pair generation rate is calculated for the pump power 100 mW applied to a waveguide of length 15.7 µm. This length corresponds to a 90° arc with radius 10 µm. For the purpose of comparing photon pair generation rates in different waveguides, the pump wavelength is fixed at 1550 nm, and only the signal and idler photons are considered to be generated across the available spectral domain. The integrals in equation (5.6) are evaluated numerically over the predefined range. The results of calculations are presented in the next section.

5.7. Influence of bending on photon pair generation rate

This section presents the outcome of the calculations for the examples listed in Table 5.1. We begin by depicting $M(\omega_{\mathrm{S}}, \omega_{\mathrm{I}})$ from equation (5.18) for a straight, silicon nitride waveguide. We show its dependency on the signal and idler wavelengths. Subsequently, we discuss in detail one of the most efficient examples in this study, namely the silicon nitride waveguide with a cross-section of 1.7 µm × 0.711 µm. Its loss is compared to the nonlinear coefficient as a function of radius of curvature. It is also observed that the photon pair generation rate changes with the radius of curvature. This observation is supplemented with a brief discussion of the relation between the bending and the length of the waveguide. Further, the same study is performed on the least efficient example, IP-Dip waveguide with a cross-section of 2.0 µm ×1.8 µm. This example demonstrates additional effects difficult to observe in the other, almost lossless structures. Later, we analyse and compare different features influencing photon pair generation rate, based on the studied waveguides. A discussion including physical interpretation follows. Finally, the results are summarised in Table 5.2.

Figure 5.4 illustrates the dependence of the absolute value of the quantity $M(\omega_{\mathrm{S}}, \omega_{\mathrm{I}})$ on the idler and signal wavelengths for a selected pump wavelength. The values are computed for straight silicon nitride waveguide of cross-section 1.7 µm × 0.711 µm and length 15.7 µm. Local maxima are observed for signal and idler wavelengths that correspond to modes satisfying the phase-matching condition. For the purpose of the plot in Figure 5.4, the modes in a straight waveguide and the quantity $M(\omega_\mathrm{S}, \omega_\mathrm{I})$ are calculated for the wavelength ranging from 1.3 µm to 1.8 µm. For bent waveguides discussed in the following subsections, a narrower wavelength range was selected due to potential convergence issues in the mode-finding software for small radii and wavelengths significantly different from the central wavelength of 1.55 µm.

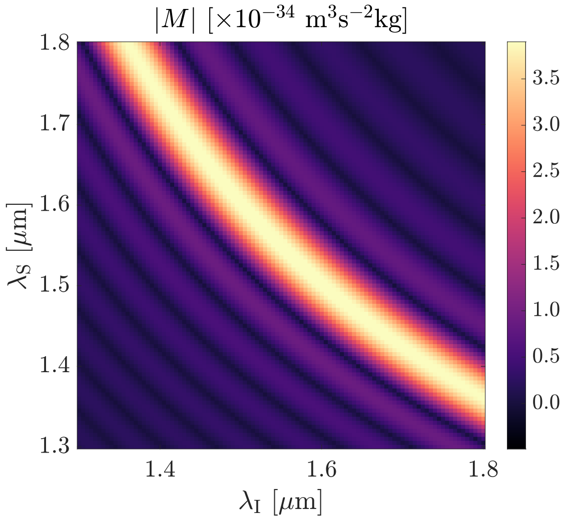

Figure 5.4: The absolute value of $M(\omega_\mathrm{S}, \omega_\mathrm{I})$ from equation (5.18) for a straight waveguide with a silicon nitride core in a silica cladding, at pump wavelength 1.55 µm, for various combinations of idler and signal wavelengths. The colorbar has been adjusted to enhance the visibility of local maxima, despite all values in the image being positive. Figure is reprinted from [P3]. Copyright © 2011 by American Physical Society.

5.7.1. Study of silicon nitride waveguides

The first studied example is silicon nitride in silica cladding, which is a widely used material platform for photonic integrated circuits. In case of silicon nitride, the bending loss is minimal, and the effective nonlinearity increases with increasing curvature.[4] These two relationships are presented in Figure 5.5. While both the nonlinear coefficient γ_SFWM and the bending loss increase as the radius of curvature decreases, the gain in nonlinearity is significantly higher and becomes apparent even for curvatures with minor bending losses.

As a result of the increasing nonlinearity, the photon pair generation rate increases for more strongly bent waveguides, as shown in Figure 5.6(a). To calculate the values for the plot in Figure 5.6(a), the arc length is fixed and only the curvature changes. It is evident that bending the waveguide is advantageous in terms of photon pair generation rate. For example, in the case of 4 µm bending radius, the photon pair generation rate nearly doubles compared to the straight waveguide. Among the various factors influencing the photon pair generation rate, we observe that the effective nonlinearity increases as the radius of curvature decreases, which significantly enhances the efficiency of nonlinear processes. This is further explained by the tighter localisation of the mode in the curved waveguide. The increase in losses does not significantly diminish the photon pair generation rate in silicon

---

[4] Curvature is defined as the inverse of radius of curvature. Increasing the curvature means decreasing the radius of curvature.

nitride. However, it is important to note that the bending loss becomes more prominent for very small radii of curvature. This functional dependency is more apparent in waveguide examples where the modes are not well localised, as demonstrated in the following example of the IP-Dip waveguide.

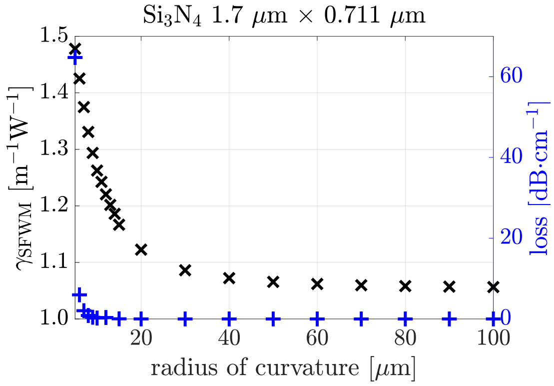

Figure 5.5: Nonlinear coefficient (black "x") and loss (blue "+") as a function of the radius of curvature for silicon nitride core 1.7 µm × 0.711 µm in silica cladding, at pump wavelength 1.55 µm. Both the nonlinear coefficient and the loss increase with decreasing radius of curvature, but at different rates. Figure is reprinted from [P3]. Copyright © 2011 by American Physical Society.

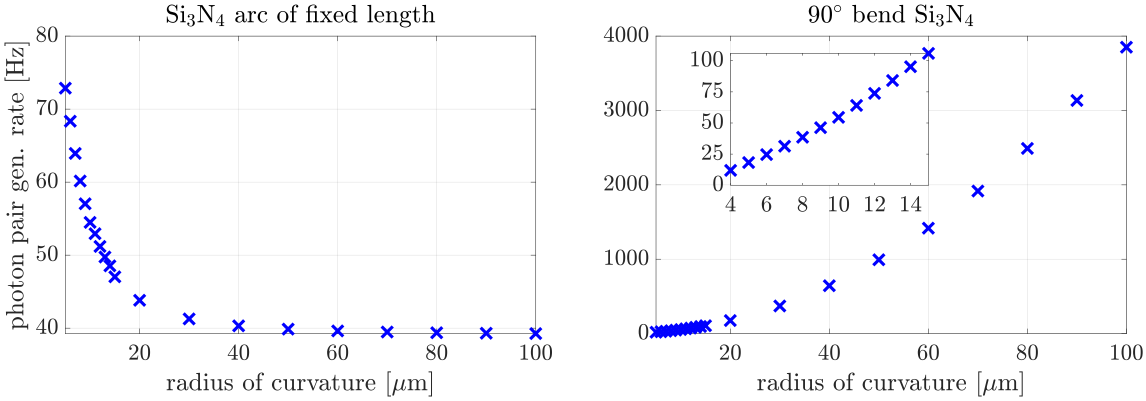

(a)

(b)

Figure 5.6.: Photon pair generation rate as a function of the radius of curvature for a silicon nitride waveguide 1.7 µm × 0.711 µm core in silicon dioxide cladding at a pump wavelength 1.55 µm. (a) The photon pair generation rate increases with decreasing radius of curvature for an arc with fixed length, equal to 15.7 µm. (b) The photon pair generation rate increases with increasing radius of curvature for 90° bow because the propagation length increases. The inset provides a detailed view of the change in photon pair generation rate for radii of curvature between 4 µm and 15 µm. Figure is reprinted from [P3]. Copyright © 2011 by American Physical Society.

It is important to note that the photon pair generation rate can be trivially enhanced by extending the length of the waveguides. This is illustrated in Figure 5.6(b), showing photon pair generation rate as a function of radius of curvature in an arc with angle 90°. In this case, increasing the radius of curvature makes the waveguide longer. In consequence the photon pair generation rate increases because it is proportional to the square of the waveguide length, cf. equation (5.19). The difference between the two possible waveguide transformations is explained graphically in Figure 5.7.

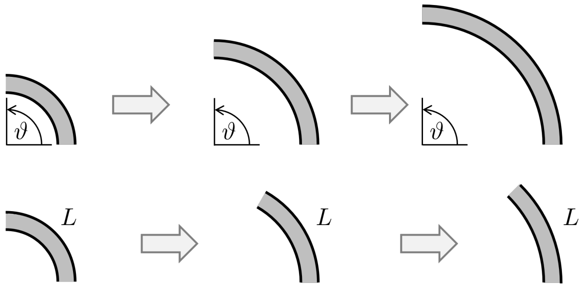

Figure 5.7: Examples of two approaches to increase the radius of curvature of a waveguide bend. In the upper row, the radius of curvature increases while keeping the constant angle of the arc ϑ. In the bottom row, the radius of curvature increases, but the waveguide length L remains constant. Adapted from [P3]. Copyright © 2011 by American Physical Society.

Given the limited space on chips in future generations of highly integrated photonic circuits, the waveguides cannot be arbitrarily long. Therefore, it is essential to consider which waveguide maximises the photon pair generation rate for a given waveguide length. By comparing plots in Figure 5.6(a) and Figure 5.6(b), one can conclude that the same generation rate achieved by 90° bows of radii of curvature between 10 µm and 15 µm can be attained with a shorter, 15.7 µm long arc of smaller radius of curvature, below 10 µm. This approach reduces the space required on the photonic integrated circuit. To conclude, regardless of the chosen length, incorporating curvature as a design feature always enhances the photon pair generation rate in silicon nitride waveguides.

Bending a waveguide can possibly increase the photon pair generation rate without increasing the length of a waveguide. Figure 5.8 shows the elongation of a straight waveguide that results in the same photon pair generation rate as bending. It can be observed, for example, that a 15.7 µm long arc of radius of curvature 10 µm is equivalent to 20 % longer straight waveguide in terms of photon pair generation rate. For sharp bends, of radius of curvature below 5 µm, the corresponding straight waveguide is almost 1.5 times longer. This fact can be used to increase the compactness of the waveguide structures in the photonic integrated circuits.

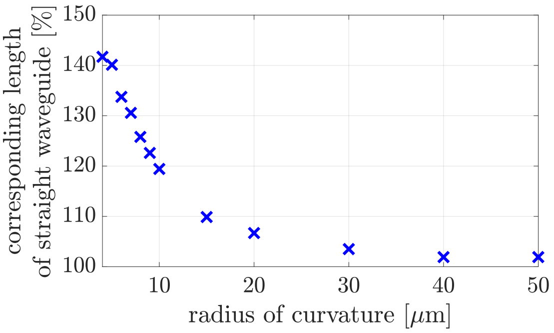

Figure 5.8: The fraction of the length of a straight waveguide to the corresponding length of a bent waveguide, resulting in the same photon pair generation rate. The values were calculated for silicon nitride bends of length 15.7 µm and core cross-section 1.7 µm × 0.711 µm. Figure is reprinted from [P3]. Copyright © 2011 by American Physical Society.

5.7.2. Study of IP-Dip waveguides

An analogous analysis to the previous subsection can be described for the weakly nonlinear material IP-Dip. Figure 5.9 presents the change in nonlinear coefficient and loss of a waveguide made of IP-Dip, with core size 2.0 µm × 1.8 µm. As shown in Figure 5.9, the small nonlinear coefficient increases slightly with bending, while the losses become substantial for a radius of curvature of 40 µm and rise dramatically with further decrease in radius of curvature. For this core material, the bending loss significantly influences photon pair generation, as illustrated in Figure 5.10.

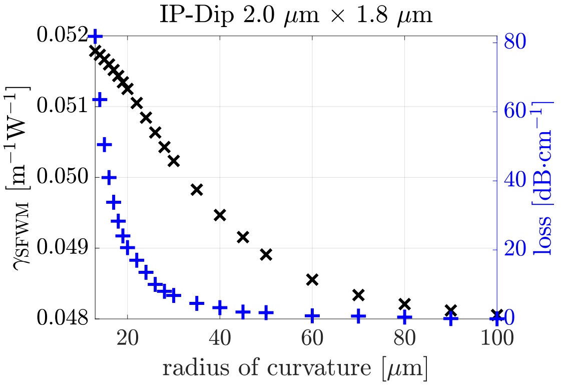

Figure 5.9: Nonlinear coefficient (black “x”) and loss (blue “+”) as a function of the radius of curvature for IP-Dip of 2.0 µm × 1.8 µm core, at pump wavelength 1.55 µm. Both the nonlinear coefficient and the loss increase with decreasing radius of curvature but at different rates. Figure is reprinted from [P3]. Copyright © 2011 by American Physical Society.

Figure 5.10 illustrates the change of the photon pair generation rate as a function of the radius of curvature, for arcs of the same length 15.7 µm. Since the generation rate depends on the propagation length, the study of IP-Dip focuses only on the influence of bending on the photon pair generation rate. The results presented in Figure 5.10 indicate that the generation rate increases with increasing radius of curvature up to 36 µm, after which a slight decline is observed. It is evident that for small bending radii, the generation rate is reduced by the radiation loss. For bigger radii of curvature, the generation rate decreases and approaches the limiting value for a straight waveguide due to the decrease in the nonlinear coefficient, as previously shown in Figure 5.9. The peak at radius of curvature around 36 µm results from the trade-off between increasing losses and increasing nonlinearity.

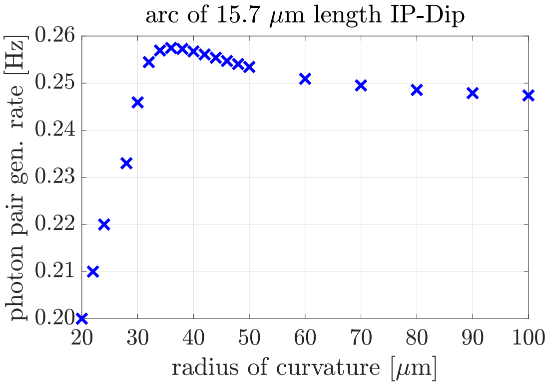

Figure 5.10: The photon pair generation rate at pump wavelength 1.55 µm as a function of the radius of curvature for free-form waveguide fabricated with IP-Dip photoresist. By balancing the increased nonlinearity and losses, it is possible to determine the optimal radius of curvature resulting in the maximum generation rate. Figure is reprinted from [P3]. Copyright © 2011 by American Physical Society.

In the case of IP-Dip, it is also possible to reduce the waveguide length by introducing bending. Figure 5.11 shows the change of the length of a straight waveguide as a function of radius of curvature of a bend corresponding to the same photon pair generation rate without changing length. Although the length of a corresponding straight waveguide increases with decreasing radius of curvature, the required length modification is very small and does not exceed 10 %. This is a lower increment compared to the previously considered silicon nitride waveguide, due to the losses induced by bending of IP-Dip waveguide.

In Figure 5.10 only a small enhancement of the photon pair generation due to a bending in very short waveguides of 15.7 µm is observed. Figure 5.12(a) presents the anticipated

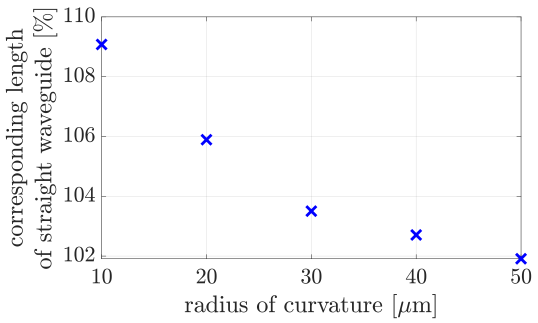

Figure 5.11: The fraction of the length of a straight waveguide that is equivalent to a bent waveguide resulting in the same photon pair generation rate, as a function of radius of curvature of that bent waveguide. The values are calculated for IP-Dip bends of length 15.7 µm and core cross-section 2.0 µm × 1.8 µm. Figure is reprinted from [P3]. Copyright © 2011 by American Physical Society.

maximum increase in photon pair generation rate as a function of waveguide length. Obviously, the generation rate increases with the length of a waveguide. Figure 5.12(b) shows the corresponding radius of curvature for which the peak photon pair generation rate is achieved. It appears that this optimal radius of curvature depends on the interaction length within the waveguide. The optimal radius of curvature increases with the interaction length. The propagation loss accumulates along the bent waveguide. When the waveguide is longer, the loss is higher, therefore, the radius of curvature needs to be increased to reduce the propagation loss.

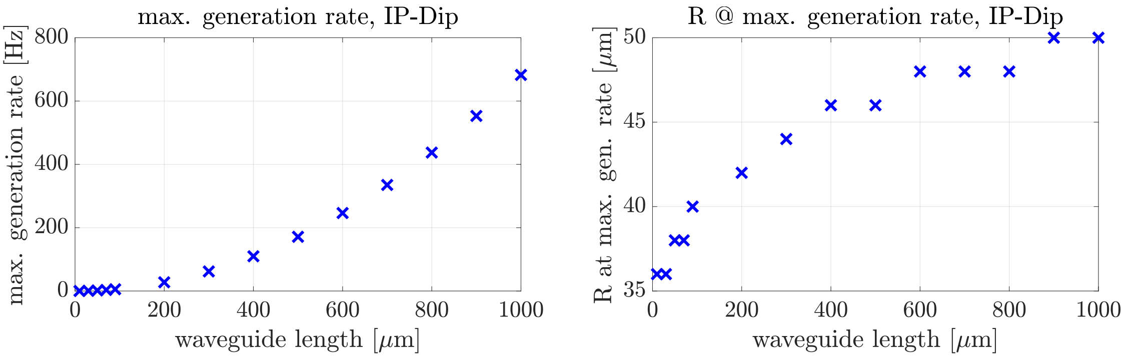

(a) (b)

Figure 5.12.: (a) Maximum photon pair generation rate in IP-Dip as a function of the waveguide length. (b) Radius of curvature, for which the maximum generation rate is attained as a function of IP-Dip waveguide length. Figure is reprinted from [P3]. Copyright © 2011 by American Physical Society.

In the following subsection, we discuss in detail the possible physical reasons for increasing photon pair generation rate in bent waveguides made of different materials and cross-sections.

5.7.3. Comparison of exemplary waveguides and discussion

This subsection discusses the potential factors contributing to the enhancement of the nonlinearity. The effects of effective mode area, effective refractive index, group velocity of the mode, and loss induced by bending are considered. The discussion concludes with a table that presents numerical values for the generation rates of all examples studied in this chapter. Afterwards, the heralding efficiency is analysed.

Figure 5.13 illustrates the mode profiles of the real part of the x-component of the electric field on the waveguide cross-section. The field is normalised to the maximum value in a straight waveguide for the same material and cross-section. The corresponding effective areas of the modes are displayed above each profile. The upper row contains the cross-section of 1.7 µm × 0.711 µm silicon nitride, while the lower row presents the field profiles for 2.0 µm × 1.8 µm IP-Dip. The profiles in different columns are plotted for different radii of curvature, indicated above each subplot. In the case of silicon nitride, increasing the curvature enhances the confinement of the electromagnetic field within the core, resulting in a reduced effective area for the mode guided in the waveguide. The field distribution within a waveguide is typically concentrated near the outer side of the waveguide bend, which effectively *squeezes* the mode profile. Consequently, the effective area of that mode decreases. However, if the radius of curvature becomes too small, the field can leak into the cladding, resulting in increased radiation loss. This effect can be observed in the case of IP-Dip, where the effective area for radius of curvature 40 µm is smaller than for a straight

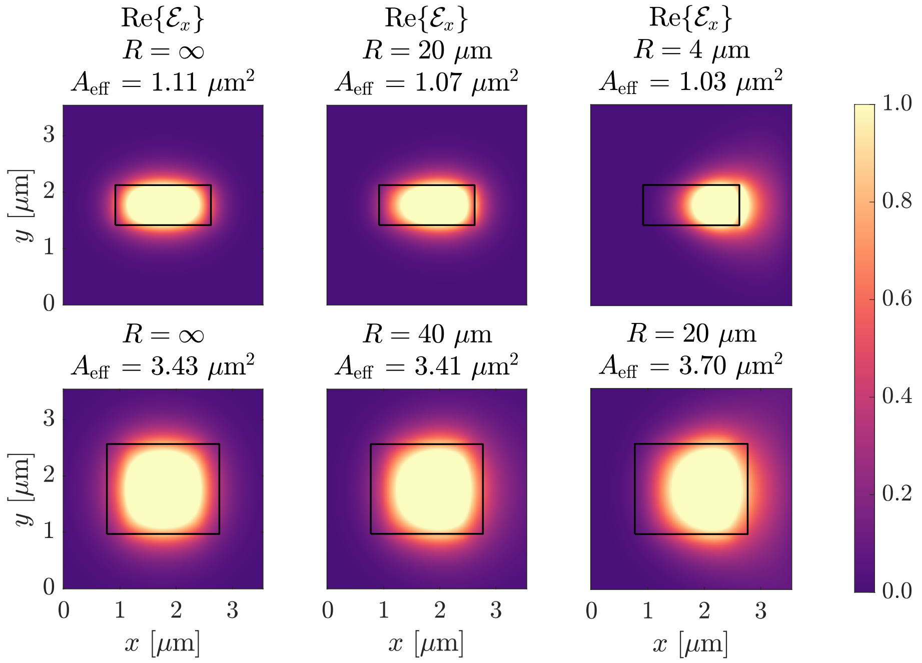

Figure 5.13.: Mode profiles of the real part of the x-component of the normalised electric field of the fundamental mode obtained with Ansys Lumerical. The top row shows the fields in the waveguide cross-section for 1.7 µm × 0.711 µm silicon nitride, while the bottom row depicts 2.0 µm × 1.8 µm IP-Dip. Each column represents mode profiles for different radii of curvature of a waveguide bent along x-axis. All fields are normalised to the maximum amplitude of the fundamental mode of the straight waveguide made of the particular material. The contour of the waveguide core is illustrated as a black rectangle in scale. Although the computational domain varies with the core size, the cladding is kept the same size for plotting purposes. For silicon nitride, the effective area of the mode decreases as the waveguide bends. In contrast, for the IP-Dip waveguide, the effective area reaches its minimum at a radius of curvature 40 µm and then increases due to mode leakage from the core to the cladding. Figure is adapted from [P3]. Copyright © 2011 by American Physical Society.

waveguide but increases for $R = 20\,\mu\mathrm{m}$ because a greater fraction of the field is localised in the cladding. The reduction in effective area leads to an increase in the nonlinear coefficient γ_{SFWM}, as demonstrated in equation (5.16).

Figure 5.14(a) shows the explicit dependence of the effective mode area on the radius of curvature for silicon nitride, IP-Dip, and also silicon on insulator for completeness, since it is the third material we study. Aluminium gallium arsenide is not included in this plot because it exhibits a similar behaviour as silicon on insulator. Note that for both silicon nitride and IP-Dip, it is possible to identify the radius of curvature at which the effective area of the guided mode is minimised. In contrast, the effective area of the mode in the case of silicon remains nearly independent of the radius of curvature.

Figure 5.14(b) shows the change in loss in the waveguide as a function of radius of curvature. The two plots placed next to each other let one compare the change in effective area to the change in loss. In the case of IP-Dip, the effective area decreases for radii of curvature smaller than 40 µm, reaching a minimum around 20 µm. For larger curvatures (smaller radii of curvature), the mode radiates into the cladding, resulting in an increased effective area. This effect is evident in Figure 5.14(b), where the loss begins to rise significantly for radii of curvature smaller than 30 µm. Therefore, the optimal radius of curvature is expected to be between 20 µm and 40 µm, as previously indicated in Figure 5.10 and Figure 5.12(b). A similar tendency is observed for silicon nitride. However, the mode with the minimal effective area occurs at smaller radii, and the loss is much lower, and increases only for radii of curvature smaller than 8 µm.

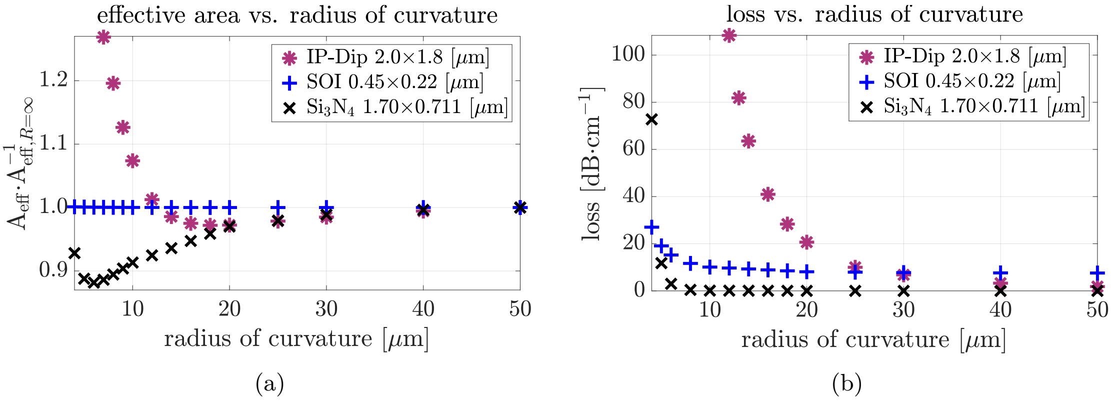

Figure 5.14.: (a) Effective area of the mode as a function of radius of curvature for IP-Dip, silicon on insulator and silicon nitride. (b) Propagation loss as a function of the radius of curvature. The values are obtained with Ansys Lumerical. The legend shows the materials and core cross-sections selected for the comparison. The values of the effective mode area are normalised to the corresponding values of a straight waveguide. Figure is reprinted from [P3]. Copyright © 2011 by American Physical Society.

In contrast, silicon exhibits different behaviour – its loss increases without a significant gain in the effective area of the mode. This situation leads to a decline in the photon pair generation rate, as presented in Table 5.2. This table summarises the values of nonlinear coefficients and generation rates for the structures studied in this chapter.

When comparing Figure 5.14(a) to the previously shown Figure 5.6(a) and Figure 5.10, which depict photon pair generation rates, it becomes clear that the optimal radius of curvature for generating photon pairs differs from the radius at which the effective area reaches its minimum. This observation suggests that the maximum photon pair generation rate is influenced by additional factors such as the effective refractive index of the mode and the group velocity, both of which also affect the nonlinearity of the waveguide. The dependence of these additional parameters on the radius of curvature is studied in the following.

Variation in the radius of curvature affects the propagation constant of the fundamental mode, which in turn alters the effective refractive index n_{eff} of the waveguide. The effective refractive index is defined as $n_{\text{eff}}(R) = \beta(R)\frac{\lambda_0}{2\pi}$, where λ_0 represents the wavelength in vacuum. Figure 5.15(a) illustrates how the real part of the effective refractive index varies with the radius of curvature for four different materials. For IP-Dip and silicon nitride waveguides, the real part of the effective refractive index increases as the waveguide is bent, whereas it remains constant for silicon and AlGaAs. This change is relevant for phase-matching, because the dispersion relation for certain materials may shift. Therefore, it is crucial to select a radius of curvature for which the corresponding propagation constants satisfy the phase-matching condition, or additionally compensate for the phase shift. The relation between the curvature and propagation constant can be exploited regarding birefringence of the core material, as bending in a specific direction may facilitate phase matching.

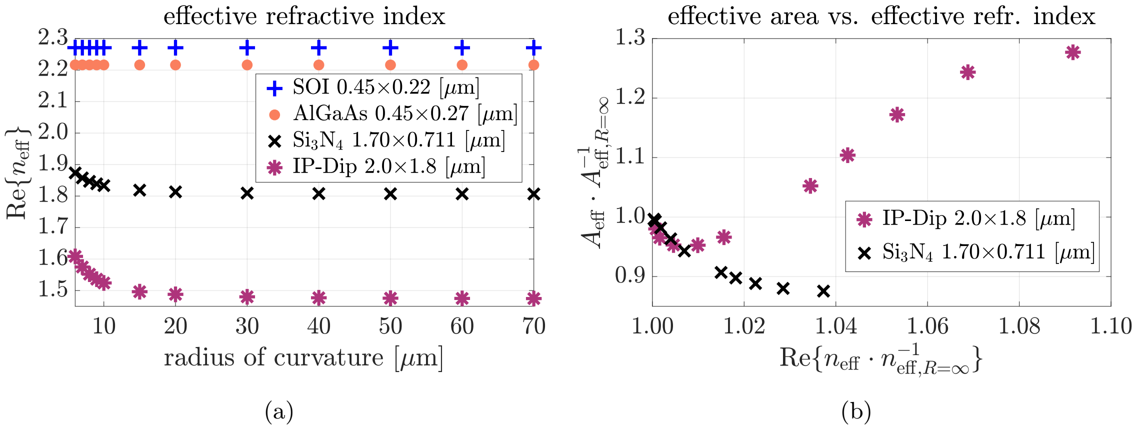

(a) (b)

Figure 5.15.: (a) Real part of the effective refractive index of the fundamental mode as a function of radius of curvature for silicon on insulator, aluminium gallium arsenide, silicon nitride and IP-Dip, at a wavelength of 1.55 µm. Waveguide made of different materials are characterised by different cross-section sizes, indicated in the legend. (b) The effective area of the fundamental mode as a function of the real part of the effective refractive index of silicon nitride and IP-Dip. The parameters are normalised to their respective values for a straight waveguide. Figure is reprinted from [P3]. Copyright © 2011 by American Physical Society.

In addition to examining how the effective area and effective refractive index of the fundamental mode change with the radius of curvature, one also analyses the direct relationship between these two parameters, as shown in Figure 5.15(b). This figure presents the normalised effective area of the fundamental mode in IP-Dip and Si_3N_4 as a function of normalised effective refractive index. For silicon nitride, the effective area decreases as the effective refractive index increases, confirming a connection between the effective refractive index and the mode's confinement within the waveguide core. However, in the case of IP-Dip, even though the effective refractive index continues to rise with increased curvature, the effective area initially decreases and then increases again after reaching a minimum. This behaviour is attributed to the mode radiating into the cladding.

Another parameter affecting the photon pair generation rate is the group velocity of the mode. This expectation is justified by equations (5.6) and (5.19). Figure 5.16 illustrates the variation of the group velocity with changing radius of curvature of the four selected waveguides. Some materials, such as silicon nitride and IP-Dip, show a strong dependence of group velocity on the radius of curvature. The group velocity decreases as the radius of curvature becomes smaller, leading to an increase in photon pair generation rate. The decline in the group velocity with decreasing radius of curvature can be also observed for SOI and AlGaAs, however, the change is minimal. As a result, the photon pair generation rate does not vary significantly with changes in the radius of curvature of 0.45 µm × 0.22 µm SOI or 0.45 µm × 0.27 µm AlGaAs. Also, the effective mode area for these waveguides remains effectively unchanged in Figure 5.14(a), related to equation (5.14).

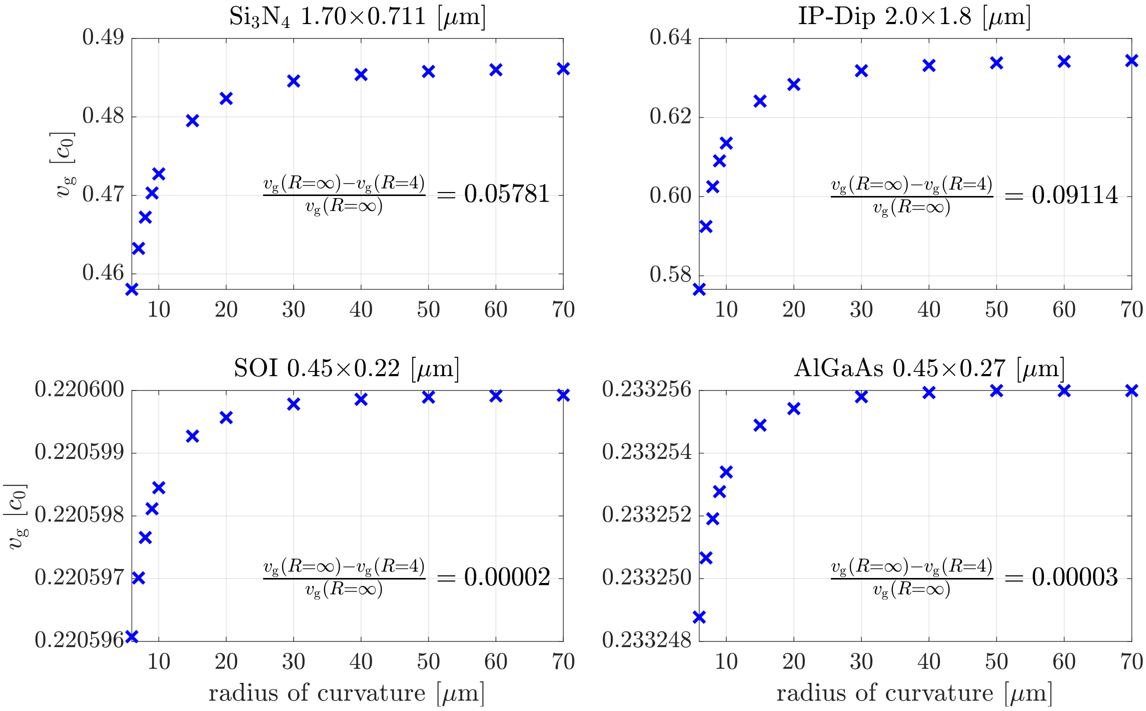

Figure 5.16.: Group velocity of a fundamental mode as a function of radius of curvature, for wavelength $\lambda = 1.55$ µm, represented as a multiple of speed of light in vacuum, c_0. Each plot shows the group velocity for different exemplary material together with the relative change of group velocity between the straight waveguide and bent waveguide of a radius of curvature of 4 µm. Figure is reprinted from [P3]. Copyright © 2011 by American Physical Society.

Table 5.2 presents the results of calculating the nonlinear coefficients and the generation rate, along with the potential increment in the generation rate with respect to the generation rate in the straight waveguide, and the radius of curvature at which this increment can be achieved. The nonlinearity varies based on the materials of the core and cladding, as well as the dimensions of the waveguide's cross-section. In highly nonlinear structures with very small cross-sections for which $\gamma_{\mathrm{SFWM}} > 100\,(\mathrm{W\,m})^{-1}$, increasing nonlinearity is challenging because the light is already tightly confined within the waveguide core, and this confinement does not significantly change with bending. As the dimensions of the core increase, the increment in the photon pair generation rate can range from 5 % for IP-Dip to 210 % for AlGaAs. Larger silicon nitride cores lead to enhancement in the photon pair generation rate up to 150 %. The increase in nonlinearity for Si_3N_4, silicon, and AlGaAs is significantly higher compared to the gain from the weakly nonlinear material, IP-Dip, with the same cross-section.

Table 5.2.: Results of calculation of nonlinear coefficients γ_{SFWM} and photon pair generation rates for chosen waveguides, for pump wavelength 1.55 µm.

Waveguide type[a]	$\gamma_{\mathrm{SFWM,min}}$[b]	$\gamma_{\mathrm{SFWM,max}}$[b]	generation rate[c]	increment[d]	peak radius[e]
IP-Dip 2.0 × 1.8	0.048	0.052	0.25	5	36
Si_3N_4 2.0 × 1.8	0.33	0.53	4	150	7
Si_3N_4 1.7 × 0.711	1.06	1.51	40	90	4
Si_3N_4 1.0 × 1.0	0.79	0.95	21	45	5
Si_3N_4 1.0 × 0.5	–	1.64	90	–	∞
Si_3N_4 0.46 × 0.3	–	0.33	6	–	∞
Si 2.0 × 1.8	6.83	18.57	10^3	172	4
Si 0.45 × 0.22	–	116.80	10^5	–	∞
SOI 1.0 × 0.32	52.57	62.38	10^4	40	4
SOI 0.45 × 0.22	142	142	10^5	< 0.02	4
AlGaAs 2.0 × 1.8	35.6	100.1	10^4	210	4
AlGaAs 0.45 × 0.27	687.8	687.9	10^7	< 0.02	5

[a] described by core material followed by cross-section size in µm × µm.

[b] values given in $(\mathrm{W\,m})^{-1}$.

[c] generation rate $\mathcal{R}$ in Hz, for straight waveguide of length 15.7 µm and pump power 100 mW.

[d] increment of $\mathcal{R}$ in % with respect to a straight waveguide, defined as $\frac{\mathcal{R}_{\max}-\mathcal{R}_{R=\infty}}{\mathcal{R}_{R=\infty}} \times 100\,\%$.

[e] radius of curvature in µm for which the maximum generation rate was achieved numerically.

When the losses outweigh the mode confinement, the generation rate decreases with increasing curvature. The generation rate enhancement effect may not be observed due to insufficient mode confinement to the core. The effective area of the mode increases, as the radius of curvature decreases, which reduces the nonlinear coefficient γ_{SFWM}. In this case, it is possible to identify the radius of curvature at which the photon pair generation rate is maximised, cf. Figure 5.10.

Table 5.2 indicates that both nonlinearity and the photon pair generation rate depend on the core size. In particular, for a given core height, an optimal core width can be identified to enhance nonlinearity. However, in practice, the choice of dimensions and materials primarily depends on their availability and the fabrication methods that can be employed. Therefore, it may not always be possible to fabricate the most optimal cross-section in terms of photon pair generation rate. The study in this chapter demonstrates that bending can improve the nonlinearity if the choice of the cross-section is constrained, or a waveguide with lower nonlinearity is considered in certain experiments.

The final aspect considered in this section, is the heralding efficiency (HE), which is expressed using the formula (5.23). The HE is calculated for exemplary SOI, Si_3N_4, AlGaAs, and IP-Dip waveguides, taking the imaginary part of the propagation constant as α. Figure 5.17 presents the resulting HE as a function of the radius of curvature. The minimum radius of curvature in the plot is 5 µm for clarity, as the heralding efficiency drops below 0.8 for smaller radii of curvature. The HE of silicon starts at 0.958 for a radius of curvature of 5 µm, while for silicon nitride, it is higher and equals 0.998. AlGaAs is characterised by HE = 0.963 for a radius of curvature 6 µm. The photoresist IP-Dip only exceeds a heralding efficiency of 0.98 for bending radii greater than 18 µm. Comparing Figure 5.10 and Figure 5.17 shows that the maximum photon pair generation rate for IP-Dip occurs for the radius of curvature with high heralding efficiency. Similarly in the case of silicon nitride, the photon pair generation rate can be increased without drop in HE. Depending on the desired heralding efficiency in an experiment, an appropriate radius of curvature can be selected for waveguide design.

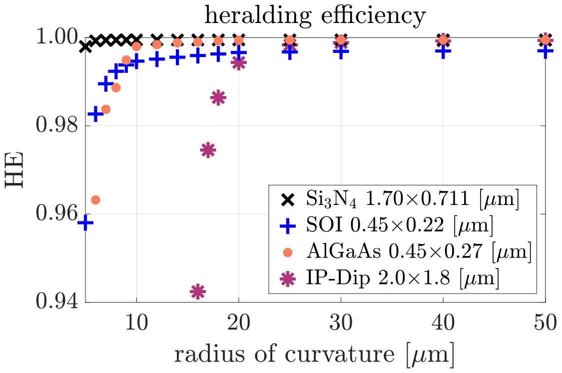

Figure 5.17: Heralding efficiency for different materials and cross-sections as a function of radii of curvature between 5 µm and 50 µm. The values are calculated for interaction length 15.7 µm and pump wavelength 1.55 µm. Figure is reprinted from [P3]. Copyright © 2011 by American Physical Society.

5.8. Summary and conclusions

In this chapter, we have examined the influence of varying waveguide curvature on effective nonlinearity and photon pair generation rate in the bent waveguides. We studied how the photon pair generation rate in the spontaneous four-wave mixing (SFWM) process changes with increasing waveguide curvature. The SFWM process has been selected because it is significant for technology as it is used to generate quantum states of light, which serve as sources for on-chip quantum devices. Since SFWM is a third-order nonlinear process, the third-order strongly nonlinear materials such as silicon nitride, silicon, and aluminium gallium arsenide have been studied in this chapter. Their performance was compared to that of the weakly nonlinear material IP-Dip, which was studied in the previous chapters. It was shown that increasing the curvature of the waveguide enhances the mode confinement in the waveguide core, thereby reducing the effective area of the mode and consequently increasing the nonlinear coefficient. Moreover, the group velocity of the mode decreases as the waveguide bends. These effects contribute to an increase in the photon pair generation rate. This enhancement of nonlinearity and the photon pair generation rate due to bending is particularly pronounced in waveguides with larger core cross-sections.

However, decreasing the radius of curvature also increases propagation losses. Depending on the rate of change of both the losses and the nonlinearity, as a function of radius of curvature, it is possible to identify an optimal radius of curvature for maximising the photon pair generation rate. This optimal radius of curvature can depend on the interaction length, which is an important factor to consider during waveguide design. Due to the possible loss of photon pairs, the required heralding efficiency becomes an important consideration for experimental setups. Bending changes the effective refractive index of the modes, which affects the phase-matching, an essential condition for operation of nonlinear devices.

Bending the waveguide offers an advantage in terms of confining guided modes. This spatial confinement strengthens the nonlinear interaction and can reduce interaction lengths in the waveguides. As a result, the increase in photon pair generation rate can be achieved through bending rather than elongating the waveguides. In this chapter, the photon pair generation enhancement was demonstrated for very short waveguides. In practical situations where longer waveguides are fabricated, the spatial gain may be significantly greater, provided that the radius of curvature remains within the low-loss range.

The next chapter is devoted to mode interactions in whispering gallery resonators (WGRs). Among many applications, WGRs are used as the sources of quantum states of light, ring couplers between waveguides, or amplifiers of optical waves. Therefore, an example of a WGR is included as part of this doctoral research, and the results are presented in the following chapter.

6 | Identifying interacting modes in whispering gallery resonators

The on-chip generation of entangled photon pairs, discussed in the previous chapter, often requires photon collection and routing, which can be achieved by using microcavities coupled to channel waveguides [245]. Depending on the chip design and fabrication facility, these microcavities take the form of ring or disk resonators [246]. To design and fine-tune the resonators, it is required to understand the nature of the ring or disk structures, in particular their eigenmodes [247]. Here, we analyse the interaction of modes in disk-shaped whispering gallery resonators (WGRs), using some of the concepts already discussed in the previous chapters. In particular, the modes in a WGR correspond to the modes in a curved waveguide with a constant radius of curvature. The modes are no longer purely guided, but they tend to radiate into the far field which poses challenges in capturing their properties. However, by applying methods presented in the previous chapters and incorporating new contributions described here, we can explore the modal properties of the resonators in depth.

This study was inspired by the work of M.Sc. Lukas Rebholz and Dr. Simon Woska *et al.* [248–250]. In this specific setting, the WGRs take the form of cylindrical disks with a finite thickness. The authors noted that with varying thickness of the disk, the mode profiles of some modes deform and cannot be separated into independent radial and axial components. The authors identified a mode coupling by overlapping field profiles and avoided crossings of the modes' resonance frequencies. The identification of the interaction between the modes was based on the symmetries of the field profiles of the modes. Here, this analysis is continued, and we investigate the orthogonality of the fields radiated by the modes with a suitable scalar product. The material contained in this chapter is a result of a close collaboration with M.Sc. Lukas Rebholz and Dr. Ivan Fernandez-Corbaton. These results were published in [S1].

This chapter presents a formalism to identify the interaction between modes in whispering gallery resonators. In Section 6.1, we introduce the WGR and elaborate on their importance in photonics. Then, Section 6.2 presents the method to calculate resonant modes using a Maxwell solver. These modes are in general leaky, causing the radiation of the electromagnetic fields into the surrounding of WGR. In Section 6.3, we establish a method to obtain the field radiated by a given leaky mode. We find the relation between the modes computed with the Maxwell solver and the radiating fields outside the WGR. Finally, in Section 6.4, we introduce a scalar product to calculate the energy of a given radiating field. We apply this energy scalar product to the resonant modes of WGR to identify coupling modes and analyse the occurrence of anti-crossings as the thickness of the disk changes. We conclude with a summary in Section 6.5.

6.1. Introduction

WGRs can be fabricated in form of spheres, rings, or disks, to name just a few [57]. In a ray-optical picture, the resonators sustain resonances upon consecutive total internal reflections of the rays at the circular boundary between the WGR and its surrounding medium that lead to closed ray paths, forming a standing wave [55, 57]. Upon dense reflections, the electromagnetic fields are localised near the circumference of the WGR, which reduces optical losses and leads to high Q factors.[1] Reducing the size of WGRs, while maintaining a relatively high Q factor leads to strong optical confinement, which can minimise the size of optical instruments in photonic structures [55]. Due to their low losses and small size, WGRs can be integrated into optical networks [59]. WGRs are also appealing for numerous applications due to their unique spectral properties, such as tunability, narrow linewidth, and exceptional stability of resonant frequencies against environmental changes [55, 59]. WGRs are utilised as ring couplers and amplifiers for optical waves [56, 57], low threshold lasers [251, 252], spectral filters [58], switches, modulators, frequency stabilisers, and sensors [59, 253], as well as sources of quantum states of light [60, 61, 254, 255].

WGRs can be studied through their resonant modes [256], which are the natural damped resonances of the system. Also called whispering gallery modes (WGMs), the resonant modes are used for diverse tasks, including the study of light-matter interactions [257–272], or the expansion of scattered fields as a linear combination of the resonant modes [273, 274]. Introducing multiple resonant modes can also be utilised to enhance the bandwidth of antennas in comparison to those usually based on one resonance [275]. While WGMs are analytically calculated to be orthogonal, a coupling between them has been reported in experiments [249, 276]. The interaction between modes can be utilised to demonstrate Kerr frequency comb generation [277], coupled-mode induced transparency and absorption [278] or narrow-band high reflectivity of resonators [276].

The analysis of mode coupling in WGR and resulting modal anti-crossing behaviour has been studied recently with the use of a vectorial perturbation theory[2] for resonators made of anisotropic materials [279, 280] or investigation of the symmetries of the modes obtained with finite-element method simulations [249]. In this chapter, we describe the use of an energy scalar product in the context of resonant modes to determine the geometry of the disk resonator for which the anti-crossings occur.

6.2. Resonant modes in whispering gallery resonator

The considered WGM resonator consists of a disk of radius 25 µm and a thickness that varies from 1.8 µm to 3.1 µm, in 0.01 µm steps. The disk is made of a material characterised by a real permittivity $\varepsilon_{\text{res}}^{(r)} = (1.481)^2$ and imaginary permittivity $\varepsilon_{\text{res}}^{(i)} = 10^{-4}$, surrounded by air of permittivity $\varepsilon_{\text{sur}} = (1.000275)^2$, following [249]. For each disk thickness, the electric fields

---

[1] The Q factor is proportional to the confinement time in units of the optical period. An ideal cavity, without loss, confines light indefinitely and is characterised by precise resonant frequencies [57]. The lower the Q factor, the higher the damping of the oscillations in the resonator.

[2] The vectorial perturbation theory is based on electric and magnetic field components in the axial direction of the disk. These components obey two separate Helmholtz equations in a bulk material. In the presence of a boundary between the disk and air, the field components can couple. The boundary conditions are derived in a perturbative manner, including both coupling and noncoupling terms. The details of this method can be found in [279].

$\boldsymbol{\mathcal{E}}(\mathbf{r})$ and magnetic fields $\boldsymbol{\mathcal{H}}(\mathbf{r})$, as well as the resonance frequencies ω are computed with the FEM simulation software JCMsuite. This FEM solver addresses the resonant mode problem by determining the complex electric and magnetic eigenfields $(\boldsymbol{\mathcal{E}}_f(\mathbf{r}), \boldsymbol{\mathcal{H}}_f(\mathbf{r}))$ of the mode f and the corresponding eigenvalue $\omega_f = \omega_f^{(r)} - \mathrm{i}\omega_f^{(i)}$, where $\omega_f^{(r)}, \omega_f^{(i)} \in (0, \infty)$. These pairs of electric and magnetic fields together with their eigenfrequencies satisfy the time-harmonic Maxwell equations in a source-free medium. Using the rotational symmetry of the disk with respect to the z-axis, the eigenmode computation is reduced to a two-dimensional problem in the plane $(\rho,\ \varphi = 0,\ z)$,[3] as illustrated in Figure 6.1. The resonant modes are described by radial N_ρ^f, azimuthal N_φ^f, and axial N_z^f *mode numbers*, which count the number of intensity antinodes along the radial, azimuthal, and axial directions of the disk, respectively.

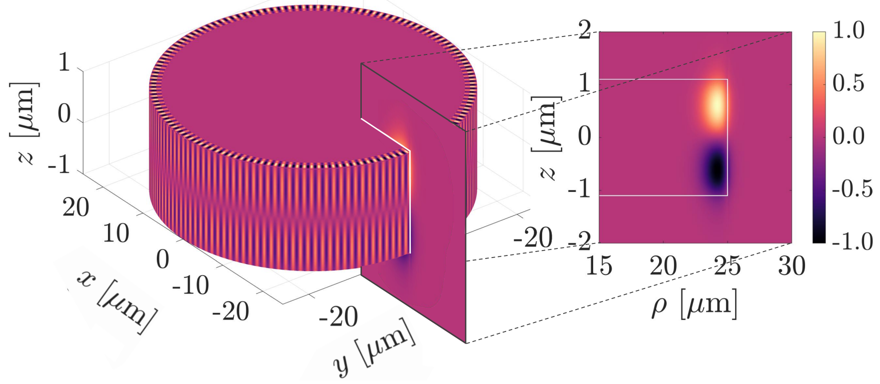

Figure 6.1.: (left) The radial component of the real part of the electric field of the mode characterised by $(N_\rho^f, N_z^f) = (1, 2)$, shown on the disk surface. (right) Projection of a slice of the disk in the plane $(\rho,\ \varphi = 0,\ z)$, representing a part of the computational domain in JCMsuite. The field decreases by several orders of magnitude at the boundaries of the chosen computational domain. For the sake of visibility, the domain in the figure differs from the size of the actual computational domain, and the scale of the z-axis is different from that of the remaining two axes. The field is normalised to its maximum value. The figure has also been published in [S1].

At any point $\mathbf{r}$ of the disk, the field of a given resonant mode (in Cartesian coordinates) satisfies

$$\boldsymbol{\mathcal{E}}_f(\rho\cos\varphi, \rho\sin\varphi, z) = \mathbf{R}(\varphi)\cdot\boldsymbol{\mathcal{E}}_f(\rho, 0, z)\mathrm{e}^{\mathrm{i}N_\varphi^f\varphi}, \tag{6.1}$$

with azimuthal angle φ, radial distance ρ, integer azimuthal mode number[4] $N_\varphi^f = 139$ (following [249]), and the rotation matrix[5] [65]

$$\mathbf{R}(\varphi) = \begin{pmatrix} \cos\varphi & -\sin\varphi & 0 \\ \sin\varphi & \cos\varphi & 0 \\ 0 & 0 & 1 \end{pmatrix}. \tag{6.2}$$

---

[3] Where: $\rho = \sqrt{x^2 + y^2}$ and $\varphi = \arctan 2(y, x)$.

[4] It is important to note that any integer number is a valid azimuthal mode number, also referred to as *azimuthal wavenumber* [65]. Here, the $N_\varphi^f = 139$ was selected because this number was chosen for study in [249], which serves as a reference for the computation of modes performed here. Moreover, the modes with different azimuthal mode numbers are orthogonal under the scalar product introduced in Section 6.4. Therefore, it is enough to study modes for one selected N_φ^f.

[5] Note that JCMsuite follows a different convention with the y-axis being the axis of rotational symmetry.

Due to the localisation of the electric field near the rim of the resonator, the region from which the eigenfields are extracted is limited to $[19.5, 27.0]$ µm along the radial direction ρ and $[-3, 3]$ µm in the axial z-direction. The discretisation in the radial direction is nonuniform and finer close to the rim. The simulation settings are as follows: the target relative precision for the resonance frequencies is set to 10^{-6}, and an adaptive mesh refinement scheme is employed with a maximum of two refinement steps. The computational domain is surrounded by PMLs [65].

Figure 6.2 shows the real part of the resonance frequencies of selected modes as a function of the disk thickness within the considered range. The resonance frequencies of the modes change with varying thickness of the disk. The modes are assigned a *spectral order number* according to the increasing real part of their eigenfrequency. The modes are organised into pairs, representing the same spectral order number but differing in *parity*, represented with $m_z = 1$ or $m_z = -1$. Parity is defined here as an eigenvalue of the mirror reflection $z \mapsto -z$ of the radial electric field distribution $\mathcal{E}_\rho^f(\mathbf{r})$ of each mode f, which serves as an eigenstate of this reflection. For instance, the field illustrated in Figure 6.1 transforms with an eigenvalue of $m_z = -1$. It is worth noting that the corresponding magnetic field distribution $\mathcal{H}_\rho^f(\mathbf{r})$ also acts as an eigenstate of the reflection $z \mapsto -z$ but with eigenvalue $-m_z$.

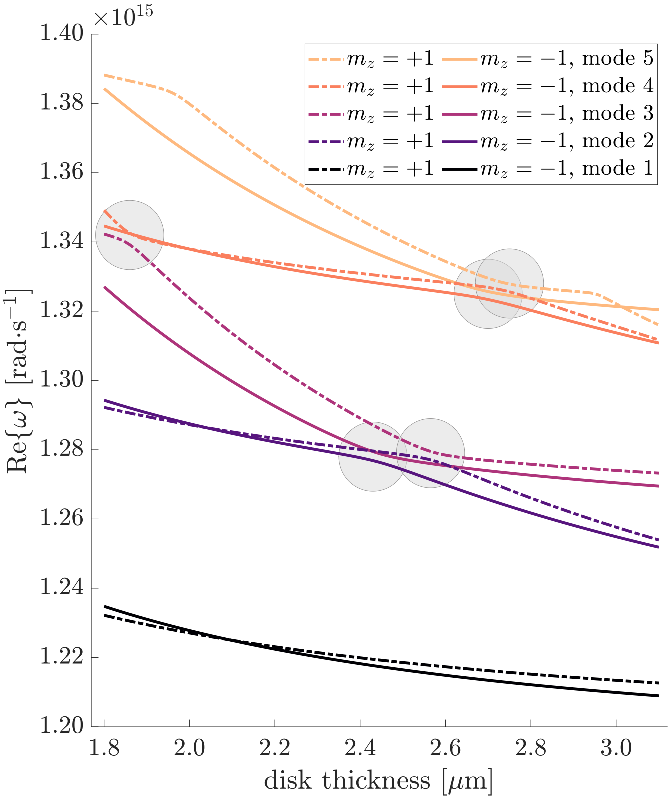

Figure 6.2.: Real part of the angular resonance frequency of the five pairs of lowest spectral order modes as a function of the disk thickness. Each pair consists of one mode of a positive parity $m_z = 1$ and one mode of a negative parity $m_z = -1$ upon a $z \mapsto -z$ mirror transformation. Modes of equal parity m_z undergo avoided crossings at the spots marked with grey circles. Solid lines follow eigenfrequencies of modes with negative parity, and dashed lines mark the resonance frequencies of modes with positive parity. The figure has also been published in [S1].

While the disk itself is invariant under the mirror reflection $z \mapsto -z$, the field distributions exhibit two distinct parities. Moreover, these parities characterise particular modes and do not change as the thickness of the disk changes. From the symmetry analysis in [249], it is known that some modes exhibit *crossings* while others display *avoided crossings*, also referred to as *anti-crossings*, during changes in disk thickness. It can be seen in Figure 6.2 that as the modes come spectrally close, which means the difference between the real parts of their eigenfrequencies is minimal, the lines for modes with opposite parities cross each other, while the lines for modes with the same parity exhibit anti-crossings. The anti-crossings are marked by grey circles in Figure 6.2. The crossings indicate a lack of interaction between the modes, while anti-crossings signify that the modes couple with each other [249].

Based on the FEM computations, the modes are sorted and assigned spectral order numbers according to their increasing real part of the resonance frequency, independently for each disk thickness. Here, the modes are labelled with numbers, according to the spectral ordering of modes for a disk of thickness 1.8 µm. However, the crossings influence the spectral ordering of the modes. As the disk thickness increases, the order derived from the numerical tool may swap the labels for modes that cross. Therefore, these labels do not accurately reflect the true spectral order of the modes. In our analysis, this labelling issue can be addressed by considering the spectral order of modes separately for different m_z values, since crossings exclusively occur between modes of opposite m_z. However, the symmetry approach may not be possible in cases of resonators with more complicated shapes. In the following, we present the formalism to identify the modes and the disk thicknesses at which the anti-crossings occur, employing the orthogonality of the radiated fields.

6.3. Electromagnetic fields radiated by a leaky mode

The electromagnetic fields of the resonant modes are present inside and outside the disk resonator. The modes that are present in the cladding and radiate into the far field are called *leaky modes*. The electromagnetic fields on a boundary between the disk and the surrounding medium act as sources of radiation fields [281][282, Chapter 5]. The components of the electric and magnetic fields that are tangential to the surface determine the entire field outside the enclosed volume. This principle implies that the tangential components of the electric and magnetic fields uniquely define the radiation field beyond the volume, allowing us to derive the field radiated by a given leaky mode.

Figure 6.3 presents a 2D cross-section of a closed surface in $\mathbb{R}^3$ that defines a volume D of the disk with a boundary ∂D. The boundary ∂D is assumed to have continuous first derivatives. This volume is surrounded by an *achiral*,[6] non-absorbing, homogeneous, and isotropic background medium, which we simplify by assuming it is vacuum.[7] We assume the existence of time-dependent *helical fields* $\widetilde{\mathbf{F}}_\Lambda(\mathbf{r}, t)$ with helicity $\Lambda = \pm 1$ for $\mathbf{r} \in \partial D$, on the boundary surface ∂D. These fields are given in SI units as

$$\widetilde{\mathbf{F}}_\Lambda(\mathbf{r}, t) = \sqrt{\frac{\varepsilon_0}{2}} \left[\widetilde{\mathbf{E}}(\mathbf{r}, t) + \mathrm{i}\Lambda Z_0 \widetilde{\mathbf{H}}(\mathbf{r}, t) \right], \tag{6.3}$$

---

[6] A structure is called chiral if it cannot be superimposed onto its mirror image by any combination of translations or rotations. An example of chiral objects are left and right hands.

[7] Any other similar surrounding medium can be incorporated into the formulas by substituting the vacuum permittivity and permeability with those of the surrounding medium.

with vacuum permittivity ε_0, vacuum impedance Z_0, time and spatially dependent complex electric field $\widetilde{\mathbf{E}}(\mathbf{r}, t)$, and complex magnetic field $\widetilde{\mathbf{H}}(\mathbf{r}, t)$.

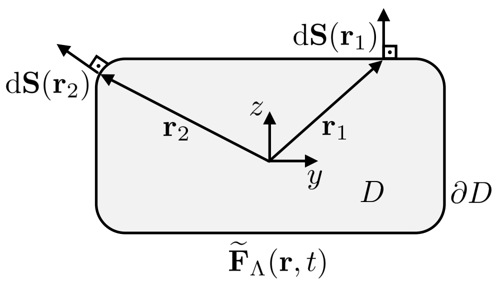

Figure 6.3: A cross-section of a volume D in $\mathbb{R}^3$ is delimited by a closed surface ∂D having continuous first derivative. The $\mathrm{d}\mathbf{S}(\mathbf{r})$ denotes an outwards-pointing normal vector of the surface element at each point $\mathbf{r} \in \partial D$. The y and z denote the Cartesian coordinate system. Fields $\widetilde{\mathbf{F}}_\Lambda(\mathbf{r}, t)$ for $\mathbf{r} \in \partial D$, on the surface produce electromagnetic radiation towards spatial infinity. This figure has been adapted from [S1].

The boundary of the disk ∂D is required to be once continuously differentiable [282, Chapter 5] because the Maxwell equations for helical fields involve only first-order derivatives [282, §1-2.3]. This condition is satisfied by a *continuous tangent* surface of a disk with rounded corners.

The helical field $\widetilde{\mathbf{F}}_\Lambda(\mathbf{r}, t)$ can be also defined through a one-sided inverse Fourier transform:

$$\widetilde{\mathbf{F}}_\Lambda(\mathbf{r}, t) = \frac{1}{\sqrt{2\pi}} \int_0^\infty \mathbf{F}_\Lambda(\mathbf{r}, |\mathbf{k}|) \mathrm{e}^{-\mathrm{i}c_0|\mathbf{k}|t} \mathrm{d}|\mathbf{k}|, \tag{6.4}$$

where $|\mathbf{k}|$ is the absolute value of the angular wavevector, and c_0 denotes the speed of light in vacuum. It is important to note that physically, the time-harmonic angular frequency is restricted to positive values,[8] meaning $\omega = c_0|\mathbf{k}| > 0$ [283]. The $|\mathbf{k}|$ is referred to as a *wavenumber*.

Equation (6.4) holds only if we consider solely the eigenfrequencies ω, computed by the FEM solver, without taking into account their complex conjugated counterparts $-\omega^*$. This approximation is explained in more detail in Appendix C.2.

The helical fields, defined with equation (6.3), produced by a given leaky mode at the surface ∂D are related to the eigenmodes of the resonator as follows:

$$\widetilde{\mathbf{F}}_\Lambda(\mathbf{r}, t) = \sqrt{\frac{\varepsilon_0}{2}} \left[\boldsymbol{\mathcal{E}}(\mathbf{r}) + i\Lambda Z_0 \boldsymbol{\mathcal{H}}(\mathbf{r})\right] \mathrm{e}^{-\mathrm{i}\omega t}\Theta(t) = \boldsymbol{\mathcal{M}}_\Lambda(\mathbf{r})\mathrm{e}^{-\mathrm{i}\omega t}\Theta(t)\,, \tag{6.5}$$

where we introduce the notation for the *helical modal field* $\boldsymbol{\mathcal{M}}_\Lambda(\mathbf{r})$. Examples of fields $\boldsymbol{\mathcal{M}}_\Lambda(\mathbf{r})$ are presented in Figure 6.4 and Figure 6.5. The function $\Theta(t)$ is the Heaviside step function that equals 1 if $t \geq 0$ and equals 0 if $t < 0$. The Heaviside function indicates that the leaky mode is excited at some point in time, which we set to $t = 0$. This approach avoids the amplification that would occur in the exponential term in equation (6.5) for $t < 0$, while retaining the damping effect for $t > 0$. Moreover, the fields $\mathbf{F}_\Lambda(\mathbf{r}, |\mathbf{k}|)\mathrm{e}^{-\mathrm{i}c_0|\mathbf{k}|t}$ in equation (6.4) produce radiated fields that decay as $1/|\mathbf{r}|$ as $|\mathbf{r}| \to \infty$ [281, Eq. (33, 35)]. Therefore, the formulation in equation (6.5) effectively avoids two unphysical exponential

---

[8] In practice, this could mean integrating over some range of $|\mathbf{k}| > 0$. However, here the integral is evaluated analytically, which is shown in Appendix C.1.

growths of the modal field: one as $t \to -\infty$ and another as $|\mathbf{r}| \to \infty$. These two growths are interconnected by causality[9] [284]. The wavenumbers of the source fields on ∂D are considered to be real. Identifying a complex eigenfrequency with a complex wavenumber would result in an exponential growth of the field outside the resonator as $\mathbf{r}$ increases.

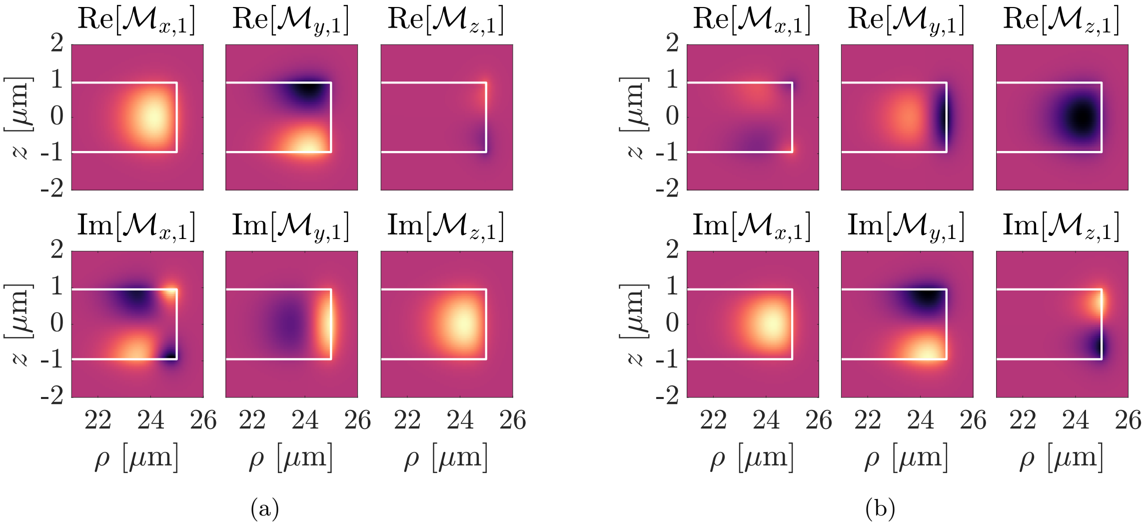

Figure 6.4.: Cartesian components of the real (upper row) and imaginary (bottom row) part of the field $\boldsymbol{\mathcal{M}}_{\Lambda=+1}(\mathbf{r})$ of the first modes, characterised by (a) $m_z = +1$ and (b) $m_z = -1$. These are examples of crossing modes, characterised by different eigenvalue of the mirror function $z \to -z$. The figure has also been published in [S1].

The monochromatic field $\mathbf{F}_\Lambda(\mathbf{r}, |\mathbf{k}|)$, present in equation (6.4), can now be found with the Fourier transform of equation (6.5):

$$\int_{-\infty}^{\infty} \widetilde{\mathbf{F}}_\Lambda(\mathbf{r}, t) \mathrm{e}^{\mathrm{i}c_0 q t} \mathrm{d}t = \int_{0}^{\infty} \boldsymbol{\mathcal{M}}_\Lambda(\mathbf{r}) \mathrm{e}^{\mathrm{i}(c_0 q - \omega)t} \mathrm{d}t = \frac{\mathrm{i}\boldsymbol{\mathcal{M}}_\Lambda(\mathbf{r})}{c_0 q - \omega}\,, \tag{6.6}$$

with parameter $q > 0$, corresponding to the positive, real wavenumber.

At the same time, the Fourier transform of equation (6.4) results in[10]

$$\begin{aligned} \int_{-\infty}^{\infty} \widetilde{\mathbf{F}}_\Lambda(\mathbf{r}, t) \mathrm{e}^{\mathrm{i}c_0 q t} \mathrm{d}t &= \frac{1}{\sqrt{2\pi}} \int_{0}^{\infty} \mathbf{F}_\Lambda(\mathbf{r}, |\mathbf{k}|) \int_{-\infty}^{\infty} \mathrm{e}^{-\mathrm{i}c_0(|\mathbf{k}|-q)t} \mathrm{d}t \, \mathrm{d}|\mathbf{k}| \\ &= \frac{1}{\sqrt{2\pi}} \int_{0}^{\infty} \mathbf{F}_\Lambda(\mathbf{r}, |\mathbf{k}|) \frac{2\pi}{c_0} \delta(|\mathbf{k}| - q) \, \mathrm{d}|\mathbf{k}| = \frac{\sqrt{2\pi}}{c_0} \mathbf{F}_\Lambda(\mathbf{r}, q)\,. \end{aligned} \tag{6.7}$$

---

[9] Note the dependence of the electromagnetic fields on $\mathrm{e}^{\mathrm{i}(\mathbf{k}\cdot\mathbf{r} - \omega t)}$, for example in equations (2.15) or (2.16), or implicit $\mathrm{e}^{\mathrm{i}(\mathbf{k}\cdot\mathbf{r} - c_0|\mathbf{k}|t)}$ in equation (6.4).

[10] Using the relation $\frac{1}{2\pi}\int_{-\infty}^{\infty} \mathrm{e}^{\mathrm{i}x(a-b)} \mathrm{d}x = \delta(a - b)$.

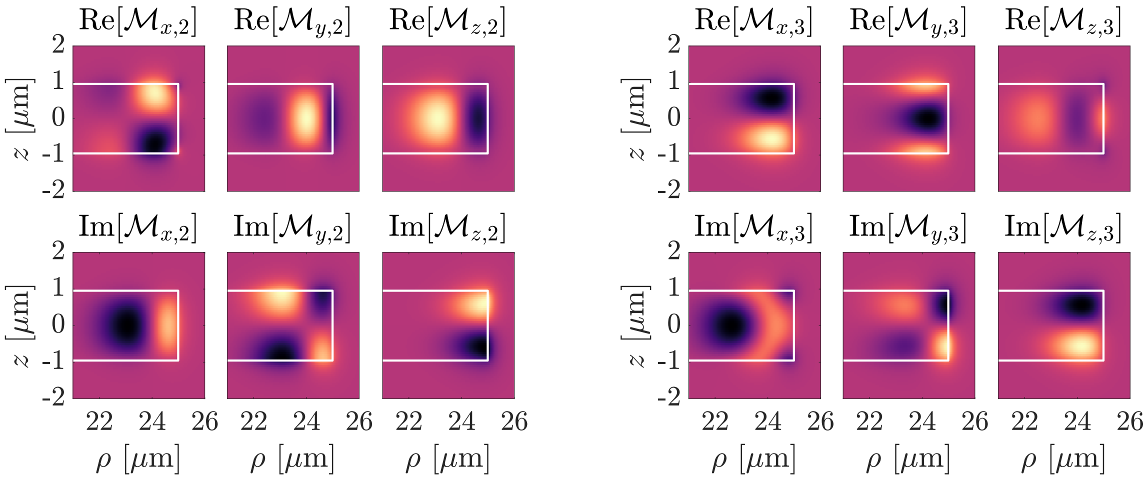

(a) (b)

Figure 6.5.: Cartesian components of the real (upper row) and imaginary (bottom row) part of the field $\boldsymbol{\mathcal{M}}_{\Lambda=+1}(\mathbf{r})$ of the (a) second and the (b) the third mode, both characterised by the eigenvalue of the mirror function $m_z = -1$ upon $z \to -z$. These are examples of anti-crossing modes. The figure has also been published in [S1].

The monochromatic field component $\mathbf{F}_\Lambda(\mathbf{r}, |\mathbf{k}|)$ can be determined by substituting $q \to |\mathbf{k}|$ and equating (6.6) and (6.7), which results in

$$\mathbf{F}_\Lambda(\mathbf{r}, |\mathbf{k}|) = \frac{\mathrm{i}c_0 \boldsymbol{\mathcal{M}}_\Lambda(\mathbf{r})}{\sqrt{2\pi}(c_0|\mathbf{k}| - \omega)} \,. \tag{6.8}$$

It is important to note that the monochromatic field (6.8) does not reproduce (6.5) accurately, using one-sided Fourier transform (6.4). The inverse derivation is correct when using full inverse Fourier transform including negative frequencies. The correction to formula (6.8) is shown in Appendix C.2. The new formulation in Appendix C.2 belongs to the (not yet published) revision of [S1] written mostly by M.Sc. Lukas Rebholz and Dr. Ivan Fernandez-Corbaton, and, therefore, is beyond the scope of this thesis.

The helical modal fields $\boldsymbol{\mathcal{M}}_\Lambda(\mathbf{r})$ are constructed from electric and magnetic fields ($\boldsymbol{\mathcal{E}}(\mathbf{r})$, $\boldsymbol{\mathcal{H}}(\mathbf{r})$) according to the definition in equation (6.5). It is important to note that the surrounding medium of the considered disk is not vacuum, as assumed for the derivation of equation (6.8). However, since $\varepsilon_{\mathrm{sur}}$ is only marginally different from unity, we can neglect its influence, as the results remain basically the same as in the vacuum case.

The monochromatic surface fields $\mathbf{F}_\Lambda(\mathbf{r}, |\mathbf{k}|)$ act as sources for the radiation fields in the surrounding medium. In the following section, we introduce an energy scalar product that involves the integrals of the monochromatic fields derived here.

6.4. The cross-energy scalar product for interaction between modes

An electromagnetic scalar product between radiation fields, which only involves integrals of the radiation fields over closed spatial surfaces, was derived in [283]. Specifically, the quantity $\mathbf{F}_\Lambda(\mathbf{r}, |\mathbf{k}|)$ appears in the expression for the energy $\langle\mathcal{F}|\mathrm{H}|\mathcal{F}\rangle$ [283, Equation (21)] of a given mode $|\mathcal{F}\rangle$, with the energy operator H. The energy can be computed as an integral over a closed boundary:

$$\langle\mathcal{F}|\mathrm{H}|\mathcal{F}\rangle = \sum_{\Lambda=\pm1} (-\mathrm{i}\Lambda) \int\limits_0^\infty \mathrm{d}|\mathbf{k}| \int\limits_{\partial D} [\mathbf{F}^*_\Lambda(\mathbf{r}, |\mathbf{k}|) \times \mathbf{F}_\Lambda(\mathbf{r}, |\mathbf{k}|)] \cdot \mathrm{d}\mathbf{S}(\mathbf{r})\,, \tag{6.9}$$

where $\mathrm{d}\mathbf{S}$ is the infinitesimal surface element at position $\mathbf{r}$, and the integral is taken over any piecewise smooth surface ∂D that encloses a compact volume containing the radiation sources [283]. The cross-energy between arbitrary modes $|\mathcal{F}\rangle$ and $|\mathcal{G}\rangle$ is calculated with

$$\langle\mathcal{F}|\mathrm{H}|\mathcal{G}\rangle = \sum_{\Lambda=\pm1} (-\mathrm{i}\Lambda) \int\limits_0^\infty \mathrm{d}|\mathbf{k}| \int\limits_{\partial D} [\mathbf{F}^*_\Lambda(\mathbf{r}, |\mathbf{k}|) \times \mathbf{G}_\Lambda(\mathbf{r}, |\mathbf{k}|)] \cdot \mathrm{d}\mathbf{S}(\mathbf{r})\,. \tag{6.10}$$

The energy operator H is self-adjoint with respect to the inner product $\langle\mathcal{F}|\mathcal{G}\rangle$ and therefore the inner product (6.10) is a proper scalar product, satisfying the condition $\langle\mathcal{F}|\mathrm{H}|\mathcal{G}\rangle = (\langle\mathcal{G}|\mathrm{H}|\mathcal{F}\rangle)^*$. The use of the energy scalar product is consistent with the use of the scalar product derived from the time-averaged Poynting vector for the propagating modes in waveguides in Subsection 2.2.4. The scalar product is a measure of orthogonality of the modes. The scalar product equal to zero means that the modes are orthogonal. The scalar product deviates from zero when the orthogonality of the modes is broken, cf. Subsection 2.2.4.

The surface integral in equation (6.10) ensures that only the components tangential to the surface impact the results. The tangential components of the electric and magnetic fields remain continuous at the interface between the disk and the surrounding medium, therefore they can be used for calculation of the scalar product (6.10).

The cross-energy scalar product $\langle\mathcal{F}|\mathrm{H}|\mathcal{G}\rangle$ between arbitrary modes $|\mathcal{F}\rangle$ and $|\mathcal{G}\rangle$ can be derived by plugging in the relation (6.8) into (6.10), and results in:

$$\langle\mathcal{F}|\mathrm{H}|\mathcal{G}\rangle = \frac{\ln(-\omega_g) - \ln(-\omega_f^*)}{(\omega_f^* - \omega_g)} \frac{c_0}{2\pi} \left\{ \sum_{\Lambda=\pm1} (-\mathrm{i}\Lambda) \int\limits_{\partial D} \left[\boldsymbol{\mathcal{M}}^*_{\Lambda,f}(\mathbf{r}) \times \boldsymbol{\mathcal{M}}_{\Lambda,g}(\mathbf{r})\right] \cdot \mathrm{d}\mathbf{S}(\mathbf{r}) \right\}\,, \tag{6.11}$$

where the subscripts f and g refer to the two considered modes, $|\mathcal{F}\rangle$ and $|\mathcal{G}\rangle$, respectively. The exact derivation is shown in Appendix C.1.

6.4.1. Application to a whispering gallery resonator

The cross-energy scalar product (6.11) can be further simplified, taking into account the cylindrical symmetry of the disk surface ∂D:

$$\langle\mathcal{F}|\mathrm{H}|\mathcal{G}\rangle = \sum_{\Lambda=\pm1} (-\mathrm{i}\Lambda c_0) \frac{\ln(-\omega_g) - \ln(-\omega_f^*)}{\omega_f^* - \omega_g} \int_{\mathcal{C}} \mathrm{d}s \rho \hat{\mathbf{n}}(\mathbf{r}) \cdot \left[\boldsymbol{\mathcal{M}}^*_{\Lambda,f}(\mathbf{r}) \times \boldsymbol{\mathcal{M}}_{\Lambda,g}(\mathbf{r})\right]\,. \tag{6.12}$$

The integration in (6.12) is performed over a piecewise continuous contour $\mathcal{C}$ obtained from the intersection of the surface ∂D and half of the axial cross-section of the disk, containing the axis of rotation. The integral in equation (6.11) is simplified by taking advantage of the cylindrical symmetry of the system, which reduces the two-dimensional surface integral to a one-dimensional contour integral. The details of this simplification are presented in Appendix C.1.

The integral (6.12) is computed using the trapezoidal rule[11] over the contour $\mathcal{C}$, which is represented with the white line in the projection shown in Figure 6.1. This white contour is composed of three continuous lines. The dimensions of the contour (both in radial and axial direction) for the actual computation are $2\,\%$ larger than the actual contour of the $\varphi = 0$ slice of the disk. This choice is motivated by the presence of regions with numerical artefacts in the simulated fields, which are found near the sharp edges of the disk resonator. The contour is increased to avoid these artefacts. To further enhance the accuracy, the contour is discretised more finely near the rim of the disk, where the fields are localised. Although the sampling points are chosen to align with the contour of a resonator with sharp edges, this does not violate the assumption of *continuous tangent* surfaces mentioned earlier since the curvature region of the contour can be considered small compared to the finite sampling.

It is important to note that the fields captured outside the resonator are associated with a complex wavenumber. Consequently, these fields exhibit exponentially divergent behaviour when they approach spatial infinity. The rate of divergence is connected to the radiative damping of the resonant modes. However, in the case of high-quality resonances discussed here, indicated by the ratio $\omega^{(r)} : \omega^{(i)}$ in the order of 10^5, the exponential divergence is slow enough to be negligible close to the resonator's surface. Therefore, the fields on the $2\,\%$ bigger contour remain a close approximation to the desired fields on the surface of the disk.

6.4.2. Analysis of the interacting modes

For the analysis of the orthogonality properties of the modes in the WGR, we use the following quantity

$$|\,\langle\hat{\mathcal{F}}|\mathrm{H}|\hat{\mathcal{G}}\rangle\,|^2 = \frac{|\langle\mathcal{F}|\mathrm{H}|\mathcal{G}\rangle|^2}{\langle\mathcal{F}|\mathrm{H}|\mathcal{F}\rangle\,\langle\mathcal{G}|\mathrm{H}|\mathcal{G}\rangle}\,, \tag{6.13}$$

which expresses the normalisation of each considered mode with respect to the radiated energy. The quantity (6.13) is referred to as the *normalised scalar product.*

Figure 6.6 illustrates the outcomes of expression (6.13) for selected pairs of modes with the same parity as a function of the disk thickness. Each line in the figure shows a notable peak for the disk thickness for which the real frequencies of a particular pair of modes approach one another, as depicted in Figure 6.2. The positions of the peaks align with the thicknesses at which the particular modes anti-cross, indicating interactions between the modes that result in an increased non-orthogonality. In contrast, the modes that intersect in Figure 6.2 are characterised by opposite parity and are orthogonal under the cross-energy scalar product. In such cases, the cross-energy scalar product is zero and not depicted in Figure 6.6. Vanishing of the scalar product can be demonstrated easily by dividing the

---

[11] It was checked by the convergence analysis that the basic trapezoidal rule produces satisfactory results, for the selected discretisation of the contour.

surface integral in equation (6.12) into two parts: one for $z > 0$ and the other for $z < 0$. Their sum (including the sum over helicity) cancels out if the modes have opposite parity.

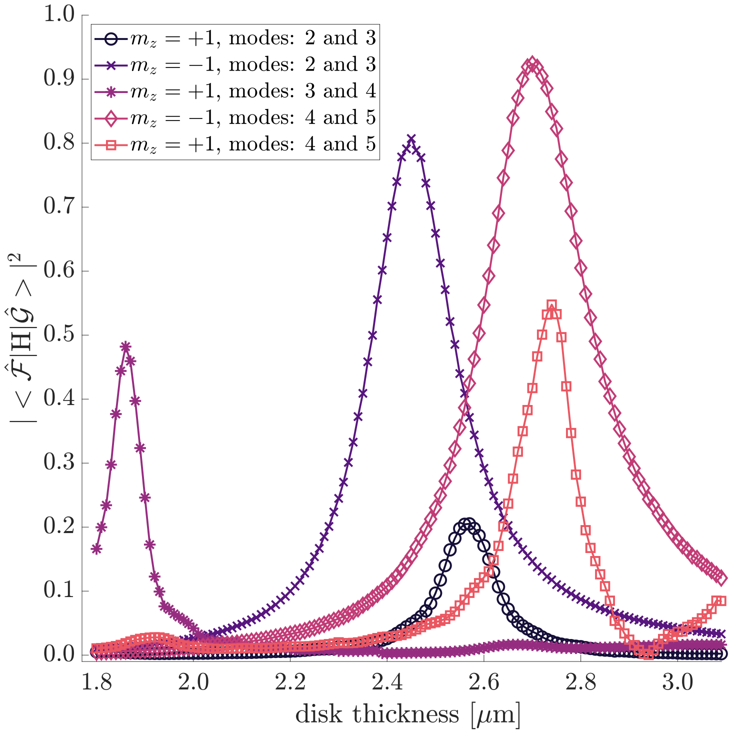

Figure 6.6.: Normalised scalar product (6.13) as a function of disk thickness for selected pairs of modes characterised by the same parity. The positions of the peaks coincide with the thicknesses for which the anti-crossings occur between the particular modes, as marked in Figure 6.2. The figure has also been published in [S1].

Figure 6.7 presents the normalised scalar product (6.13) for an isolated pair of modes characterised with $m_z = -1$. The insets show the electric field energy density profiles of the modes from the pair for selected disk thickness values. When the normalised scalar product is low in a thin disk, the mode profiles of mode 2 and mode 3 can be described by modal numbers $(2, 1)$ and $(1, 2)$, respectively. In this description, the first digit denotes the number of maxima in radial direction, while the second digit indicates the number of maxima in the axial direction. With the increment of the disk thickness, the profiles deform, reach a similar shape and overlap, when the normalised scalar product reaches its peak value. This shape cannot be decomposed into axial and radial projections, and therefore, the description with modal numbers is not possible. When the disk thickness increases further, the modes separate, but with interchanged modal numbers $(1, 2) \leftrightarrow (2, 1)$. This analysis confirms the observation described in [249]. The normalised cross-energy scalar product peaks precisely when the two mode profiles have maximal overlap, which correlates with the maximal expected coupling in terms of energy exchange between the modes.

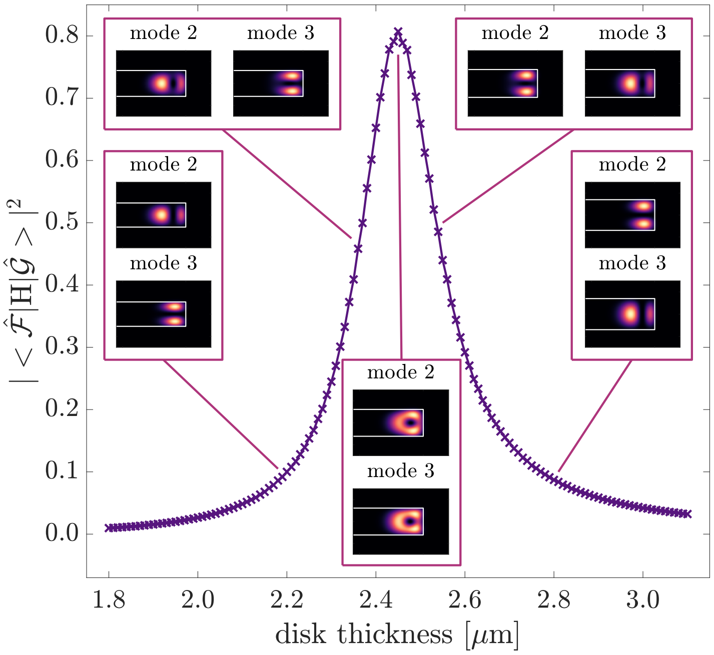

Figure 6.7.: Normalised scalar product (6.13) as a function of the disk thickness for the modes of spectral order 2 and 3 and parity $m_z = -1$. The inset figures show the normalised energy density distribution of the modes at selected values of the disk thickness. The field distributions plotted here are closely related to the ones in [249, Figure 3]. The figure has also been published in [S1].

6.5. Summary and conclusions

We presented a further study of interaction of modes in guiding structures. Alongside waveguides, ring- and disk-shaped resonators are common components confining light in photonic integrated circuits. The localisation of electromagnetic field close to the disks' rim resembles the modes in a curved waveguide with a constant radius of curvature. The ability to form resonances at particular frequencies makes the resonators suitable as spectral filters, amplifiers, or as sources of non-classical light. The resonators are often used to enhance the efficiency of nonlinear processes. At the same time, the electromagnetic field of the resonant modes at the surface of the resonators is the source of radiation into the far field. We use this fact to analyse the modal properties of this kind of systems.

This chapter focused on the interaction between eigenmodes of the same azimutal mode number in whispering gallery resonators. This interaction can be spotted when the real parts of the eigenfrequencies of the modes are plotted against varying thickness of the disk resonator. When the modes approach spectrally one another, the eigenfrequencies of the interacting modes anti-cross. The modes interact if they exhibit the same symmetry properties along the axial direction of the disk. The commercial Maxwell solvers may sort and assign labels to the modes, based on increasing real parts of eigenfrequencies. Therefore, the anti-crossing of the modes can be a potential problem because the labels would not be assigned properly when analysing changes of some parameters of the resonator.

The anti-crossing and crossing behaviour of resonant modes is related to the orthogonality of the associated fields on the surface of the disk. These fields on the surface generate polychromatic radiation free of divergences. The radiation modes are defined with use of helical fields based on the numerical eigenmodes obtained from the Maxwell solver JCMsuite on the surface of the resonator. We identified a cross-energy expression between the radiations of any two given eigenmodes as a suitable scalar product. The application of the proposed scalar product to the modes of a disk-shaped WGR revealed that the cross-energy scalar product provides physically relevant information to predict the interaction between modes as the geometrical parameters of the disk change gradually.

The use of the presented cross-energy scalar product between radiation fields can serve as a general method for tracking the resonant modes as certain parameters of the resonator change smoothly. This can be achieved by projecting the radiation field of each mode for a given set of parameters onto the radiation fields of each mode in the subsequent set. The connection between a mode from the first set and a mode from the second set is established by identifying which projection yields the maximum value. Even though in the case of a disk resonator this mode tracking can be performed using symmetry arguments, for more complex resonators, such an approach may not be possible.

7 | Conclusions and outlook

This thesis presented a modal approach to analyse light propagation, losses, and the enhancement of nonlinearity in planar and free-form waveguides, as well as the interaction of resonant modes in whispering gallery resonators. The considered structures are key components of photonic integrated circuits and their packaging. Free-form waveguides, also called photonic wire bonds (PWBs), enable connections between different chips, even if the chips are fabricated on incompatible material platforms. Free-form waveguides allow us to package multiple chips into one functional photonic device. We introduced a multi-mode approximation (MMA) for calculating the power transmission that serves as a merit function for optimising the trajectories of the PWBs. As a result of this approximation, an optimal trajectory can be identified in less than few minutes, which is crucial for the *in situ* fabrication. Highly nonlinear waveguides can be utilised for the on-chip generation of quantum states of light, which are important for quantum communication and computation. The nonlinearity can be enhanced by bending a waveguide because this increases the localisation of the electromagnetic field near the outer side of the bend. The non-classical states of light can also be generated using microring or disk resonators. To design a resonator effectively, a solid understanding of its modal properties is indispensable. We presented an analysis of radiation modes using a cross-energy scalar product, which indicates the dimensions of a whispering gallery resonator for which the resonant modes interact with each other.

Conclusions

Chapter 2 introduced waveguide theory, beginning with Maxwell's equations. It covered light confinement and propagation in slab and channel waveguides, along with the eigenmode expansion of the electromagnetic field. Numerical solvers for Maxwell's equations based on FEM, FIT, and FDTD method were employed to determine the modes and compute the waveguide transmission. The chapter also explained the fundamental mode approximation (FMA), which simplifies calculations of transmission through waveguides. This method was further developed in a following chapter to incorporate the excitation and propagation of higher-order modes.

Chapter 3 discussed approximation methods for fast calculation of the transmission through free-form waveguides. It focused on two approaches for calculating the objective function used in optimising trajectories within a 2D plane: MMA and the application of artificial neural networks (ANNs). The MMA expands the FMA to include higher-order modes, providing the transmission of these modes that is not accessible through FMA. The accuracy of both MMA and FMA was validated through comparison with full-wave simulation results, using examples such as a 90° bend, a *snake*-waveguide, and an S-bend. These approximation methods are effective in predicting transmission, particularly for waveguides with gradual curvature changes. However, both FMA and MMA are limited by the neglect of back-propagating and radiation modes. Nevertheless, in cases of optimal trajectories, the impact of radiation and back-propagation of modes is minimal, if not negligible.

Another method for computing transmission involved the use of ANNs. Section 3.4 presented the implementation and training of a multilayer perceptron, where the input trajectory was represented either as a vector of Cartesian coordinates or as a vector composed of arc lengths and corresponding radii of curvature. Using the second representation yielded more accurate transmission results, as it was independent of the waveguide's orientation. Both MMA and ANN significantly reduced the computation time for transmission, decreasing it from several hours to tenths of a second compared to full-wave solvers. Although neural networks offer faster results once trained, they require mode computation and substantial data resources for training.

Next, Chapter 4 discussed methods for optimising the trajectories of free-form waveguides, potentially utilising approximation methods in the computation of the merit function. We simplified the problem by assuming that bending occurred within a 2D plane. We thoroughly studied an optimisation procedure in which the Cartesian coordinates of the trajectory were represented by a fifth order polynomial. The algorithm determined the coefficients of the polynomial that yielded a trajectory with the lowest objective function while satisfying the specified constraints. The objective to be minimised consisted of the loss functional calculated using MMA, along with a penalty for intersections with obstacles. The results showed that the optimal trajectories could be determined within minutes, making the algorithm suitable for the *in situ* fabrication of photonic wire bonds.

Chapter 5 expanded the study of light propagation in waveguides by considering nonlinear effects. It appears that increasing the curvature of the waveguide may enhance its effective nonlinearity. As a result, the rate of photon pair generation from spontaneous four-wave mixing may be higher in bent waveguides than in straight ones. We analysed how bending affected the effective mode area, effective refractive index, and group velocity, which helped to explain the impact of curvature on the photon pair generation rate. Strongly nonlinear materials such as silicon nitride, silicon, and aluminium gallium arsenide were studied, demonstrating that increased curvature enhanced mode confinement, and consequently boosted photon pair generation. We observed a maximal improvement in the photon pair generation rate ranging from 5 % to 210 % for an optimal bending radius. However, increased curvature also leads to higher propagation losses. This trade-off between enhanced nonlinearity and propagation loss determines the optimal curvature for maximum photon pair generation. The relationship between bending and photon pair generation rate provides an alternative method for improving generation rates. Instead of elongating the waveguide, bending them can yield similar results.

Chapter 6 investigated the interaction of modes in disk-shaped whispering gallery mode resonators. These resonators can confine light and enhance resonances, making them effective as spectral filters, amplifiers, and sources of non-classical light. Understanding the modal properties of these resonators is essential for their design. The spectral order of modes may change with varying geometrical parameters of the disk, such as its thickness. Some modes experience crossing while others undergo anti-crossing as they come spectrally close to each other. The anti-crossings suggest an interaction between the modes. We introduced a cross-energy scalar product for radiating modes on the surface of the resonator, which allowed for the prediction of mode interactions as the disk's geometric parameters change.

The scalar product is expressed as a surface integral involving the modal fields multiplied by a closed-form factor incorporating the complex frequencies. This formulation enables normalisation and comparison of resonant modes using their corresponding radiation fields. These fields are polychromatic and free of divergences, determined by each mode's complex frequency and the modal field on the surface of the resonator. Applying the scalar product to the modes revealed that, for certain dimensions of the disk, the modes are not orthogonal and can interact with one another. This method aids in tracking resonant modes by projecting the radiation fields of modes from one parameter set onto another. While symmetry arguments can also be utilised for tracking modes in disk resonators, more complex resonators may require this scalar product approach.

Outlook

This thesis offers tools for analysing losses in multi-mode waveguides and calculating photon pair generation rates in bent waveguides. It also proposes a scalar product for studying leaky modes in resonating structures. While these tools are ready for use, there is still a potential for further development and applications.

In the multi-mode approximation we consider waveguide trajectories confined to a single plane. This method can be expanded to encompass 3D structures, including waveguide twisting and bending in arbitrary lateral direction. The accuracy of the MMA can be improved by incorporating an additional, third-order mode into the analysis.

Neural networks can be trained using full-wave simulation results for different trajectories. Besides predicting transmission, ANNs could directly optimise waveguide trajectories taking into account all constraints. ANNs seem to be naturally suited for optimisation tasks because they inherently support automatic differentiation, calculating gradients of the objective function with respect to input parameters. When a trajectory is the input, it can be directly optimised. The choice of the neural network architecture depends on the trajectory representation. For example, graph neural networks [285] could be used for graph-represented trajectories. Autoencoders (AEs), encode the training data and are trained based on reconstruction of the corresponding variables with the decoder [152]. AEs reduce the design space dimensionality, extracting only essential features needed to optimise optical devices [286]. Therefore, AEs have been applied to the inverse design of electromagnetic scatterers [287, 288] and could be effective for waveguides if the trajectory would be stored as an image or the optimal guided field distribution would be searched for. Convolutional neural networks can also be used, performing convolutional operations on each layer's output.

The formalism for calculating the enhancement of photon pair generation in bent waveguides is applicable also to materials and structures not included in this thesis. While this study focuses on short waveguides, longer waveguides may be fabricated in practice, offering higher gain in pair generation rates. Understanding nonlinearity improvements can guide the design of integrated photonic devices for quantum optical applications, especially when chip space is limited.

The cross-energy scalar product between eigenmodes can be used for tracking modes as resonator parameters change in structures where the modes cannot be traced using symmetry arguments. A scalar product that includes the conjugate of the modes and their eigenfrequencies can be applied to complex structures lacking rotational symmetry.

This thesis presents a purely theoretical study, verified using numerical tools. It can be beneficial to experimentally test the results presented herein. The transmission obtained with the MMA should be benchmarked against practical measurements. Experimental testing could verify accuracy, especially for sharp bends. Furthermore, the optimisation algorithm for the trajectories as well as the predicted enhancement of photon pair generation rate and heralding efficiency could be tested in real-world scenarios.

Funded by the Deutsche Forschungsgemeinschaft (DFG, German Research Foundation) – Project-ID 258734477 – SFB 1173.

List of symbols and abbreviations

Unless otherwise specified in the text, the symbols and abbreviations used in this thesis are defined as follows:

Abbreviations

1D	one-dimensional
2D	two-dimensional
3D	three-dimensional
AE	Autoencoder
AlGaAs	aluminium gallium arsenide
ANN	artificial neural network
arb. unit	arbitrary unit
B-spline	basis spline
CMOS	complementary metal–oxide–semiconductor
CW	continuous-wave
ELU	exponential linear unit
FCA	free carrier absorption
FDE	finite difference eigenmode
FDTD	finite-difference time-domain
FMA	fundamental mode approximation
FWM	four-wave mixing
HE	heralding efficiency
IP-Dip	Nanoscribe IP resin used for two-photon polymerisation
LSTM	long short-term memory
MLP	multi-layer perceptron
MMA	multi-mode approximation
MSE	mean squared error
PIC	photonic integrated circuit
PML	perfectly matched layers
PWB	photonic wire bond
Q factor	quality factor
ReLU	rectified linear unit
SEM	scanning electron microscope

SFWM	spontaneous four-wave mixing
SGD	stochastic gradient descent
Si	silicon
Si_3N_4	silicon nitride
SiO_2	silicon dioxide (silica)
SNR	signal-to-noise ratio
SOI	silicon-on-insulator
SPDC	spontaneous parametric down-conversion
SPM	self-phase modulation
SpRS	spontaneous Raman scattering
SQP	sequential quadratic programming
TE	transverse-electric
THG	third-harmonic generation
TM	transverse-magnetic
TPA	two-photon absorption
UV	ultraviolet
WGM	whispering gallery mode
WGR	whispering gallery resonator

Symbols: Greek letters

α	absorption coefficient	$[\,-\,]$
β	propagation constant	$[\,\mathrm{m}^{-1}\,]$
β_m	propagation constant of mode m	$[\,\mathrm{m}^{-1}\,]$
Γ_3^{ijkl}	normalised nonlinearity	$[\,\mathrm{C}^{-4}\cdot\mathrm{kg}^{2}\cdot\mathrm{m}^{6}\cdot\mathrm{s}^{-4}\,]$
γ	parametrised curve	[arb. unit]
γ_{SFWM}	nonlinear coefficient	$[\,\mathrm{m}^{-1}\cdot\mathrm{W}^{-1}\,]$
Δ_j	error term for unit j	[arb. unit]
$\delta(\cdot)$	Dirac delta distribution	[arb. unit]
δ_{ij}	Kronecker delta	$[\,-\,]$
ε	electric permittivity	$[\,\mathrm{C}^{2}\cdot\mathrm{kg}^{-1}\cdot\mathrm{m}^{-3}\cdot\mathrm{s}^{2}\,]$
ε_0	vacuum permittivity	$[\,\mathrm{C}^{2}\cdot\mathrm{kg}^{-1}\cdot\mathrm{m}^{-3}\cdot\mathrm{s}^{2}\,]$
ε_r	relative dielectric function	$[\,-\,]$
ζ	learning rate	$[\,-\,]$
Θ	Heaviside step function	$[\,-\,]$
θ	angle of incidence	[rad]
θ_1	angle of incidence	[rad]
θ_2	angle of refraction	[rad]
θ_c	critical value of angle of incidence	[rad]
ϑ	angle of a bend	[rad]
κ	curvature	$[\,\mathrm{\mu m}^{-1}\,]$
Λ	helicity	$[\,-\,]$
λ	wavelength	[µm]
λ_0	vacuum wavelength	[µm]
μ	magnetic permeability	$[\,\mathrm{kg}\cdot\mathrm{m}\cdot\mathrm{s}^{-2}\cdot\mathrm{A}^{-2}\,]$
μ_0	vacuum magnetic permeability	$[\,\mathrm{kg}\cdot\mathrm{m}\cdot\mathrm{s}^{-2}\cdot\mathrm{A}^{-2}\,]$
μ_r	relative magnetic permeability	$[\,-\,]$
ν	arbitrary complex parameter	[arb. unit]
ρ	radial distance	[m]
ϱ	electric charge density	$[\,\mathrm{C}\cdot\mathrm{m}^{-3}\,]$
σ	standard deviation	[arb. unit]
τ	arbitrary complex parameter	[arb. unit]
ϕ	phase shift	[rad]
ϕ_j	j-th local basis function	[arb. unit]
φ	azimuthal angle	[rad]
χ_n	tensor of n-th-order electric susceptibility	$[\,\mathrm{m}^{n-1}\cdot\mathrm{V}^{-n+1}\,]$
χ_3^{ijkl}	tensor of 3$^{\mathrm{rd}}$-order electric susceptibility	$[\,\mathrm{m}^{2}\cdot\mathrm{V}^{-2}\,]$
$\bar{\chi}_3$	characteristic value of the susceptibility tensor components of the waveguide core	$[\,\mathrm{m}^{2}\cdot\mathrm{V}^{-2}\,]$
ψ_m	transverse field of mode m	[arb. unit]
Ω	bounded domain	[arb. unit]
ω	angular frequency	$[\,\mathrm{rad}\cdot\mathrm{s}^{-1}\,]$

Symbols: Latin letters

A	area	$[\mathrm{m}^2]$
A_{eff}	effective mode area	$[\mathrm{m}^2]$
a_j	local amplitude of j-th component	[arb. unit]
a_o	amplitude of an obstacle penalty function	[–]
$\mathbf{B}$	magnetic induction in frequency domain	[T]
$\widetilde{\mathbf{B}}$	magnetic induction in time domain	[T]
b	bias	[arb. unit]
b_j	j-th coefficient in a polynomial	[arb. unit]
$\mathbb{C}$	set of complex numbers	[–]
$\mathfrak{C}$	piecewise continuous contour	[arb. unit]
C^k	the space of k-times continuously differentiable functions	[arb. unit]
c_0	speed of light in vacuum	$[\mathrm{m{\cdot}s}^{-1}]$
$\mathbf{D}$	electric displacement in frequency domain	$[\mathrm{C{\cdot}m}^{-2}]$
$\widetilde{\mathbf{D}}$	electric displacement in time domain	$[\mathrm{C{\cdot}m}^{-2}]$
$\boldsymbol{\mathcal{D}}$	electric displacement amplitude	$[\mathrm{C{\cdot}m}^{-2}]$
$\mathcal{D}_i$	i-th Cartesian component of electric displacement amplitude	$[\mathrm{C{\cdot}m}^{-2}]$
$\mathfrak{D}$	computational domain	[arb. unit]
D	volume of the disk resonator	[arb. unit]
d	computational domain size	[µm]
d_j	desired output of j-th element	[arb. unit]
$\mathbf{E}$	electric field in frequency domain	$[\mathrm{V{\cdot}m}^{-1}]$
$\widetilde{\mathbf{E}}$	electric field in time domain	$[\mathrm{V{\cdot}m}^{-1}]$
$\boldsymbol{\mathcal{E}}$	transverse electric eigenfield	$[\mathrm{V{\cdot}m}^{-1}]$
$\mathcal{E}_i$	i-th Cartesian component of electric field amplitude	$[\mathrm{V{\cdot}m}^{-1}]$
e	Euler number	[–]
$\mathbf{F}$	arbitrary vector field	[arb. unit]
$\mathbf{F}_{\Lambda}$	helical field in frequency domain	[arb. unit]
$\widetilde{\mathbf{F}}_{\Lambda}$	helical field in time domain	[arb. unit]
$\mathcal{F}$	arbitrary mode in a disk resonator	[arb. unit]
f	scalar function	[arb. unit]
$\mathbf{G}$	arbitrary vector field	[arb. unit]
$\mathcal{G}$	arbitrary mode in a disk resonator	[arb. unit]
g	scalar function	[arb. unit]
$\mathbf{H}$	magnetic field in frequency domain	$[\mathrm{A{\cdot}m}^{-1}]$
$\widetilde{\mathbf{H}}$	magnetic field in time domain	$[\mathrm{A{\cdot}m}^{-1}]$
$\boldsymbol{\mathcal{H}}$	transverse magnetic eigenfield	$[\mathrm{A{\cdot}m}^{-1}]$
$\mathcal{H}_i$	i-th Cartesian component of magnetic field amplitude	$[\mathrm{A{\cdot}m}^{-1}]$

H	energy operator	[arb. unit]
h	height	[µm]
$\hbar$	reduced Planck constant	$[\mathrm{kg{\cdot}m^{2}{\cdot}s^{-1}}]$
i	imaginary unit	[–]
$\mathrm{Im}\{\cdot\}$	imaginary part	[arb. unit]
$\mathbf{J}$	current density in frequency domain	$[\mathrm{A{\cdot}m^{-2}}]$
$\widetilde{\mathbf{J}}$	current density in time domain	$[\mathrm{A{\cdot}m^{-2}}]$
$\mathbf{k}$	wave vector	$[\mathrm{m^{-1}}]$
k	wavenumber	$[\mathrm{m^{-1}}]$
k_0	vacuum wavenumber	$[\mathrm{m^{-1}}]$
$\mathcal{L}$	waveguide mode on the incident (left) interface side	[arb. unit]
L	length of waveguide	[m]
l	segment length, arc length	[m]
l_n	length of n-th segment	[m]
ℓ	varying computational domain size	[µm]
$\mathbf{M}$	magnetisation in frequency domain	$[\mathrm{A{\cdot}m^{-1}}]$
$\widetilde{\mathbf{M}}$	magnetisation in time domain	$[\mathrm{A{\cdot}m^{-1}}]$
$\boldsymbol{\mathcal{M}}$	helical modal field	$[\mathrm{V{\cdot}C{\cdot}s{\cdot}kg^{-\frac{1}{2}}{\cdot}m^{-\frac{5}{2}}}]$
$\mathcal{M}$	waveguide mode	[arb. unit]
M	SFWM generation efficiency	$[\mathrm{m^{3}{\cdot}s^{-2}{\cdot}kg}]$
m	mode number	[–]
m_z	parity	[–]
N	number of waveguide segments	[–]
N_x	number of grid points in x-direction	[–]
N_y	number of grid points in y-direction	[–]
N_ρ^f	radial mode number	[–]
N_φ^f	azimuthal mode number	[–]
N_z^f	axial mode number	[–]
n_1	refractive index of the waveguide core	[–]
n_2	refractive index of the waveguide cladding	[–]
n_{cl}	refractive index of the waveguide cladding	[–]
n_{co}	refractive index of the waveguide core	[–]
n_{eff}	effective refractive index	[–]
$\bar{n}_{\mathrm{J}}$	refractive index of the waveguide core at wavelength λ_{J}	[–]
$\hat{\mathbf{n}}$	unit normal vector	[–]
$\mathbf{P}$	polarisation in frequency domain	$[\mathrm{C{\cdot}m^{-2}}]$
$\widetilde{\mathbf{P}}$	polarisation in time domain	$[\mathrm{C{\cdot}m^{-2}}]$
$\mathcal{P}$	time-averaged power flow	[W]

$\mathcal{P}_\mathrm{P}$	pump power	[W]
P_j	j-th Cartesian component of polarisation vector	[C·m^{-2}]
$\hat{\boldsymbol{p}}$	propagation matrix	[–]
$\hat{\boldsymbol{p}}_n$	propagation matrix in the n-th waveguide segment	[–]
q	parameter related to radiation modes	[–]
$\mathbb{R}$	set of real numbers	[–]
$\mathbf{R}$	rotation matrix	[–]
$\mathcal{R}$	waveguide mode on the transmitted (right) interface side	[arb. unit]
$\mathscr{R}$	photon pair generation rate	[Hz]
R	radius of curvature	[µm]
R_min	minimum radius of curvature	[µm]
r_m	reflection coefficient of mode m	[–]
r_q	coefficient of a radiation mode q	[–]
$\hat{\boldsymbol{r}}$	reflection matrix	[–]
$\mathbf{r}$	position vector in 3D space	[arb. unit]
$\mathbf{r}_\perp$	position vector in 2D space perpendicular to the propagation direction of wave	[arb. unit]
$\mathrm{Re}\{\cdot\}$	real part	[arb. unit]
$\mathbf{S}$	outward pointing surface vector	[arb. unit]
$\overline{\mathbf{S}}$	time-averaged Poynting vector	[W·m^{-2}]
s	curve parameter	[–]
$\mathbf{T}$	vector of amplitude transmissions	[–]
T	power transmission	[–]
T_b	power transmission impaired by bending	[–]
T_m	amplitude transmission of mode m	[–]
T_t	power transmission at the interface	[–]
t	time	[s]
t_m	transmission coefficient for mode m	[–]
t_{mn}	transmission of mode n into mode m	[–]
$\bar{t}_0$	asymptotic value of $\lvert t_0 \rvert$ for infinite computational domain	[–]
$\hat{\boldsymbol{t}}$	transmission matrix	[–]
$\hat{\boldsymbol{t}}_n$	transmission matrix through the n-th interface	[–]
$\mathbf{u}$	vector function	[arb. unit]
V	normalised frequency	[–]
v_g	group velocity	[m·s^{-1}]
v_J	group velocity of signal (J=S), idler (J=I) or pump (J=P) mode	[m·s^{-1}]
v_ph	phase velocity	[m·s^{-1}]
$\mathbf{v}$	vector function	[arb. unit]

$\hat{\mathbf{v}}$	unit vector tangential to the curve	[arb. unit]
$\overline{\mathbf{v}}$	test vector function	[arb. unit]
w	width	[µm]
$w_{ij,n}$	weight for multiplication of value $Y_{j,n+1}$ with $Y_{i,n}$	[–]
$\mathbf{X}$	input vector for ANN	[arb. unit]
X_i	component of vector $\mathbf{X}$	[arb. unit]
x	Cartesian coordinate	[arb. unit]
$\hat{\mathbf{x}}$	unit vector in x-direction	[arb. unit]
Y	value of the output node of final ANN layer	[arb. unit]
$Y_{i,j}$	value of i-th node of j-th ANN layer	[arb. unit]
y	Cartesian coordinate	[arb. unit]
$\hat{\mathbf{y}}$	unit vector in y-direction	[arb. unit]
Z_0	vacuum impedance	[$\mathrm{V{\cdot}A^{-1}}$]
z	Cartesian coordinate	[arb. unit]
$\hat{\mathbf{z}}$	unit vector in z-direction	[arb. unit]

List of Figures

List of Tables

A | Selected integral identities for vector fields

The aim of this appendix is to show the integral identities for vector fields, necessary to derive equation (2.67).

A.1. Integration by parts

The weak formulation (2.67) is derived utilising integration by parts. We consider a bounded domain $\Omega \subseteq \mathbb{R}^3$ with a boundary $\partial\Omega$ and outer normal vector $\hat{\mathbf{n}}$. The standard integration by parts for sufficiently smooth vector field $\mathbf{u}$ and a function $g : \Omega \to \mathbb{R}$ reads [89, Theorem 6.7]

$$\int_\Omega \mathbf{u} \cdot (\nabla g) \,\mathrm{d}\mathbf{r} = -\int_\Omega g(\nabla \cdot \mathbf{u}) \,\mathrm{d}\mathbf{r} + \int_{\partial\Omega} g(\hat{\mathbf{n}} \cdot \mathbf{u}) \,\mathrm{d}s\,. \tag{A.1}$$

We consider now $\nabla\times$ in $\mathbb{R}^3$. For smooth vector fields $\mathbf{u}$ and $\mathbf{v}$ the following identity holds [89, Theorem 6.7]

$$\int_\Omega \mathbf{v} \cdot (\nabla \times \mathbf{u}) \,\mathrm{d}\mathbf{r} = \int_\Omega \mathbf{u} \cdot (\nabla \times \mathbf{v}) \,\mathrm{d}\mathbf{r} + \int_{\partial\Omega} (\hat{\mathbf{n}} \times \mathbf{u}) \cdot \mathbf{v} \,\mathrm{d}s\,. \tag{A.2}$$

An integrable vector field $\mathbf{u} : \Omega \to \mathbb{R}^3$ has a weak curl $\mathbf{w} : \Omega \to \mathbb{R}^3$ if $\mathbf{w}$ is an integrable vector field and

$$\int_\Omega \mathbf{u} \cdot \nabla \times \mathbf{v} \,\mathrm{d}\mathbf{r} = \int_\Omega \mathbf{w} \cdot \mathbf{v} \,\mathrm{d}\mathbf{r} \quad \forall \mathbf{v} \in C_0^\infty(\Omega)^3. \tag{A.3}$$

Then $\nabla \times \mathbf{u} := \mathbf{w}$. We use the weak curl formulation and the conditions $\hat{\mathbf{n}} \times \mathbf{u} = 0$ and $\hat{\mathbf{n}} \times \mathbf{v} = 0$ to derive the weak formulation (2.67), as described in Section 2.3.1. The function $\mathbf{v}$ is of class $C_0^\infty(\Omega)^3$, which means it is infinitely differentiable function in Ω and has compact support.

B | Material parameters used for calculating photon pair generation rates

The relationship between wavelength and the refractive indices of waveguide cores in Chapter 5 is calculated with the Sellmeier equation [241, 242] as

$$n^2(\lambda) = a + \frac{b_1\lambda^2}{\lambda^2 - c_1} + \frac{b_2\lambda^2}{\lambda^2 - c_2} + \frac{b_3\lambda^2}{\lambda^2 - c_3}\,, \tag{B.1}$$

where λ denotes wavelength in µm.

The values of the coefficients for equation (B.1) were determined from sample data points with a built-in MATLAB function *nlinfit*, which performs nonlinear regression using iterative least squares estimation [119]. The sample data points were obtained from Ansys Lumerical database, and from [237, 243, 244] as explained in Section 5.6. The estimated coefficients are listed in Table B.1. The resulting refractive indices are plotted against wavelength in Figure B.1.

Table B.1.: Coefficients of Sellmeier equation (B.1) for waveguide materials studied in Chapter 5. The accuracy of the estimation is given by the MSE, calculated with the default error model [119], as follows: $5.793{\cdot}10^{-10}$ for AlGaAs, $9.154{\cdot}10^{-8}$ for IP-Dip, $8.475{\cdot}10^{-6}$ for Si, and $1.177{\cdot}10^{-4}$ for Si_3N_4.

Material	a	b_1	c_1	b_2	c_2	b_3	c_3
AlGaAs	4.4302974	2.0204167	0.3475250	2.0204037	0.29956242	2.0203885	0.3238461
IP-Dip	1.9601145	0.3939766	0.2120315	32223721	-71846.197	4277751336	-53422328
Si	3.3906663	8.1959014	0.3550445	266.83067	-28.508148	-1201578462	59199.975
Si_3N_4	2.2301091	-0.0025954	0.4088873	1.6933328	0.1626338	-19224095	8764403.6

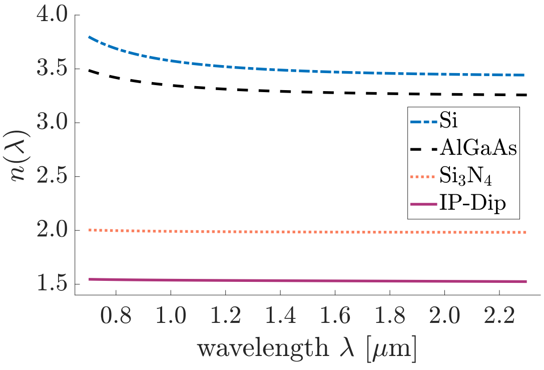

Figure B.1: Dependence of refractive indices on wavelength, calculated with Sellmeier equation (B.1) for the materials and coefficients from Table B.1.

The values of the component χ_3^{1111} of the third-order susceptibility, used for calculations in Chapter 5, are presented in Table B.2.

Table B.2.: Values of χ_3^{1111} in $\mathrm{m}^2/\mathrm{V}^2$ for waveguide core and cladding materials studied in Chapter 5.

AlGaAs	IP-Dip	Si	Si_3N_4	SiO_2	air
$5.7114 \cdot 10^{-19}$	$2.8169 \cdot 10^{-22}$	$1.1047 \cdot 10^{-19}$	$3.3391 \cdot 10^{-21}$	$2.5 \cdot 10^{-22}$	$1.7 \cdot 10^{-25}$

The group velocity of a bulk material is calculated, based on [193, equation (69)], as

$$v_{\mathrm{g}}(\omega) = \frac{v_{\mathrm{ph}}(\omega)}{1 + \frac{\omega}{n(\omega)} \frac{\partial n(\omega)}{\partial \omega}}\,, \tag{B.2}$$

with $n(\omega)$ calculated from equation (B.1), $v_{\mathrm{ph}}(\omega) = c_0 n(\omega)^{-1}$, and $\omega = 2\pi c_0 \lambda^{-1}$.

C | Remarks to the chapter on whispering gallery resonators

This appendix presents complementary derivations to Chapter 6. The derivations are based in significant extent on the ideas of M.Sc. Lukas Rebholz and Dr. Ivan Fernandez-Corbaton.

C.1. Derivation of the formula for an energy scalar product

This section shows the derivation of equation (6.11) from the cross-energy scalar product (6.9). Inserting (6.8) into (6.9) results in

$$\langle \mathcal{F}|\mathrm{H}|\mathcal{G}\rangle = \sum_{\Lambda=\pm 1}(-\mathrm{i}\Lambda)\frac{c_0^2}{2\pi}\int\limits_0^\infty \frac{\mathrm{d}|\mathbf{k}|}{(c_0|\mathbf{k}|-\omega_f^*)(c_0|\mathbf{k}|-\omega_g)}\int\limits_{\partial D}[\boldsymbol{\mathcal{M}}_{\Lambda,f}(\mathbf{r})^*\times\boldsymbol{\mathcal{M}}_{\Lambda,g}(\mathbf{r})]\cdot\mathrm{d}\mathbf{S}(\mathbf{r})\,, \tag{C.1}$$

where the subscripts f and g refer to the considered resonant modes.

The integral over $|\mathbf{k}|$ can be solved analytically by partial fraction decomposition in the lower limit of integration $|\mathbf{k}| \to 0$:

$$\int\limits_0^\infty \frac{\mathrm{d}|\mathbf{k}|}{(c_0|\mathbf{k}|-\omega_f^*)(c_0|\mathbf{k}|-\omega_g)} = \frac{\ln(-\omega_g)-\ln(-\omega_f^*)}{c_0(\omega_f^*-\omega_g)}\,. \tag{C.2}$$

Figure C.1 presents real and imaginary parts of the integral in (C.2) calculated for anti-crossing modes of $m_z = -1$ and for modes with themselves.

To calculate the surface integral in equation (C.1) the surface element of the disk can be written as $\mathrm{d}\mathbf{S}(\mathbf{r}) = \rho \mathrm{d}s\mathrm{d}\varphi\hat{\mathbf{n}}(\mathbf{r})$, in cylindrical coordinates (ρ, φ, z), with surface normal vector $\hat{\mathbf{n}}$. The contour $\mathcal{C}$ refers to the one-dimensional curve defined at the $\varphi = 0$ slice of ∂D, and $\mathrm{d}s$ denotes the differential curve length along $\mathcal{C}$. Calculating the integral over φ, for the modes (6.1) with equal N_φ, yields a prefactor of 2π. The values of the surface integrals, summed for both helicities, are plotted as a function of disk thickness in Figure C.2.

The intention of the plots in Figure C.2 is to show the general behaviour of the surface integral as a function of disk thickness. The actual values are not physically meaningful, as they depend on the normalisation scheme of JCMsuite. For example, the current normalisation apparently permits relative changes in sign between modes evaluated at different disk thicknesses, as can be observed in the left column in Figure C.2. This freedom of normalisation is implied by the fact that scaling the numerical modal fields, $\boldsymbol{\mathcal{E}}_f(\mathbf{r})$ and $\boldsymbol{\mathcal{H}}_f(\mathbf{r})$, by an arbitrary (complex) factor, still represents valid solutions to the resonance problem. This observation does not impact the data discussed in the main text since we only consider the absolute values of the normalised scalar product in (C.1).

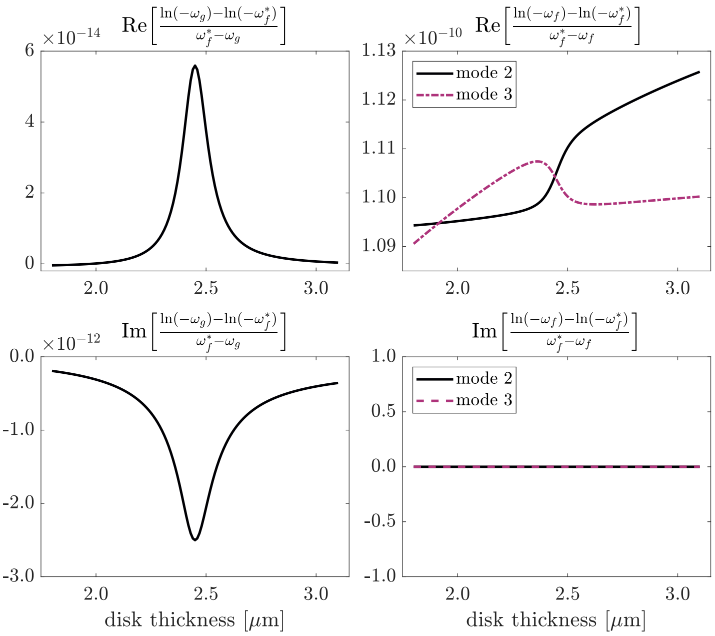

Figure C.1.: Real (top) and imaginary parts (bottom) of the integral over $|\mathbf{k}|$ for two anti-crossing modes with $m_z = -1$ are presented in the left column. Right column presents the real (top) and imaginary (bottom) parts of the integral in (C.2) for the particular modes with themselves. This figure has been published also in [S1].

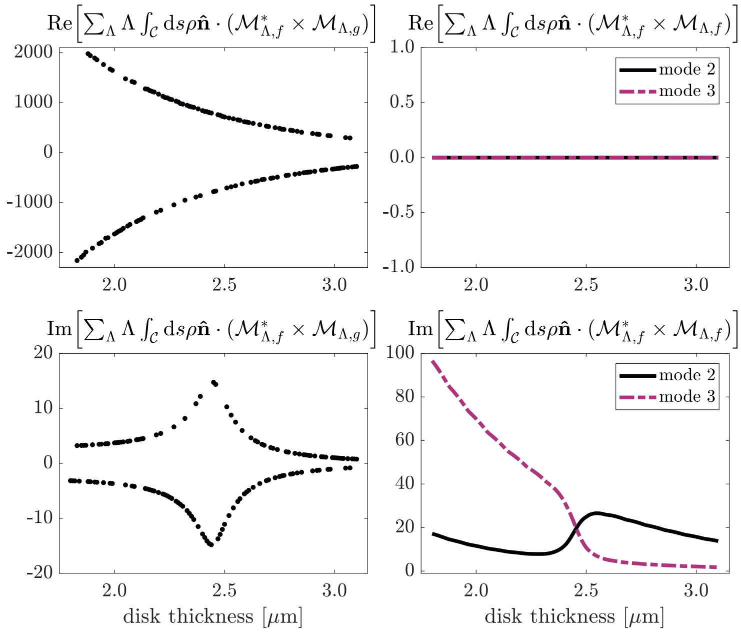

Figure C.2.: Real (top) and imaginary parts (bottom) of the contour integral of two anti-crossing modes with $m_z = -1$ are presented in the left column. Right column presents the real (top) and imaginary (bottom) parts of the contour integral for the modes with themselves. This figure has been published also in [S1].

Concluding, the final formula for the cross-energy scalar product reads

$$\langle\mathcal{F}|\mathrm{H}|\mathcal{G}\rangle = \sum_{\Lambda=\pm 1}(-\mathrm{i}\Lambda c_0)\frac{\ln(-\omega_g)-\ln(-\omega_f^*)}{\omega_f^*-\omega_g}\int\limits_{\mathcal{C}}\rho\hat{\mathbf{n}}(\mathbf{r})\cdot\left[\boldsymbol{\mathcal{M}}_{\Lambda,f}(\mathbf{r})^*\times\boldsymbol{\mathcal{M}}_{\Lambda,g}(\mathbf{r})\right]\mathrm{d}s\,. \tag{C.3}$$

The following section explains the approximation influencing the form of helical fields and consequently the formulation of the scalar product (C.3).

C.2. Approximated expression for the helical fields

To date, it is known that the correct expression for the helical field is

$$\mathbf{F}_\Lambda(\mathbf{r},|\mathbf{k}|) = \frac{\mathrm{i}c_0\boldsymbol{\mathcal{M}}_\Lambda(\mathbf{r})}{\sqrt{2\pi}\,(c_0|\mathbf{k}|-\omega)} + \frac{\mathrm{i}c_0\boldsymbol{\mathcal{M}}_\Lambda(\mathbf{r})^*}{\sqrt{2\pi}\,(c_0|\mathbf{k}|+\omega^*)}\,. \tag{C.4}$$

This field $\mathbf{F}_\Lambda(\mathbf{r},|\mathbf{k}|)$ defines a physical radiation field, satisfying the condition

$$\mathbf{F}_\Lambda(\mathbf{r},|\mathbf{k}|) = \mathbf{F}_\Lambda(\mathbf{r},-|\mathbf{k}|)^*\,. \tag{C.5}$$

The reason for this condition is that in electromagnetism the information contained in the negative frequency solution must be the same as the information carried by the positive frequency solution [289, §3.1]. Therefore, the eigenmodes obtained from the FEM solver are complemented by their conjugate counterparts $\{\boldsymbol{\mathcal{E}}(\mathbf{r})^*, \boldsymbol{\mathcal{H}}(\mathbf{r})^*\}$ with a complex frequency $-\omega^*$ [290, Section 2.8]. This fact is accounted for in expression (C.4).

The formulation (C.4) implies changes on the cross-energy scalar product, which are described in the revised version of [S1], submitted on 10th February 2025. The calculations were performed by M.Sc. Lukas Rebholz and Dr. Ivan Fernandez-Corbaton and, therefore, not included as part of this thesis. However, it was also observed that the solution obtained with the new formulation does not change qualitatively in the context of the disk resonator.

Therefore, in the case of this thesis, it is permitted to use the approximation, in which only the positive real parts of the eigenfrequencies are considered for the cross-energy scalar product (6.11). This approximation is based on the observation that the contribution from the negative counterpart is negligible, as shown qualitatively in Figure C.3. Figure C.3 depicts the influence of the eigenfrequencies on the field defined in equation (C.4), both the real part (Figure C.3(a)) and imaginary part (Figure C.3(b)). The two peaks come from the two components of the sum. In our approximation, we consider only positive wavenumbers k, for which the peak from ω is not influenced by the other peak, as the spectral distance between these peaks is to large.

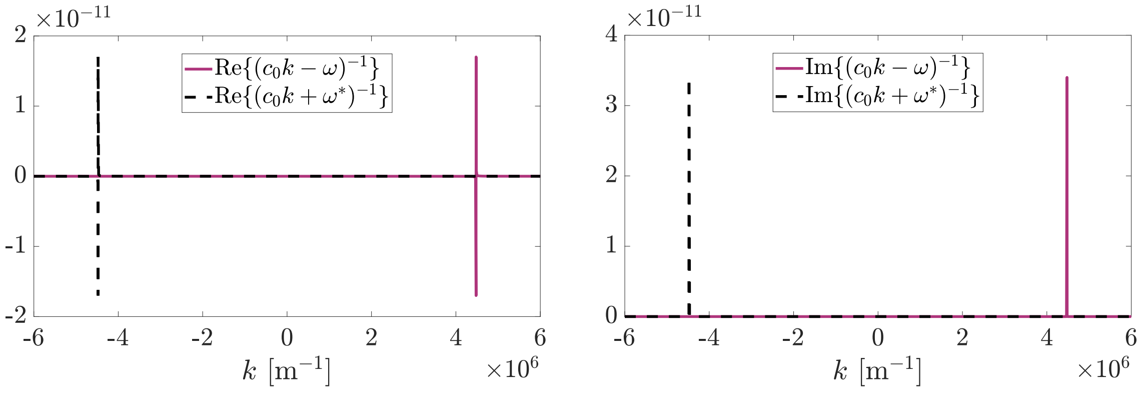

(a)

(b)

Figure C.3.: (a) Real part and (b) imaginary part of the components of the sum in equation (C.4) mostly influencing the result of equation (C.4), as a function of k, for $\omega = 1.34 \cdot 10^{15} + \mathrm{i}\,2.94 \cdot 10^{10}$ [rad$\cdot$s^{-1}]. The values in the positive range of k are assumed not to be influenced by the *tail* of the peak in the negative range of k.

Bibliography

[1] Kish, F., Lal, V., Evans, P., Corzine, S. W., Ziari, M., Butrie, T., Reffle, M., Tsai, H.-S., Dentai, A., Pleumeekers, J., "System-on-chip photonic integrated circuits," IEEE Journal of Selected Topics in Quantum Electronics **24**, 1–20 (2017).

[2] Miller, S. E., "Integrated optics: an introduction," The Bell system technical journal **48**, 2059–2069 (1969).

[3] Heck, M. J., Bauters, J. F., Davenport, M. L., Doylend, J. K., Jain, S., Kurczveil, G., Srinivasan, S., Tang, Y., Bowers, J. E., "Hybrid silicon photonic integrated circuit technology," IEEE Journal of Selected Topics in Quantum Electronics **19**, 6100117–6100117 (2012).

[4] Dong, P., Chen, Y.-K., Duan, G.-H., Neilson, D. T., "Silicon photonic devices and integrated circuits," Nanophotonics **3**, 215–228 (2014).

[5] Arafin, S., Coldren, L. A., "Advanced inp photonic integrated circuits for communication and sensing," IEEE Journal of Selected Topics in Quantum Electronics **24**, 1–12 (2017).

[6] Butt, M. A., Kazanskiy, N. L., Khonina, S. N., Voronkov, G. S., Grakhova, E. P., Kutluyarov, R. V., "A review on photonic sensing technologies: status and outlook," Biosensors **13**, 568 (2023).

[7] Caulfield, H. J., Westphal, J., "The logic of optics and the optics of logic," Information Sciences **162**, 21–33 (2004).

[8] Miller, D. A., "Are optical transistors the logical next step?" Nature Photonics **4**, 3–5 (2010).

[9] Reck, M., Zeilinger, A., Bernstein, H. J., Bertani, P., "Experimental realization of any discrete unitary operator," Physical Review Letters **73**, 58 (1994).

[10] Clements, W. R., Humphreys, P. C., Metcalf, B. J., Kolthammer, W. S., Walmsley, I. A., "Optimal design for universal multiport interferometers," Optica **3**, 1460–1465 (2016).

[11] Xu, Q., Lipson, M., "All-optical logic based on silicon micro-ring resonators," Optics Express **15**, 924–929 (2007).

[12] Cheng, J., Zhou, H., Dong, J., "Photonic matrix computing: from fundamentals to applications," Nanomaterials **11**, 1683 (2021).

[13] Aghaee Rad, H., Ainsworth, T., Alexander, R., Altieri, B., Askarani, M., Baby, R., Banchi, L., Baragiola, B., Bourassa, J., Chadwick, R., "Scaling and networking a modular photonic quantum computer," Nature, 1–8 (2025).

[14] Celler, G. K., Cristoloveanu, S., "Frontiers of silicon-on-insulator," Journal of Applied Physics **93**, 4955–4978 (2003).

[15] Armenise, M., "Fabrication techniques of lithium niobate waveguides," IEE Proceedings J (Optoelectronics) **135**, 85–91 (1988).

[16] Bazzan, M., Sada, C., "Optical waveguides in lithium niobate: recent developments and applications," Applied Physics Reviews **2**, 040603 (2015).

[17] Blumenthal, D. J., Heideman, R., Geuzebroek, D., Leinse, A., Roeloffzen, C., “Silicon nitride in silicon photonics,” Proceedings of the IEEE **106**, 2209–2231 (2018).

[18] Moss, D. J., Morandotti, R., Gaeta, A. L., Lipson, M., “New CMOS-compatible platforms based on silicon nitride and hydex for nonlinear optics,” Nature Photonics **7**, 597–607 (2013).

[19] Politi, A., Cryan, M. J., Rarity, J. G., Yu, S., O’brien, J. L., “Silica-on-silicon waveguide quantum circuits,” Science **320**, 646–649 (2008).

[20] Wang, J., Santamato, A., Jiang, P., Bonneau, D., Engin, E., Silverstone, J. W., Lermer, M., Beetz, J., Kamp, M., Höfling, S., “Gallium arsenide (gaas) quantum photonic waveguide circuits,” Optics Communications **327**, 49–55 (2014).

[21] Verrinder, P. A., Wang, L., Fridlander, J., Sang, F., Rosborough, V., Nickerson, M., Yang, G., Stephen, M., Coldren, L., Klamkin, J., “Gallium arsenide photonic integrated circuit platform for tunable laser applications,” IEEE Journal of Selected Topics in Quantum Electronics **28**, 1–9 (2021).

[22] Ma, H., Jen, A.-Y., Dalton, L. R., “Polymer-based optical waveguides: materials, processing, and devices,” Advanced Materials **14**, 1339–1365 (2002).

[23] Yeniay, A., Gao, R., Takayama, K., Gao, R., Garito, A. F., “Ultra-low-loss polymer waveguides,” Journal of Lightwave Technology **22**, 154 (2004).

[24] Carroll, L., Lee, J.-S., Scarcella, C., Gradkowski, K., Duperron, M., Lu, H., Zhao, Y., Eason, C., Morrissey, P., Rensing, M., “Photonic packaging: transforming silicon photonic integrated circuits into photonic devices,” Applied Sciences **6**, 426 (2016).

[25] Borghi, M., Castellan, C., Signorini, S., Trenti, A., Pavesi, L., “Nonlinear silicon photonics,” Journal of Optics **19**, 093002 (2017).

[26] Dolgaleva, K., Ng, W. C., Qian, L., Aitchison, J. S., “Compact highly-nonlinear AlGaAs waveguides for efficient wavelength conversion,” Optics Express **19**, 12440–12455 (2011).

[27] Politi, A., Matthews, J. C., Thompson, M. G., O’Brien, J. L., “Integrated quantum photonics,” IEEE Journal of Selected Topics in Quantum Electronics **15**, 1673–1684 (2009).

[28] Chi, Y., Huang, J., Zhang, Z., Mao, J., Zhou, Z., Chen, X., Zhai, C., Bao, J., Dai, T., Yuan, H., “A programmable qudit-based quantum processor,” Nature Communications **13**, 1166 (2022).

[29] Sun, C., Wade, M. T., Lee, Y., Orcutt, J. S., Alloatti, L., Georgas, M. S., Waterman, A. S., Shainline, J. M., Avizienis, R. R., Lin, S., “Single-chip microprocessor that communicates directly using light,” Nature **528**, 534–538 (2015).

[30] Blaicher, M., Billah, M. R., Kemal, J., Hoose, T., Marin-Palomo, P., Hofmann, A., Kutuvantavida, Y., “Hybrid multi-chip assembly of optical communication engines by in situ 3D nano-lithography,” Light: Science & Applications **9**, 71 (2020).

[31] Fischer, J., Wegener, M., “Three-dimensional optical laser lithography beyond the diffraction limit,” Laser & Photonics Reviews **7**, 22–44 (2013).

[32] Von Freymann, G., Ledermann, A., Thiel, M., Staude, I., Essig, S., Busch, K., Wegener, M., “Three-dimensional nanostructures for photonics,” Advanced Functional Materials **20**, 1038–1052 (2010).

[33] Bernardeschi, I., Ilyas, M., Beccai, L., “A review on active 3D microstructures via direct laser lithography,” Advanced Intelligent Systems **3**, 2100051 (2021).

[34] Maruo, S., Nakamura, O., Kawata, S., “Three-dimensional microfabrication with two-photon-absorbed photopolymerization,” Optics Letters **22**, 132–134 (1997).

[35] Denk, W., Strickler, J. H., Webb, W. W., “Two-photon laser scanning fluorescence microscopy,” Science **248**, 73–76 (1990).

[36] Peticolas, W. L., Goldsborough, J. P., Rieckhoff, K., “Double photon excitation in organic crystals,” Physical Review Letters **10**, 43 (1963).

[37] Muller, P., “Glossary of terms used in physical organic chemistry (iupac recommendations 1994),” Pure and Applied Chemistry **66**, 1155 (1994).

[38] Fatkullin, N., Ikehara, T., Jinnai, H., Kawata, S., Kimmich, R., Nishi, T., Nishikawa, Y., Sun, H.-B., Sun, H.-B., Kawata, S., “Two-photon photopolymerization and 3D lithographic microfabrication,” NMR • 3D Analysis • Photopolymerization, 169–273 (2004).

[39] O’Halloran, S., Pandit, A., Heise, A., Kellett, A., “Two-photon polymerization: fundamentals, materials, and chemical modification strategies,” Advanced Science **10**, 2204072 (2023).

[40] Unlu, B., Álvarez-Castaño, M. I., Boniface, A., Pu, Y., Moser, C., “Single-photon-assisted two-photon polymerization,” Additive Manufacturing **94**, 104455 (2024).

[41] Kawata, S., Sun, H.-B., Tanaka, T., Takada, K., “Finer features for functional microdevices,” Nature **412**, 697–698 (2001).

[42] Lindenmann, N., Balthasar, G., Hillerkuss, D., Schmogrow, R., Jordan, M., Leuthold, J., Freude, W., Koos, C., “Photonic wire bonding: a novel concept for chip-scale interconnects,” Optics Express **20**, 17667–17677 (2012).

[43] Lindenmann, N., Dottermusch, S., Goedecke, M. L., Hoose, T., Billah, M. R., Onanuga, T. P., Hofmann, A., Freude, W., Koos, C., “Connecting silicon photonic circuits to multicore fibers by photonic wire bonding,” Journal of lightwave Technology **33**, 755–760 (2015).

[44] Thomson, D., Zilkie, A., Bowers, J. E., Komljenovic, T., Reed, G. T., Vivien, L., Marris-Morini, D., Cassan, E., Virot, L., Fédéli, J.-M., Hartmann, J.-M., Schmid, J. H., Xu, D.-X., Boeuf, F., O’Brien, P., Mashanovich, G. Z., Nedeljkovic, M., “Roadmap on silicon photonics,” Journal of Optics **18**, 073003 (2016).

[45] Billah, M. R., Blaicher, M., Hoose, T., Dietrich, P.-I., Marin-Palomo, P., Lindenmann, N., Nesic, A., Hofmann, A., Troppenz, U., Moehrle, M., Randel, S., Freude, W., Koos, C., “Hybrid integration of silicon photonics circuits and InP lasers by photonic wire bonding,” Optica **5**, 876–883 (2018).

[46] Lindenmann, N., “Photonic wire bonding as a novel technology for photonic chip interfaces,” PhD thesis (Karlsruhe Institute of Technology, 2017).

[47] Blaicher, M. J., “Photonic packaging enabled by three-dimensional micro-printing,” PhD thesis (Karlsruhe Institute of Technology (KIT), 2022), 209 pp.

[48] Lindenmann, N., Balthasar, G., Palmer, R., Schuele, S., Leuthold, J., Freude, W., Koos, C., “Photonic wire bonding for single-mode chip-to-chip interconnects,” in 8th ieee international conference on group iv photonics (IEEE, 2011), pp. 380–382.

[49] Hiremath, K. R., Hammer, M., Stoffer, R., Prkna, L., Čtyroký, J., “Analytic approach to dielectric optical bent slab waveguides,” en, Optical and Quantum Electronics **37**, 37–61 (2005).

[50] Paul, T., “Light propagation in optical metamaterials: a Bloch modal approach,” PhD thesis (Friedrich-Schiller-Universität Jena, 2012).

[51] Śmigaj, W., Lalanne, P., Yang, J., Paul, T., Rockstuhl, C., Lederer, F., “Closed-form expression for the scattering coefficients at an interface between two periodic media,” Applied Physics Letters **98**, 111107 (2011).

[52] Negredo, F., Blaicher, M., Nesic, A., Kraft, P., Ott, J., Dörfler, W., Koos, C., Rockstuhl, C., "Fast and reliable method to estimate losses of single-mode waveguides with an arbitrary 2D trajectory," Journal of the Optical Society of America A **35**, 1063–1073 (2018).

[53] Nesic, A., "3D Freeform Waveguides in Integrated Optics—Concepts, Modeling, and Applications," PhD thesis (Karlsruhe Institute of Technology (KIT), 2022).

[54] Chao, C.-y., Guo, L. J., "Polymer microring resonators fabricated by nanoimprint technique," Journal of Vacuum Science & Technology B: Microelectronics and Nanometer Structures Processing, Measurement, and Phenomena **20**, 2862–2866 (2002).

[55] Yuan, Z., Wu, P. C., Chen, Y.-C., "Optical resonator enhanced photovoltaics and photocatalysis: fundamental and recent progress," Laser & Photonics Reviews **16**, 2100202 (2022).

[56] Matsko, A. B., Ilchenko, V. S., "Optical resonators with whispering-gallery modes-part I: basics," IEEE Journal of selected topics in quantum electronics **12**, 3–14 (2006).

[57] Vahala, K. J., "Optical microcavities," Nature **424**, 839–846 (2003).

[58] Barwicz, T., Popovic, M. A., Rakich, P. T., Watts, M. R., Haus, H. A., Ippen, E. P., Smith, H. I., "Microring-resonator-based add-drop filters in SiN: fabrication and analysis," Optics Express **12**, 1437–1442 (2004).

[59] Ilchenko, V. S., Matsko, A. B., "Optical resonators with whispering-gallery modes-part II: applications," IEEE J. Sel. Top. Quantum Electron. **12**, 15–32 (2006).

[60] Steiner, T. J., Castro, J. E., Chang, L., Dang, Q., Xie, W., Norman, J., Bowers, J. E., Moody, G., "Ultrabright entangled-photon-pair generation from an al ga as-on-insulator microring resonator," PRX Quantum **2**, 010337 (2021).

[61] Fürst, J., Strekalov, D., Elser, D., Aiello, A., Andersen, U. L., Marquardt, C., Leuchs, G., "Quantum light from a whispering-gallery-mode disk resonator," Physical Review Letters **106**, 113901 (2011).

[62] Jackson, J. D., *Classical electrodynamics*, 3rd ed. (New York; Weinheim: Wiley, 1999).

[63] Griffiths, D. J., *Introduction to electrodynamics fourth edition*, 4th ed. (Pearson Education, Inc., 2012).

[64] Born, M., Wolf, E., *Principles of optics: electromagnetic theory of propagation, interference and diffraction of light* (Elsevier, 2013).

[65] JCMwave GmbH Berlin, "JCMsuite Documentation," https://www.jcmwave.com/docs/ParameterReference/ (2019).

[66] Stratton, J. A., *Electromagnetic theory*, Vol. 33 (John Wiley & Sons, 2007).

[67] Idzik, P., "Application of bifurcation theory for existence of travelling waves in examples of semilinear and quasilinear wave equations," PhD thesis (Karlsruhe Institute of Technology (KIT), 2017).

[68] Nanz, S., "Tailored light scattering and emission in solar cells and LEDs using ordered and disordered interfaces," PhD thesis (Karlsruhe Institute of Technology, 2019).

[69] Saleh, B. E., Teich, M. C., *Fundamentals of photonics* (John Wiley & Sons, 2019).

[70] Snyder, A. W., Love, J. D., *Optical waveguide theory* (Champman and Hall, 1983).

[71] Okamoto, K., *Fundamentals of optical waveguides*, 2. (Elsevier; Acadamic Press, Amsterdam, 2006).

[72] Moloney, J. V., Newell, A. C., *Nonlinear optics* (Westview Press, 2004).

[73] Iizuka, K., *Elements of photonics, volume ii: for fiber and integrated optics*, Vol. 41 (John Wiley & Sons, 2002).

[74] Hammer, M., Babel, S., Farheen, H., Padberg, L., Scheytt, J. C., Silberhorn, C., Förstner, J., “Estimation of losses caused by sidewall roughness in thin-film lithium niobate rib and strip waveguides,” Optics Express **32**, 22878–22891 (2024).

[75] Zhang, E., Zhu, X., Zhang, L., “Effective and group refractive index extraction and cross-sectional dimension estimation for silicon-on-insulator rib waveguides,” Optics Express **32**, 31375–31388 (2024).

[76] Mahfouz, A. M., Kishk, A. A., “Wideband dual mode trapezoidal to square waveguide transition,” in 2024 international telecommunications conference (itc-egypt) (IEEE, 2024), pp. 124–127.

[77] Ramker, A., McClenathan, K., Shellenbarger, Z., Poole, B. R., Kostinski, N. B., Toor, F., “2D trapezoidal waveguide design for near one terahertz quantum cascade lasers,” in Optical Modeling and Performance Predictions XIV, Vol. 13129 (SPIE, 2024), pp. 179–187.

[78] Marcatili, E. A., “Dielectric rectangular waveguide and directional coupler for integrated optics,” Bell System Technical Journal **48**, 2071–2102 (1969).

[79] Kumar, A., Thyagarajan, K., Ghatak, A. K., “Analysis of rectangular-core dielectric waveguides: an accurate perturbation approach,” Optics Letters **8**, 63–65 (1983).

[80] Tamir, T., “Beam and waveguide couplers,” in *Integrated optics* (Springer, 1975), pp. 83–137.

[81] Poulton, C. G., Koos, C., Fujii, M., Pfrang, A., Schimmel, T., Leuthold, J., Freude, W., “Radiation modes and roughness loss in high index-contrast waveguides,” IEEE Journal of selected topics in quantum electronics **12**, 1306–1321 (2006).

[82] Lecamp, G., Hugonin, J. P., Lalanne, P., “Theoretical and computational concepts for periodic optical waveguides,” Optics Express **15**, 11042–11060 (2007).

[83] Paul, T., Menzel, C., Śmigaj, W., Rockstuhl, C., Lalanne, P., Lederer, F., “Reflection and transmission of light at periodic layered metamaterial films,” Physical Review B **84**, 115142 (2011).

[84] CST Studio Suite, “CST Microwave Studio,” http://www.cst.com (2008).

[85] Lumerical Inc, *MODE: Waveguide Simulator*, version 2021 R2.3, Feb. 19, 2024.

[86] Santiago, X. G., “Numerical methods for shape optimization of photonic nanostructures,” PhD thesis (Karlsruhe Institute of Technology (KIT), 2021).

[87] Burger, S., Zschiedrich, L., Pomplun, J., Schmidt, F., “JCMsuite: An adaptive fem solver for precise simulations in nano-optics,” in Integrated photonics and nanophotonics research and applications (Optica Publishing Group, 2008), ITuE4.

[88] Mnasri, K., “Modeling optical metamaterials with strong spatial dispersion,” PhD thesis (Karlsruhe Institute of Technology (KIT), 2020).

[89] Kirsch, A., Hettlich, F., “The mathematical theory of Maxwell’s equations,” Lecture notes (2009).

[90] Monk, P., *Finite element methods for Maxwell’s equations* (Clarendon Press, Oxford, 2003).

[91] Kagerer, F., “Finite elements for Maxwell’s equations,” Bachelor’s Thesis (Johannes Kepler University Linz, 2018).

[92] Brenner, S. C., Scott, L. R., *The mathematical theory of finite element methods*, 3rd ed. (Springer, 2008).

[93] Abass, A., "Light absorption enhancement and electronic properties of thin-film solar cells," PhD thesis (Ghent University, 2014).

[94] Jin, J.-M., *The finite element method in electromagnetics*, 1st ed. (John Wiley & Sons Inc, 1993).

[95] Monk, P., "Analysis of a finite element method for Maxwell's equations," SIAM Journal on Numerical Analysis **29**, 714–729 (1992).

[96] Nédélec, J.-C., "Mixed finite elements in $\mathbb{R}^3$," Numerische Mathematik **35**, 315–341 (1980).

[97] Nicolet, A., Zolla, F., Ould Agha, Y., Guenneau, S., "Geometrical transformations and equivalent materials in computational electromagnetism," COMPEL-The international journal for computation and mathematics in electrical and electronic engineering **27**, 806–819 (2008).

[98] Berenger, J.-P., "A perfectly matched layer for the absorption of electromagnetic waves," Journal of Computational Physics **114**, 185–200 (1994).

[99] Zschiedrich, L. W., Burger, S., Klose, R., Schaedle, A., Schmidt, F., "JCMmode: an adaptive finite element solver for the computation of leaky modes," in Integrated Optics: Devices, Materials, and Technologies IX, Vol. 5728 (SPIE, 2005), pp. 192–202.

[100] Weiland, T., "A discretization model for the solution of Maxwell's equations for six-component fields," Archiv Elektronik und Uebertragungstechnik **31**, 116–120 (1977).

[101] Clemens, M., Weiland, T., "Discrete electromagnetism with the finite integration technique," Progress In Electromagnetics Research **32**, 65–87 (2001).

[102] Chen, W.-K., *Graph theory and its engineering applications*, Vol. 5 (World Scientific, 1997).

[103] Marklein, R., *The finite integration technique as a general tool to compute acoustic, electromagnetic, elastodynamic, and coupled wave fields* (IEEE Press, John Wiley, and Sons, New York, NY, USA, 2002).

[104] Yee, K., "Numerical solution of initial boundary value problems involving Maxwell's equations in isotropic media," IEEE Transactions on antennas and propagation **14**, 302–307 (1966).

[105] Hao, Y., Mittra, R., *FDTD modeling of metamaterials: Theory and applications* (Artech house, 2008).

[106] Sullivan, D. M., *Electromagnetic simulation using the FDTD method* (John Wiley & Sons, 2013).

[107] Taflove, A., Hagness, S. C., Piket-May, M., "Computational electromagnetics: the finite-difference time-domain method," The Electrical Engineering Handbook **3**, 15 (2005).

[108] Gedney, S. D., *Introduction to the finite-difference time-domain (FDTD) method for electromagnetics*, Vol. 27 (Morgan & Claypool Publishers, 2011).

[109] Yu, W., Mittra, R., "A conformal FDTD software package modeling antennas and microstrip circuit components," IEEE Antennas and Propagation Magazine **42**, 28–39 (2000).

[110] Baets, R., Lagasse, P. E., "Loss calculation and design of arbitrarily curved integrated-optic waveguides," Journal of the Optical Society of America **73**, 177–182 (1983).

[111] Hammer, M., Ebers, L., Förstner, J., “Oblique quasi-lossless excitation of a thin silicon slab waveguide: a guided-wave variant of an anti-reflection coating,” Journal of the Optical Society of America B **36**, 2395–2401 (2019).

[112] Morrison, B., Zhang, Y., Pagani, M., Eggleton, B., Marpaung, D., “Four-wave mixing and nonlinear losses in thick silicon waveguides,” Optics Letters **41**, 2418–2421 (2016).

[113] Sakai, A., Go, H., Baba, T., “Sharply bent optical waveguide silicon-on-insulator substrate,” Proceedings of SPIE - The International Society for Optical Engineering **4283**, `10.1117/12.432614` (2001).

[114] Jaberansary, E., Masaud, T. M. B., Milosevic, M., Nedeljkovic, M., Mashanovich, G. Z., Chong, H. M., “Scattering loss estimation using 2-D Fourier analysis and modeling of sidewall roughness on optical waveguides,” IEEE Photonics Journal **5**, 6601010–6601010 (2013).

[115] Ciminelli, C., Dell’Olio, F., Passaro, V. M., Armenise, M. N., “Fully three-dimensional accurate modeling of scattering loss in optical waveguides,” Optical and quantum electronics **41**, 285–298 (2009).

[116] Hagan, D. E., Knights, A. P., “Mechanisms for optical loss in SOI waveguides for mid-infrared wavelengths around 2 µm,” Journal of Optics **19**, 025801 (2016).

[117] Melati, D., Morichetti, F., Melloni, A., “A unified approach for radiative losses and backscattering in optical waveguides,” Journal of Optics **16**, 055502 (2014).

[118] Hiremath, K., Stoffer, R., Hammer, M., “Modeling of circular integrated optical microresonators by 2-d frequency domain coupled mode theory,” Optics Communications **257**, 277–297 (2006).

[119] The MathWorks Inc. *MATLAB version: 9.5.0.944444 (R2018b)*, Natick, Massachusetts, United States, 2018.

[120] Wu, H., Li, C., Song, L., Tsang, H.-K., Bowers, J. E., Dai, D., “Ultra-sharp multimode waveguide bends with subwavelength gratings,” Laser & Photonics Reviews **13**, 1800119 (2019).

[121] Liu, Y., Sun, W., Xie, H., Zhang, N., Xu, K., Yao, Y., Xiao, S., Song, Q., “Very sharp adiabatic bends based on an inverse design,” Optics Letters **43**, 2482–2485 (2018).

[122] Teng, M., Noman, A. A., Lee, Y. J., Kong, Z., Xuan, Y., Qi, M., “A 3-micron-radius bend for SOI TE0/TE1 multiplexing,” in Conference on lasers and electro-optics (2018), JW2A.13.

[123] Ebers, L., Hammer, M., Förstner, J., “Oblique incidence of semi-guided planar waves on slab waveguide steps: effects of rounded edges,” Optics Express **26**, 18621–18632 (2018).

[124] Li, C., Liu, D., Dai, D., “Multimode silicon photonics,” Nanophotonics **8**, 227–247 (2018).

[125] Lai, Y., Yu, Y., Fu, S., Xu, J., Shum, P. P., Zhang, X., “Compact double-part grating coupler for higher-order mode coupling,” Optics Letters **43**, 3172–3175 (2018).

[126] Dai, D., Mao, M., “Mode converter based on an inverse taper for multimode silicon nanophotonic integrated circuits,” Optics Express **23**, 28376–28388 (2015).

[127] Huang, Q., Liu, Q., Xia, J., “Traveling wave-like Fabry–Perot resonator-based add-drop filters,” Optics Letters **42**, 5158–5161 (2017).

[128] Dai, D., Bowers, J. E., “Novel concept for ultracompact polarization splitter-rotator based on silicon nanowires,” Optics Express **19**, 10940–10949 (2011).

[129] Dai, D., “Advanced passive silicon photonic devices with asymmetric waveguide structures,” Proceedings of the IEEE **106**, 2117–2143 (2018).

[130] Sun, C., Yu, Y., Chen, G., Zhang, X., “Ultra-compact bent multimode silicon waveguide with ultralow inter-mode crosstalk,” Optics Letters **42**, 3004–3007 (2017).

[131] Wang, X., Yin, C., Cao, Z., “Transfer matrix method and the graded-index waveguide,” Progress in Planar Optical Waveguides, Springer, Berlin, Heidelberg, 17–42 (2016).

[132] Cardoso, J. R., *Electromagnetics through the finite element method: a simplified approach using Maxwell’s equations* (Boca Raton, London, New York: CRC Press, 2016).

[133] Lavrinenko, A. V., Lægsgaard, J., Gregersen, N., Schmidt, F., Søndergaard, T., *Numerical methods in photonics* (CRC press, 2018).

[134] Jin, J.-M., *The Finite Element Method in Electromagnetics* (3rd ed., Wiley-IEEE, 2014).

[135] Kumar, A., Gallawa, R., “Bending-induced phase shifts in dual-mode planar optical waveguides,” Optics Letters **18**, 1415–1417 (1993).

[136] Jamison, S., McGowan, R., Grischkowsky, D., “Single-mode waveguide propagation and reshaping of sub-ps terahertz pulses in sapphire fibers,” Applied Physics Letters **76**, 1987–1989 (2000).

[137] Pogossian, S. P., Vescan, L., Vonsovici, A., “The single-mode condition for semiconductor rib waveguides with large cross section,” Journal of Lightwave Technology **16**, 1851–1853 (1998).

[138] Sukhova, M., “Simplified methods for transmission computation in 2D curved optical waveguides,” PhD thesis (Karlsruhe Institute of Technology (KIT), 2024), 126 pp.

[139] Bienstman, P., Six, E., Roelens, A., Vanwolleghem, M., Baets, R., “Calculation of bending losses in dielectric waveguides using eigenmode expansion and perfectly matched layers,” IEEE Photonics Technology Letters **14**, 164–166 (2002).

[140] Krasnok, A., Baranov, D., Li, H., Miri, M.-A., Monticone, F., Alú, A., “Anomalies in light scattering,” Advances in Optics and Photonics **11**, 892–951 (2019).

[141] Mohanty, A., Zhang, M., Dutt, A., Ramelow, S., Nussenzveig, P., Lipson, M., “Quantum interference between transverse spatial waveguide modes,” Nature Communications **8**, 14010 (2017).

[142] Pérot, A., Fabry, C., “On the application of interference phenomena to the solution of various problems of spectroscopy and metrology,” Astrophysical Journal **9**, 87 (1899).

[143] Vaughan, M., *The Fabry–Perot interferometer: history, theory, practice and applications* (Routledge, 2017).

[144] Märki, I., Salt, M., Stanley, R., Staufer, U., Herzig, H.-P., “Characterization of photonic crystal waveguides based on Fabry–Pérot interference,” Journal of Applied Physics **96**, 6966–6969 (2004).

[145] Wiecha, P. R., Arbouet, A., Girard, C., Muskens, O. L., “Deep learning in nanophotonics: inverse design and beyond,” Photonics Research **9**, B182–B200 (2021).

[146] LeCun, Y., Bengio, Y., Hinton, G., “Deep learning,” Nature **521**, 436–444 (2015).

[147] Bengio, Y., Goodfellow, I., Courville, A., *Deep learning*, Vol. 1 (MIT press Cambridge, MA, USA, 2017).

[148] Alagappan, G., Png, C. E., “Prediction of electromagnetic field patterns of optical waveguide using neural network,” Neural Computing and Applications **33**, 2195–2206 (2021).

[149] Chen, M., Lupoiu, R., Mao, C., Huang, D.-H., Jiang, J., Lalanne, P., Fan, J., “Physics-augmented deep learning for high-speed electromagnetic simulation and optimization,” `10.21203/rs.3.rs-807786/v1` (2021).

[150] Tahersima, M. H., Kojima, K., Koike-Akino, T., Jha, D., Wang, B., Lin, C., Parsons, K., “Deep neural network inverse design of integrated photonic power splitters,” Scientific Reports **9**, 1368 (2019).

[151] Gabr, A. M., Featherston, C., Zhang, C., Bonfil, C., Zhang, Q.-J., Smy, T. J., “Design and optimization of optical passive elements using artificial neural networks,” Journal of the Optical Society of America B **36**, 999–1007 (2019).

[152] Ma, W., Liu, Z., Kudyshev, Z. A., Boltasseva, A., Cai, W., Liu, Y., “Deep learning for the design of photonic structures,” Nature Photonics **15**, 77–90 (2021).

[153] Augenstein, Y., Rockstuhl, C., “Inverse design of nanophotonic devices with structural integrity,” ACS Photonics **7**, 2190–2196 (2020).

[154] Liu, D., Tan, Y., Khoram, E., Yu, Z., “Training deep neural networks for the inverse design of nanophotonic structures,” Acs Photonics **5**, 1365–1369 (2018).

[155] Peurifoy, J., Shen, Y., Jing, L., Yang, Y., Cano-Renteria, F., DeLacy, B. G., Joannopoulos, J. D., Tegmark, M., Soljačić, M., “Nanophotonic particle simulation and inverse design using artificial neural networks,” Science Advances **4**, eaar4206 (2018).

[156] Jiang, J., Chen, M., Fan, J. A., “Deep neural networks for the evaluation and design of photonic devices,” Nature Reviews Materials **6**, 679–700 (2021).

[157] Wilamowski, B. M., “Neural network architectures and learning algorithms,” IEEE Industrial Electronics Magazine **3**, 56–63 (2009).

[158] Paszke, A., Gross, S., Chintala, S., Chanan, G., Yang, E., DeVito, Z., Lin, Z., Desmaison, A., Antiga, L., Lerer, A., *Automatic differentiation in PyTorch* (https://openreview.net/forum?id=BJJsrmfCZ, 2017).

[159] Akiba, T., Sano, S., Yanase, T., Ohta, T., Koyama, M., “Optuna: a next-generation hyperparameter optimization framework,” in Proceedings of the 25th ACM SIGKDD international conference on knowledge discovery & data mining (2019), pp. 2623–2631.

[160] Lu, L., Pestourie, R., Yao, W., Wang, Z., Verdugo, F., Johnson, S. G., “Physics-informed neural networks with hard constraints for inverse design,” SIAM Journal on Scientific Computing **43**, B1105–B1132 (2021).

[161] Cuomo, S., Di Cola, V. S., Giampaolo, F., Rozza, G., Raissi, M., Piccialli, F., “Scientific machine learning through physics–informed neural networks: where we are and what’s next,” Journal of Scientific Computing **92**, 88 (2022).

[162] Ioffe, S., “Batch normalization: accelerating deep network training by reducing internal covariate shift,” arXiv preprint arXiv:1502.03167 (2015).

[163] Clevert, D.-A., “Fast and accurate deep network learning by exponential linear units (elus),” arXiv preprint arXiv:1511.07289 (2015).

[164] De Boor, C., “On calculating with B-splines,” Journal of Approximation theory **6**, 50–62 (1972).

[165] Hochreiter, S., “Long short-term memory,” Neural Computation MIT-Press (1997).

[166] Farin, G., *Curves and surfaces for computer-aided geometric design: a practical guide* (Elsevier, 2014).

[167] Freudenburg, G., Freudenburg, J., “Curves defined by Chebyshev polynomials,” arXiv preprint arXiv:0902.3440 (2009).

[168] Gao, F., Wu, W., Lin, Y., Shen, S., “Online safe trajectory generation for quadrotors using fast marching method and Bernstein basis polynomial,” in 2018 IEEE International Conference on Robotics and Automation (ICRA) (IEEE, 2018), pp. 344–351.

[169] Rogers, D. F., Adams, J. A., *Mathematical elements for computer graphics* (McGraw-Hill, Inc., 1989).

[170] Wang, C., Xu, T., Tomizuka, M., “Continuous Trajectory Optimization via B-splines for Multi-jointed Robotic Systems,” arXiv preprint arXiv:2212.10500 (2022).

[171] De Boor, C., “A practical guide to splines,” Springer **2**, 4135–4195 (1978).

[172] De Boor, C., “Package for calculating with B-splines,” SIAM Journal on Numerical Analysis **14**, 441–472 (1977).

[173] Van Rossum, G., Drake, F. L., *Python 3 reference manual* (CreateSpace, Scotts Valley, CA, 2009).

[174] Lemaréchal, C., “Cauchy and the gradient method,” Doc Math Extra **251**, 10 (2012).

[175] Kraft, P., “A hierarchical solver for time-harmonic Maxwell’s equations,” PhD thesis (Karlsruhe Institute of Technology (KIT), 2022).

[176] Lagarias, J. C., Reeds, J. A., Wright, M. H., Wright, P. E., “Convergence properties of the Nelder–Mead simplex method in low dimensions,” SIAM Journal on Optimization **9**, 112–147 (1998).

[177] Manyam, S. G., Casbeer, D. W., Weintraub, I. E., Taylor, C., “Trajectory optimization for rendezvous planning using quadratic Bézier curves,” in 2021 IEEE/RSJ International Conference on Intelligent Robots and Systems (IROS) (IEEE, 2021), pp. 1405–1412.

[178] Shewchuk, J. R., “Delaunay refinement algorithms for triangular mesh generation,” Computational Geometry **22**, 21–74 (2002).

[179] Jacobs, P., Canny, J., “Planning smooth paths for mobile robots,” in *Nonholonomic motion planning* (Springer, 1993), pp. 271–342.

[180] Dijkstra, E. W., “A note on two problems in connexion with graphs,” Numerische Mathematik **1**, 269–271 (1959).

[181] Chamorro-Posada, P., “Silicon nitride bent asymmetric coupled waveguides with partial Euler bends,” Photonics **11**, 218 (2024).

[182] Vogelbacher, F., Nevlacsil, S., Sagmeister, M., Kraft, J., Unterrainer, K., Hainberger, R., “Analysis of silicon nitride partial Euler waveguide bends,” Optics Express **27**, 31394–31406 (2019).

[183] Cherchi, M., Ylinen, S., Harjanne, M., Kapulainen, M., Vehmas, T., Aalto, T., “The Euler bend: paving the way for high-density integration on micron-scale semiconductor platforms,” in Silicon photonics ix, Vol. 8990 (SPIE, 2014), pp. 20–26.

[184] Nocedal, J., Wright, S. J., *Numerical optimization* (Springer, 1999).

[185] Boyd, R. W., *Nonlinear Optics* (Academic Press, 2008).

[186] Agrawal, G. P., *Nonlinear fiber optics* (Academic press, 2013).

[187] Shen, Y.-R., *Principles of nonlinear optics* (Wiley-Interscience, Wiley Classics Library, 2002).

[188] Mills, D. L., *Nonlinear optics* (Springer-Verlag, 1998).

[189] Chettri, P., Srivastava, S., "Time dependent third order nonlinear optical susceptibility tensor components of the carbon disulfide molecule using femtosecond degenerate four-wave mixing," arXiv preprint arXiv:2101.10929 (2021).

[190] Le, H. Q., Goodhue, W., Rauschenbach, K., "Measurement of third-order optical nonlinear susceptibility using four-wave mixing in a single-mode ridge waveguide," Optics Letters **15**, 1126–1128 (1990).

[191] Wynne, J., "Optical third-order mixing in GaAs, Ge, Si, and InAs," Physical Review **178**, 1295 (1969).

[192] Scully, M. O., Zubairy, M. S., *Quantum optics* (Cambridge University Press, 1997).

[193] Quesada, N., Helt, L. G., Menotti, M., Liscidini, M., Sipe, J. E., "Beyond photon pairs: nonlinear quantum photonics in the high-gain regime," Advances in Optics and Photonics **14**, 291 (2021).

[194] Banic, M., Sipe, J. E., Liscidini, M., "Integrated photonic sources of frequency-bin-encoded multipartite entangled states," Physical Review A **109**, 013505 (2024).

[195] Azzini, S., Grassani, D., Strain, M. J., Sorel, M., Helt, L. G., Sipe, J., Liscidini, M., Galli, M., Bajoni, D., "Ultra-low power generation of twin photons in a compact silicon ring resonator," Optics Express **20**, 23100–23107 (2012).

[196] Davanco, M., Ong, J. R., Shehata, A. B., Tosi, A., Agha, I., Assefa, S., Xia, F., Green, W. M., Mookherjea, S., Srinivasan, K., "Telecommunications-band heralded single photons from a silicon nanophotonic chip," Applied Physics Letters **100** (2012).

[197] Shin, W., Park, K., Kim, H., Lee, D., Kwon, K., Shin, H., "Photon-pair generation in a lossy waveguide," Nanophotonics **12**, 531–538 (2023).

[198] Silverstone, J. W., Bonneau, D., Ohira, K., Suzuki, N., Yoshida, H., Iizuka, N., Ezaki, M., Natarajan, C. M., Tanner, M. G., Hadfield, R. H., "On-chip quantum interference between silicon photon-pair sources," Nature Photonics **8**, 104–108 (2014).

[199] Silverstone, J. W., Santagati, R., Bonneau, D., Strain, M. J., Sorel, M., O'Brien, J. L., Thompson, M. G., "Qubit entanglement between ring-resonator photon-pair sources on a silicon chip," Nature Communications **6**, 7948 (2015).

[200] Zhong, H.-S., Wang, H., Deng, Y.-H., Chen, M.-C., Peng, L.-C., Luo, Y.-H., Qin, J., Wu, D., Ding, X., Hu, Y., "Quantum computational advantage using photons," Science **370**, 1460–1463 (2020).

[201] Crespi, A., Lobino, M., Matthews, J. C., Politi, A., Neal, C. R., Ramponi, R., Osellame, R., O'Brien, J. L., "Measuring protein concentration with entangled photons," Applied Physics Letters **100**, 233704 (2012).

[202] Orieux, A., Versteegh, M. A., Jöns, K. D., Ducci, S., "Semiconductor devices for entangled photon pair generation: a review," Reports on Progress in Physics **80**, 076001 (2017).

[203] Azzoune, A., Delaye, P., Pauliat, G., "Modeling photon pair generation by second-order surface nonlinearity in silica nanofibers," Journal of the Optical Society of America B **38**, 1057–1068 (2021).

[204] Lin, Q., Agrawal, G. P., "Silicon waveguides for creating quantum-correlated photon pairs," Optics Letters **31**, 3140–3142 (2006).

[205] Alibart, O., Fulconis, J., Wong, G., Murdoch, S., Wadsworth, W., Rarity, J., "Photon pair generation using four-wave mixing in a microstructured fibre: theory versus experiment," New Journal of Physics **8**, 67 (2006).

[206] Lacava, C., Ettabib, M. A., Petropoulos, P., "Nonlinear silicon photonic signal processing devices for future optical networks," Applied Sciences **7**, 103 (2017).

[207] Cherchi, M., Ylinen, S., Harjanne, M., Kapulainen, M., Vehmas, T., Aalto, T., “Low-loss spiral waveguides with ultra-small footprint on a micron scale SOI platform,” in Silicon Photonics IX, Vol. 8990 (SPIE, 2014), pp. 27–33.

[208] Wang, H., Zeng, Q., Ma, H., Yuan, Z., “Progress on chip-based spontaneous four-wave mixing quantum light sources,” Advanced Devices & Instrumentation **5**, 0032 (2024).

[209] Carmon, T., Yang, L., Vahala, K. J., “Dynamical thermal behavior and thermal self-stability of microcavities,” Optics Express **12**, 4742–4750 (2004).

[210] Ebers, L., Hammer, M., Förstner, J., “Oblique incidence of semi-guided planar waves on slab waveguide steps: effects of rounded edges,” Optics Express **26**, 18621–18632 (2018).

[211] Banic, M., Zatti, L., Liscidini, M., Sipe, J. E., “Two strategies for modeling nonlinear optics in lossy integrated photonic structures,” Physical Review A **106**, 043707 (2022).

[212] Dirac, P. A. M., “The quantum theory of the emission and absorption of radiation,” Proceedings of the Royal Society of London. Series A, Containing Papers of a Mathematical and Physical Character **114**, 243–265 (1927).

[213] Fermi, E., *Nuclear physics: a course given by Enrico Fermi at the University of Chicago* (University of Chicago press, 1950).

[214] Cohen-Tannoudji, C., Diu, B., Laloë, F., *Quantum mechanics volume 2* (John Wiley & Sons, 2005).

[215] Sakurai, J. J., Napolitano, J., *Modern quantum mechanics* (Cambridge University Press, 2020).

[216] Banic, M., “Quantum state generation with nonlinear integrated photonics: conventional and unconventional approaches,” PhD thesis (University of Toronto (Canada), 2024).

[217] Banic, M., Liscidini, M., Sipe, J. E., “Resonant and nonresonant integrated third-order parametric down-conversion,” Physical Review A **106**, 013710 (2022).

[218] Leuthold, J., Koos, C., Freude, W., “Nonlinear silicon photonics,” Nature Photonics **4**, 535–544 (2010).

[219] Koos, C., Jacome, L., Poulton, C., Leuthold, J., Freude, W., “Nonlinear silicon-on-insulator waveguides for all-optical signal processing,” Optics Express **15**, 5976–5990 (2007).

[220] Panoiu, N. C., McMillan, J. F., Wong, C. W., “Theoretical analysis of pulse dynamics in silicon photonic crystal wire waveguides,” IEEE Journal of Selected Topics in Quantum Electronics **16**, 257–266 (2010).

[221] Driscoll, J. B., Grote, R. R., Liu, X., Dadap, J. I., Panoiu, N. C., Osgood Jr, R. M., “Directionally anisotropic Si nanowires: on-chip nonlinear grating devices in uniform waveguides,” Optics Letters **36**, 1416–1418 (2011).

[222] Osgood, R., Panoiu, N., Dadap, J., Liu, X., Chen, X., Hsieh, I.-W., Dulkeith, E., Green, W., Vlasov, Y. A., “Engineering nonlinearities in nanoscale optical systems: physics and applications in dispersion-engineered silicon nanophotonic wires,” Advances in Optics and Photonics **1**, 162–235 (2009).

[223] Liang, T.-K., Tsang, H. K., “Role of free carriers from two-photon absorption in Raman amplification in silicon-on-insulator waveguides,” Applied Physics Letters **84**, 2745–2747 (2004).

[224] Claps, R., Raghunathan, V., Dimitropoulos, D., Jalali, B., “Influence of nonlinear absorption on Raman amplification in silicon waveguides,” Optics Express **12**, 2774–2780 (2004).

[225] Liang, T.-K., Tsang, H.-K., “Nonlinear absorption and Raman scattering in silicon-on-insulator optical waveguides,” IEEE Journal of Selected Topics in Quantum Electronics **10**, 1149–1153 (2004).

[226] Apiratikul, P., Wathen, J. J., Porkolab, G. A., Wang, B., He, L., Murphy, T. E., Richardson, C. J. K., “Enhanced continuous-wave four-wave mixing efficiency in nonlinear AlGaAs waveguides,” Optics Express **22**, 26814–26824 (2014).

[227] Basak, J., Liao, L., Liu, A., Rubin, D., Chetrit, Y., Nguyen, H., Samara-Rubio, D., Cohen, R., Izhaky, N., Paniccia, M., “Developments in gigascale silicon optical modulators using free carrier dispersion mechanisms,” Advances in Optical Technologies **2008**, 678948 (2008).

[228] Clemmen, S., Huy, K. P., Bogaerts, W., Baets, R. G., Emplit, P., Massar, S., “Continuous wave photon pair generation in silicon-on-insulator waveguides and ring resonators,” Optics Express **17**, 16558–16570 (2009).

[229] Hong, C., Mandel, L., “Experimental realization of a localized one-photon state,” Physical Review Letters **56**, 58 (1986).

[230] Kaneda, F., Garay-Palmett, K., U’Ren, A. B., Kwiat, P. G., “Heralded single-photon source utilizing highly nondegenerate, spectrally factorable spontaneous parametric downconversion,” Optics Express **24**, 10733–10747 (2016).

[231] Ramelow, S., Mech, A., Giustina, M., Gröblacher, S., Wieczorek, W., Beyer, J., Lita, A., Calkins, B., Gerrits, T., Nam, S. W., “Highly efficient heralding of entangled single photons,” Optics Express **21**, 6707–6717 (2013).

[232] Hojo, M., Tani, S., Kobayashi, Y., Tanaka, K., “Coincidence measurements of two quantum-correlated photon pairs widely separated in the frequency domain,” Scientific Reports **13**, 8520 (2023).

[233] Unternährer, M., Bessire, B., Gasparini, L., Stoppa, D., Stefanov, A., “Coincidence detection of spatially correlated photon pairs with a monolithic time-resolving detector array,” Optics Express **24**, 28829–28841 (2016).

[234] Nunn, C. M., Franson, J. D., Pittman, T. B., “Heralding on the detection of zero photons,” Physical Review A **104**, 033717 (2021).

[235] Levy, J. S., Gondarenko, A., Foster, M. A., Turner-Foster, A. C., Gaeta, A. L., Lipson, M., “CMOS-compatible multiple-wavelength oscillator for on-chip optical interconnects,” Nature Photonics **4**, 37–40 (2010).

[236] Mahmudlu, H., May, S., Angulo, A., Sorel, M., Kues, M., “AlGaAs-on-insulator waveguide for highly efficient photon-pair generation via spontaneous four-wave mixing,” Optics Letters **46**, 1061–1064 (2021).

[237] Schmid, M., Ludescher, D., Giessen, H., “Optical properties of photoresists for femtosecond 3D printing: refractive index, extinction, luminescence-dose dependence, aging, heat treatment and comparison between 1-photon and 2-photon exposure,” Optical Materials Express **9**, 4564–4577 (2019).

[238] Bürger, J., Valero, A. C., Weiss, T., Maier, S. A., Schmidt, M. A., “Impact of coordinate frames on mode formation in twisted waveguides,” Physical Review B **109**, 165301 (2024).

[239] Cherchi, M., Ylinen, S., Harjanne, M., Kapulainen, M., Aalto, T., "Dramatic size reduction of waveguide bends on a micron-scale silicon photonic platform," Optics Express **21**, 17814–17823 (2013).

[240] Vlasov, Y. A., McNab, S. J., "Losses in single-mode silicon-on-insulator strip waveguides and bends," Optics Express **12**, 1622–1631 (2004).

[241] Sellmeier, W., "Über die durch die Aetherschwingungen erregten Mitschwingungen der Körpertheilchen und deren Rückwirkung auf die ersteren, besonders zur Erklärung der Dispersion und ihrer Anomalien," Annalen der Physik **223**, 525–554 (1872).

[242] Gooch, J. W., "Sellmeier equation," Encyclopedic Dictionary of Polymers, 653–654 (2011).

[243] BATOP GmbH, *Refractive index n of AlGaAs* (https://www.batop.de/information/n_AlGaAs.html, Accessed on: 2024-10-13).

[244] Adachi, S., "GaAs, AlAs, and $\mathrm{Al}_x\mathrm{Ga}_{1-x}\mathrm{As}$: material parameters for use in research and device applications," Journal of Applied Physics **58**, R1–R29 (1985).

[245] Thomas, N., Barbour, R. J., Song, Y., Lee, M. L., Fu, K.-M. C., "Waveguide-integrated single-crystalline gap resonators on diamond," Optics Express **22**, 13555–13564 (2014).

[246] Ying, Z., Wang, Z., Zhao, Z., Dhar, S., Pan, D. Z., Soref, R., Chen, R. T., "Comparison of microrings and microdisks for high-speed optical modulation in silicon photonics," Applied Physics Letters **112**, 111108 (2018).

[247] Derntl, C. G., Bachmann, D., Unterrainer, K., Darmo, J., "Disk patch resonators for cavity quantum electrodynamics at the terahertz frequency," Optics Express **25**, 12311–12324 (2017).

[248] Rebholz, L., "Modenhybridisierung in scheibenförmigen Flüstergalerieresonatoren," Master's thesis, Karlsruhe Institute of Technology (2021).

[249] Woska, S., Rebholz, L., Rietz, P., Kalt, H., "Intrinsic mode coupling in mirror-symmetric whispering gallery resonators," Optics Express **30**, 32847–32860 (2022).

[250] Woska, S., "Tunable photonics based on whispering gallery resonators on an all-polymeric chip-scale platform," PhD thesis (Karlsruhe Institute of Technology (KIT), 2022).

[251] Sandoghdar, V., Treussart, F., Hare, J., Lefevre-Seguin, V., Raimond, J.-M., Haroche, S., "Very low threshold whispering-gallery-mode microsphere laser," Physical Review A **54**, R1777 (1996).

[252] Grossmann, T., Schleede, S., Hauser, M., Christiansen, M. B., Vannahme, C., Eschenbaum, C., Klinkhammer, S., Beck, T., Fuchs, J., Nienhaus, G. U., "Low-threshold conical microcavity dye lasers," Applied Physics Letters **97**, 063304 (2010).

[253] Vollmer, F., Arnold, S., "Whispering-gallery-mode biosensing: label-free detection down to single molecules," Nature Methods **5**, 591–596 (2008).

[254] Banic, M., Liscidini, M., Sipe, J., "Generation of photon pairs by stimulated emission in ring resonators," Optics Letters **47**, 1802–1805 (2022).

[255] Kumar, R. R., Wang, Y., Zhang, Y., Tsang, H. K., "Quantum states of higher-order whispering gallery modes in a silicon micro-disk resonator," Journal of the Optical Society of America B **37**, 2231–2237 (2020).

[256] Kristensen, P. T., Herrmann, K., Intravaia, F., Busch, K., "Modeling electromagnetic resonators using quasinormal modes," Advances in Optics and Photonics **12**, 612–708 (2020).

[257] Lalanne, P., Yan, W., Gras, A., Sauvan, C., Hugonin, J.-P., Besbes, M., Demésy, G., Truong, M. D., Gralak, B., Zolla, F., Nicolet, A., Binkowski, F., Zschiedrich, L., Burger, S., Zimmerling, J., Remis, R., Urbach, P., Liu, H. T., Weiss, T., "Quasinormal mode solvers for resonators with dispersive materials," Journal of the Optical Society of America **36**, 686–704 (2019).

[258] Sauvan, C., Wu, T., Zarouf, R., Muljarov, E. A., Lalanne, P., "Normalization, orthogonality, and completeness of quasinormal modes of open systems: the case of electromagnetism," Optics Express **30**, 6846–6885 (2022).

[259] Ge, R.-C., Hughes, S., "Quantum dynamics of two quantum dots coupled through localized plasmons: an intuitive and accurate quantum optics approach using quasinormal modes," Physical Review B **92**, 205420 (2015).

[260] Kamandar Dezfouli, M., Hughes, S., "Regularized quasinormal modes for plasmonic resonators and open cavities," Physical Review B **97**, 115302 (2018).

[261] Binkowski, F., Betz, F., Colom, R., Hammerschmidt, M., Zschiedrich, L., Burger, S., "Quasinormal mode expansion of optical far-field quantities," Physical Review B **102**, 035432 (2020).

[262] Colom, R., McPhedran, R., Stout, B., Bonod, N., "Modal expansion of the scattered field: causality, nondivergence, and nonresonant contribution," Physical Review B **98**, 085418 (2018).

[263] Wu, T., Gurioli, M., Lalanne, P., "Nanoscale light confinement: the Q's and V's," ACS Photonics **8**, 1522–1538 (2021).

[264] Ge, R.-C., Kristensen, P. T., Young, J. F., Hughes, S., "Quasinormal mode approach to modelling light-emission and propagation in nanoplasmonics," New Journal of Physics **16**, 113048 (2014).

[265] Gorkunov, M. V., Antonov, A. A., Mamonova, A. V., Muljarov, E. A., Kivshar, Y., "Substrate-induced maximum optical chirality of planar dielectric structures," Advanced Optical Materials, 2402133 (2024).

[266] Kristensen, P. T., Van Vlack, C., Hughes, S., "Generalized effective mode volume for leaky optical cavities," Optics Letters **37**, 1649–1651 (2012).

[267] Franke, S., Hughes, S., Dezfouli, M. K., Kristensen, P. T., Busch, K., Knorr, A., Richter, M., "Quantization of quasinormal modes for open cavities and plasmonic cavity quantum electrodynamics," Physical Review Letters **122**, 213901 (2019).

[268] Gippius, N. A., Weiss, T., Tikhodeev, S. G., Giessen, H., "Resonant mode coupling of optical resonances in stacked nanostructures," Optics Express **18**, 7569–7574 (2010).

[269] Coenen, T., Van De Groep, J., Polman, A., "Resonant modes of single silicon nanocavities excited by electron irradiation," ACS Nano **7**, 1689–1698 (2013).

[270] Martin-Cano, D., Haakh, H. R., Rotenberg, N., "Chiral emission into nanophotonic resonators," ACS Photonics **6**, 961–966 (2019).

[271] Wu, T., Lalanne, P., "Exact Maxwell evolution equation of resonator dynamics: temporal coupled-mode theory revisited," Optics Express **32**, 20904–20914 (2024).

[272] Betz, F., Hammerschmidt, M., Zschiedrich, L., Burger, S., Binkowski, F., "Efficient rational approximation of optical response functions with the AAA algorithm," Laser Photonics Rev., 2400584 (2024).

[273] Ren, J., Franke, S., Hughes, S., "Connecting classical and quantum mode theories for coupled lossy cavity resonators using quasinormal modes," ACS Photonics **9**, 138–155 (2022).

[274] Kamandar Dezfouli, M., Hughes, S., “Quantum optics model of surface-enhanced Raman spectroscopy for arbitrarily shaped plasmonic resonators,” ACS Photonics **4**, 1245–1256 (2017).

[275] Xiao, R., Geyi, W., Wu, W., “Theory of resonant modes and its application,” IEEE Access **9**, 114945–114956 (2021).

[276] Kippenberg, T., Spillane, S., Vahala, K., “Modal coupling in traveling-wave resonators,” Optics Letters **27**, 1669–1671 (2002).

[277] Savchenkov, A., Matsko, A., Liang, W., Ilchenko, V., Seidel, D., Maleki, L., “Kerr frequency comb generation in overmoded resonators,” Optics Express **20**, 27290–27298 (2012).

[278] Rosenberger, A., “Effects of polarization mode coupling and superposition in a whispering-gallery microresonator,” in Advances in Slow and Fast Light VII, Vol. 8998 (SPIE, 2014), pp. 88–95.

[279] Sturman, B., Podivilov, E., Werner, C. S., Breunig, I., “Vectorial perturbation theory for axisymmetric whispering gallery resonators,” Physical Review A **99**, 013810 (2019).

[280] Werner, C. S., Sturman, B., Podivilov, E., Manjeshwar, S. K., Buse, K., Breunig, I., “Control of mode anticrossings in whispering gallery microresonators,” Optics Express **26**, 762–771 (2018).

[281] Kress, R., *Chap. 1.4.1 electromagnetic waves scattering: specific theoretical tools.* Edited by E. Pike and P. C. Sabatier (Academic Press, London, 2001).

[282] Lakhtakia, A., *Beltrami fields in chiral media* (World Scientific, 1994).

[283] Vavilin, M., Rockstuhl, C., Fernandez-Corbaton, I., “Electromagnetic scalar product in spatially bounded domains,” Physical Review A **109**, 043506 (2024).

[284] Abdelrahman, M. I., Gralak, B., “Completeness and divergence-free behavior of the quasi-normal modes using causality principle,” OSA Continuum **1**, 340–348 (2018).

[285] Kuhn, L., Repän, T., Rockstuhl, C., “Exploiting graph neural networks to perform finite-difference time-domain based optical simulations,” APL Photonics **8**, 036109 (2023).

[286] Kiarashinejad, Y., Abdollahramezani, S., Zandehshahvar, M., Hemmatyar, O., Adibi, A., “Deep learning reveals underlying physics of light–matter interactions in nanophotonic devices,” Advanced Theory and Simulations **2**, 1900088 (2019).

[287] Augenstein, Y., Repan, T., Rockstuhl, C., “Neural operator-based surrogate solver for free-form electromagnetic inverse design,” ACS Photonics **10**, 1547–1557 (2023).

[288] Augenstein, Y., “Inverse design of free-form nanophotonic devices,” PhD thesis (Karlsruhe Institute of Technology (KIT), 2024).

[289] Bialynicki-Birula, I., “V photon wave function,” Progress in Optics **36**, edited by E. Wolf, 245–294 (1996).

[290] Lalanne, P., Yan, W., Vynck, K., Sauvan, C., Hugonin, J.-P., “Light interaction with photonic and plasmonic resonances,” Laser & Photonics Reviews **12**, 1700113 (2018).

Acknowledgements

> *Landing on the Moon: One small step for man, one giant leap for mankind.*
> *Getting a Ph.D.: Giant leap for one person, tiny, insignificant step for mankind.*
> – PHD Comics, Jorge Cham 2014

When I was accepted for the PhD position at KIT, I was the happiest person in Karlsruhe. But the happiness did not last long. Until the end of the second year of my work, the only thesis I could write would be entitled *365 ways to say 'It doesn't work'.* Unfortunately, that would suffice only for one year. The figure below presents the hours I worked monthly during my contract at KIT. It felt as though my efforts were leading me nowhere.

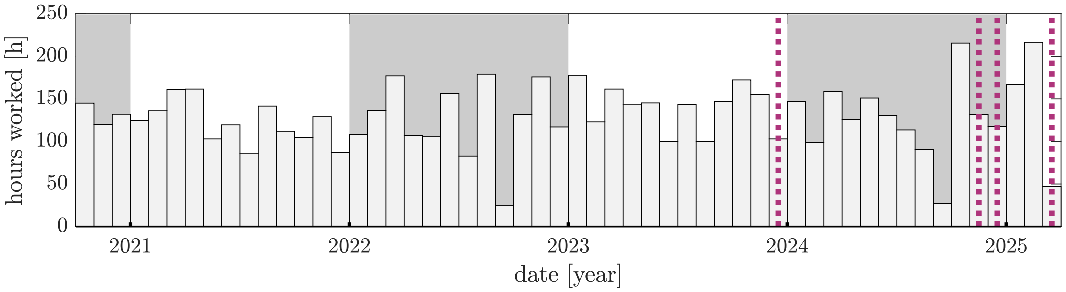

I am very thankful to my supervisor, Carsten Rockstuhl, for his patience. It was only after these two years that he suggested that I should have some results to publish. *Somehow*, I was finally able to mark the months in the figure when my manuscripts were accepted; with the last mark indicating that after 6,978 hours of work, I submitted this PhD thesis. I am grateful to everyone that contributed to this miracle.

Thank you, Prof. Rockstuhl, for being an invaluable scientific supervisor and such a good, genuine person, supportive and understanding. Thank you for your time, for your corrections at 3 AM, for patiently adding articles to my sentences and for tolerating my disruptive ideas. I appreciate your exceptional leadership of an amazing research group that I had the pleasure to be a part of and have so much fun with.

I want to thank my second PhD advisor, Willy Dörfler, for his support on our joint project, for feedback on this thesis and for introducing me to Mariia Sukhova who became not only a priceless collaborator but also a supportive friend.

I would like to express my gratitude to John Sipe for his supervision at the University of Toronto. I appreciate all the meetings and helpful discussions we had. I want to thank also Milica Banic and Colin Vendromin from the University of Toronto for their additional scientific support during my research project there.

I am thankful to Yiyang Bao for our joint project on neural networks. I appreciate her hard work and great ideas. I am thankful to her and Christian Koos for this cooperation, including sharing the Ansys Lumerical licence.

Many thanks to Lukas Rebholz and Ivan Fernandez-Corbaton for saving my three letters. Lukas is a superhero – helped me understand the computational and physical aspects of whispering gallery resonators. Ivan is a great scientist, it was an honour to work with him.

I appreciate my mathematics advisors, Mariia Sukhova and Piotr Idzik. Even though the mathematicians cause many problems, they are truly good people.

I want to thank Lina Kuhn for teaching me how to use PyTorch for the very first time.

Thanks to Jasmin Hörter and Ivan Kondov from the Scientific Computing Center at KIT for allowing me to continue my PhD research.

I am grateful to Elli Stamatopoulou and Piotr Idzik for reading the entire thesis and providing suggestions for improvement; to Marie Louise Schubert for reviewing Chapter 2 and 3, to Lukas Rebholz for checking Chapter 6, and to Mariia Sukhova for suggested corrections to Subsection 2.3.1 and Appendix A.

I would like to thank my current office-mates: Mariia Poleva for always being open to gossip and life talks, and Nigar Asadova for her inspiring focus on work.

Thanks to Xavier García Santiago for helping me getting started and to Marjan Krstić for being friendly and supportive colleague.

I want to thank Mitchell Whittam for his invaluable mental support and that we could go through this *PhD drama* together and... accomplish it!

I am thankful to Raghavendran Sivasubramanian for understanding the PhD drama and his hints on pushing my project forward.

No one mentions this in academia but I want to say it: thanks to the Reviewer no. 2.

I appreciate the financial support from CRC 1173 *Wave phenomena: analysis and numerics*, Karlsruhe House of Young Scientists (KHYS), Mitacs Globalink Research Award and NHR@KIT. I am thankful to the company JCMwave for providing the FEM Maxwell solver JCMsuite free of charge.

Thank God that throughout nearly five years of PhD work, the PhD drama was my biggest concern. I am glad I did not encounter serious life issues. Thank You for sparing me from them.

I would like to thank my family and friends – it is hard to list all of you and difficult to specify how you have influenced me before and during my work on this thesis.

I want to say *dziękuję* to my mum, Bogusława Czupryńska-Paszkiewicz. Thank you for believing in me, for encouraging me to solve 20 more maths problems in primary school, and that you solved 100 more to support me while I was preparing to mathematics exams during studies. I also want to thank my dad, Adam Paszkiewicz. He was the first to help me understand the concept of waves and Maxwell's equations many years ago, even before I knew I would need them for my PhD.

I want to thank Piotr Idzik for his love, endless support, constructive feedback and... forgiving me breaking that pebble!

Selbstständigkeitserklärung

Eidesstattliche Versicherung gemäß § 13 Absatz 2 Ziffer 3 der Promotionsordnung des Karlsruher Instituts für Technologie (KIT) für die KIT-Fakultät für Physik:

1. Bei der eingereichten Dissertation zu dem Thema
   "Light propagation in free-form dielectric waveguides:
   a modal perspective"
   handelt es sich um meine eigenständig erbrachte Leistung.
2. Ich habe nur die angegebenen Quellen und Hilfsmittel benutzt und mich keiner unzulässigen Hilfe Dritter bedient. Insbesondere habe ich wörtlich oder sinngemäß aus anderen Werken übernommene Inhalte als solche kenntlich gemacht.
3. Die Arbeit oder Teile davon habe ich wie folgt/ bislang nicht[1] an einer Hochschule des In- oder Auslands als Bestandteil einer Prüfungs- oder Qualifikationsleistung vorgelegt.

   Titel der Arbeit:

   Hochschule und Jahr:

   Art der Prüfungs- oder Qualifikationsleistung:
4. Die Richtigkeit der vorstehenden Erklärungen bestätige ich.
5. Die Bedeutung der eidesstattlichen Versicherung und die strafrechtlichen Folgen einer unrichtigen oder unvollständigen eidesstattlichen Versicherung sind mir bekannt.

Ich versichere an Eides statt, dass ich nach bestem Wissen die reine Wahrheit erklärt und nichts verschwiegen habe.

Ort und Datum   Unterschrift

---

[1] Nicht Zutreffendes streichen. Bei Bejahung sind anzugeben: der Titel der andernorts vorgelegten Arbeit, die Hochschule, das Jahr der Vorlage und die Art der Prüfungs- oder Qualifikationsleistung.